# Multiscale X-ray Approaches Towards the Structure and Function of Pyrolysis and Hydrothermal Carbons

LUKE JOSEPH ROY HIGGINS
SCHOOL OF CHEMICAL & PROCESS ENGINEERING
UNIVERSITY OF LEEDS


SUBMITTED IN ACCORDANCE WITH THE REQUIREMENTS FOR THE DEGREE OF
DOCTOR OF PHILOSOPHY AND MASTER OF SCIENCE

31st March 2021

# Intellectual Property and Publication Statement

The candidate confirms that the work submitted is his own, except where work which has formed part of jointly authored publications has been included. The contribution of the candidate and the other authors to this work has been explicitly indicated below. The candidate confirms that appropriate credit has been given within the thesis where reference has been made to the work of others.

The work in Chapter 3 – "Evidence for a Core-Shell Structure of Hydrothermal Carbon" was published in *Carbon*:

Higgins, L. J. R., Brown, A. P., Harrington, J. P., Ross, A. B., Kaulich, B., Mishra, B. Evidence for a core-shell structure of hydrothermal carbon. *Carbon*. (2020). 161, 423–431.

The candidate conceptualised the project, designed the experimental methodology, collected the majority of the experimental data (STXM, TEM imaging, Laser Diffraction, Elemental Analysis and XRD), performed all experimental data analysis and drafted the article. Mr John P Harrington performed FIB-milling and FIB-SEM imaging, Dr. Elizabeth Wilneff performed environmental XPS and Dr. Jeanine Williams performed pyrolysis GC-MS.

The work in Chapter 4 – "Bulk Structural Insight for Sustainable Carbon by X-ray Raman Scattering" was published in *Physical Chemistry Chemical Physics (PCCP)*:

Higgins, L. J. R., Sahle, C. J., Balasubramanian, M., & Mishra, B. (2020). X-ray Raman scattering for bulk chemical and structural insight into green carbon. *Physical Chemistry Chemical Physics*, 22(33), 18435–18446.

The candidate conceptualised the project, designed the experimental methodology, collected all experimental data (STXM-NEXAFS, XRSS, Elemental Analysis), performed the majority of experimental data analysis and drafted the article. The candidate acknowledges Dr. Chrisoph Sahle (ESRF) who performed DFT calculations using the ERKALE software to calculate simulated XRS spectra using structures initially prepared by the candidate.

# *Acknowledgements*

My supervisors, Andy Ross, Andy Brown and Bhoopesh have been a constant inspiration to me throughout this project. Thank you each for your patience, insight and humour, without which, this project would not have been nearly as productive or enjoyable. Bhoopesh, I would not have stayed past the first few weeks of this PhD without you. You have been a mentor throughout and have driven me to where I am now. For this, I am eternally thankful and I hope both our friendship and collaboration continues long into the future.

I am thankful for joining the Centre for Doctoral Training in Bioenergy in 2016. Thank you to each of the many people who have made my progression through postgraduate training so smooth, especially Jenny, James and Emily. My time in the CDT also led to the formation of solid friendships built on a love of science, coffee and beer. Thank you to all the 2016 cohort of CDT students, in particular Toby, Andy, Fernando & Aaron for sticking through it with me. I have enjoyed our time putting the world right on St. George's field over strong coffee and *Bakery 164* sandwiches.

Throughout my PhD I have relied on the skill and experience of others. In particular, Christoph Sahle performed some DFT calculations for me, Jeanine Williams provided assistance with pyrolysis GC-MS and Beth Willneff performed the NAP-XPS used here. I would also like to thank those within the wider synchrotron community who have been invaluable sources of knowledge and enthusiasm. From the Advanced Photon Source, thank you to Mali, Matt and Steve - your kindness and deep knowledge of synchrotron radiation has been inspiring. At the ESRF, thank you to Chiara, Anna, Blanca, Marco and Christoph for taking me on at ID-20 for six weeks and for introducing me to *La Toscana*. At Diamond, thank you to Burkhard, Majid and Tohru from I08, Shashi from I13, Giannantonio from B18 and Fred from I20, who first introduced me to X-ray science at UKC. I would especially like to thank both Mali and Christoph who have taught me the mysteries of X-ray Raman scattering and make returning to their sectors feel more like visiting friends than performing user science.

Beyond the beamline, there have been many people who have influenced both me and this project, more than I can mention in this space - I thank each of you. I would particularly like to thank the skilled technicians who have lent their practised hands to this project: Rob, Martin, Simon and Adrian. Those members of the hydrothermal carbon community who I look forward to collaborating with in the future: Magda, Jingyu, Aidan and Kenneth. Those members of the School of Chemical and Process Engineering who have been invaluable to me and this project: Sven, Rik, Beth, Nicole, John, Zabeeda, Mark, Martha, Thoko, Laila, Sin-Yuen, Bethan, Jeanine, Helen and Tim. Finally I want to thank the current members of the Mishra group, Flora, Innes, Stella and Katherine, each of whom are remarkable scientists with whom I am excited to continue working.

Beyond the science, there are those that have provided their support in a less tangible, but more important, way - I take none of you for granted. Thank you to my Family for their constant support, despite their total lack of comprehension about what I do (honestly it is very refreshing to talk about something else sometimes). Thanks also to my close friends Michael, Joe and Ewan, who have remained constant companions over the past sixteen years. Finally and most importantly, I want to thank my partner Jenny, without whom this project would not have been possible.

I acknowledge the EPSRC who funded this project, granted me a six month funded extension in response to COVID-19 and who are funding the next stage of my development.

# *Acknowledgements - Facilities Access*

**APS Sector 20**
This research used resources of the Advanced Photon Source, an Office of Science User Facility operated for the U.S. Department of Energy (DOE) Office of Science by Argonne National Laboratory, and was supported by the U.S. DOE under Contract No. DE-AC02-06CH11357.

**APS Sector 13**
Portions of this work were performed at GeoSoilEnviroCARS (University of Chicago, Sector 13), Advanced Photon Source (APS), Argonne National Laboratory. GeoSoilEnviroCARS is supported by the National Science Foundation – Earth Sciences (EAR – 1634415) and Department of Energy- GeoSciences (DE-FG02-94ER14466). This research used resources of the Advanced Photon Source, a U.S. Department of Energy (DOE) Office of Science User Facility operated for the DOE Office of Science by Argonne National Laboratory under Contract No. DE-AC02-06CH11357.

**APS Sector 10**
MRCAT operations are supported by the Department of Energy and the MRCAT member institutions. This research used resources of the Advanced Photon Source, a U.S. Department of Energy (DOE) Office of Science User Facility operated for the DOE Office of Science by Argonne National Laboratory under Contract No. DE-AC02-06CH11357.

**European Synchrotron Radiation Facility Beamline ID-20**
Portions of this work were carried out with the support of the European Synchrotron radiation Facility on Beamline ID-20 (Inelastic X-ray Scattering).

**Diamond Lightsource Beamline I-08**
Portions of this work were carried out with the support of Diamond Light Source, scanning transmission X-ray microscope on beamline I-08 (proposals: MG23583, MG22730, SP19228)

**Diamond Lightsource Beamline I-13**
Portions of this work were carried out with the support of Diamond Light Source, X-ray microtomography on beamline I-13-2 (proposal: MT20657)

**Leeds Electron Microscopy and Spectroscopy Centre (LEMAS)**
Electron microscopy and focussed ion beam milling were carried out at the Leeds Electron Microscopy and Spectroscopy (LEMAS) centre at the University of Leeds, UK.

**Versatile X-ray Spectroscopy Facility**
Near ambient pressure XPS data were collected at the Versatile X-ray Spectroscopy Facility (VXSF) at the University of Leeds, UK.

**Advanced Research Computing Facility**
Portions of this work was undertaken on ARC3, part of the High Performance Computing facilities at the University of Leeds, UK.

**ESRF RNICE cluster**
Portions of this work was undertaken on RNICE, part of the High Performance Computing facilities at the European Synchrotron Radiation Facility.

# *Abstract*

**Multiscale X-ray Approaches Towards the Structure and Function of Pyrolysis and Hydrothermal Carbons**

A paradigm shift is required to reduce current dependence on finite fossil resources and to remain within planetary boundaries. In response, a 21st century bioeconomy, where materials, chemicals and fuels are produced sustainably from biomass, is being developed. Pyrolysis and Hydrothermal Carbonisation (HTC) represent two biorefinery approaches to produce high-value carbon devices from biomass. To realise their potential, a mechanistic understanding of these carbonisation processes is required. This thesis utilises synchrotron X-ray science to study the structure and function of pyrolysis and hydrothermal carbon.

Scanning transmission X-ray and electron microscopy provide experimental evidence for a core-shell structure of carbohydrate-derived hydrothermal carbon. Mechanistic pathways differ between the core and shell of hydrothermal spherical carbons. Near-edge X-ray absorption spectra (NEXAFS) show that, at the water-carbon interface, carboxylic species drive growth. In the core, condensation dominates, removing linking units between polyfuranic domains.

X-ray Raman scattering spectroscopy (XRSS) is presented as a novel tool to study the C *K*-edge of sustainable carbons in bulk and *in-situ*. Experiment and density functional theory demonstrate that biomass-derived hydrothermal carbon is composed of a furanic local structural motif linked at the $\alpha$-carbon. Two pyrolysis carbons produced at 450 °C and 650 °C are used to demonstrate XRSS as a route to a semi-quantitative measurement of aromatic condensation and highlight the advantages of XRSS over NEXAFS for these materials.

Pyrolysis carbon is widely used a sorbent for aqueous inorganic species. A multi-scale X-ray and electron spectromicroscopy approach provides mechanistic insight into the adsorption of $Au^{III}_{(aq)}$ onto pyrolysis carbon. Pyrolysis carbon shows a large capacity for reducing $Au^{III}_{(aq)}$ to nanoparticulate and micrometre-sized $Au^{0}$ clusters. Electron energy loss spectroscopy highlights mixed valence $Fe^{II:III}$ oxides as an active site for $Au^{III}_{(aq)}$ reduction. X-ray extended fine structure modelling shows that the maximum average $Au^{0}$ size forms between 13 - 26 $\mathrm{mg\,g^{-1}}$ gold:char ratio, above this, ultrafine $Au^{0}$ dominates.

# Contents

# List of Figures

# List of Tables

# Abbreviations

| | |
|---|---|
| AAS | Atomic Absorption Spectrometry |
| AC | Activated Carbon |
| APS | Advanced Photon Source |
| BSE | Back-Scattered Electron |
| DLS | Diamond Light Source Ltd. |
| DDSC | Double Differential Scattering Cross Section |
| EAC | Electron Accepting Capacity |
| EDC | Electron Donating Capacity |
| EDX | Energy Dispersive X-ray Spectroscopy |
| EEL | Electron Energy Loss (spectroscopy) |
| EXAFS | Extended X-ray Absorption Fine Structure (spectroscopy) |
| FCC | Face Centred Cubic (lattice) |
| FIB | Focused Ion Beam |
| GAC | Granular Activated Carbon |
| GHGs | Green House Gases (e.g. $CO_2, CH_4, NOx,$ Halogens etc) |
| HAADF | High-Angle Annular Dark Field (imaging) |
| HCW | Hot-Compressed Water |
| HMF | 5-Hydroxymethylfurfural $C_6H_6O_3$ |
| HRTEM | High-Resolution Transmission Electron Microscope |
| HTC | Hydrothermal Carbonisation |
| NEXAFS | Near edge X-ray Absorption Fine Structure (spectroscopy) |
| NRIXS | Non-Resonant Inelastic X-ray Scattering |
| NMR | Nuclear Magnetic Resonance (spectroscopy) |
| PAC | Powdered Activated Carbon |
| PCA | Principal Component Analysis |
| SAED | Selected Area Electron Diffraction |
| SAXS | Small Angle X-ray Scattering |
| SEM | Scanning Electron Microscopy |
| SRF | Synchrotron Radiation Facility |
| S/TEM | (Scanning) Transmission Electron Microscopy |
| STXM | Scanning Transmission X-ray Microscopy |
| UK | United Kingdom of Great Britain and Northern Ireland |
| UN | United Nations |
| WAXS | Wide Angle Scattering |
| XANES | X-ray Absorption Near-Edge Structure |
| XAS | X-ray Absorption Spectroscopy |
| X$\mu$T | X-ray microtomography |
| XRD | X-ray Diffraction (powder) |
| XRSS | X-ray Raman Scattering Spectroscopy |

# Chapter 1

# Introduction

The concentration of $CO_2$ in the Earth's atmosphere has increased rapidly since the beginning of the 20th century, to surpassing 415 ppm in December 2020 from a pre-industrial average of 275 ppm [1, 2]. Global emissions of $CO_2$ and other greenhouse gases (GHGs) are responsible for the continuing rise of global temperatures, resulting in a likely increase of $2.0\,^{\circ}\mathrm{C}$ to $4.89\,^{\circ}\mathrm{C}$ over the next 80 years [3]. The long-term impacts of global warming are difficult to predict, however some effects are now starkly apparent (i.e. sea-level rise, extreme weather) [4]. As acknowledged by the 2015 Paris agreement, these climatic changes are directly linked to the release of GHGs through human activities (e.g. fossil fuel combustion) [5]. However, GHG emissions are merely one symptom of humanity existing beyond Earth's planetary boundaries. Human development to date has been guided by a flawed model of economic growth at any cost. This growth model exploits Earth's soil, water and fossil resources for profit.

Prior to the 20th century, most materials such as solvents, fuels and fibres were derived from non-edible biomass. However, the emergence of cheap oil has led to many products being produced almost solely from fossil resources. Currently, almost all this "stuff" inevitably and invisibly transforms into "waste", damaging the environment and releasing GHGs. In order to remain within Earth's planetary boundaries, we must transition to a circular economy whereby "waste" is captured as a valued resource. This biorefinery model requires thermochemical processes, able to produce useful materials and re-capture resources safely and sustainably. To achieve this goal, a mechanistic understanding of the chemistry underpinning potential processes must be achieved. This thesis attempts to understand the structure and function of carbon materials produced from waste biomass by applying multiscale X-ray techniques.

## 1.1 Planetary Boundaries

For the past 10,000 years, planet Earth has existed in a period of relative climate stability known as the holocene epoch. Prior to this period, ice-core measurements have shown that the climate had been in an extended period of flux, unsuitable for human civilisation to thrive [6, 7]. The holocene epoch has offered a planet with stable temperatures, widely available freshwater and stable biogeochemical processes, providing a safe-space for humanity to thrive and innovate. Since the early 20th century, changes in the state of the Earth system have been shown to be occurring rapidly. Biogeochemical and carbon flows have been interrupted by climate extremes and intensive farming [8, 9], human pollution has resulted in toxification of landscapes [10, 11] and climate change is being driven by anthropogenic emissions [12]. Such rapid changes to the delicate Earth system balance have been shown to be directly related to human activities [4]. A new era of human induced instability has dawned: the anthropocene [13].

It is considered likely that the rapid anthropic changes to the Earth system state could trigger climate destabilisation or other non-linear changes to our environment. *Rockström et.al.* have proposed a series of planetary boundaries, which represent nine key Earth systems that if significantly modified, could result in non-linear, rapid changes to the environment [14, 15]. These are: (i) climate change, (ii) ocean acidification, (iii) chemical pollution, (iv) biochemical flows (e.g. N,P cycle), (v) freshwater availability, (vi) land-use change, (vii) biosphere integrity (e.g. biodiversity loss), (viii) air pollution and (ix) ozone depletion. The planetary boundaries are not necessarily of equal importance, with climate change and biosphere integrity recognised as of core importance. These boundaries provide humanity with guidelines for monitoring Earth-system changes and planning sustainable growth. However, whilst the planetary boundaries protect the Earth system as a whole, they do not consider the impact that changes in human emissions might have on social cohesion. For example, to protect the Earth system it might be recommended to cease the use of Haber-Bosch derived fertilisers to reduce nitrogen and phosphorous loading in the environment [16]. However, this would have a direct impact on feeding growing populations around the world by reducing crop yields, resulting in starvation, mass migration and other human catastrophes. In order to guide sustainable development for both planetary and human well-being, the economist *Raworth* proposed the Doughnut model in her book *Doughnut Economics* [17].

The Doughnut (Figure 1.1) nicely represents the balance between the nine planetary boundaries and the standards of human well-being established in 2015 by the UN sustainable development goals [18]. The nine planetary boundaries are shown around the circumference. The radar plot values in red show the extent that we are overshooting our planetary boundaries, or falling short of our social foundations. The principle of the doughnut is for humanity to exist and thrive within the safe space (light green) between the planetary boundaries and our social foundations (e.g. water, food, healthcare, literacy, and energy availability). In our societies, if we *overshoot* our planetary boundaries we place a pressure on the environment which could drive irreversible change. Likewise, a *shortfall* in our social foundation results in a suppression of human potential.

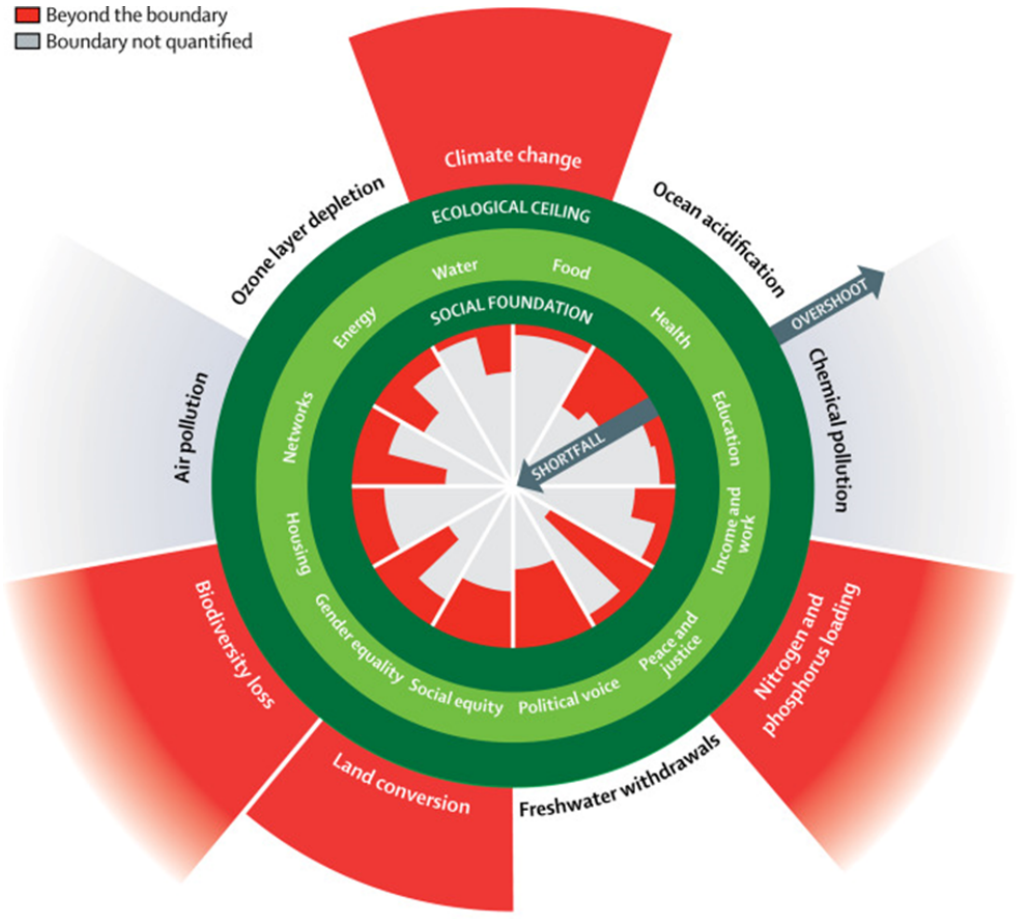


FIGURE 1.1: The Doughnut. Dark green circles show the social foundation, which no one should fall below and the ecological ceiling of the planetary boundary. Between the two lies a safe and just space for humanity. Red wedges show shortfalls in the social foundation or overshoot of the ecological ceiling. Figure reproduced from Ref. [17] under the CC BY 4.0 license.

The Doughnut acts as a simple and concise compass for assessing the current state of human and planetary well-being. It has been implemented for this purpose within academia, policy-making, progressive business, urban planning and civil society [17]. However, whilst The Doughnut might act a useful tool for guiding social and environmental change, it does not provide any pathway for sustainable development. Instead, governments are intentionally left to design and enact policy to meet legal obligations, such as those signed up to by UN member states (e.g. 2015 Sustainable Development Goals, 2015 Paris Agreement) [19].

Given that planetary boundaries only guide our choices, rather than define them, we must consider policy options which yield the greatest impact in guiding us to an ecological safe space. It is clear that unilateral change is required in multiple sectors, from transport to construction to monetary policy. However, this thesis forms part of research aiming to tackle climate change, which is thought to represent the current largest risk for irreversible planetary change [15, 20]. The currently proposed climate boundary is based on the principle of meeting the target of not exceeding $2\,^{\circ}\mathrm{C}$ of anthropogenic warming since the baseline year of 1990 [5, 12]. It is clear that this will require deep cuts to current GHG emissions, including a reduction of 25% in $CO_2$ emissions by 2030, with net zero emissions around 2070. To achieve these large reductions in GHG emissions, the use of fossil resources will need to be significantly curtailed. The manufacture of petrochemicals and their derivatives absorbs an increasing proportion of the world's oil and gas – approximately 14% for oil and 8% for gas [21]. If unrestricted, GHG emissions from the petrochemicals sector are expected to increase by 30% by the year 2050; increased emissions would be concomitant with increased land use change, fresh water usage and particulate pollution [21]. To limit this, chemistry must transition from the use of fossil resources wherever possible and create new processes and technologies for producing sustainable, efficient and performant materials.

## 1.2 The 21st Century Bioeconomy

Petrochemicals are set to become the largest driver of global oil consumption in the future [21, 22]. Transitioning from fossil to renewable carbon resources for the production of materials, chemicals and fuels can therefore result in significant GHG reductions. Waste biomass represents the most globally available and regenerative resource of renewable carbon [23].

This makes the utilisation of waste biomass an attractive alternative to fossil resources, providing future renewable bioenergy and bio-based chemicals with much lower GHG emissions [24, 25]. A key benefit of this approach is that waste biomass (e.g. agricultural residue, non-avoidable food waste) is recovered as a resource. This principle is called a circular economy. In comparison to a linear economy, where resources are produced into useful materials then disposed of as waste, a circular economy recovers these resources and re-uses or recycles them (Figure 1.2) [26]. In the proposed circular bio-economy, resources are derived from biomass wherever possible. The utilised biomass resource should neither compete with human food resources nor result in land-use change. Typically biomass feedstocks are wastes, such as agricultural residues (e.g. corn stover, rice husks), trimmings (e.g. forestry management cuttings), grasses and other non-food crops, waste natural fibres and food wastes. In particular food waste is a rich resource for biorefinery in most advanced economies [27]. In the UK, food waste from households and businesses is around $9.5\,\mathrm{Mt\,yr^{-1}}$, of which 70% is edible and only 30% is inedible. In 2019, this resulted in $25\,\mathrm{MtCO_2e}$ of associated emissions of a UK total of $460\,\mathrm{MtCO_2e}$ [28–30]. Such waste materials represent a treasure trove of untapped chemical potential for refinement and offers a sustainable path to replacing fossil resources.

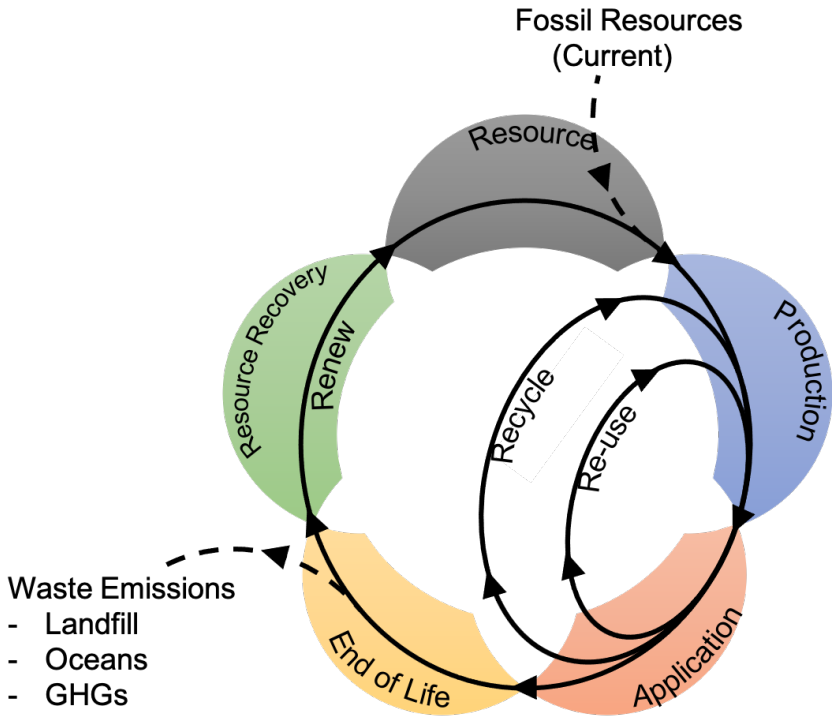


FIGURE 1.2: A model of a circular economy.

An increasing amount of new research is focused on the application of different technologies (including fermentation, hydrothermal conversion, pyrolysis and microwave treatment) to make chemicals from bio-waste and thus improve resource utilisation. When implemented together, the processes used to extract useful bio-chemicals, bio-fuels and bio-materials from waste biomass form a *Biorefinery* [25, 31]. A biorefinery, in many ways, mirrors a typical petrorefinery. Waste biomass is separated into building blocks (e.g. carbohydrates, proteins, waxes) which may be converted to value-added products, biofuels and chemicals. The production of chemicals and materials from biomass was common at the beginning of the 20th century before cheaper petroleum derivatives were available. Many fuels, dyes, solvents and synthetic fibres were directly produced from lignocellulosic biomass. However their synthesis, whilst sustained from biomass, was often unsafe and damaging to the environment. In contrast, modern biorefineries are designed around the principles of the circular economy and *Green Chemistry* [32]. Green chemistry offers a protocol when developing biorefinery processes and may play an important role in facilitating production of commodity chemicals from biomass [24, 33]. Throughout the whole product life cycle, energy demands should be minimised, safer processes used and hazardous chemical use and production avoided [34]. Biorefinery products should be designed with their end-of-life in mind, with simple approaches for resource recovery wherever possible. The final product should be non-toxic, degradable into innocuous chemicals and with minimum production of waste [32].

Biorefinery processes can be divided into four main groups: mechanical, biochemical, chemical and thermochemical processes [31]. Mechanical treatment is often applied first, changing the size, shape and density of the starting feedstock so that the following processes in the biorefinery can work more effectively. Biochemical treatments include enzymatic approaches, fermentation and anaerobic digestion, the latter of which is currently the most widely implemented [35]. These processes typically breakdown sugars to produce alcohols and organic acids. Enzymatic approaches may be used to produce useful sugars from municipal solid waste, whilst anaerobic digestion can be used to produce biogas for combustion. Chemical processes result in a change in the chemical structure of an existing molecule by reacting with other substances. The most common chemical processes in biomass conversion are hydrolysis and transesterification, both of which are used to produce biofuel [36]. However other chemical treatments such as Fisher-Tropsch synthesis and steam reforming are also valuable tools

to produce high-value chemicals and fuels [37]. Finally, thermochemical treatments include gasification, torrefaction, pyrolysis and hydrothermal treatments. These thermochemical processes can be used to produce syngas ($CO, H_2, CH_4$), bio-oils and carbons. Syngas can be used as a fuel, or upgraded for use in other process. Bio-oils can be refined to produce aromatic platform chemicals, including so-called BTX (benzene, toluene, xylene) chemicals, which are valuable and challenging to produce from non-fossil resources. Last, but not least, are the carbons produced from these processes, which represent an exciting route from waste biomass to sustainable carbon devices.

Carbons have been produced thermochemically from biomass for millennia. Charcoal, the product of incomplete combustion of biomass, has been utilised since pre-history as fuel, pigments and sorbents [38]. The microscopic structure of charcoal, derived from the initial biomass, was found to be an effective tool for purifying chemicals and removing pollutants. Johann Tobias Lowitz was one of the earliest to study the adsorptive properties of charcoal for the purification of beers, waxes and vinegar in the early 18th century [39]. An understanding of the local structure and chemistry of carbons was developed in the early 20th century. Activated carbon sorbents were produced from biomass, as well as coal, by applying an activation stage to increase the surface area of the final product [38, 40]. This allowed for highly effective sorbents, as well as carbon electrodes, pigments and catalyst supports. More recently, new allotropes of carbon, other than amorphous carbon, graphite or diamond, have been discovered with well-defined nanostructures such as graphene, fullerenes, carbon nanotubes (CNTs) and carbon foams. Development of these carbon materials for specific applications has been advancing rapidly. Energy storage devices (e.g. supercapacitors), embedded catalyst supports and electronics applications have all been investigated [41, 42]. The science of carbon has rapidly evolved from an understanding of two-dimensional structures, to a full range of dimensionality. In this way, carbon science is advancing into the realms of multi-scale control. This control allows for the construction of well-ordered three-dimensional bulk materials from lower-dimensional carbon building blocks. However, these advanced carbon materials generally come at a cost; requiring non-sustainable platform materials, producing poor yields and utilising high energy input techniques (e.g. chemical-vapour deposition, arc deposition) [43]. The race is now on to produce high-value carbon materials efficiently from waste biomass [44].

## 1.3 Sustainable Carbon Materials

The current challenge is to integrate advances in our understanding of carbon nanostructure and function with the principles of the biorefinery and green chemistry. The goal is to produce carbon materials using waste biomass, with very little environmental impact, yet to retain their functionality and efficacy. Figure 1.3 summarises the seven key principles of sustainable carbon production considered in this project, which are based on the principles of green chemistry [32, 44]. These principles may be summarised as the utilisation of natural, abundant and more sustainable precursors, coupled with atom-efficient, lower-energy synthetic processes to produce effective, well-characterised carbon materials designed with their global implementation and end-of-life in mind. Carbons that fulfil these criteria are called *Sustainable Carbons*.


FIGURE 1.3: The key principles of sustainable carbon materials.

Currently there is an explosion in research considering sustainable carbon materials from biomass [45]. The excitement in this field is driven by careful exploitation of structure and functionality within materials derived from the natural world. Examples of this biomimetic approach to highly-structured carbon materials derived from natural materials, such as crustacean shells or plant tissues, have been demonstrated [46]. These highly structured carbons allow for applications where fluid flow is critical, such as catalysis, adsorption and electrochemistry [41, 47, 48]. Furthermore, carbons with novel functionalities can be produced through

careful selection of the starting biomass, such as minerals within algae or organic functionalities within citrus fruits. This diversity of structure and function from the natural world has led to many successful sustainable carbon materials already finding their way into the marketplace. An example of a market-ready sustainable carbon would be Starbons [49]. Starbons are a class of ultra-high porosity carbon foams, derived from the pyrolysis of biomass-derived starch. Through careful choice of the starting biomass materials, it is possible to control the pore sizes of starbons whilst also introducing specific chemical functionalities (e.g. metal oxide nanoparticles). Other examples of successful sustainable carbons include glucose-derived aerogels and hydrothermally-produced carbon nanodots and supercapacitors. These high-technology applications of sustainable carbons are becoming increasingly common in the literature [50]. However, another application of sustainable carbons is in waste-management and agriculture. Carbonisation of wastes is being closely investigated as a way of producing non-hazardous carbon materials which can be used as an effective, low-carbon fuel [51]. Furthermore, the pyrolysis of waste biomass, can be used to produce biochar - the term for pyrolysis carbon applied directly to the soil [52, 53]. Pyrolysis carbons have been shown to produce significant improvements in terms of soil quality and fertility, whilst also offering a potential route to negative emissions through their widespread implementation [54, 55].

Other than the starting biomass resource itself, a range of thermochemical techniques are receiving renewed attention as routes towards sustainable carbons. These techniques have been utilised as part of the biorefinery for many years. However, the processes governing the production of sustainable carbons from biomass require further investigation. It is hoped that through building an understanding of the mechanisms underpinning the production of sustainable carbons, it might be possible to have increased structural and functional control over the final material, whilst also more efficiently using resources and energy. Using this approach, it might be possible to link the nanostructural control from multidimensional carbon materials with their sustainable production from biomass. This thesis focuses on the two most common thermochemical processes for the production of sustainable carbon: pyrolysis and hydrothermal carbonisation.

### 1.3.1 Pyrolysis

Pyrolysis carbon is the solid product produced by the thermal decomposition of biomass under anoxic or quasi-anoxic conditions - a process called pyrolysis. As well the solid pyrolysis carbon, pyrolysis also produces an oily product known as bio-oil and a mixture of gases ($CO, CH_4, H_2$) known as syngas. A significant amount of control over the ratio of the formed products can be exerted by altering the heating rate and heating temperature during pyrolysis [56]. In this way pyrolysis is typically classified as either *fast* or *slow*. Fast pyrolysis involves the rapid heating (< 2 s) of biomass at moderate temperatures of around 500 °C to produce high yields of bio-oil of up to 75 wt.% [57]. Bio-oil is a valuable product which may be used as a fuel, or further upgraded to produce valuable chemicals [58]. Alternatively slow pyrolysis, the focus of this project, focuses on the production of pyrolysis carbon and is performed over extended periods (typically greater than 30 mins) at higher temperatures. During slow pyrolysis, the ligninocellulosic structure of the starting biomass is altered (Figure 1.4), producing materials with large pore volumes, high surface areas and a wide variety of surface oxygen functionality. As a carbonisation technique, pyrolysis has been extensively applied to the production of industrial activated carbons.

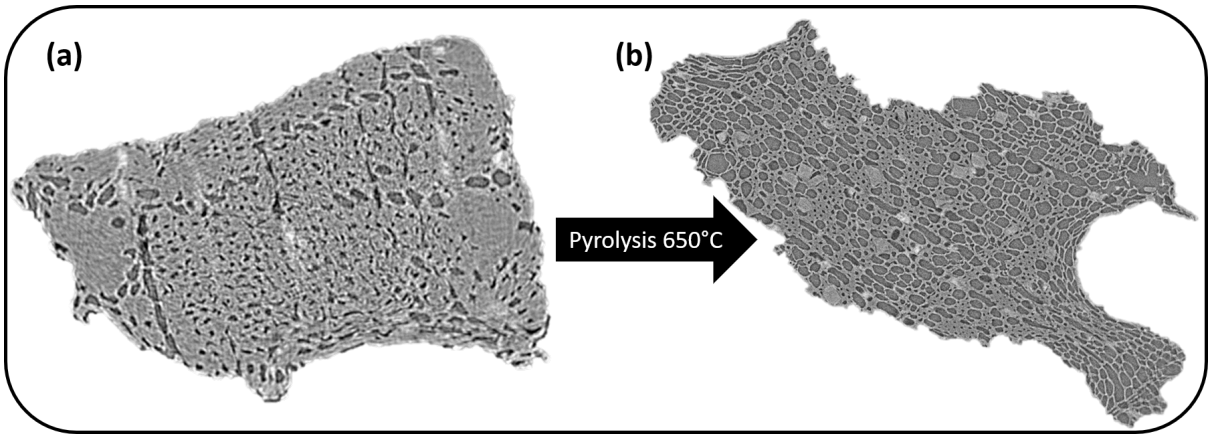


FIGURE 1.4: X-ray radiographs of oak wood (a) before and (b) after pyrolysis at 650 °C. The internal structure of the biomass is 'opened' producing large pore volumes and high surface areas.

Recently, attention has returned to pyrolysis carbonisation as a route to produce more sustainable carbon materials from biomass. The pyrolysis process itself results in the decomposition of the biomass components into a disordered carbon (see Section 1.4). In the last decade, pyrolysis carbon has become an internationally relevant topic in soil science, as a way of both

improving soil fertility, but also locking away carbon in the soil as a form of carbon sequestration [53, 54, 59]. Whilst this interest in pyrolysis carbons was initially focused on its roles in soil fertility, research has returned to pyrolysis as a process for producing sustainable carbon devices (e.g. supercapacitors, catalyst supports) [60, 61].

### 1.3.2 Hydrothermal Carbonisation

Hydrothermal carbon is the solid carbonaceous product formed during the thermochemical decomposition of biomass in a hot, autogenically-pressurised, aqueous environment (approx. 200 °C, 30 bar). This process is known as hydrothermal carbonisation (HTC) and, since its discovery over 100 years ago, it has re-emerged as a sustainable route to advanced carbonaceous materials (hydrothermal carbon) and chemicals (e.g. hydroxymethylfurfural) [62]. The development of hydrothermal carbonisation came during the early 20th century as Germany, a country with no crude oil resources, attempted to produce synthetic chemicals and fuels from coal [63]. Building on the advancements in high-pressure synthesis developed for the Haber-Bosch process, a range of new techniques for high pressure synthesis of hydrogen and synthetic fuel were introduced. These included hydrothermal liquefaction of coal and the Bergius process, which was strategically important during the inter-war and second world war era for the production of synthetic fuels and explosives.

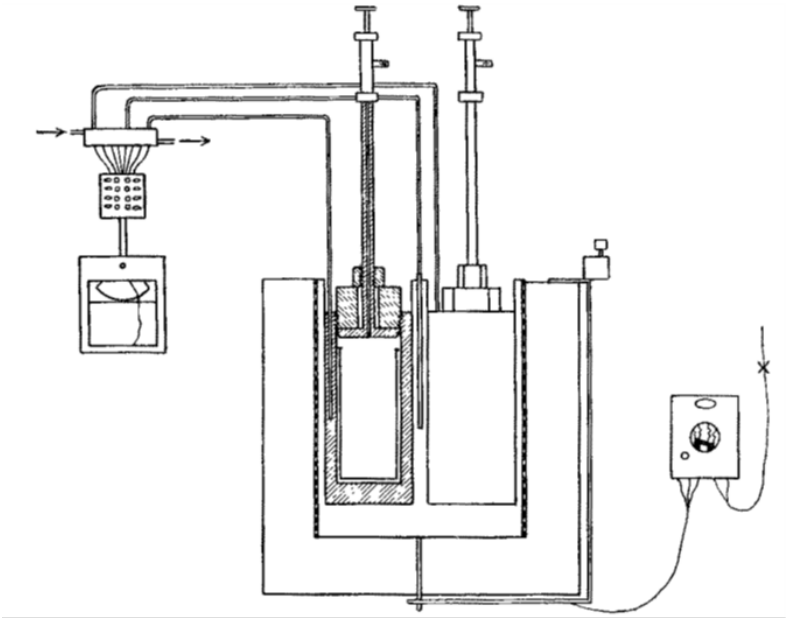

FIGURE 1.5: Semi-automatic, steel autoclave design used to perform coalification by Fredereich Bergius. Reprinted by permission from Springer Nature Ref. [64] (1928).

During the early stages of the development of high-pressure chemistry in Germany, Bergius investigated the process of coalification, whereby peat (and later cellulose) was transformed into a material with similar properties to coal (Figure 1.5). Bergius was awarded the 1931 nobel prize for his work in high-pressure chemistry with Carl Bosch. During the inter-war years, several studies were conducted in order to monitor the formation of 'bio-coal' through hydrothermal carbonisation, since the structure of coal was not known [64]. However, the introduction of cheap fossil resources in the years following the second world war combined with the banning and removal of high-pressure liquefaction technologies by the Russian army, meant that these sites were converted into petrorefineries and the science became temporarily irrelevant [63].

During the early 2000s a resurgence in HTC science was driven by the principles of biorefinery [43]. Since then, products from both the aqueous process water, which contains some important monomers, and the amorphous hydrothermal carbon material have maintained a high-level of research interest. This interest has been maintained, not only because of its credentials as a sustainable carbon, but because the process has some significant advantages over pyrolysis [65]. In a typical HTC process, the energy input required to produce HTC is much lower than pyrolysis, this is because the process is carried out at relatively low temperatures and under auto-generated pressures. Furthermore, HTC has the key benefit of being able to process 'wet' biomass, where the extremely costly pre-processing steps of drying and milling can be completely avoided. The char material produced is often comprised of spherical microparticles, which can fuse into a variety of shapes, their porosity can be well controlled using casting procedures and surface functionality easily controlled [44]. The (re)development of hydrothermal carbon materials has been rapid with laboratory scale production of carbon quantum dots, energy storage devices, fabrics and catalysts. Industrial application of HTC has also occurred in the waste management sector as a way to produce coal-like fuels from waste materials, as well as a route to make-safe hazardous biological and chemical wastes [66, 67].

## 1.4 X-ray Characterisation of the Structure and Function of Carbons

### 1.4.1 Graphitising and Non-Graphitising Carbon

Pyrolysis and HTC are now well-established thermochemical processes for the production of sustainable carbon materials. However, the structure and chemistry of the resulting carbons and the mechanisms producing them are still not fully understood. Pyrolysis carbons, carbon blacks (the solid carbon material produced from the pyrolysis of hydrocarbons in the gaseous phase) and coals have been under investigation for centuries [38]. The element carbon exists in a multiplicity of structural forms, more than any other element, due to its ability to form stable cyclical structures. These structural forms exhibit a huge range of properties, both physical and chemical. It is recognised that knowledge of the structure of both pyrolysis carbon and hydrothermal carbon at the molecular level is essential to the understanding and prediction of their valuable physical and chemical properties.

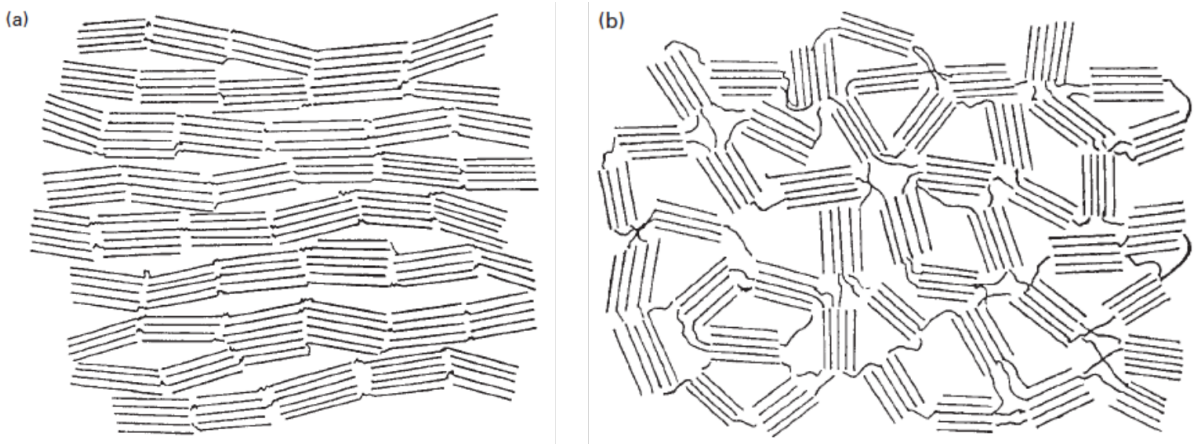


FIGURE 1.6: Franklin's representations of (a) graphitising and (b) non-graphitising carbon [68]

The study of the structure of carbon materials has been inextricably linked with X-ray science since the beginning. The structures of several carbon allotropes, namely graphite, diamond and lonsdaleite, were among the first to be solved using X-ray diffraction. Graphite was solved in this way by J. D. Bernal in 1924 [69]. The first studies of the local structure of pyrolysis carbon were performed by Rosalind Franklin whose pioneering powder X-ray diffraction (XRD) work defined two carbon types: *graphitising* and *non-graphitising* carbon [70, 71]. Franklin concluded that the structure of pyrolysis carbons depended not only on the process temperature, but

also on the nature of the starting material. Figure 1.6 shows Franklin's representations of non-graphitising and graphitising carbon. Graphitising carbons are composed of cross-linked crystallite domains, in which hexagonally-packed carbon atoms (graphene sheets) are aligned into planes. In non-graphitising carbon, the structural units are oriented randomly and the linking units are sufficiently strong to impede movement of the layers into a more parallel arrangement [72]. Franklin's model has since been shown to be incomplete, the supposed cross-linked graphitic crystallites are not strong-enough to inhibit graphitisation at temperatures > 2000 °C [73]. The atomic structure of chars and their resistance to graphitisation is still not understood [74]. This resistance to ordering, even at high temperatures, may be explained by the presence of fullerene-like $C_{60}$ structures [75, 76]. This model suggests non-graphitising carbons are composed of curved carbon sheets, in which fullerene-like structures are randomly dispersed throughout networks of 'traditional' six-membered carbon rings (Figure 1.7) [72, 76]. Evidence for the fullerene model of pyrolysis carbon is growing, and has been provided by HRTEM and EELS studies [77, 78]. Despite these advances however, the local structure of non-graphitising chars remains unsolved.

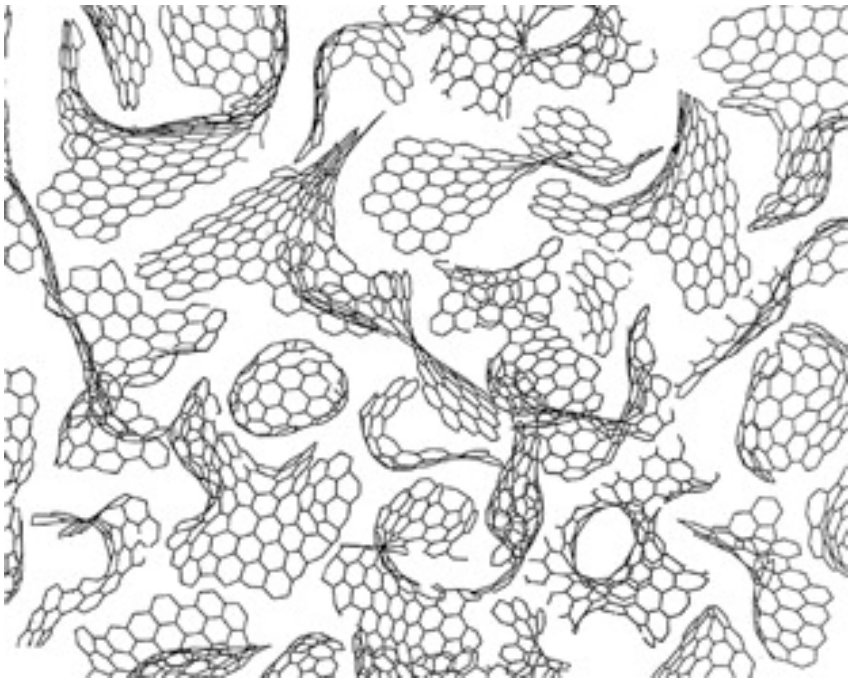

FIGURE 1.7: Schematic illustration of a model for the structure of non-graphitising carbons based on fullerene-like elements. Taken from *Harris et.al.* [75].

Both pyrolysis carbon and hydrothermal carbon have been classified as non-graphitising carbon [73, 79]. Neither carbon exhibits any significant degree of graphitic ordering, making the

understanding of their local structure very challenging. In addition, identification of surface functionalities becomes very important for their respective applications. Specifically, surface oxygen functionalities are highly relevant for the application of both hydrothermal and pyrolysis carbons in many fields, such as lithium-ion batteries, supercapacitors, catalyst supports and filtration. X-ray photoelectron spectroscopy, Raman spectroscopy and FT-IR in conjunction with wet chemistry experiments such as Boehm titration, have highlighted the wide range of surface oxide functionalities and other heteroatom functionalities (e.g. O, N, S) responsible for the chemical properties of these carbons [80, 81]. However, whilst a reasonable understanding of the chemistry and processes underpinning HTC and pyrolysis are now available, there is still a significant amount yet to learn. Amorphous carbon materials such as pyrolysis carbon and hydrothermal carbon, are naturally difficult to characterise due to their lack of long-range ordering. This is compounded by the difficulty of performing spectroscopy under the high-temperature or high-pressure conditions under which both HTC and pyrolysis are performed. A new approach is required to study the local-structure of these complex non-graphitising sustainable carbons.

### 1.4.2 A Modern Reductionist Approach

Many of the properties of sustainable carbons, which make them attractive for their traditional applications, are macroscopic and well-understood [82, 83]. For example, carbons have been produced from biomass for applications such as filtration and soil amendment for centuries, if not millennia. Techniques for processing carbons for these applications have slowly evolved through trial and error by their practical implementation - the result of practised hands passing down their knowledge. Examples of this include: isolating certain biomass which produce very large surface areas for improved adsorption (e.g. coconut husks) and fine-tuning pyrolysis conditions for producing fuels or pigments [84]. It is true that this 'top-down' approach to producing carbon materials has been very effective; pyrolysis-derived products are both widespread and performant. However, the design and implementation of sustainable carbon materials for new applications relevant for the 21st century must be more agile, less tolerant of inefficiencies and must have a firm understanding of the mechanisms governing useful properties. In order to achieve this goal, a new reductionist approach is required to seek mechanisms and pathways which can be exploited.

This project has taken a reductionist approach to studying sustainable carbon materials. Central to this approach are the "four elements" of materials science: processing, structure, physical properties & function and technological implementation [85]. Here, the structure and function of both pyrolysis carbon and hydrothermal carbon is studied at the molecular scale. It is hoped that this will provide insight into the carbon properties and the processes which form them. To achieve this, this project utilises state-of-the-art synchrotron radiation imaging and spectroscopy. The modern 3rd generation synchrotron is an electron accelerator, built to provide ultra-bright (brilliant) X-rays for probing the structure and chemistry of materials. In particular, this thesis utilises the ability to tune the energy of the extremely brilliant X-rays to perform spectroscopy, and the high-collimation of the X-rays to perform imaging [86, 87]. Together, the properties of synchrotron radiation allow one to conduct science that is not possible in the laboratory. This project has applied Scanning Transmission X-ray Microscopy and X-ray Raman Scattering Spectroscopy to pyrolysis and hydrothermal carbon for the first time, to attempt to capture the complexity and scale of these materials and to guide future technological development.

## 1.5 Scope of this Thesis

There is an urgent need for sustainable technologies to reduce the emission of GHGs and limit the impact of climate change. The biorefinery of chemicals, fuels and materials from waste biomass appears to be one key pathway to the production of materials currently available only from fossil resources. These biorefineries will likely produce carbohydrates or lignin-based materials that are not currently suitable for refinement into chemicals, but are a valuable resource for producing sustainable carbon. Many other industries produce a significant amount of waste biomass (e.g. agricultural waste, municipal waste, organic food waste, sewage sludge and paper pulps) which is currently left to decompose, releasing large quantities of GHGs. Carbonisation technologies may therefore present a resource-recovery option for current biomass wastes and future biorefinery byproducts. Produced sustainable carbons may be utilised as lower-impact combustion fuels, as soil amendments or as a route to high-technology products. However, the carbonisation processes underpinning the production of sustainable carbon materials require a more detailed level of understanding than is currently available. Much of the carbon chemistry underpinning the production of these carbons is not yet fully understood. This thesis applies recent advances in synchrotron radiation science to perform multiscale investigations on sustainable carbons produced by pyrolysis and HTC (Figure 1.8).

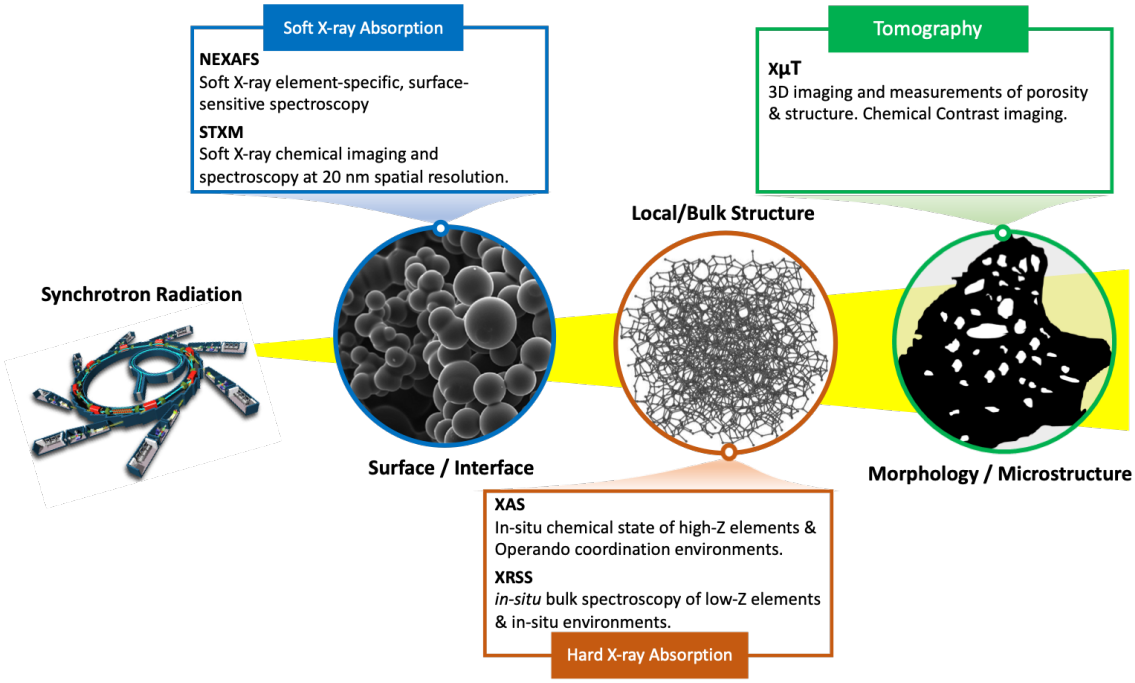


FIGURE 1.8: A multi-scale X-ray approach for investigating both the structure and function of sustainable carbon

In chapter 2, a brief outline of the techniques used throughout this thesis is given. This includes an introduction to theory of synchrotron radiation, X-ray absorption spectroscopy, scanning transmission X-ray spectroscopy, X-ray Raman scattering spectroscopy and X-ray microtomography. Chapter 2 also discusses the application of several other techniques used throughout this thesis such as electron microscopy, ion-beam milling and other laboratory techniques.

The main results of this work are presented in chapters 3, 4 and 5. Each chapter is composed of a brief summary of relevant literature, a summary of experimental methods used and the results themselves. The main aims of this thesis were as follows:

- To prove or disprove the presence of a core-shell type structure in carbohydrate-derived hydrothermal carbon and investigate implications for the accepted mechanism of HTC (Chapter 3).
- To assess the bulk local structure of hydrothermal carbon as a polymeric-like furan structure using X-ray Raman scattering spectroscopy (Chapter 4).
- To develop X-ray Raman scattering spectroscopy as a tool for investigating the local structure of both pyrolysis and hydrothermal carbons, making relevant comparisons with surface-based NEXAFS spectroscopy (Chapter 4).
- To study the uptake of $Au^{III}_{(aq)}$ reduction onto pyrolysis carbon, providing mechanistic insight into the function of carbon sorbents (Chapter 5).

It is hoped that the results presented in this thesis will guide future work in the production of sustainable carbon materials with tuneable properties for future applications. In addition, the results presented here should guide future X-ray based approaches for studying the complex structure and function of chars.

# Chapter 2

# Analytical Methodology

This chapter sets out the materials and techniques utilised within this project. A brief introductory theory of the key electron and X-ray techniques are presented here. General methodologies for techniques used in this project are also shown. However, where relevant and required, further details on methods and instrumentation are also discussed in a short methodology section at the beginning of each results chapter. Finally, X-ray and electron techniques are abbreviated throughout this thesis, a full list of abbreviations are provided for the reader.

## 2.1 Materials

Well characterised starting materials were used for the production of both pyrolysis carbon and hydrothermal carbon. This was done in order to have *a priori* knowledge of the material chemistry and the carbons produced after processing.

### 2.1.1 Carbohydrates

Standard carbohydrates were used as precursors for producing hydrothermal carbon. Carbohydrate derived hydrothermal carbon was used to study HTC formation and growth in Chapter 3. D-(+)-glucose (GLC), D-(+)-sucrose (SUC), D-(-)-Fructose (FRC) and D-(+)-xylose (XYL) were purchased from Sigma Aldrich with a purity of $\geq$ 99.5% and used as received.

### 2.1.2 Biomass

An important category of waste feedstocks for any potential medium to large scale production of both hydrothermal carbon and pyrolysis carbon is lignocellulosic biomass. In this project,

Spanish holm oak (*Quercus Ilex*), was selected as a model lignocellulosic feedstock. This material has previously been well-characterised as part of a European Union study on pyrolysis carbon production[1]. The holm oak biomass used for the study was donated by an industrial-scale pyrolysis facility. Both the industrial biochar, produced at 400 °C & 600 °C, and the raw biomass has been characterised by the Energieonderzoek Centrum Nederland (Netherlands Energy Research Centre) and the raw data is publicly available through the Phyllis-2 database [88]. In this study, the raw biomass was initially prepared by manual removal of the bark, before being milled (SM300 cutting mill, Retsch), sieved into a 1.0 - 2.0 mm size fraction then dried at 105 °C overnight. The resulting biomass was stored in sealed glassware. The hydrothermal carbon and pyrolysis carbon used in this project were produced in-house at the University of Leeds using the prepared holm oak biomass.

## 2.2 Pyrolysis

Laboratory pyrolysis of lignocellulosic biomass was performed using a modified vertical tube furnace. The modified furnace allowed for better temperature control as well as a tight seal to prevent ingress of oxygen during pyrolysis. All pyrolysis was conducted under nitrogen gas.

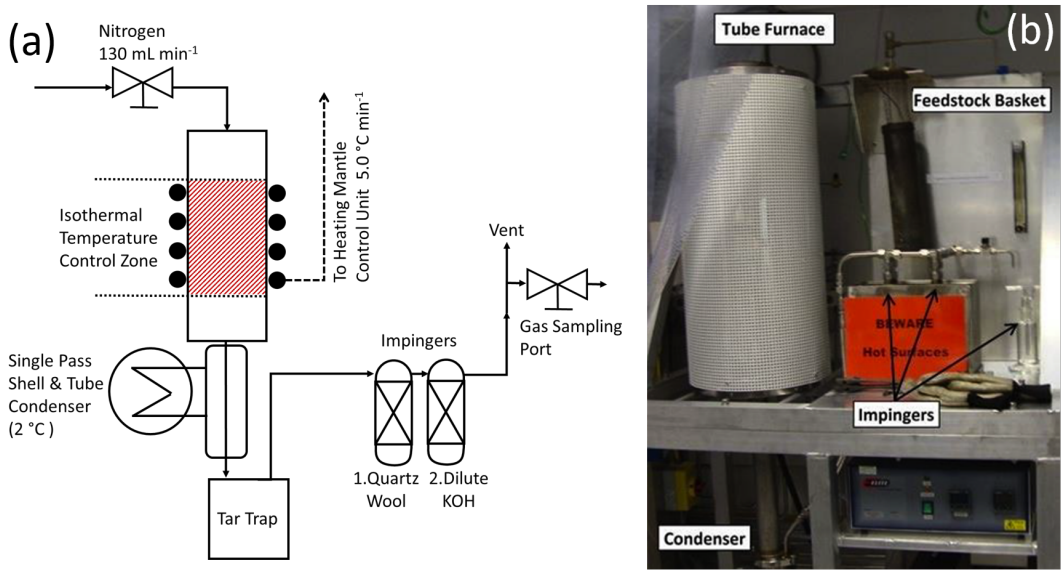


FIGURE 2.1: Schematic (a) and photograph (b) of the modified vertical pyrolysis reactor used to produce pyrolysis carbon.

[1]The project FERTIPLUS (Grant Agreement N° 289853) was co-funded by the European Commission, Directorate General for Research & Innovation, within the 7th Framework Programme of RTD, Theme 2 - Biotechnologies, Agriculture & Food.

Figure 2.1 shows a diagram and a photograph of the pyrolysis reactor used during this project. The furnace bore was 95 mm x 820 mm. Samples are mounted vertically within the tube furnace on a mesh basket with small $20\,\mathrm{ml}$ nickel crucibles, with $5\,\mathrm{g}$ of sample per crucible. Nitrogen gas (BOC, N2.0 grade) was fed through the top of the furnace at a rate of $130\,\mathrm{ml\,min^{-1}}$ to remove volatile organic compounds and create an inert atmosphere. Exhaust gases were passed through a condenser system, held at 2 °C using a water chiller, in order to cool volatile organic compounds and remove tars from the exhaust into the tar-trap below. After the tar-trap, the exhaust gases flow through two impingers. The first impinger contains fine quartz wool to trap further liquid or solid residues in the exhaust, whilst the second impinger contains a dilute solution of potassium hydroxide (0.05 $\mathrm{mol}$), to neutralise acid gases. The heating rate of the furnace was set to $5\,\mathrm{°C\,min^{-1}}$, held for 1 hour at the specified temperature, then cooled naturally at a rate of $0.4\,\mathrm{°C\,min^{-1}}$ to $1.4\,\mathrm{°C\,min^{-1}}$.

## 2.3 Hydrothermal Carbonisation

Hydrothermal carbonisation of both carbohydrates and lignocellulosic biomass was conducted in a modified, non-stirred $600\,\mathrm{ml}$ 4560 series Parr autoclave constructed in 316 stainless steel. The autoclave is rated to $350\,\mathrm{°C}$ and $200\,\mathrm{bar}$. This autoclave was selected for the ability to produce gram-scale amounts of carbon with close control and monitoring of temperature and pressure.

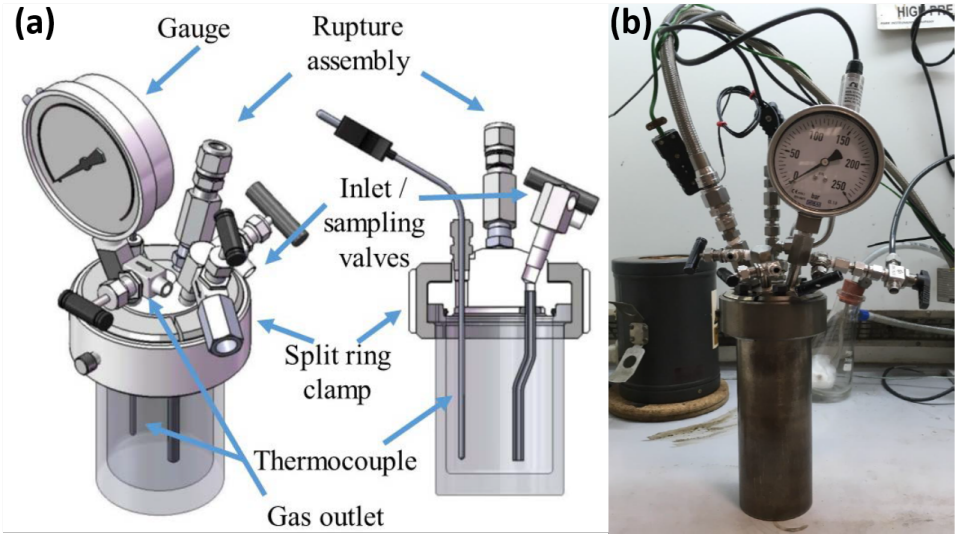


FIGURE 2.2: (a) Diagram and (b) photograph of the $600\,\mathrm{ml}$ Parr autoclave used in this project. Diagram taken with permission [89].

Figure 2.2 shows a diagram and photograph of the $600\,\mathrm{ml}$ autoclave. HTC was performed at temperatures between $200\,°\mathrm{C}$ to $250\,°\mathrm{C}$ under autogenic pressure. A 10% solid loading rate was used for all experiments; $24\,\mathrm{g}$ of feedstock and $220\,\mathrm{ml}$ of destilled, deionised water ($\geq 18\,\Omega\,\mathrm{cm}$). Aqueous/hydrated feedstock was loaded into an acid-washed (10% v/v $HNO_3$) quartz liner, then placed into the autoclave. Temperature was controlled using a 4836 temperature controller and a $1.1\,\mathrm{kW}$ heating mantle (Parr, USA). A proportional integral derivative controller controlled the heating mantle which was regularly calibrated using an 'autotune' function for water at $200\,°\mathrm{C}$ and $250\,°\mathrm{C}$. During an experiment, the autoclave was heated to the desired temperature at approximately $5\,°\mathrm{C\,min^{-1}}$; the reaction temperature was held for $1\,\mathrm{h}$. After reaction completion, the autoclave was cooled naturally by removing it from the heating mantle (approx. $120\,\mathrm{min}$ to room temperature from $200\,°\mathrm{C}$; $360\,\mathrm{min}$ from $250\,°\mathrm{C}$). Resulting carbons were recovered by filtration (Whatmann, grade 3) using copious water. The carbon was dried at $80\,°\mathrm{C}$ for 24 h and stored in sealed glass jars. Percentage yield was calculated by the quotient of the initial feedstock and the produced carbon on a dry basis.

## 2.4 General Laboratory Techniques

### 2.4.1 Elemental Analysis (CHNS & O)

Elemental analysis was performed using a FLASH-EA2000 instrument fitted with an autosampler and thermal conductivity detector (Thermo Scientific). He gas was used as a carrier (CP Grade), with flow rates of $140\,\mathrm{ml\,min^{-1}}$ (sample side) and $100\,\mathrm{ml\,min^{-1}}$ (reference side). For CHNS analysis, 1.5 – 2.5 $\mathrm{mg}$ of sample were sealed in tin squares. A pre-packed CHNS redox reactor (CE Instruments Ltd) was used with $O_2$ as the oxidising gas (BOC) at $900\,°\mathrm{C}$. Oxygen analysis was performed with 2 – 3.5 $\mathrm{mg}$ of sample sealed in silver squares. O analysis used a pre-packed pyrolysis reactor (Elemental Microanalysis Ltd) at $1050\,°\mathrm{C}$. CHNS analysis was performed using the following analytical reference materials: oatmeal (Elemental Microanalysis Ltd, B2276), BBOT (Sigma, 223999) and polystyrene (Elemental Microanalysis Ltd, B2023), barley flour (Elemental Microanalysis Ltd, B2277) was used for quality control. Oxygen analysis was performed using the following analytical reference materials: acetanilide (Elemental Microanalysis Ltd, B2000), aspartic acid (Elemental Microanalysis Ltd, B2042) and cysteine (Fisher), atropine (Elemental Microanalysis Ltd, B2002) was used for quality control.

### 2.4.2 Pyrolysis Gas Chromatography with Mass Spectroscopy (GC-MS)

GC-MS was applied using a pyrolyser unit to investigate the volatile organic compounds present on hydrothermal carbon. A Shimadzu 2010 GC-MS linked to a CDS 5200 series pyrolyser operating in trap mode was used. In the pyrolyser, the sample was heated to temperatures of $200\,^{\circ}\mathrm{C}$, $300\,^{\circ}\mathrm{C}$, $400\,^{\circ}\mathrm{C}$ up to a maximum of $500\,^{\circ}\mathrm{C}$ under an inert nitrogen gas (BOC N2.0) atmosphere and desorbed separately into the GC-MS. After pyrolysis the resulting products are trapped onto an adsorbent trap (Tenax TA) at $40\,^{\circ}\mathrm{C}$ by operating the CDS pyrolyser in adsorbent mode. The trap was then desorbed at $300\,^{\circ}\mathrm{C}$ in a flow of helium onto the chromatographic column. Gaseous pyrolysis products ($H_2, CO, CO_2, CH_4$ etc) were not trapped onto Tenax TA and were vented. The CDS 5200 pyrolysis unit was connected to a Shimadzu 2010 GC-MS. The products were separated on an RTX 1701 ($60\,\mathrm{m}$ capillary column, $0.25\,\mathrm{mm}$ inner diameter, $0.25\,\mu\mathrm{m}$ film thickness), using a temperature program of $40\,^{\circ}\mathrm{C}$, held for 2 mins, ramped to $280\,^{\circ}\mathrm{C}$ at a ramp rate of $10\,^{\circ}\mathrm{C\,min^{-1}}$ and held for 25 mins. The ion source was operated in electron ionisation (EI, $70\,\mathrm{eV}$) mode. The mass spectrometer interface temperature was held at $280\,^{\circ}\mathrm{C}$. A total ion current (TIC) mass range of 50-600 m/z was scanned. Chromatogram peaks were assigned using the NIST11 Mass Spectral Library Database.

### 2.4.3 Flame Atomic Absorption Spectrometry (flame AAS)

Flame AAS allows for the determination of the concentration of a given element, or analyte, within a sample. The sample analyte is nebulised into an acetylene, or mixed acetylene - nitrous oxide flame. The flame is used to dissociate the ions present in the introduced analyte, since complexes of the element of interest may introduce interference. A monochromatic light source of energy $E$ is shone down the length of the burner, of path-length $t$, containing the analyte flame. By selecting $E$ to be equal to a valence electron transition of the element of interest (typically in the UV or IR range), a reduction in initial intensity, $I_0$, proportional to the element's concentration in the analyte is observed. This relationship is called the Beer-Lambert law. Consider a beam of light passing though a burner flame of path length $t$, containing $N$ atoms per unit volume, as illustrated in Figure 2.3. As the beam passes through the flame, it reaches a point $x$ and travels a further infinitesimally small distance, $dx$ through the flame.

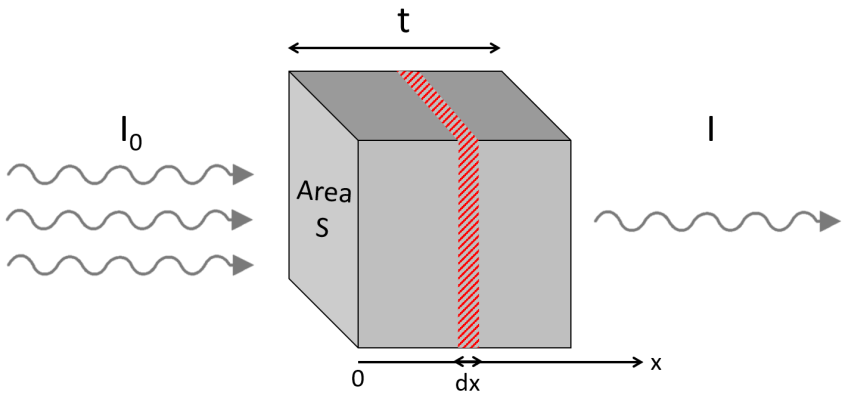


FIGURE 2.3: Illustration of the Beer-Lambert law.

The probability of an interaction between a photon and an atom is governed by the interaction cross-section $\sigma_A$. The number of atoms in the infinitesimal region is proportional to the illuminated area, S, and can be written as $NSdx$. The net probability of an atom being absorbed in the infinitesimal region is equal to:

$$(\sigma_A/S) \cdot NSdx = \sigma_A N dx$$

Given this, the number of photons emerging from the infinitesimal region per unit time is equal to the number of incident photons minus the average number removed:

$$dI(x) = I(x + dx) - I(x) = -I(x)\sigma_A N dx$$

This rearranges to:

$$\frac{dI((x)}{I(x)} = -\sigma_A N dx$$

Which may be integrated over the whole path length, $t$. The solution to this integral is:

$$\frac{I(t)}{I(0)} = \exp\left[-\sigma_A N t\right]$$

The quantity $\sigma_A N$ is commonly called the *attenuation coefficient*, has the unit $\mathrm{cm}^{-1}$ and describes how easily a volume of material can be penetrated by a beam of light. Substituting $\sigma_A N$ as the attenuation coefficient, $\mu$, gives the Beer-Lambert law:

$$\boxed{I = I_0 \exp\left[-\mu t\right]} \tag{2.1}$$

Using the Beer Lambert law (Equation 2.1), it is possible to calculate the concentration of the element of interest within the analyte. This is achieved by measuring the reduction in received photon intensity, $I$, at the detector, assuming that the attenuation coefficient $\mu$ is equivalent between a measured standard and the element of interest. Prepared samples were analysed using an Agilent Technologies 240FS flame Atomic Absorption Spectrometer. The spectrometer was fitted with a hollow cathode lamp and an Agilent Sample Introduction Pump System (SIPS). The SIPS system allows for semi-automatic dilution of the analyte. Atomisation was carried out by an air/acetylene flame. Standard additions of both the analyte and reagent blanks were performed using an external standard (utilised standards are further discussed in the relevant results chapters).

### 2.4.4 Laser Diffraction Particle Size Analysis

Particle size analysis was performed using laser diffraction in order to measure the particle size distribution of produced sustainable carbon materials. The technique uses laser diffraction to measure the mean particle size.

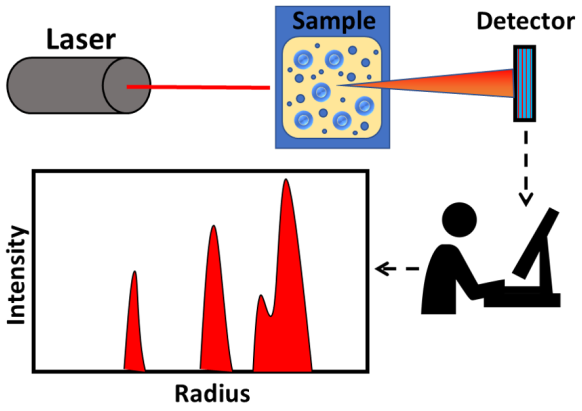


FIGURE 2.4: Schematic showing the principle of laser diffraction particle size analysis.

As in Figure 2.4, particles in suspension are passed through a laser beam which is scattered. The resultant scattering pattern is interpreted using Mie theory to produce a particle size distribution [90]. The particle size distribution is determined by matching the observed pattern with that expected from spherical particles of different sizes. During this project, a Malvern Instruments Mastersizer 2000 instrument was used to measure the mean particle size distribution by volume (D[4,3]) of hydrothermal carbon dispersed in water.

## 2.5 Electron Microscopy & Spectroscopy

Electron microscopy was used throughout this project to monitor changes in surface features, morphology and micro-structure at micrometre and sub-micrometre resolutions. The fundamental understanding that the electron can behave as a wave-like system with a wavelength much shorter than an optical photon is described by De Broglie's equation, which relates the wavelength of a particle $\lambda$ to its momentum $\mathbf{p}$ by the Planck constant $\hbar$ (Equation 2.2).

$$\boxed{\lambda = \frac{\hbar}{p}} \tag{2.2}$$

Given this understanding, it was shown that electrons, when in a vacuum, may be focused, bent and diffracted as if they were photons by applying an electromagnetic field [91]. The first electron microscope was patented in 1931, soon followed by the first published paper on the inelastic scattering of electrons for spectroscopy in 1941 [92]. These early experiments using electron optics were followed by a boom in the practical applications of electron optics after the Second World War. Since then, electron microscopy and spectroscopy has proved invaluable for the study of microstructure and structure-property relationships within all forms of matter.

### 2.5.1 Electron Interactions with Matter

Fundamental to the understanding of electron microscopy are the ways in which an accelerated electron may interact with the sample. Electrons may be used for both imaging and spectroscopy using elastically and inelastically scattered electrons respectively. These interactions are also relevant for other techniques discussed in this chapter.

Figure 2.5 shows a schematic representing the main interactions between sample and electron within an electron microscope. In a transmission electron microscope (TEM), the most common electron-sample scenario is a non-interaction, in which the electron passes unimpeded through a thin sample, typically less than a few hundred nanometres thick. Alternatively, an incident electron may be scattered. Electron scattering may be separated into elastic and inelastic scattering. Both elastic and inelastic scattering result in a change to the incident electron's momentum, with an inelastically scattered electron also changing its energy. Scattering

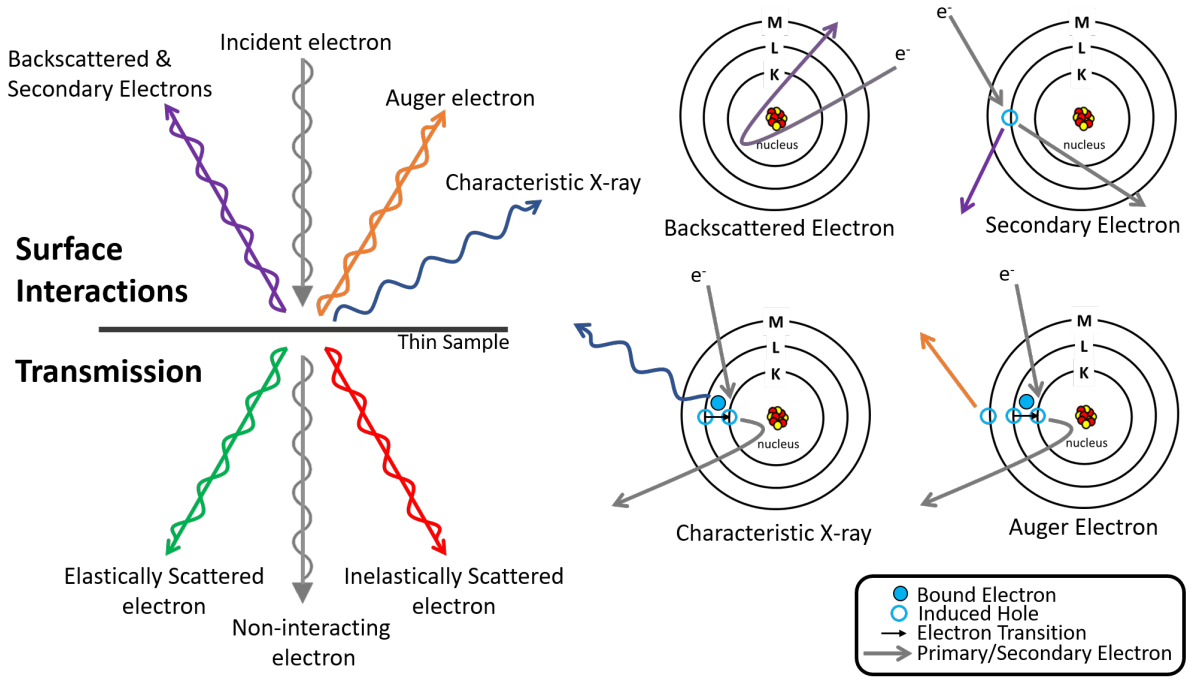


FIGURE 2.5: Schematic showing the interactions by which electrons may interact with matter in an electron microscope.

can further be defined by being either coherent or incoherent, where the electron wave remains in-phase or becomes out-of-phase respectively. Elastic and inelastic electron scattering are the principle interactions which enable the operation of a TEM. Elastic scattering is important in providing image contrast as well as for diffraction imaging. Inelastic scattering, due to the energy loss of the incident electron, is useful for electron spectroscopy. If the energy difference between the incident electron and the inelastically scattered electron is equivalent to a core electron energy, the inelastically scattered electron may be used to perform core electron energy loss (EEL) spectroscopy. EEL spectroscopy can be used to provide information regarding the valence, structure and bonding of an atom within the sample and is discussed separately in Section 2.5.2. Alternatively, at the surface of the sample, an electron may result in the ejection of a core electron producing a hole. After the ionisation of a core electron, the atom relaxes by either X-ray fluorescence, releasing a characteristic X-ray, or the ejection of an outer shell bound electron, called an Auger electron. Characteristic X-rays are measured using energy dispersive X-ray (EDX) spectroscopy, which can be used to fingerprint for the presence and quantities of specific atoms within the sample. Auger electrons may be used to perform Auger electron spectroscopy (AES), which is a surface-sensitive technique used to determine the specimen composition, but is beyond the scope of this project.

In a scanning electron microscope (SEM), there are two types of electrons used to produce an image: secondary and back-scattered electrons (BSE). These electrons are produced by surface interactions between the sample and incident electron. A back-scattered electron is produced by the coulombic interaction of the incident electron and the nucleus of a sample atom, resulting in a large back-scattering angle of some incident electrons. The average number of back scattered incident electrons is proportional to the charge on the scattering nucleus, providing a BSE image with chemical information about the sample. Secondary electrons are produced by the ionisation of a sample atom, resulting in secondary electron emission. Secondary electrons have very low energies (i.e. < 50 eV) which means they can only escape the sample from regions a few nanometres away from the surface. Images produced using secondary electrons can provide surface topographic information.

### 2.5.2 Transmission Electron Microscopy

Transmission electron microscopy is an electron imaging technique whereby a beam of electrons is transmitted through a thin specimen (e.g. < 200 $\mathrm{nm}$) to form an image using a series of electromagnetic optics. Transmission electron microscopy allows a user to investigate, with nanometre resolution, the structure and chemistry of the sample at sub-nanometre resolution. A typical TEM layout is shown in Figure 2.6. A beam of electrons is generated using an electron gun, which emits electrons with a known accelerating potential by thermionic emission (or by thermally-assisted tunnelling in field emission guns). Below the electron gun, there are two or more condenser lenses that de-magnify and control the size and brightness of the beam that illuminates the sample. Between the condenser lenses there is a condenser aperture which is used to control the convergence angle of the incident beam, which is a crucial factor in deciding both the resolution and the depth of field of the microscope. Below the condenser system is the specimen chamber, which is mechanically isolated to reduce any vibrations and is held under an ultra high vacuum (~$10 \times 10^{-10}$ $\mathrm{mbar}$). An energy dispersive X-ray (EDX) spectrometer is located in the same chamber to measure the characteristic X-rays generated from the illuminated region of the sample. As shown in Figure 2.6, between the objective lens and the projector lens is an intermediate lens and a series of apertures. The objective lens, situated around the sample chamber, forms the first intermediate image at the objective lens image plane. The ratio of the distance between the initial image to the objective lens, and the

objective lens to the specimen determines the image magnification. To form an image, the intermediate lens is focussed onto the intermediate image from the objective lens, this forms a secondary image which is magnified onto a detector or fluorescent screen by the projector lens system. Imaging can be carried out using either bright field or dark field modes. Bright field imaging employs an objective aperture that collects the direct unscattered electrons and scattering objects appear dark on a bright background. In dark field imaging, the objective aperture is shifted, so that higher scattering electrons appear bright on a dark background.

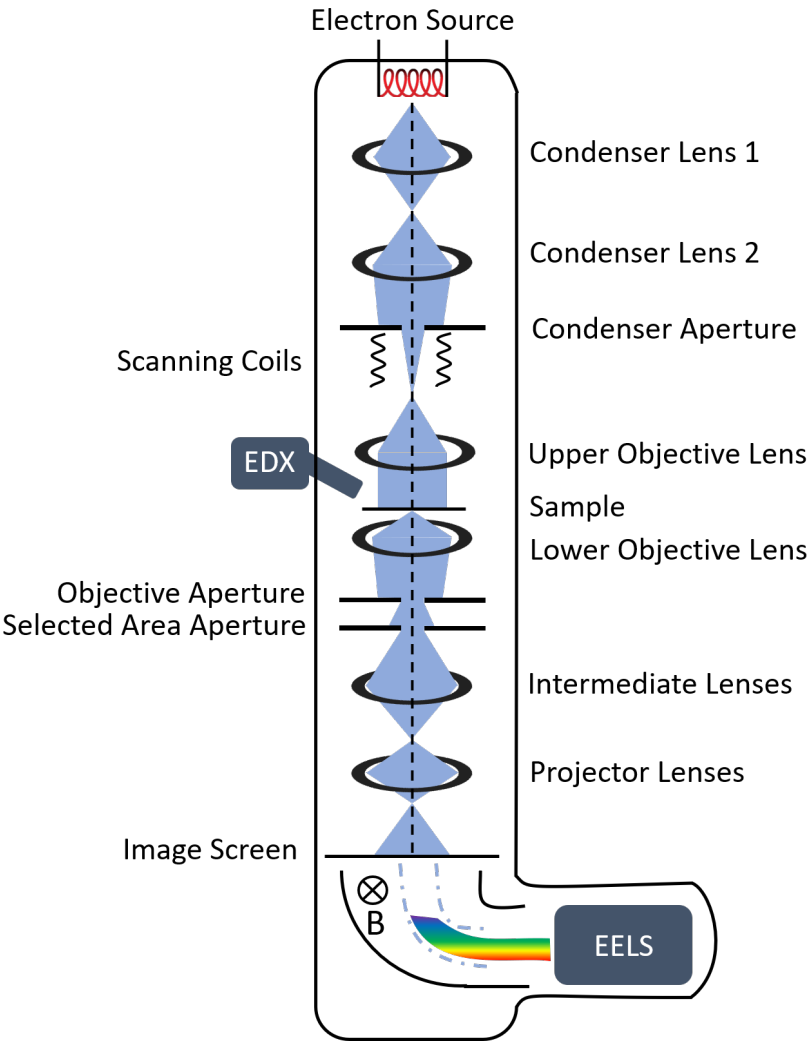


FIGURE 2.6: Schematic of a modern analytical TEM showing the lenses and apertures required to produce an image. This example shows a twin-objective setup in bright field mode with an attached EDX detector and EEL spectrometer.

Contrast may be given to an image by three main mechanisms: (i) mass contrast (ii) diffraction contrast and (iii) phase contrast. In mass contrast imaging, regions of the sample which are thicker or contain higher atomic number elements, will result in fewer transmitted electrons,

and thus a darker region in the formed image. Diffraction contrast makes use of diffraction of electrons by crystalline samples. If the Bragg criterion (Equation 2.3) is met, bright diffraction spots will form in the back focal plane of the objective lens at scattering angles that are characteristic of the crystalline phase of the sample. Diffraction contrast is introduced into an image by using the objective aperture in the back focal plane to enhance contrast from diffracting regions in the image since in bright field imaging the diffracted rays are blocked, whilst in dark field the diffracted rays are accepted. Diffraction contrast dominates both bright and dark field images of any thin crystalline specimen and was first understood and quantified in the analysis of thin metal films. Alternatively, the selected area aperture can be inserted into the initial image plane (between the objective lens and the intermediate lens) to select an area of the image. Diffracted electrons from this area may then be imaged as a diffraction pattern by exciting the intermediate lens to focus on the back focal plane of the objective lens rather than the image plane. By focusing the intermediate lens onto the back focal plane of the objective lens, a diffraction pattern (rather than an image) is produced; this is called selected area electron diffraction (SAED). Phase contrast imaging may be used to provide atomic lattice images and individual atomic columns to be resolved at high magnification. Phase contrast is achieved by adding an additional 1/4 wavelength phase shift to the 1/4 wavelength shifted diffracted electron waves by changing the defocus of the objective lens and requires both diffracted and undiffracted electrons to interfere in the image plane (i.e. insertion of a large objective aperture). This is the basis for ultra high-resolution imaging and relies on the specimen being ultra-thin (typically $< 10\,\mathrm{nm}$ thick) so that it behaves as a weak phase object.

**Scanning Transmission Electron microscopy**

In STEM, unlike in conventional TEM, the incident electron is focused to a sub-nanometre sized probe and rastered across the sample by the scanning coils (Figure 2.6). Many modern microscopes can function in both TEM and STEM mode (S/TEM). In S/TEM microscopes, the condenser lenses are used to demagnify and focus the electron beam. The scanning coils are then used to scan the demagnified probe across the sample. STEM, like a conventional TEM, has the ability to record spatially resolved characteristic X-rays through EDX, secondary electrons and electron energy loss (EEL) spectroscopy. However, scanning transmission electron

microscopy is also able to provide nanometre or better spatial resolution to these measurements not available using a conventional TEM. At scattering angles > $5°$ the amount of elastically scattered electrons is almost only proportional to the square of the atomic number of the atoms in the sample. In a STEM, electrons may be collected at these high angles using an annular dark field detector. This is referred to as high angle annular dark field (HAADF) imaging which can be used to give atomic mass contrast in STEM mode images.

#### Electron Energy-Loss (EEL) Spectroscopy

TEMs and STEMs may be fitted with an EEL spectrometer at the base of the microscope (Figure 2.6). EEL spectroscopy measures the energy loss of an inelastically scattered electron. This is done by passing the inelastically scattered electrons through a strong magnetic field ($\mathbf{B}$). The Lorentz force on an inelastically scattered electron in an electrically isolated region ($F = q \cdot \nu \times \mathbf{B}$) causes a deflection of the electron proportional to its kinetic energy. A spectrum is then recorded by counting these incident electrons as a function of their deflection on a charge coupled device (CCD) detector. The information in the recorded energy loss spectra may be divided into two regions: low loss and core loss. In the low loss region, at an energy shift of zero is the elastic peak which shows the electrons which have lost no, or almost no kinetic energy in transmission through the sample. Measurement of the full-width-half maximum (FWHM) of the elastic peak is a good indicator of the energy resolution of the instrument. The low loss region also contains features due to valence excitations and plasmon resonances, which may be of significant interest in certain cases. The core loss region contains useful chemical information regarding the atoms in the sample, and can be used to produce energy loss near-edge spectra (ELNES). The physics of this technique is analogous to X-ray Raman scattering, and is discussed in more detail in Section 2.7.3.

### 2.5.3 Scanning Electron Microscopy

An SEM is used to image the surface of a sample. During this project scanning electron microscopy was used to study the morphology of both pyrolysis carbons and hydrothermal carbons. A diagram of a typical SEM is shown in Figure 2.7. Unlike in the TEM, the condenser lens is used to demagnify and converge the electron beam. The objective lens then focuses the electron beam into a small probe at the sample surface. The focused probe is scanned across

the sample using a set of electromagnetic scanning coils; this is similar to the operation of a S/TEM. SEM imaging can be conducted by detection of either secondary or back-scattered electrons. Secondary electrons are typically valence electrons that are ejected from the sample by the incoming beam. Most of these electrons are re-absorbed by the sample, however those near the surface are able to escape and be detected to form an image. Images formed using secondary electrons have a much higher depth of field compared to images from a TEM, allowing much better resolution of surface morphology, despite reduced resolution (approximately $1\,\mathrm{nm}$ to $10\,\mathrm{nm}$) compared to a TEM.

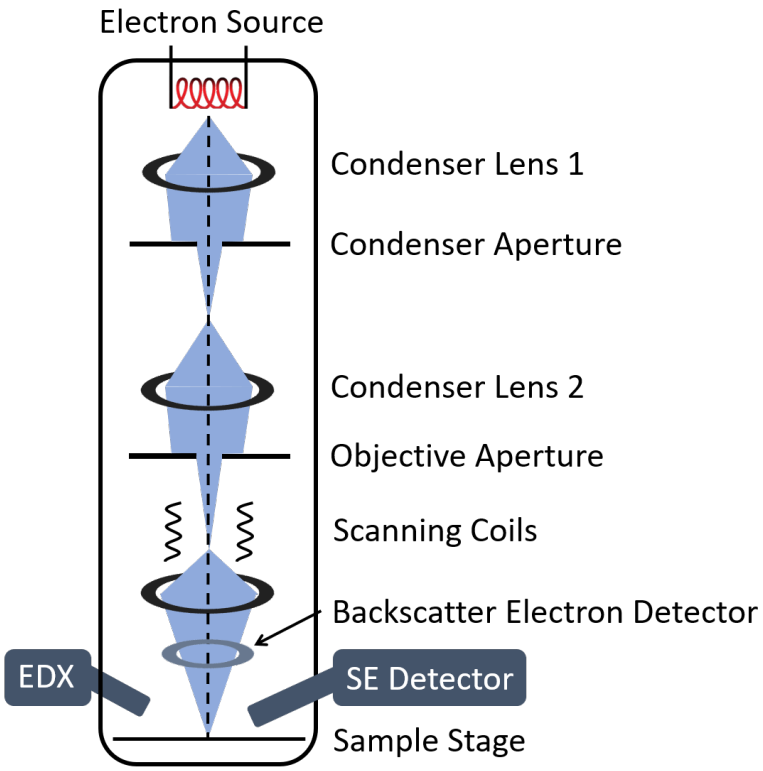


FIGURE 2.7: Schematic of a SEM, showing the lenses and apertures used to produce an image.

Back-scattered incident electrons are more strongly scattered by elements with higher atomic numbers and may be used to differentiate regions with higher average atomic mass. Back-scattered electrons are affected by the geometry of the sample, so provide information about topology and sample composition (if the surface is not flat). Similarly to a S/TEM, EDX may also be carried out using an X-ray fluorescence detector in the vacuum environment. However the spatial resolution of EDX in the SEM is limited by the interaction volume of the beam (typically $0.5\,\mu\mathrm{m}^2$), whereas in a TEM it is limited by the X-ray intensity from a thin sample.

**Focused Ion Beam (FIB)**

Focused ion beam microscopy is a similar technique to SEM, but a beam of ions are used instead of electrons. The greater mass of these charged particles allows material to be removed from the sample via sputtering and ablation. A dual beam SEM-FIB uses both an electron beam and a focused ion beam, typically Ga. The electron beam allows for high-resolution scanning electron microscopy, whilst the FIB can be used for the removal of material from the sample. In this way a FIB system can be considered as an addition to an SEM.

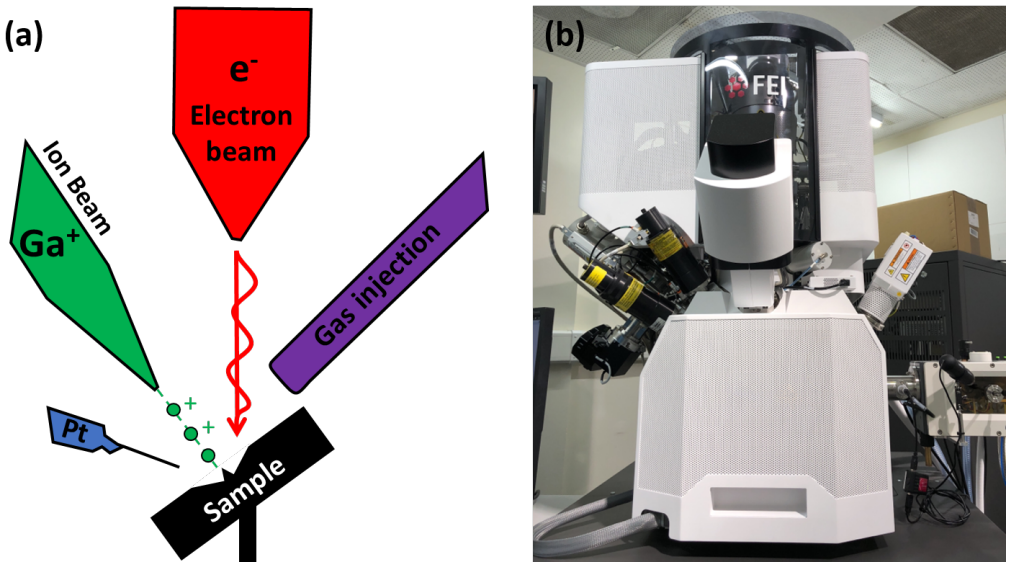


FIGURE 2.8: (a) Schematic demonstrating the principle of a dual beam Focused Ion Beam Scanning Electron Microscope. (b) Photograph of the FEI Helios G4 CX Dual Beam FEGSEM with FIB used in this project.

Figure 2.8 shows the general layout of a FIB system within an SEM. As discussed, the electron beam is used for standard secondary electron or back-scattered electron imaging. However a beam of ions (here shown as $Ga^+$), is used to ablate material from the sample surface. In order to prevent the surface from becoming charged, a charge compensation gas (e.g. Ar) is injected into the system near the sample. The power of the dual-beam FIB-SEM is that it may be used to prepare ultra-thin samples for transmission X-ray and electron imaging with unprecedented control over the spatial location of the section and facile transfer to the microscope. Furthermore dual-beam FIB-SEM allows for reduced-dose preparation of lamellae through the lift-out method [93, 94]. A lamella of a size 6 may be cut using the ion beam and attached, using electron beam deposited Pt, to a sample holder for further analysis.

The FIB lamellae studied in Chapter 3 were prepared to a $6\,\mu m$ x $6\,\mu m$ x $100\,nm$ size using the lift-out method. This was achieved by setting a few milligrams of powdered sample in Epofix resin (Agar Scientific, UK) for $48\,h$ at $25\,°C$. The produced resin block was then polishing to a finish using $6\,\mu m$ diamond paste (Buehler, MetaDi II). A FEI Helios G4 CX Dual Beam - High resolution monochromated, field emission gun, scanning electron microscope (FEGSEM) with precise Focused Ion Beam (FIB) was used. After transferring the coated resin block to the Dual Beam microscope, $500\,nm$ of electron beam Platinum (Pt) was deposited (at $5\,kV$, $6.4\,nA$ for the electron source) to the surface of the target area. This was followed by a second Pt layer ($1\,\mu m$) using the FIB (at $30\,kV$, $80\,pA$ for the liquid Ga ion source). A bulk lamella was initially cut (by the FIB at $30\,kV$, $47\,nA$), before a final cut-out was performed (at $30\,kV$, $79\,nA$). Final thinning and polishing of the lamellae to electron translucency was performed with a final polish/clean with a gentle ion beam ($5\,kV$, $41\,pA$). The lamellae were attached, using Ion Beam Pt, to a copper FIB lift-out grid (Omniprobe, USA) mounted within the SEM chamber (*in-situ*) and then stored under vacuum before and during transport to and from the TEM and synchrotron radiation source.

## 2.6 Laboratory Source X-ray techniques

### 2.6.1 Powder X-ray Diffraction (XRD)

Powder XRD was used to identify and fingerprint crystalline phases within the sustainable carbon materials produced. XRD is able to provide information regarding the interatomic lattice spacing between atoms ($d_{hkl}$) when Bragg's law is satisfied. Consider Figure 2.9, where an incoming X-ray of wavelength, $\lambda$, and incident angle $\theta$ interacts with a regular crystalline lattice with interatomic spacing $d$. The reflected rays ($R_0$, $R_1$, ..., $R_n$) are in phase if the difference between the path length of the radiation between them is an integer number of wavelengths.

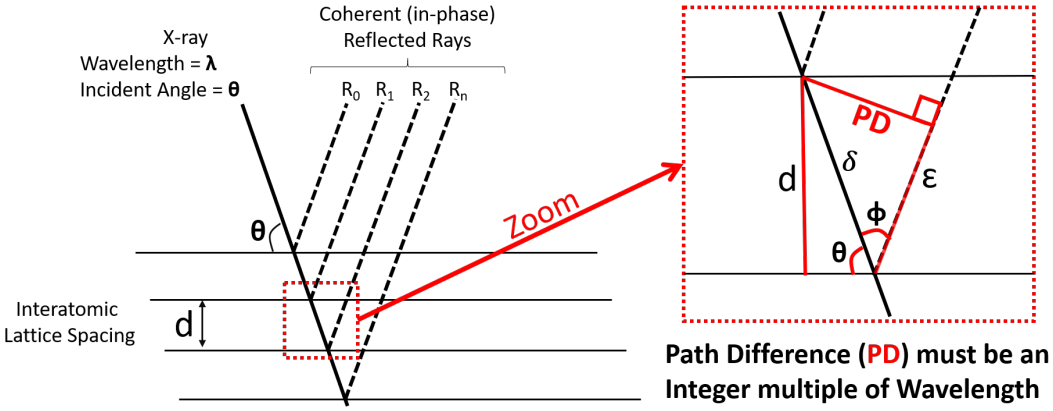


FIGURE 2.9: Illustrating Bragg's law of diffraction.

From the geometry shown in Figure 2.9:

$$\delta = \frac{d}{\sin\theta} \qquad\qquad \frac{\epsilon}{\delta} = \cos\phi = \cos\left(180 - 2\theta\right)$$

Combining these gives:

$$\epsilon = \frac{d}{\sin\theta} \cdot \cos\left(180 - 2\theta\right)$$

The path difference (PD) must be an integral number of wavelengths, therefore $n\lambda = \delta + \epsilon$:

$$n\lambda = \frac{d}{\sin\theta} + \frac{d}{\sin\theta} \cdot \cos\left(180 - 2\theta\right) = \frac{d}{\sin\theta} \cdot \left[1 - \cos 2\theta\right]$$

Substituting the trigonometric relation $\cos 2\theta = 1 + 2\sin^2(\theta)$ gives Bragg's law as:

$$\boxed{n\lambda = 2d\sin\theta} \tag{2.3}$$

Powder XRD patterns were obtained using a Phillips X'Pert diffractometer with a Ni-filtered (0.02 mm) Cu $K_\alpha$ rotating anode source ($8.048\,\mathrm{keV}$) at 40 kV and 40 mA. Finely ground sample was mounted on a zero background plate and spun whilst under irradiation. A programmable divergence slit was used to reduce scatter at low angles. A scanning rate of $0.08\,^\circ\mathrm{s}^{-1}$ and a dwell time of 3 s was employed in the $2\theta$ range from $10°$ to $70°$.

### 2.6.2 X-ray Photoelectron Spectroscopy (XPS)

XPS is a surface science technique, which probes the first few layers of atoms within a sample ($\sim 10\,\mathrm{nm}$). The surface chemistry of sustainable carbons is known to differ from the bulk material and is likely to have a significant influence on their interactions within the environment. In this project, XPS was used to monitor the surface atomic ratio between carbon and oxygen within carbohydrate-derived hydrothermal carbons. In XPS, the specimen to be analysed is irradiated by a soft beam of X-rays, typically with an approximate energy of $1486\,\mathrm{eV}$ (Al $K_\alpha$). XPS may be performed using either synchrotron or laboratory-source X-rays. In this case, a laboratory rotating anode source was used.

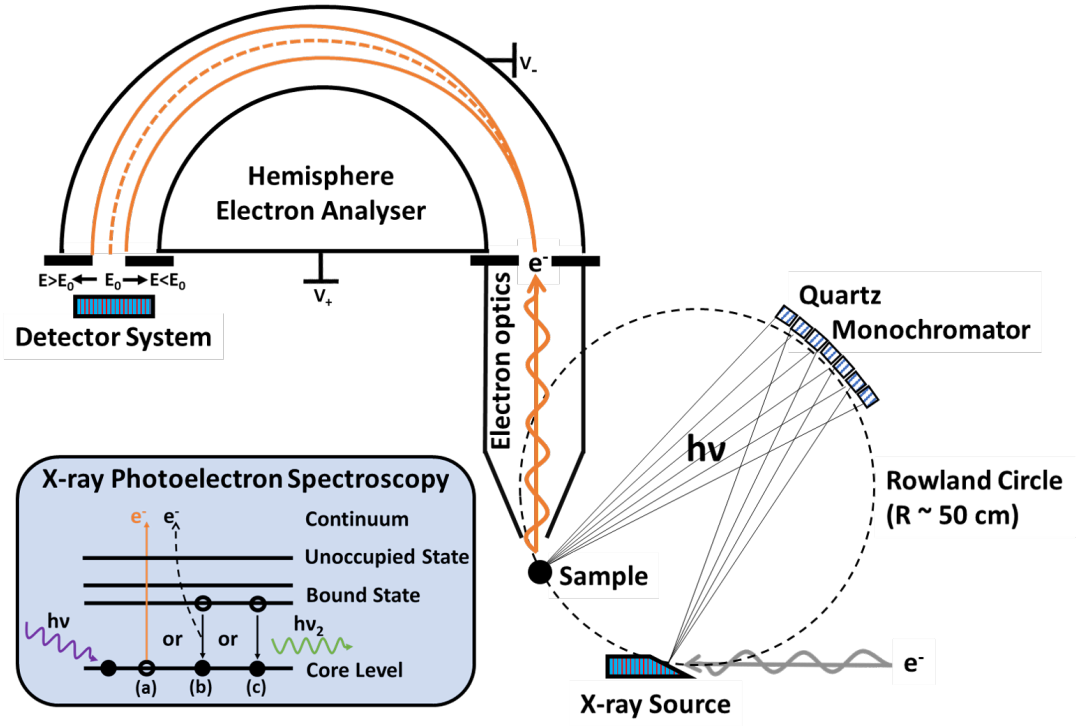


FIGURE 2.10: Diagram of a X-ray photoelectron spectrometer and the principle of the X-ray photoelectric effect.

XPS measures the energy of a photoelectron ejected from the surface of a material. An incoming monochromatic X-ray of energy $E = h\nu$ excites an electron with the same energy. The atom relaxes from the excited state by the emission of a photoelectron, which is ejected into the continuum with an energy $E_B$ equal to the binding energy of initial core electron. If the emitted photoelectron reaches the surface without inelastic interactions with nearby atoms, it is emitted. The energy required to move the photoelectron from within the solid to a point in the vacuum outside the surface is called the workfunction $\Phi$. The free photoelectron is collected at the spectrometer nozzle with a kinetic energy $E_k$ given by Equation 2.4.

$$E_k = h\nu - E_B - \Phi \tag{2.4}$$

A schematic of an XPS spectrometer is shown in Figure 2.10. Incident X-rays are typically produced using a rotating anode source, the energy resolution can then be controlled by the use of a monochromator. Using a monochromated Al $K_\alpha$ source typically gives an improved resolution of ~$0.4\,\mathrm{eV}$. The incident beam is focused onto the sample to a spot. Emitted photoelectrons are collected and retarded by an electrostatic lensing system and focused onto the input aperture of the electron analyser. Whilst other configurations are available, the analyser is typically hemispherical. The inner hemisphere is made positive with respect to the energy of the emitted photoelectron and the outer hemisphere is negative. The voltage of the hemispheres is scanned to measure a photoelectron spectrum using a position-sensitive detector.

XPS is typically conducted under ultra-high vacuum conditions ($1 \times 10^{-9}\,\mathrm{mbar}$ or better). This is done to protect the equipment from oxidation, reduce contamination and to allow photoelectrons to travel without interactions with gas atoms. However, recent advances now allow for near-ambient pressure NAP-XPS, which is conducted under millibar pressures [95]. NAP-XPS was performed here using an Enviro-ESCA spectrometer (SPECS, Ger) to reduce any loss of volatile surface organic compounds from the carbon samples. NAP-XPS was carried out at $3.3\,\mathrm{mbar}$ pressure using a monochromated Al $K_\alpha$ ($1.487\,\mathrm{keV}$) source. Samples were mounted as $6\,\mathrm{mm}$ pressed pellets and $^{48}$Ar gas was used for charge compensation purposes. The surface atomic ratios of the O 1s and C 1s peaks were analysed using CasaXPS (version 2.3.15), using a Shirley-type background and 70% Gaussian/30% Lorentzian (product form) curves.

## 2.7 Synchrotron Radiation Techniques

Synchrotron radiation is electromagnetic radiation produced by the acceleration of charged particles to relativistic speeds. Electromagnetic radiation produced by synchrotron sources, specifically X-rays, have been used extensively throughout this project in order to characterise both the chemistry and formation mechanisms underpinning sustainable carbon materials.

### 2.7.1 The Synchrotron

#### Introduction and Context

Since the first observation of synchrotron radiation in 1947, there have been rapid advances in both the science of accelerators and the X-ray techniques that are used inside them[2] [96]. First generation synchrotrons were parasitic of sub-atomic research, since X-ray radiation was an undesirable byproduct from accelerators designed to study subatomic structure. From the late 1960s and early 1970s, particle accelerators based on storage rings began to emerge, a type of synchrotron accelerator capable of keeping the particle beams circulating for long periods of time, replenishing the energy lost by the particles due to the emission of radiation. This led to, among other factors, the construction of dedicated synchrotron radiation facilities, with diameters of a few hundred metres, specifically designed to produce X-rays (e.g. the SRS at Daresbury, UK). These 2nd generation synchrotrons were an advancement on the first generation, offering a controlled source of dedicated synchrotron radiation, but lacked the flux required for more challenging experiments. The construction of the European Synchrotron Radiation Facility (ESRF) in 1994 and the Advanced Photon Source (APS) in 1996 heralded the first third generation synchrotrons to be constructed. Third generation synchrotrons are designed to produce much higher X-ray flux using X-ray-producing magnet arrays called undulators and wigglers. Third generation lightsources have since led to significant progress in all aspects of science and many techniques discussed in this project are dependent on the highly brilliant, coherent, monochromatic and tuneable X-rays they produce. The impending upgrade of both the Diamond Lightsource (DLS) and the Advanced Photon Source (APS) combined with the newly upgraded European Synchrotron Radiation Facility Extremely Brilliant Source (ESRF-EBS) makes for a fascinating period for synchrotron experimenters.

[2]Other wavelengths of radiation e.g. UV, IR are produced at SRFs, though this project focuses on X-rays.

**Principle of Operation**

The production of synchrotron radiation begins with three main stages, an electron source produces a *bunch* of electrons which are subsequently fed into a linear accelerator, or linac. The linac accelerates the electrons to ~100 MeV, and injects the electrons into the booster ring. The booster ring is a pre-accelerator where the electrons are accelerated to an energy of ~1 GeV. At this point the electron bunches may be be injected into the main holding location for the electron bunches - the storage ring. Here, the electrons are held within an ultra-high vacuum tube, roughly 800 m in diameter, by a series of different magnets located around the storage ring (Figure 2.11). In the curved sections, *bending magnets* are used to accelerate the electrons in a circular path, producing a broad spectrum of X-rays concurrently. Arrays of magnets may also be placed in the straight sections of the storage ring. These straight sections contain arrays of magnets used to produce intense beams of X-rays called *insertion devices* (e.g. wigglers, undulators) and higher order magnets (e.g. quadrupole, sextupole, octapole), which are used to focus the electrons, and keep them in tight bunches (Figure 2.11). The storage ring also contains radio-frequency (RF) cavities, which are used to accelerate the bunches around the ring, compensating for energy lost by the emission of synchrotron radiation.

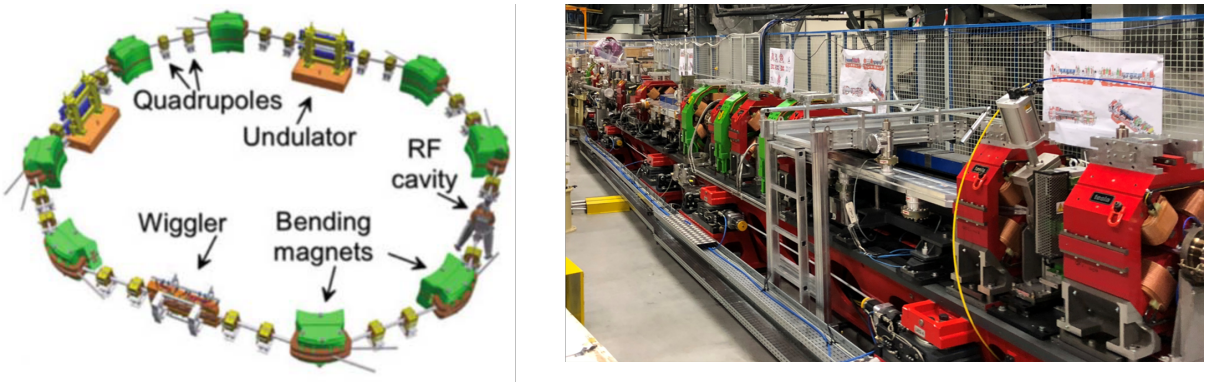


FIGURE 2.11: Left: Schematic of a typical storage ring. Right: Photograph of a girder from the Extremely Brilliant Source, ESRF before installation. Red sections are quadrupole magnets, green sections are higher order magnets for focusing. A dipole bending magnet can be seen at the far end of the girder.

The X-rays produced by the bending magnets or insertion devices are then channelled via shielded pipework to a *beamline*. A beamline is an experimental station, where an instrument or set of instruments are located. Beamlines are separated into bending magnet, or insertion device beamlines. The major difference between bending magnets and insertion devices is their *brilliance*, which is how the brightness of an X-ray source is measured. Equation 2.5

shows the definition of brilliance, where the denominator denotes the cross sectional area of the source, solid angular divergence of the beam and the spectral distribution of the produced photons.

$$Brilliance = \frac{Number\ of\ Photons\ per\ second}{(mrad)^2 \cdot (mm^2 source\ area) \cdot (0.1\% Bandwidth)} \tag{2.5}$$

Bending magnets and insertion devices work by the principal that an accelerating charged particle emits energy in the form of radiation. At the relativistic speed of electron in the storage ring, an induced change in direction results in the preferential emission of light in the forwards direction - this is known as relativistic beaming. From special relativity, the Lorentz factor (Equation 2.6) is the factor by which time, length, and relativistic mass change for an object moving at relativistic speed. As the electron speed ($\nu$) approaches the speed of light, the angle of emitted photons from the tangentially accelerated electron is equivalent to $1/\gamma$ which, for an electron moving at $0.94c$, is less than $1/3600°$.

$$\gamma = \left(1 - \frac{\nu^2}{c^2}\right)^{-\frac{1}{2}} \tag{2.6}$$

Bending magnets are dipole magnets stationed at the curved sections of the storage ring. Bending magnets are necessary for curving the path of the electron bunches, but also produce X-rays tangentially to the ring. The third generation of synchrotrons were designed to include insertion devices. Ther are two types of insertion devices: wigglers and undulators. Both wigglers and undulators produce much greater brilliance than bending magnets, by placing a series of magnets with opposite polarity in the path of an electron bunch at straight sections of the storage ring. Undulators, unlike wigglers, have the opposite polarity magnetic sections at much shorter distances, causing constructive X-ray interference, resulting in a dramatic increase in brightness. However, undulators must be tuned for a specific energy range by changing the gap between the magnets, and are only very brilliant at specific energies. X-rays produced from bending magnets have lower brilliance than those produced by either undulators or wigglers, but produce this brilliance over a wide energy range. For many X-ray absorption experiments, it may be beneficial to use a bending magnet instead of a more brilliant insertion device,

due to the complex background signals produced by the narrow energy ranges insertion devices are tuned for [3]. In general however, the brightness of synchrotron radiation sources is increasing as technologies mature and improve, the latest generation of SRF (e.g. ESRF-EBS) have a brilliance of ~$10 \times 10^{20}\,\mathrm{photon\,s^{-1}\,mm^{-2}\,mrad^{-2}\,0.1\%BW^{-1}}$.

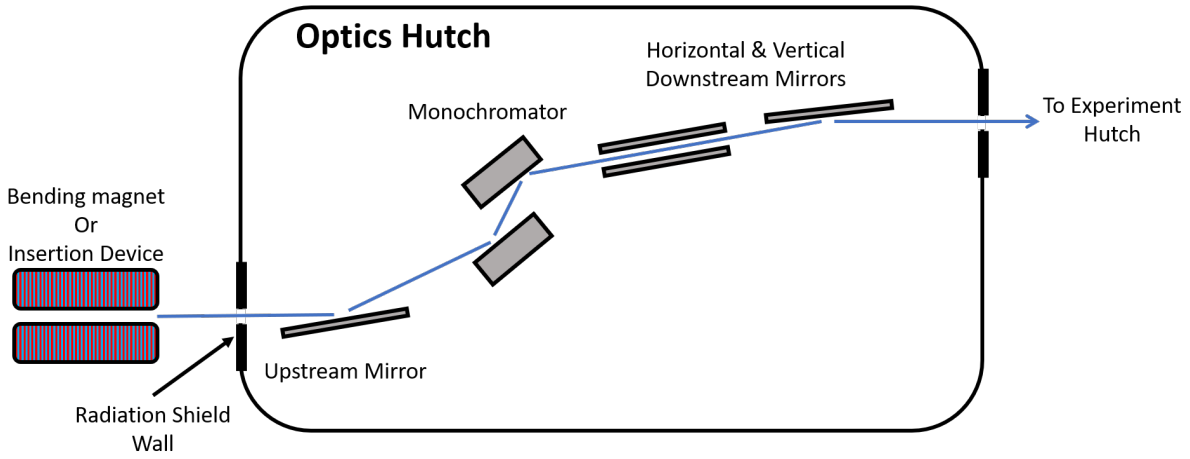


FIGURE 2.12: Simplified schematic of a typical beamline optics hutch.

After the bending magnet or insertion device, the X-rays are fed to the beamline. It is beyond the scope of this section to fully describe all possible beamline set-ups, since every experiment may require a different beamline layout. However, the key optical components necessary for a spectroscopy beamline are discussed here. The first stage in the beamline, called the optics hutch (Figure 2.12), accepts the generated X-rays through the radiation shield. At this point a collimating X-ray mirror is typically used for focusing, collimation and harmonic rejection of the beam before the monochromator. The monochromator is a device that uses diffraction from a pair of crystals to produce X-rays of a well-defined energy. Typically the monochromator is defined by the crystal material and their crystallographic orientations (e.g. Si(111) ). The monochromator crystal undergoes significant thermal load under the intense beam of X-rays, so is typically cooled using water or cryogenic gases. The energy of the produced beam is selected by changing the angle that the monochromator makes with the incident beam. The energy of the X-rays leaving the monochromator is governed by Bragg's law (Equation 2.3), which can also be written as: $E = hc/\left[2d_{hkl} \cdot \sin\left(\theta_{Bragg}\right)\right]$. The monochromator will pass this energy of photon on, including any harmonics (multiples of $d_{hkl}$) to the downstream mirrors. The downstream mirrors are then used to reject any monochromator harmonics, and to

[3] The complex background can be removed from insertion devices, but is more challenging than using a bending magnet.

produce a well collimated and focused beam to the experimental station - where the instrumentation is located. Further information on synchrotron radiation and optics maybe found in chapter 3 of reference [86].

#### Benefits of Synchrotron Radiation

Benefits of synchrotron radiation over a laboratory source may be summarised as follows:

- High brightness: synchrotron light is extremely intense and highly collimated. The intense flux means that very small or dilute amounts of material can be studied, and measurements can be performed faster than with conventional laboratory instruments.
- Wide energy spectrum: synchrotron light is emitted with energies ranging from infrared light to hard X-rays.
- Highly polarised: the synchrotron emits highly polarised radiation, which can be linear, circular or elliptical. This can be used to study magnetism and dynamics in materials.
- Emitted in very short pulses: pulses emitted are typically less than a nano-second. The use of pulsed X-rays can be used in so-called "pump-probe" experiments, following time-resolved chemical reactions.

### 2.7.2 X-ray Absorption Spectroscopy (XAS)

X-ray absorption spectroscopy (XAS) is a powerful tool for understanding the chemical state of a sample. Unlike in X-ray diffraction, no long range structural order is required and the technique is able to be applied to amorphous solids, (poly)crystalline solids, liquids and molecular gases. XAS is a product of the modulation of the attenuation coefficient (Equation 2.1) at energies at and above the characteristic *X-ray Absorption Edges* formed by the excitation of an atomic core electron in a sample to an unoccupied state or the continuum (Figure 2.13a).

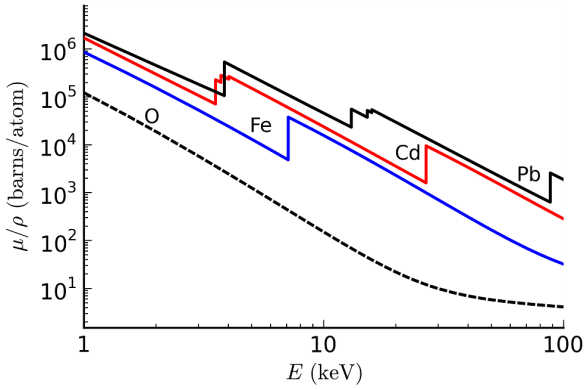


(A) Characteristic 'edges' in the absorption coefficients for O, Fe, Cd & Pb.

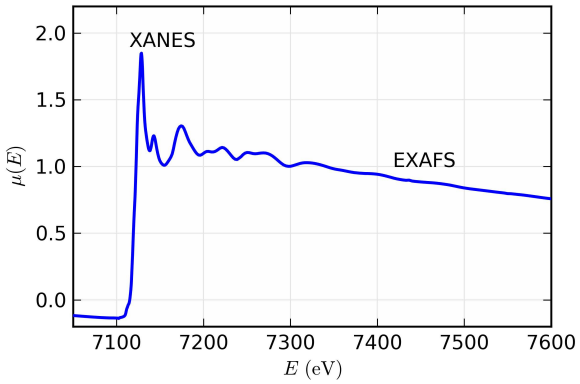


(B) Example Fe *K*-edge XAS data.

FIGURE 2.13: (a) XAS is simply the result of the modulation of the X-ray absorption coefficient, $\mu$, with changing photon energy. (b) A measured X-ray absorption spectrum for the Iron *K*-edge. (Image courtesy M.Newville [97])

The first observations of an X-ray absorption edge were carried out independently by Maurice De-Broglie and Julius Hedwig in 1913. Both Hedwig and De-Broglie used a modified X-ray spectrometer, of the type developed at the University of Leeds by W.H.Bragg and W.L.Bragg, to shine X-ray light on a rotating single crystal. As the crystal was rotated through all angles between the incident and diffracted beam (e.g. all X-ray energies), the diffracted X-rays were shone onto a metal film which resulted in a pattern on a photographic film [98]. These patterns were the first X-ray absorption spectra and led De Broglie to postulate that X-rays behaved in a way similar to light [98, 99]. This was soon followed by the initial observation of the fine structure by Hugo Fricke in 1921 whilst working at Lunde University [99]. In 1911, work by Charles Barkla had proved that the jumps in the absorption coefficient were due to the characteristic absorption of X-rays specific to the core-level energies of the atom, though there was little understanding of what caused the fine structure [100]. This early work led to two regions of an X-ray photoabsorption spectrum to be identified: the near-edge and the fine structure

(Figure 2.13b). Whilst the distinction between near-edge and fine structure is somewhat arbitrary, typically the near-edge spectrum continues until $50\,\mathrm{eV}$ after the main feature - which is historically called the 'white line' or edge. XAS may be used to study both the near-edge and the fine structures, these techniques are called X-ray absorption near-edge spectroscopy (XANES) and X-ray absorption fine structure (EXAFS) respectively.

#### X-ray Absorption Near-Edge Spectroscopy (XANES)

XANES is due to a complex superposition of quantum-mechanically allowed states, which include dipole-allowed transitions to higher electronic states within the absorbing atom, and is not easily described here [101, 102]. The term XANES is used to describe the near-edge structure using hard X-rays, whilst the term NEXAFS is used to describe the process for soft X-rays ($< 2500\,\mathrm{eV}$). XANES, gives information regarding the site geometry, chemical selectivity and valence. Treatment of XANES data is typically performed through comparison of experimental data with measured standards using principal component analysis (PCA) or linear combination fitting. However, modern density functional theory codes are now beginning to allow for the *ab-initio* calculation of XANES spectra [103, 104].

#### Extended X-ray Absorption Fine Structure (EXAFS)

EXAFS is a property of the photoelectric effect. An X-ray photon is absorbed by an atom in the specimen, promoting an electron to the continuum and producing a photoelectron with energy equal to the difference between the transition energy and the initial photon energy. The EXAFS oscillations, typically measured until $1000\,\mathrm{eV}$ after the white line, are a result of the destructive and constructive interference between the photoelectron and the electrons of nearby systems. EXAFS contains information regarding the local structural environment of the absorbing atom, such as coordination number and bond lengths to local atoms. The benefit of measuring EXAFS comes from the ability to calculate the fine structure via *ab initio* modelling.

#### Development of the Theory of EXAFS

The development of Quantum Theory at the beginning of the twentieth century led to an understanding of the photoelectric effect, the wave-particle nature of photons and of the quantisation of electronic states in the atom. These advances helped lead to a development of a suitable

theory for X-ray fine structure. The sharp characteristic edges in the absorption spectra (Figure 2.13a) were shown to be caused by a number of phenomena, but the largest contributor is the photoelectric effect. When an electron is excited to the continuum state, a photoelectron is produced with an energy equivalent to the difference between the photon energy and the core electron binding energy (Figure 2.14a).

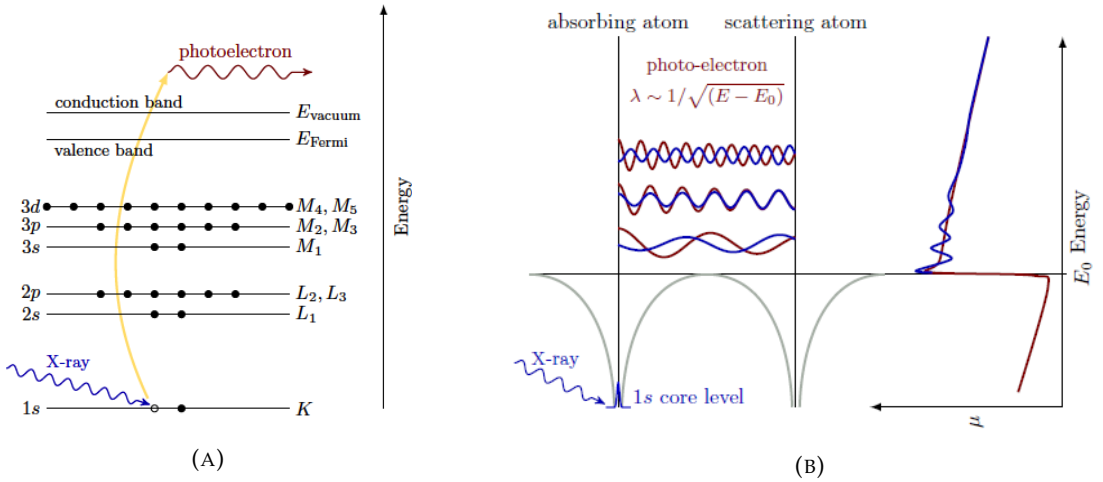


FIGURE 2.14: (a) An atom absorbs an X-ray due to a core electron transitioning to the continuum, producing a photoelectron and leaving the atom in an excited state. (b) A representation of multiple scattering theory, the produced photoelectron scatters of an adjacent atom causing fine structure.[97]

The first formal theories for the fine structure in recorded XAS experiments were given by Kronig in 1931 [98, 105]. Kronig attributed the oscillatory structure to the scattering of the produced photoelectron by atoms surrounding the emitting atom. However the first "modern day" EXAFS theory and measurements was published by Dale Sayers, Ed Stern and Farrel Lytle in 1971 at the University of Washington [106]. In their paper they assert that the measured fine structure arises from *"oscillations in the photoelectric cross section due to scattering of the ejected photoelectron by atoms surrounding the absorbing atom"* [106]. In the same paper they published the EXAFS equation, which describes the behaviour of the absorption coefficient due to the interference of the photoelectron. However, the main contribution of this paper and the final key point in the discussion of the treatment of EXAFS is the Fourier transform. The transformation of the EXAFS perturbation from energy space, $\chi(E)$, into canonical momentum space, $\chi(k)$ can be used to extract the distances of atoms nearby the absorbing atom. The EXAFS equation is a summation of De-Broglie momentum plane waves, and a summation of waves can be separated by the Fourier transform. By taking the Fourier transform of the momentum-space

data we see the position-space, $R$, data. Since the EXAFS equation contains other non-Bloch terms, it is not a simple radial distribution function, but does contain information about the bond distances between the absorbing atom and the scattering atom.

**EXAFS Equation**

The EXAFS equation can be described and qualitatively derived by an understanding of the EXAFS experiment and some basic principles of modern physics. The first of which is Fermi's golden rule (Equation 2.7).

$$\mu(E) \propto |\langle\psi_{initial}|\,\hat{\epsilon}\cdot\mathbf{r}e^{i\mathbf{k}\cdot\mathbf{r}}\,|\psi_{final}\rangle\,|^2 \tag{2.7}$$

Which states that when a photon with polarisation vector, $\hat{\epsilon}$, wavevector, $\mathbf{k}$ and position vector $\mathbf{r}$ interacts with an electron with an initial state $\langle\psi_{initial}|$ producing a change in state to $|\psi_{final}\rangle$, there must be a finite state for each photon. For instance, when an X-ray enters the region occupied by an atom, the X-ray photon exists in a superposition of possible states with different probabilities (e.g. pass straight through, scatter or be absorbed) but, when a measurement is taken, one of these must have happened for each photon. Therefore, one photon must interact with one electron. This approximation is true so long as the mass of the incoming photon is approximately zero (i.e. $e^{i\mathbf{k}\cdot\mathbf{r}} \approx 1$) - this is called the dipole approximation.

The second key principle is the wave-like property of the produced photoelectron. Here, an assumption is made that the produced photoelectron is plane-wave like and radiates out with spherical geometry. The wavevector of the scattered photon can be derived from the equation for kinetic energy and the De-Broglie relation $\mathbf{p} = \hbar\mathbf{k}$ where $\mathbf{p}$, $\mathbf{k}$ are the momentum and wavevector of the photoelectron respectively. In Equation 2.8, $m_e$ is the electron rest mass and $(E - E_0)$ is the difference in energy between the incoming photon energy and the energy required to remove the photoelectron from the absorbing atom (Figure 2.14b).

$$|\mathbf{k}| = \frac{\sqrt{2m_e(E - E_0)}}{\hbar} \tag{2.8}$$

In order to analyse the data, we must extract the EXAFS signals oscillations, $\chi$, from the atomic background. The EXAFS signal is considered to be a small perturbation on the atomic background photoabsorption spectrum (i.e. the spectrum of the atom with no fine structure):

$$\mu(E) = \mu_0(E)\,[1 + \chi(E)] \tag{2.9}$$

which can also be expressed, using Fermi's golden rule (Equation 2.7), as Equation 2.10:

$$\mu(E) \propto |\,\langle\psi_{initial}|\,\hat{\epsilon}\cdot\mathbf{r}e^{i\mathbf{k}\cdot\mathbf{r}}\,|\psi_{final}\rangle\,|^2 \cdot [1 + \langle\psi_{initial}|\,\hat{\epsilon}\cdot\mathbf{r}e^{i\mathbf{k}\cdot\mathbf{r}}\,|\Delta\psi_{final}\rangle] \tag{2.10}$$

In order to do this, a background absorption function $\mu_0$ is produced by modelling the background atomic signal. All XAS spectra in this project were normalised to the size of the edge jump $\Delta\mu_0$, with a pre-edge region of at least $20\,\mathrm{eV}$ before the edge and a post-edge region at least $100\,\mathrm{eV}$ afterwards. A spectrum is then extracted by subtracting $\mu_0$ by Equation 2.11.

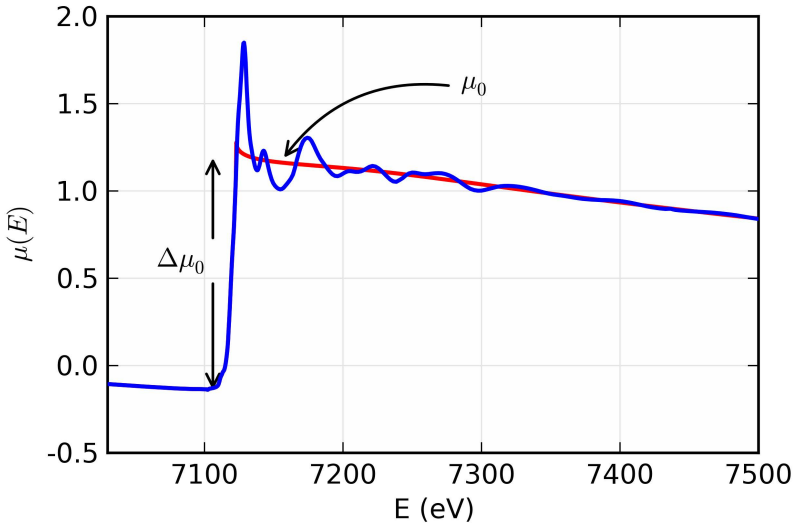


FIGURE 2.15: The Fe *K*-edge spectra with $\mu_0$ and $\Delta\mu_0$ labelled.

$$\chi(E) = 1 + \frac{\mu(E) - \mu_0(E)}{\Delta\mu_0(E_0)} \tag{2.11}$$

For EXAFS analysis, the background subtracted spectrum may be transformed from energy space to momentum space by Equation 2.8. The fine structure perturbation $\chi(E)$ is typically expressed in terms of the photoelectron wavevector (i.e. $\chi(k)$).

The scattering probability of the produced photoelectron can be described by the following equation:

$$\chi(k) = \sum_i N_i f_i(k) cos(2kD_i) \tag{2.12}$$

This part of the EXAFS equation describes the probability of a photoelectron scattering event occurring, rather than inelastic scattering, or no scattering at all. Here, $f(k)$ is a proportionality constant that describes how likely a scattering event is to happen, for example this would be much higher in lead than in carbon since lead has much higher electron density. This also gives the EXAFS equation its sensitivity to the mass of nearby scattering atoms. $D$ is the distance between the absorber and the scattering atom and gives the EXAFS equation its sensitivity to distances. The equation is summed over all the possible scattering atoms to represent the presence of multiple nearest neighbours. Since some of these scattering atoms may be the same (for example other Cu atoms in Cu metal), a degeneracy factor ($N$) is introduced, which is also called the coordination number for a single scattering path. In nanomaterials, the coordination number is often reduced because atoms at the 'edge' of the nanocrystal are 'missing' some of their neighbours - this can be a useful tool for modelling nanoparticle size.

$$\chi(k) = \sum_i N_i f_i(k) sin(2kD_i + \delta_i(k)) \tag{2.13}$$

The produced photoelectron is able to traverse not just a single path, but also a variety of more complicated paths around the local scattering atoms. In order to account for this in Equation 2.13, the average path distance $D_i$ is defined as half the distance travelled by the photoelectron. Furthermore, scattering atoms are not perfect 'soft boundaries' and they change the phase of the scattered photoelectron. To account for this, a phase-shift is applied to the scattered photoelectron $\delta_i(k)$.

$$\chi(k) = S_0^2 \sum_i N_i f_i(k) e^{-\frac{2D_i}{\lambda(k)}} sin(2kD_i + \delta_i(k)) \tag{2.14}$$

Since the photoelectron propagates as a spherical wavefront, the scattering probability reduces with the square of the distance from the absorbing atom. Therefore an inverse-square probability factor $\frac{1}{kD_i^2}$ is added in Equation 2.14. The amplitude reduction factor $S_0^2$ is then added to

account for a change in potential around the nucleus of the absorbing atom. The addition of an interference correction factor $e^{-\frac{2D_i}{\lambda(k)}}$ accounts for the destructive interference that occurs due to phase-shifted interference effects. This cannot be added into the amplitude reduction factor, because it is strongly dependent on the distance that the photoelectron travels e.g. the further the distance travelled the more likely the photoelectron is to infer some sort of destructive interference. The variable $\lambda(k)$ is called the *mean free path* of the photoelectron, and ensures that scattering at distances greater than $10$ Å is negligible.

$$\boxed{\chi(k) = S_0^2 \sum_i N_i \frac{f_i(k)}{kD_i^2} e^{-\frac{2D_i}{\lambda(k)}} e^{-2k^2\sigma_i^2} sin(2kD_i + \delta_i(k))} \tag{2.15}$$

Each of these components form the EXAFS equation (Equation 2.15). The only change here is the addition of a new variable $\sigma_i^2$. This factor was one of the key steps forward in the theory proposed by Stern, Sayers and Lytle in 1971 [106]. In this paper it is called the *temperature factor* and it takes a general Debye temperature form where $\sigma_i^2$ is the mean square amplitude of the relative displacement of the atoms in the i$^{th}$ shell. This factor takes into account temperature changes, but it is also powerful for understanding the general disorder of the material in questions whether this is due to frustration, static disorder in an amorphous material or other reasons.

Through extracting the fine structure from measured XAS spectra it is thereby possible to measure a range of material properties. This is done by taking a known structure and using the EXAFS equation to calculate the corresponding fine structure. Using the Fourier transform, it is possible to model bond lengths, thermal disorder, nanoparticle sizes and other relevant properties of a material.

### 2.7.3 X-ray Raman Scattering Spectroscopy (XRSS)

X-ray Raman scattering spectroscopy (XRSS) is non-resonant inelastic X-ray scattering (NRIXS) by core-electron excitations. The key benefit of XRSS exploited in this project is the ability to measure the core electron transitions of low-Z elements using hard X-rays (~10 keV). X-ray photoabsorption spectra for low-Z elements (e.g. C, N, O) have traditionally been measured using spectroscopic techniques such as EEL spectroscopy, NEXAFS or XPS. However, direct measurement of core-electron spectra using these techniques brings specific challenges. Soft X-ray techniques are typically conducted under vacuum conditions and are sensitive to surface chemistry only. XRSS has now been applied to study samples not suited for traditional soft X-ray techniques. These include studies of liquids [107], materials under extreme pressures [108], sensitive historical materials [109], time-resolved measurements [110], *in-situ* measurements and most recently, pyrolysis and hydrothermal carbons [111].

#### Non-Resonant Inelastic Scattering (NRIXS)

The result of inelastic X-ray scattering is a scattered X-ray photon with modified momentum and energy. By measuring the difference in energy and momentum between the initial incoming X-ray photon and the scattered photon, it is possible to extract physical and chemical information from a sample. A complete understanding of NRIXS is beyond the scope of this section and is described more fully elsewhere [112, 113].

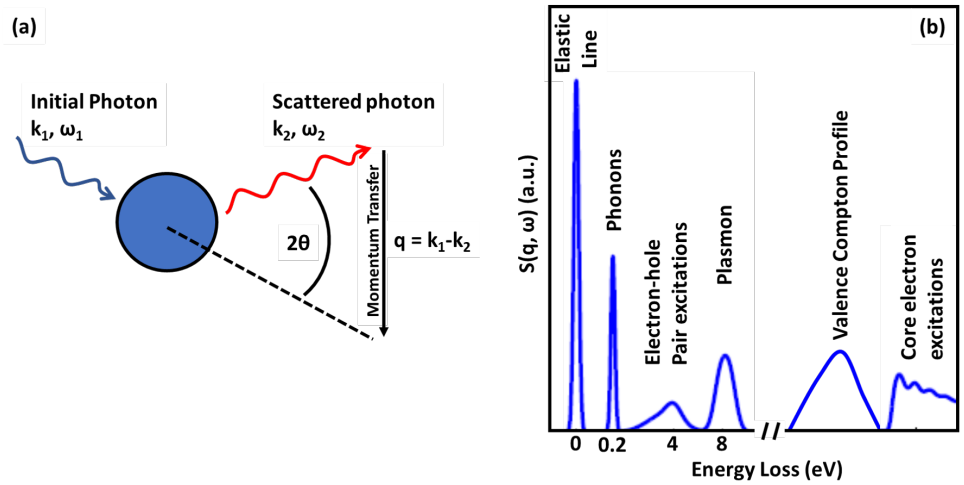


FIGURE 2.16: (a) NRIXS diagram for a scattered photo with energy $\omega$ and momentum $\mathbf{k}$. The momentum transfer when the photon is scattered by an angle $\theta$ is $\mathbf{q}$. (b) Example dynamic structure factor $S(q, \omega)$ spectrum from an NRIXS measurement. The elastic peak, plasmons and other excitations are visible at low energies, whilst the Compton profile and core electron features are visible at high energies.

Figure 2.16a shows a schematic representing NRIXS. An incident X-ray photon with energy $\omega_1$ and momentum vector $\mathbf{k_1}$ interacts with an electron in the sample and is scattered inelastically. This produces a scattered photon with energy $\omega_2$ and momentum vector $\mathbf{k_2}$. The energy and momentum transferred to the sample may be written as $\omega = \omega_1 - \omega_2$ and $\mathbf{q} = \mathbf{k_1} - \mathbf{k_2}$ respectively. The absolute value of the momentum transfer $\mathbf{q}$ is given by $|\mathbf{q}|^2 = 1/c^2 \cdot \left[\omega_1^2 + \omega_2^2 - \omega_1\omega_2 \cos(2\theta)\right]$, by the cosine law. Unlike XAS, NRIXS describes an inelastic X-ray scattering event where the incoming photon has an energy far from any electron binding energy of the system. In an XRSS experiment, the measured quantity is called the double differential scattering cross section (DDSC) which is shown in Equation 2.16 [113].

$$\frac{d^2\theta}{d\Omega_2 \hbar\omega_2} = \left(\frac{d\omega}{d\Omega_2}\right)_{Thompson} S(\mathbf{q},\omega) \tag{2.16}$$

The DDSC measures the photon flux scattered by an angle $2\theta$ into the solid angle element $d\Omega$ at the energy $h\omega_2$. The DDSC is composed of the Thompson scattering factor, which is the low-energy limit of Compton scattering, and the dynamic structure factor $S(\mathbf{q},\omega)$ which contains all the chemical information available from NRIXS. $S(\mathbf{q},\omega)$ is given by Equation 2.17.

$$S(\mathbf{q},\omega) = \sum_f |\langle\psi_{initial}| \sum_j \exp -i\mathbf{q}\cdot\mathbf{r}_j |\psi_{final}\rangle|^2 \cdot \delta(E_{initial} - E_{final} + \hbar\omega) \tag{2.17}$$

The dynamic structure factor is derived from Fermi's golden rule (Equation 2.7). Using the same notation as discussed in section 2.7.2, it can be seen that the dynamic structure factor is simply the sum over all possible states (sum over $f$) and electrons (sum over $j$). Expanding the transition operator in Equation 2.17 in the limit of small momentum transfers give the result that dipolar transitions dominate. These dipole-allowed transitions are equivalent to those that are probed during an XAS experiment. This result has the important consequence that, at small momentum transfers, NRIXS is equivalent to XAS.

#### X-ray Raman Scattering

Since the dynamic structure factor contains all the same information as XAS at small scattering angles, NRIXS can be used to study core X-ray photoabsorption spectra using X-rays with energies not equal to the transition energy. This is the principle of X-ray Raman scattering

spectroscopy. XRSS is a special case of NRIXS where the energy loss part of the dynamic structure factor (but not the initial photon energy) is tuned to the energy of a core-electron transition of an element of interest. This is done by varying the energy of the incoming photon (i.e. $E_{XAS} = \omega_1 - \omega_2$). As NRIXS is equivalent to photoabsorption spectroscopy at low-$\mathbf{q}$, so is XRSS. By tuning the energy-loss to soft X-ray photoabsorption edges between $20\,\mathrm{eV}$ and $2000\,\mathrm{eV}$, it is is possible to record soft X-ray photoabsorption spectra using hard X-ray photons as the source. This gives some key advantages to XRSS over conventional soft XAS:

- XRSS is able to measure soft X-ray absorption spectra without the need for vacuum environments in standard conditions.
- XRS spectra may be collected for samples in *in-situ* environments such as diamond anvil cells or flow cells.
- Soft X-ray absorption spectra commonly suffer from self-absorption artefacts or other saturation effects which are not present in XRS spectra.
- The hard X-ray photons used in XRSS are able to give bulk spectroscopic information unlike soft X-ray techniques which are limited to only surface information.

The major drawback of XRSS however, is the significantly reduced interaction cross section for inelastic scattering events as compared to XAS. An inelastic scattering event is less likely than absorption by a factor of around $10^{-5}$. This means that the sample must be illuminated by a highly brilliant synchrotron radiation source. Furthermore, experiment times for XRSS measurements may be quite extended (> 1 hour) depending on the concentration of the element of interest within the sample.

**Instrumentation**

XRS spectra are collected by measuring the energy and momentum of the scattered photon for a given solid angle. In order to conduct an XRSS experiment, both the momentum and the energy of the scattered photon must be measured. This has been achieved in the majority of spectrometers by the use of spherical crystal analysers. Analyser crystals are optical devices for X-rays consisting of a thin single-crystal wafer (typically silicon) bonded onto a shaped glass surface. By Bragg's law $E = hc/\left[2d_{hkl} \cdot \sin\left(\theta_{Bragg}\right)\right]$, the crystal analysers act as a band-pass

filter, selecting a certain energy of scattered photons. In this way the energy of the photoabsorption edge of interest can be selected by tuning the energy difference between the beamline monochromator and the analyser crystal to the required energy $E_{XAS} = E_{mono} - E_{crystal}$. The scattered photon is then reflected to a detector, which measures counts at a given monochromator position. Other than the beamline monochromator, the crystal analyser is a key factor in the overall resolution of an XRSS instrument.

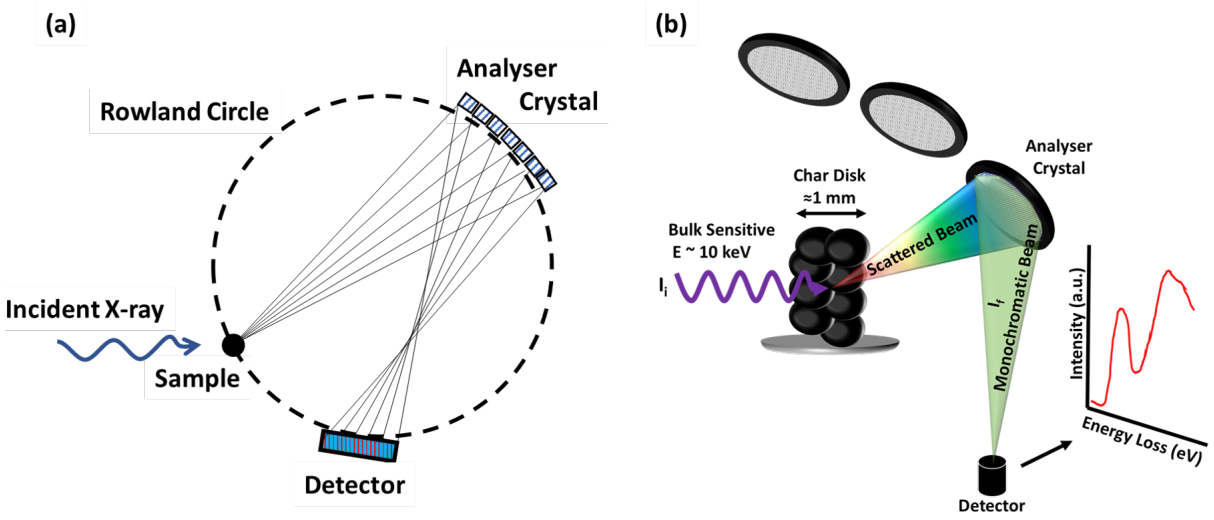


FIGURE 2.17: (a) Schematic representation of an XRS spectrometer in the Rowland geometry (b) schematic of a Rowland Geometry setup.

The layout of a modern X-ray Raman spectrometer is shown in Figure 2.17. Modern X-ray Raman spectrometers are fitted with an array of crystal analysers at known scattering angles. The analysers are arranged in a Rowland circle geometry with the sample and X-ray detector. The incoming monochromatic photon is scattered from the sample. Inelastically scattered photons with the correct energy are reflected from the analyser, where they are recorded by the detector. The monochromator energy is scanned to produce a spectrum.

**APS - 20-ID** XRS spectroscopy was performed using the lower-energy resolution inelastic X-ray scattering (LERIX) spectrometer at sector 20-ID of the Advanced Photon Source (APS), Chicago USA (Figure 2.18) [114]. At 20-ID, an undulator beamline, a cryogenically-cooled Si (311) double crystal monochromator was used to produce the monochromatic beam. The produced monochromatic beam was focused using the rhodium stripe of a torroidal mirror to an approximate size of 0.5 x 0.5 mm. The LERIX instrument contains 19 spherically bent crystal analysers (R=1 m) in the vertical scattering plane at 9° intervals, each subtending a solid

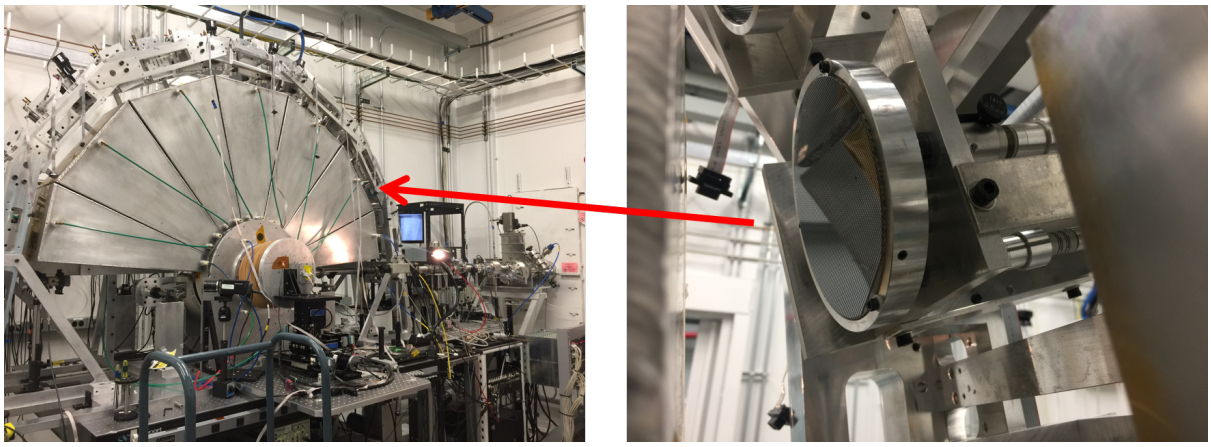

FIGURE 2.18: The LERIX spectrometer at beamline 20ID of the Advanced Photon Source. 19 crystal analysers in vertical plane (zoom of a crystal analyser shown on right).

angle of $8.3 \times 10^{-3}\,\mathrm{sr}$ [114]. Opposite each analyser crystal is a NaI scintillator detector, with the sample-analyser-detector positions lying on a $1\,\mathrm{m}$ Rowland circle geometry. The analyser crystals were tuned at the Si (555) reflection to maximise the elastic scattering profile for a nominal X-ray energy of $9.8915\,\mathrm{keV}$. XRS spectra were measured by scanning the incident photon energy and keeping the analyser energy fixed. Each set of energy scans were carried out with a scan over the elastic scattering peak ($-3\,\mathrm{eV}$ to $3\,\mathrm{eV}$). The centroid of the elastic peak was used to place measured spectra onto the energy-loss scale. Details on the software written by the candidate for extracting XRS spectra from the raw data can be found in Appendix B. Typically, the uncertainty of the extracted energy loss scale was less than $100\,\mathrm{meV}$. The LERIX sample chamber was flushed with helium gas to reduce air-scattering from the beam, which can introduce noise. In order to reduce any beam damage, samples were pressed into $13\,\mathrm{mm}$ pellets and rotated on a spinner. Scattering was recorded at a shallow angle to spread the beam across the sample.

### 2.7.4 Scanning Transmission X-ray Microscopy (STXM)

In this project, STXM provides spatially-resolved evidence for differences in carbon chemistry between the surface and bulk of sustainable carbon. STXM is a spectromicroscopy technique that provides chemically sensitive imaging at spatial resolutions down to ~$10\,\mathrm{nm}$. Imaging is performed by scanning a monochromatic beam of soft X-rays (typically between $100\,\mathrm{eV}$ to

2000 eV) across a sample in transmission geometry. As well as scanning the position, the energy of the beam is also scanned over a photoabsorption edge of interest. In this way, image stacks contain both images and X-ray absorption near-edge spectra (NEXAFS) for soft X-ray edges, including those important for biological and carbonaceous materials (e.g., C, N, O, S, Ca, Fe). STXM has been successfully applied to study a variety of carbonaceous macromolecules in the past including: soils [115, 116], humic acids [117, 118], soot [119] and polymers [120].

**Instrumentation**

STXM is used to measure spatially resolved XAS spectra. The theory covering the measurement of XAS has been covered in Section 2.7.2 and will not be discussed again here. However, the major benefit of STXM over other soft XAS measurements is the ability to create an X-ray probe on the order of a few tens of nanometres in size to provide spatially resolution.

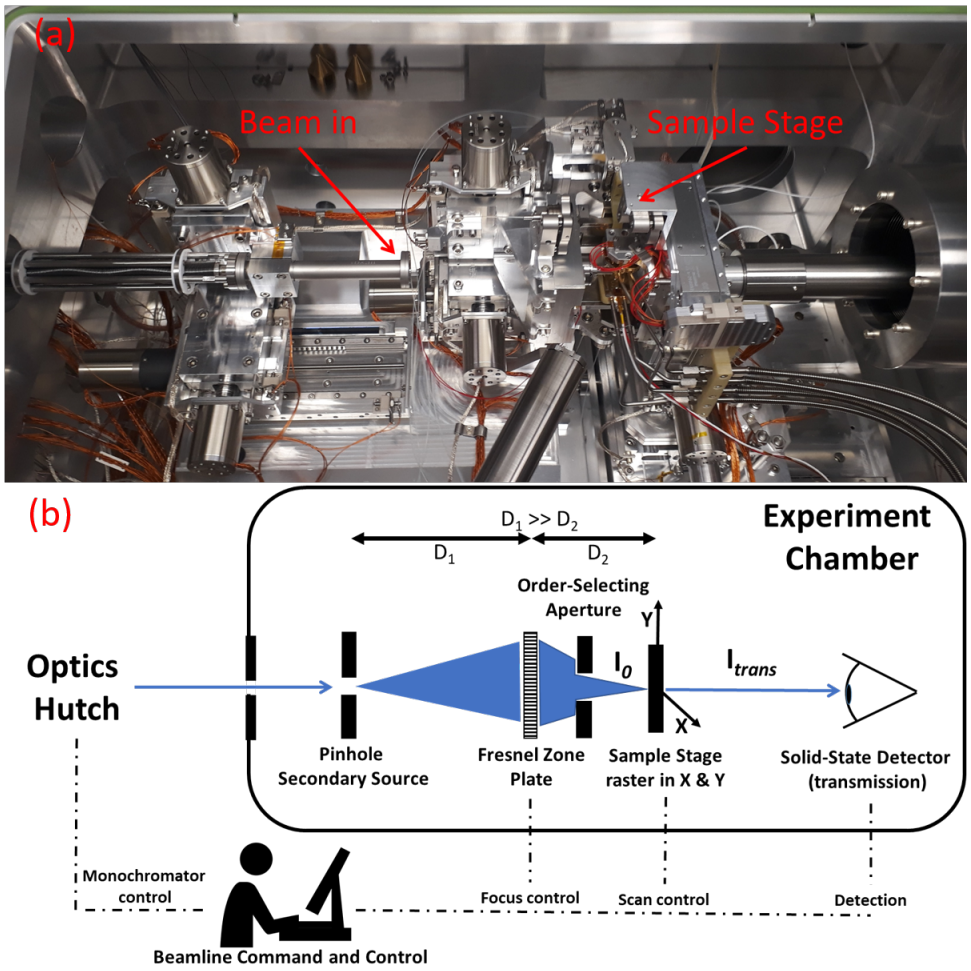


FIGURE 2.19: (a) X-ray microscope at beamline I-08, Diamond Lightsource. (b) Simplified diagram of the STXM at I-08 at Diamond Lightsource.

A simplified diagram of the STXM microscope used in this project is shown in Figure 2.19. Synchrotron X-ray radiation is required for STXM, and must be made to form a nanometre sized probe. This presents a considerable challenge in terms of the stability and thermal load on the monochromator and optics in the optics hutch. The beamline optics are used to create a millimetre sized, monochromatic beam in the order of $100\,\mu m$ size. A pinhole is then used to accept the monochromatic beam and acts a the secondary source, which is then demagnified using a Fresnel zone plate to form the focused probe. A Fresnel zone plate consists of concentric pattern of alternating absorbing and X-ray transparent rings forming a circular diffraction grating. The zone plate is designed to produce constructive X-ray interference at a point, and in this way a focused X-ray source is produced. Using zone plates, record spatial resolutions of $10\,nm$ has been achieved [121]. As in Figure 2.19, the sample is positioned at the focal point of the zone plate for imaging. The focus of the image may be controlled by moving the zone plate in the Z direction (the direction of the beam). It should be noted that the focal point of the Fresnel optic is energy dependent and that at low energies (e.g. C *K*-edge ~$285\,eV$), the distance between the sample and the zone plate is on the order of a few micrometres. An order selecting aperture, which is a pinhole measuring ~$50\,\mu m$, is used to remove undesirable higher-order diffraction from the zone plate by only allowing first-order diffracted light onto the sample. An image is recorded by scanning the focussed X-ray beam of the sample in a raster pattern (Figure 2.19).

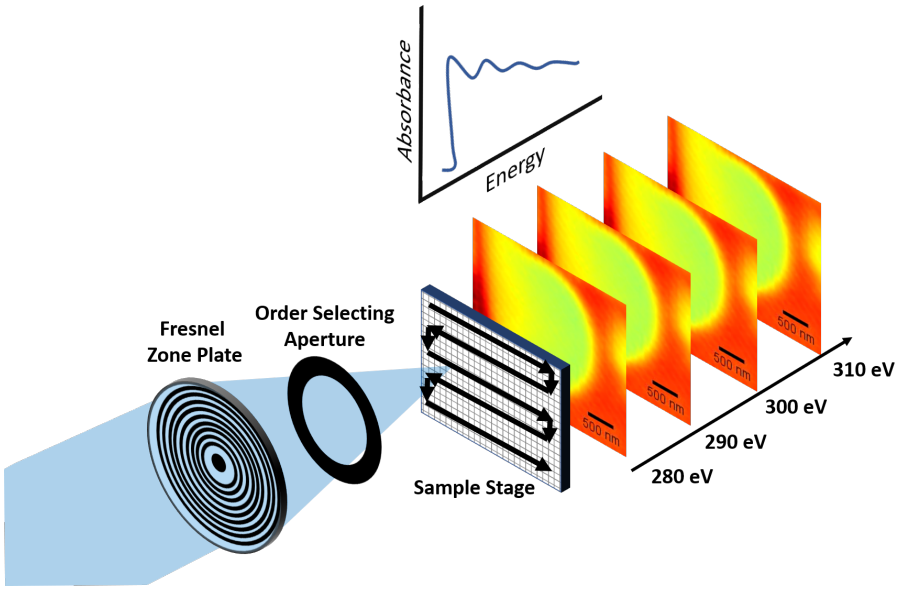


FIGURE 2.20: schematic of the collection of an *image stack* in STXM.

For each (x,y) position in the raster scan, the intensity of transmitted X-rays is recorded by either a CCD or photodiode detector. This approach produces a stack as shown in Figure 2.20. For each pixel, optical density is recorded by measuring the ratio between the intensity of the initial and transmitted beam ($O.D. = -\ln[I_{trans}/I_0]$).

STXM was performed at the Diamond Light Source (UK) using beamline I-08. Radiation from an APPLE-II type undulator was used to produce the primary beam. The beamline utilises an SX700 type plane grating monochromator ($250 \leq \mathrm{E} \geq 4400\ \mathrm{eV}$) to produce monochromatic X-rays. These monochromatic source is then focused by a pair of X-ray mirrors to a stigmatic, low-aberration secondary source ($300\,\mu\mathrm{m}$ horizontal, $50\,\mu\mathrm{m}$ vertical). The secondary source was focused to form a ~$30\,\mathrm{nm}$ X-ray probe using a Fresnel zone plate optic; undesired diffraction was removed by an $30\,\mu\mathrm{m}$ order-selecting aperture. Image stacks (6 x 6 $\mu\mathrm{m}$) were acquired with ~$40\,\mathrm{nm}$ spatial resolution, $5\,\mathrm{ms}$ dwell time and $0.15\,\mathrm{eV}$ spectral resolution over the main features of the carbon *K* edge ($283\,\mathrm{eV}$ to $300\,\mathrm{eV}$), and $0.5\,\mathrm{eV}$ resolution in the energy regions below ($280\,\mathrm{eV}$ to $283\,\mathrm{eV}$) and above ($300\,\mathrm{eV}$ to $320\,\mathrm{eV}$) the carbon *K* edge region. As-received signals were converted to optical density using incident signal ($I_0$) measurements from an adjacent, empty region of the image above the carbon *K* edge ($284.5\,\mathrm{eV}$).

**Advantages of STXM over STEM-EELS**

X-ray microscopy can be considered to be similar to STEM-EEL spectromicroscopy. Both techniques rely on the the ability to scan a nanometre sized probe over the surface of a sample and spatially resolve changes in chemical speciation. Indeed, sample preparation, image analysis and the requirement for thin ($< 100\,\mathrm{nm}$) samples are similar between STEM and STXM. However STXM comes with three major advantages over STEM-EELS imaging:

- Improved spectral resolution over STEM-EELS - As discussed, the interaction cross-section for photoabsorption is much higher than for inelastic scattering techniques such as EELS. There is an inherent trade-off between spectral resolution and dose/measurement time, allowing photoabsorption experiments (e.g. STXM) to provide higher spectral resolution. Improved spectral resolution in STXM may be used to monitor important spectral features, such as pre-edge structure, otherwise not resolvable by STEM-EELS.

- Measurements of hydrated samples - STXM can operate in the *water window*, a region of X-ray energies between $200\,\mathrm{eV}$ to $520\,\mathrm{eV}$ where water is X-ray transparent [122]. STXM can be used for biological samples where hydration is fundamental to the chemistry and morphology of cell structures [122–124].
- Reduction in dose of around 50% compared to conventional STEM-EELS for similar quality data [125] - High doses may damage samples, by changing their chemistry. For carbon materials, beam damage occurs primarily by radiolysis, the cleavage of chemical bonds resulting in the formation of amorphous carbon. STXM has been shown to reduce beam damage in carbon materials similar to those studied in this project [119].

However, it should be noted that S/TEM has significantly improved spatial resolution over STXM. Therefore STEM-EELS is often used in tandem with STXM to provide complementary high spatial and high spectral resolution information.

### 2.7.5 Synchrotron X-ray Microtomography (XμT)

X$\mu$T was used in this project to investigate the porous structure of sustainable carbon materials produced by pyrolysis. Microtomography is a three dimensional imaging technique, originally developed for medical imaging in the 1980s, and is now used extensively to non-destructively monitor changes in material structure. X$\mu$T does not require a monochromatic source of X-rays and can therefore be performed with both laboratory and synchrotron sources. However, synchrotron radiation has three key benefits over the laboratory source for microtomography: (i) brilliance, (ii) coherence and (iii) the ability to produce a monochromatic source. The high brilliance of synchrotron radiation is used to perform microtomography with extremely short scan times (seconds to minutes). This can be highly advantageous or even necessary for the measurement of dynamic systems and processes (e.g. crystallisation, *in-operando* devices) [126]. The use of a collimated, parallel beam in synchrotron microtomography allows for measurements to be performed with improved contrast, fewer artefacts and higher spatial resolutions. Modern X-ray tube CT systems can now achieve spatial resolutions down to $1\,\mu\mathrm{m}$ [127]. However, synchrotron X$\mu$T may be performed with resolutions on the order of $50\,\mathrm{nm}$. Indeed, with the use of zone plate optics nanometre scale resolution may be performed but with limitations

on sample thickness and the total field of view. The use of a monochromator before the secondary source can also be used to gain chemical contrast in the sample by tuning the energy of the X-ray to above and below a relevant X-ray photoabsorption edge. Finally the highly coherent X-rays produced by synchrotron sources can be used to perform phase-contrast measurements. Phase contrast measurements provide enhanced contrast for low-Z elements, which may prove highly beneficial for organic solutions or carbon materials [128].

### Instrumentation

X$\mu$T is a projection imaging technique. A schematic of the collection of X$\mu$T is shown in Figure 2.21. In absorption contrast mode, the attenuation of X-ray beam is dependent on the thickness and the attenuation coefficient of the sample as described in the Beer-Lambert law (Equation 2.1). The transmitted X-rays are converted into visible light using a scintillator. The produced optical light is then magnified using an objective lens onto the CCD which records a single projection as a 2D radiograph. Single projections are collected as the sample is rotated, producing a stack of radiographs as a function of the angle of sample rotation.

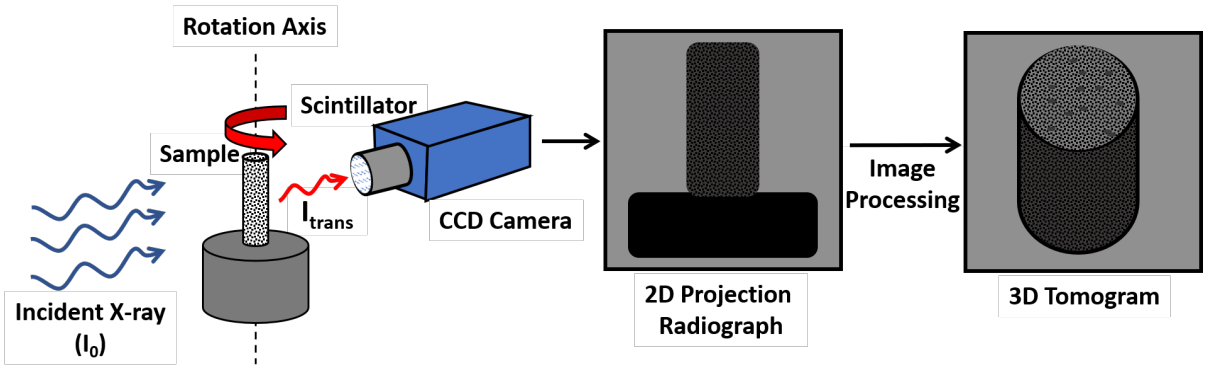


FIGURE 2.21: schematic of the collection of a tomogram using X$\mu$T .

A series of radiographs which are taken as the sample rotates in the vertical plane from 0-180° are then reconstructed, typically by using back filter projection methods, to form a three dimensional image. X$\mu$T may suffer from several different forms of artefacts including ring artefacts from a poorly callibrated centre of rotation, movement artefacts from changes in sample position during the scan and zingers from high-energy particles impacting the scintillator during measurements. Such artefacts severely complicated the reconstruction of projections in 3D tomograms, notwithstanding the total data size of the radiographs, which could be tens of gigabytes or more. Image enhancement can be carried out using powerful colour and contrast

filters, including Fast Fourier Transforms (FFT), phase retrieval, drift correction and normalisation.

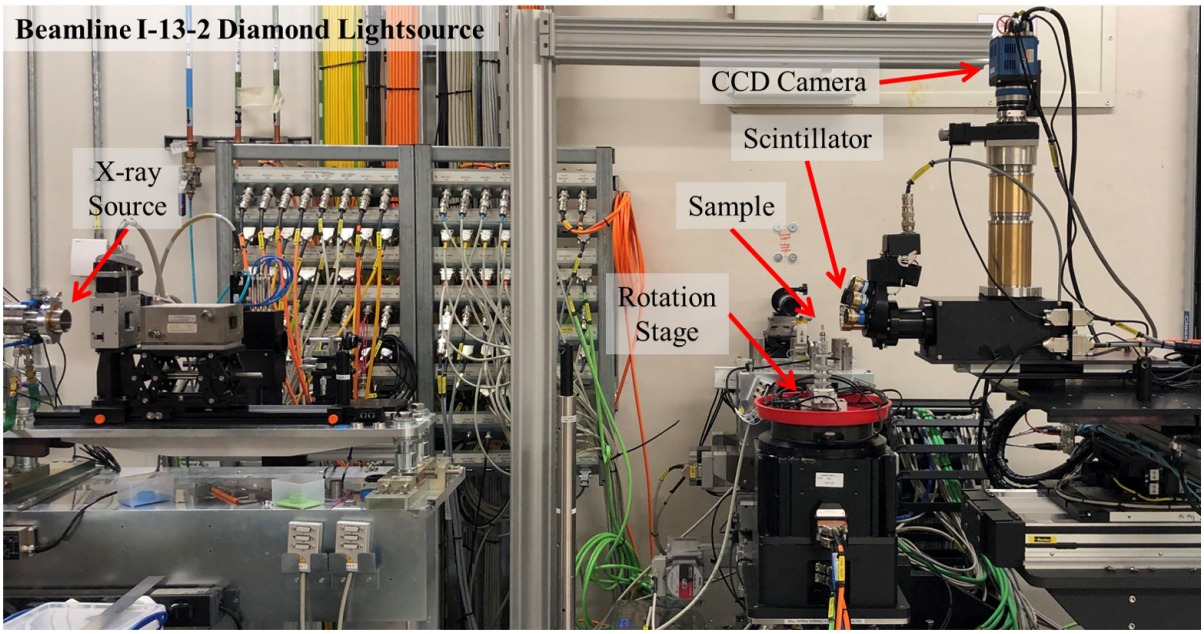


FIGURE 2.22: X$\mu$T in this project was performed at beamline i13-2 at Diamond Lightsource Ltd.

**DLS - I13-2** X$\mu$T in this project was performed at the Manchester beamline (I13-2) of the Diamond Light Source, UK (Figure 2.22). Monochromatic X-ray radiation was formed using a Si(111) liquid-cooled double crystal monochromator. Samples of biochar were affixed to steel pins using adhesive, then rotated in the beam by 180 degrees at 1.26 mrad per projection. Tomograms were acquired using a 2560 × 2160 pixel PCO Edge 5.5 CMOS camera that was optically coupled to a $CdWO_4$ scintillator crystal. In this way, each tomogram was formed from 2500 projections with an exposure time of $500\,\mathrm{ms}$ and a pixel size of $0.325\,\mu\mathrm{m}$. Analysis of the tomography data was performed on the I13-2 data beamline at the Diamond Light Source using the available powerful graphic workstations [129]. Initially images were converted to 8 bit image depth. Following conversion TomoPy, a python-based software library for tomographic reconstruction, was used to perform alignment and reconstruction of the tomograms [130]. A non-local median filter was applied to the tomogram after reconstruction in order to improve contrast between features. Subtraction of the pre and post-edge tomograms was performed using a developed python script. Image processing was performed using Thermo Scientific Amira-Avizo 9.5 software.

# Chapter 3

# Evidence for a Core-Shell Structure of Hydrothermal Carbon

## 3.1 Introduction

The treatment of carbon feedstocks in hot, compressed water (HCW, 150 - 350 °C) is known as hydrothermal carbonisation (HTC). HTC produces a disordered, non-graphitising carbon product known as hydrothermal carbon and an aqueous liquor which predominantly contains a range of organic acids and water-soluble furan derivatives. As discussed in Section 1.3.2, HTC was initially performed in a series of experiments by Frdereich Bergius in attempts to produce synthetic coal from biomass following attempts to improve the kinetics of producing hydrogen from coal [63]. Bergius' discovery was that a starting feedstock must be kept in intimate contact with sub-critical water in order to prevent the premature breakdown of carbohydrates. This led to a series of authors commenting on the mechanisms underpinning the formation of coal from biomass, not least Bergius himself [64]. However, after a long stagnant period in HTC research, focus has now shifted from understanding the fuels of previous centuries to understanding sustainable materials in the 21st century. Current research into the use of HTC may be split into two important branches:

i. HTC as a safe, sustainable and low-cost conversion process from complex biomass feedstocks to a useful or less-hazardous product.

ii. HTC as controlled synthetic route to convert pure or semi-pure reagents (e.g. glucose) to tailored materials for device applications.

Hydrothermal carbon is rich in oxygen functional groups and offers good propensity for chemical tuning of its surface. HTC may be performed without harmful reagents and offers higher yields, lower synthesis temperatures and lower input energies than an equivalent pyrolysis process without the need for energy-intensive feedstock drying [131]. These advantages make HTC viable for both the sustainable treatment of wastes, where it is currently being applied at pilot-scale [132, 133], but also for the production of highly-functional carbon materials [134]. In the former case, HTC has been found to be an effective strategy for treating more harmful biomass wastes (e.g. medical wastes, sewage sludge) and for producing a renewable low-ash bio-coal [51, 89, 133]. However the main focus of this project has been building an understanding of HTC for the production of sustainable materials with useful properties. Whilst HTC for the production of materials is arguably less well developed, the process has been shown to be a promising route to produce energy storage devices, catalyst supports and filtration materials directly from biomass [50, 134]. The ability to produce such materials directly from low-value biomass materials makes HTC very attractive for implementation into a biorefinery. Unfortunately, the production of hydrothermal carbon from biomass poses significant challenges due to the complexity of the feedstock. Lignocellulosic biomass is composed of cellulose, hemicellulose and lignin. Cellulose is a linear polysaccharide of glucose units linked by $\beta$-(1,4)-glycosidic bonds [135]. Hemicellulose is also a polysaccharide, but differs from cellulose in that it is composed of a number of sugar monomers, such as xylose, glucose, mannose and galactose. Lignin is a complex, high molecular weight biopolymer, that is not well defined and is not thought to react during HTC until temperatures above ~250 °C. These complex biomass structures make developing an analytical understanding of HTC challenging [136]. Furthermore, non-lignocellulosic components of biomass (e.g. inorganic components) are known to affect the morphology and chemistry of the final carbon [137]. This, coupled with the challenges of batch by batch heterogeneity in a lignocellulosic biomass feedstock, makes a controlled and repeatable biomass HTC process for materials production challenging to implement.

In order to better understand the processes governing the formation of hydrothermal carbon from lignocellulosic biomass, several groups began to investigate the hydrothermal reaction mechanisms underpinning HTC of sugars (e.g. glucose, fructose) [138, 139]. By understanding HTC of sugars, it is hoped that a better model for more general biomass conversion can be produced. This approach has successfully isolated so-called "secondary char", also known as

humins, which are defined by their spherule shape and furanic chemistry [140, 141]. Kinetic modelling experiments have shed light on the rates and kinetics involved in HTC of sugars, whilst FTIR and $^{13}C$ – NMR spectroscopy studies have been used to investigate the structure of the produced carbons [139, 142]. However, it was noticed that the use of carbohydrates (e.g. glucose, fructose) as a starting feedstock for HTC produced repeatable results with more well-defined physicochemical properties [143]. The benefit of using carbohydrates as a feedstock for HTC-derived materials lies in the control that one is able to wield over the formation of the produced hydrothermal carbon. Hydrothermal carbon with regular spherical shape and controllable size have been shown to be excellent catalyst support materials [144]. The ability to control HTC chemistry *via* addition of heteroatoms (e.g. N) can also be used to exert control over the functionality of the carbon, producing carbon with high pseudocapacitance and selective sites for efficient electrocatalysis [145, 146]. This granular control has led to cases where research has shifted to the production of sustainable catalysts and energy storage devices (e.g. electrocatalysts, supercapacitors) from carbohydrate precursors [50].

A full understanding of both the formation mechanisms governing HTC and resulting surface functionalities are critical for producing useful high-technology devices from biomass. The surface functionalities of hydrothermal carbon can be exploited by nanoparticle decoration or by increasing the concentration of surface oxygen functionalities, which are important for catalysis and filtration devices [147, 148]. The reaction mechanisms governing hydrothermal carbon formation and growth in the autoclave are poorly understood. A successful model of hydrothermal growth would likely pave the way for more efficient carbon production as well as improved control over the properties of the final product. Earlier work has proposed a shell-core model of hydrothermal carbon, with differing carbon functional groups between the surface and core of a hydrothermal carbon spherule [149]. This chapter sets out the work done to achieve the first spectroscopic evidence of a shell-core structure of glucose-derived hydrothermal carbon [111].

## 3.2 Current Mechanism of Hydrothermal Carbon Formation

### 3.2.1 Glucose as a Model Hydrothermal Carbon Precursor

In this chapter a model carbohydrate, glucose, was used to investigate the formation of hydrothermal carbon. The decision to use a model sugar, instead of lignocellulosic biomass, was taken for several reasons discussed here. Firstly, solid-solid reactions between biomass components, including the high-molecular weight lignin fraction, result in the formation of a primary char. Primary char chemistry more closely resembles pyrolysis carbon, and is typically not included in the definition of secondary char, or hydrothermal carbon, which is formed by the breakdown of carbohydrates under HCW conditions. As discussed, secondary char is usually identified by its micrometre sized spherule morphology and furanic chemistry. Secondly, the use of a model sugar instead of lignocellulosic biomass rules out the non-trivial complications of inorganic phases within the feedstock influencing the reaction mechanisms at play. Thirdly, model carbohydrates have been widely used to represent the chemistry of the non-lignin components of lignocellulosic biomass, since both cellulose and hemicellulose are composed of simple sugars as monomers [136]. In this way, a model sugar (i.e. glucose) can provide insight into the reactions governing HTC of lignocellulosic biomass. Finally, the use of common carbohydrates, produced sustainably from biomass, represent one route to produce well-controlled materials from waste [150]. For this reason, understanding the formation mechanisms at play during the HTC of sugars is directly relevant to the production of hydrothermal carbons produced for applications in devices.

### 3.2.2 Current HTC Formation Mechanism

The transformation of cellulose and hemicellulose from the lignocellulosic biomass structure is achieved through hydrolysis reactions under HCW conditions [151]. The product of these hydrolysis reactions is mainly glucose or other hexoses (e.g. mannose). More specifically, the Lobry de Bruyn van-Ekenstein transformation results in the isomerisation of glucose to fructopyranose, which is the favoured equilibrium state under HCW conditions (Figure 3.1) [152]. A full description of this mechanism is complex and fully reviewed elsewhere [153]. However, the breakdown of most cellulose to glucose under HCW conditions makes glucose a good model compound for understanding the formation of hydrothermal carbon under ideal

conditions. The concentration of hydronium ions in HCW leads to the decomposition of these early monosaccharides and disaccharides to organic acids (e.g. acetic, lactic, levulinic and formic acids) bringing about a rapid drop in pH [152]. The rapid drop in pH within the reactor catalyses the dehydration of fructofuranoses into 5-hydroxymethylfurfural (HMF) [154]. An equilibrium is reached between the dehydration of fructose to HMF and its rehydration to levulinic acid and formic acid. The final concentrations of HMF, levulinic and other organic acids depend on process temperature. Longer reaction times and higher temperatures lead to the almost complete removal of HMF from the process liquor. The removal of HMF from the process liquor has been shown to be proportional to the amount of formed hydrothermal carbon, suggesting that HMF is the principle monomer for hydrothermal carbon formation [139]. As the reaction time is increased, the concentration of HMF decays, whilst the concentration of formic acid, levulinic acid and hydrothermal carbon increases [139].

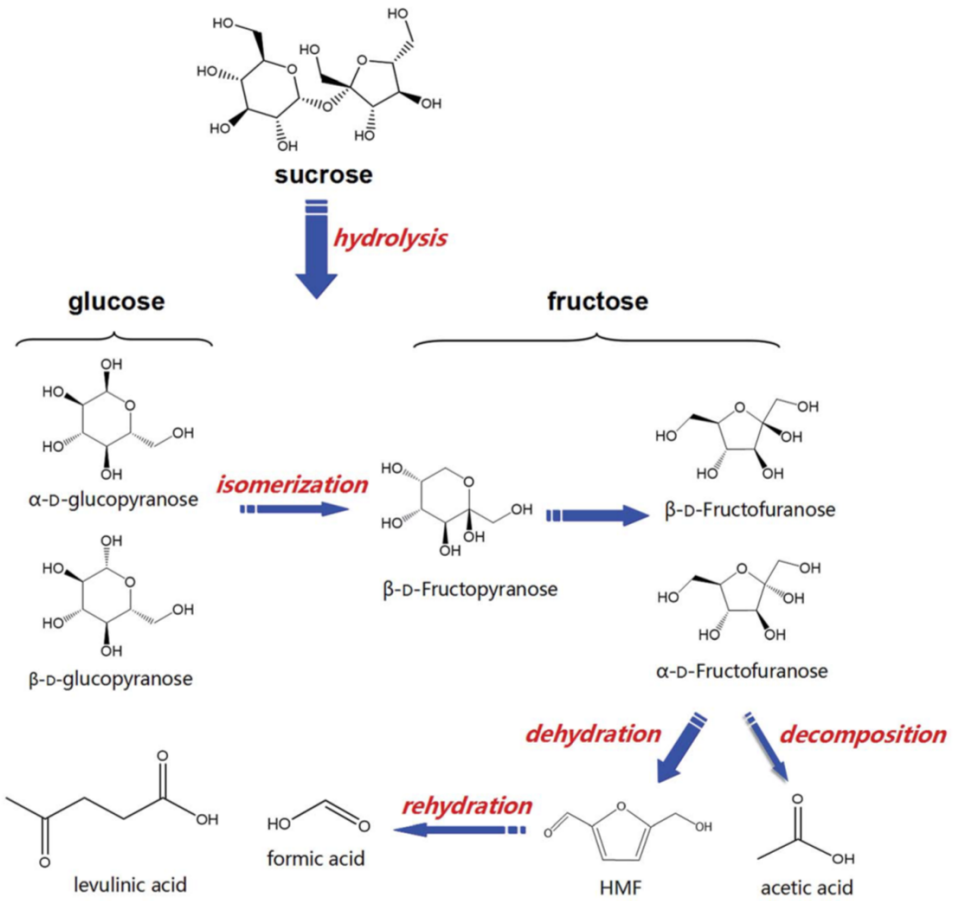


FIGURE 3.1: Illustration of the reactions governing the breakdown of sugars in hydrothermal conditions. Adapted from Ref. [155] with permission from The Royal Society of Chemistry.

**Hydrothermal Carbon Morphology**

Once HMF, or furfural the dehydration product of xlylose, are formed they polymerise to form hydrothermal carbon *via* a complex cascade of reactions. The nucleation of hydrothermal carbon has been shown to be driven by increased reaction temperature and lowered pH by the formation of organic acids [139, 156]. There appears to be an equilibrium balance between the rehydration of HMF to levulinic acid and the formation of colloidal hydrothermal carbon [141]. However the route by which HMF produces hydrothermal carbon is disputed. Initial work into understanding the nucleation of hydrothermal growth was performed by monitoring the morphology and structure of the produced carbons at different temperatures, residence times and starting sugars [141].

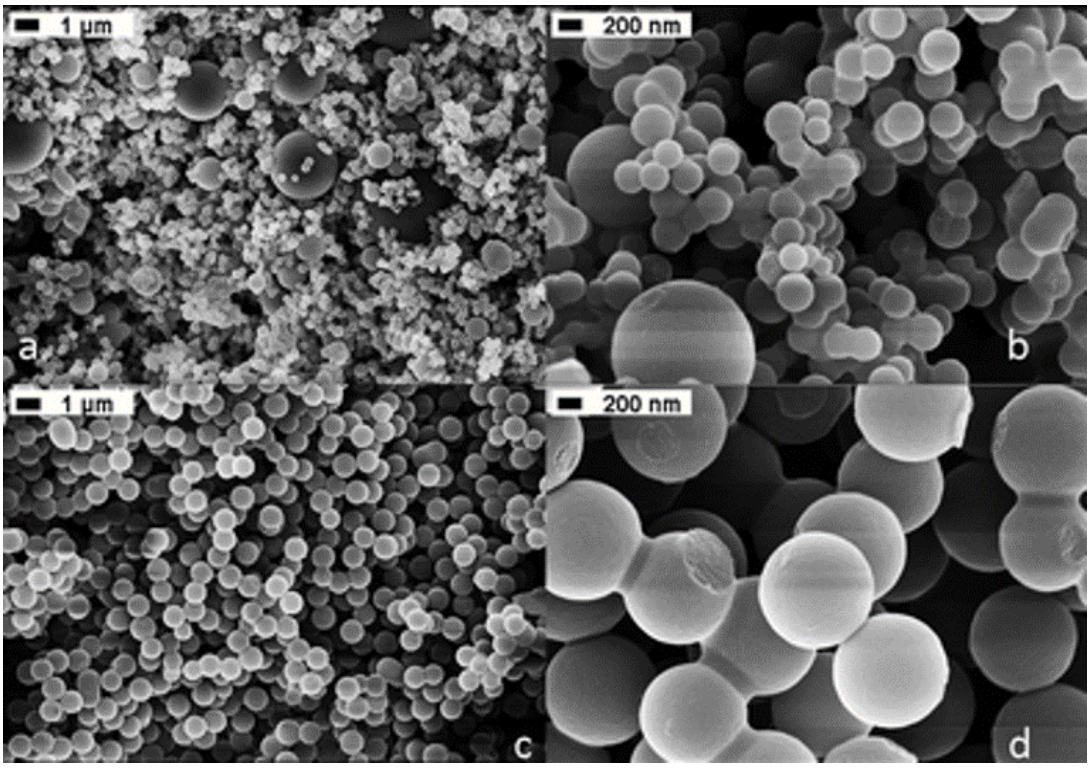


FIGURE 3.2: SEM BSE images of hydrothermal carbon derived from glucose at 160 °C (a, b) and 260 °C (c, d). Taken from [136] with permission from The Royal Society of Chemistry.

Figure 3.2 shows hydrothermal carbon produced from glucose at 160 °C and 260 °C respectively. Hydrothermal carbon from glucose produces spherule shapes which are often joined together in a characteristic 'dumbbell' shape. It was also observed that increasing the process temperature results in the formation of larger average spherule diameters [136]. Higher process temperatures also produce carbons with a more homogeneous average size. Interestingly

*Falco et.al.* observed that, at higher process temperatures, the average particle size measurements from dynamic light scattering and SEM measurements were well-matched, whilst at lower temperatures dynamic light scattering reported much large particle sizes [136]. The authors postulate that this due to the formation of polydispered clusters of hydrothermal carbon, grouping to form much larger particles. The growth of hydrothermal carbon at higher process temperatures using the same process time is most likely due to a singular growth phase. It has been shown that the growth of hydrothermal carbon occurs rapidly once the starting monomer, HMF, is completely consumed which may indicate a initial burst of nucleation followed by a coalescence phase [139].

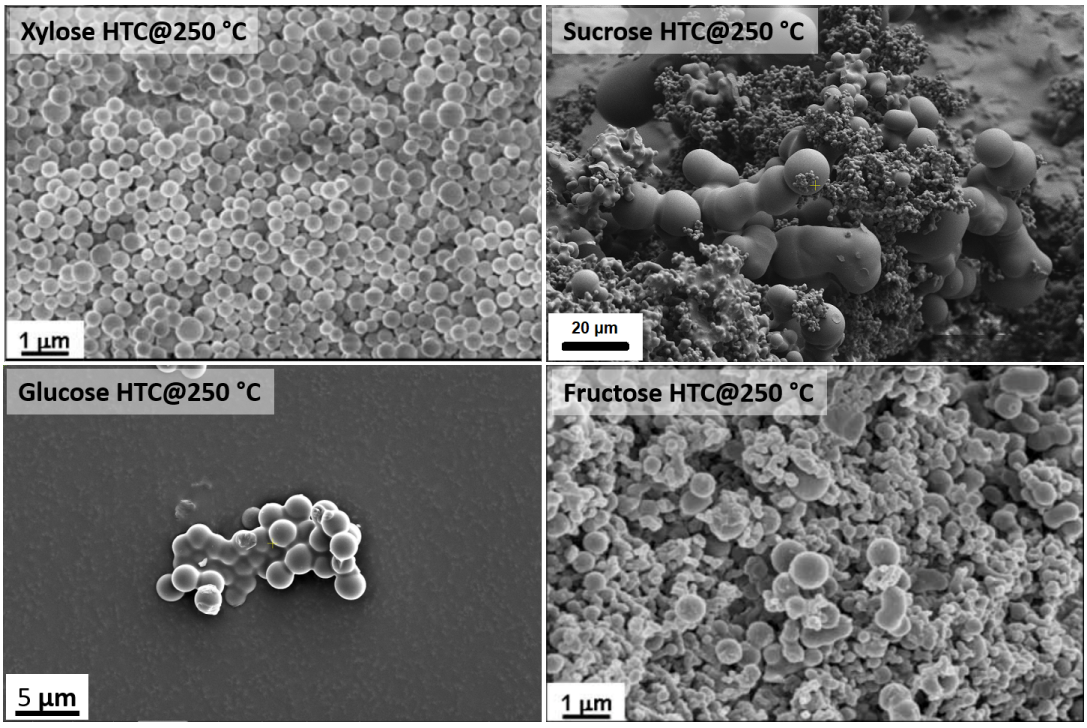


FIGURE 3.3: Scanning electron micrographs of hydrothermal carbon materials obtained from xylose, sucrose, glucose and fructose at a process temperature of 250 °C

The morphology of hydrothermal carbon produced from other carbohydrate precursors has also been investigated. Figure 3.3 shows hydrothermal carbon produced under the same process conditions at 250 °C from a range of relevant sugars. The morphology of the produced carbon remains as the familiar spherule shape, however the homogeneity and sizes of the produced carbons are remarkably different. *Titirici et.al.* described the carbons produced from pentoses (i.e. fructose, xylose) as dispersed spheres, whereas those produced from hexoses (i.e. glucose) as a mixture of interconnected particles below 200 nm and spheres between 500 nm to

1000 nm [43]. The authors suggest that the differences in morphology between hexose and pentose sugars are due to a different formation pathway, postulating that C5 sugars proceed *via* polymerisation of furfural, whilst C6 sugars are formed by the polymerisation of HMF [43]. This interesting hypothesis highlights the direct effect that mechanistic pathways can have on the final properties of the HTC derived carbon. The furfural pathway for C5 sugars and the morphology of carbohydrate-derived hydrothermal carbon at different residence times have also been investigated. It was found that at a low temperature of 180 °C no significant changes occur before 4 hours, where the process water becomes orange due to the formation of oligosaccharides. Past 5 hours, hydrothermal carbon particles 150 nm in diameter are formed [157]. The observation of small nanoparticles above a threshold temperature suggest that proto-carbon forms from oligosacharides by a rapid burst-type nucleation event.

### Hydrothermal Carbon - Nucleation and Growth

Studying the nucleation and growth of hydrothermal carbon is challenging because of the difficulty of following the cascade of reactions that form the high molecular weight carbon [141]. This difficulty is compounded by the challenge of performing *in-situ* measurements, since HTC is performed in a sealed autoclave under pressure. However the chemistry governing the formation of the monomer HMF is well understood because of the analogous breakdown of sugars under highly acidic conditions and through advances in *ab-initio* simulation [141, 158].

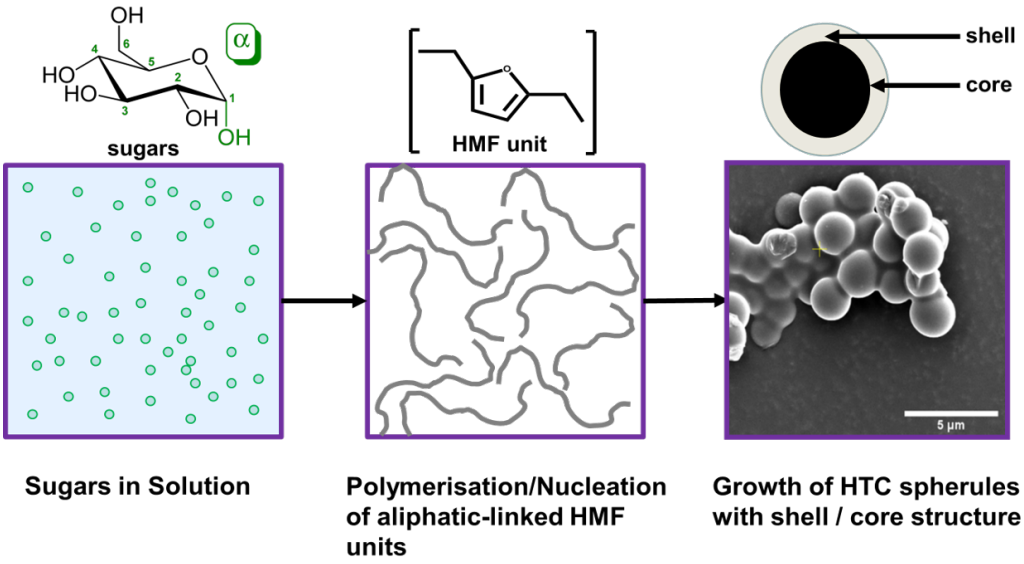


FIGURE 3.4: Schematic representing the nucleation and growth process for C6 sugar derived hydrothermal carbon.

Beyond the formation of HMF, or furfural for C5 sugars, a mechanistic understanding of hydrothermal carbon nucleation and growth becomes limited. In an early work on hydrothermal carbonisation for catalysis *Sun et.al.* published the simplified three stage mechanism shown in Figure 3.4 [148]. In the second stage of this mechanism, HMF is thought to polymerise and nucleate to form the nascent hydrothermal carbon. Observations of sub $10\,\mathrm{nm}$ proto-carbons have been reported by TEM imaging of process water from the HTC of fructose at $150\,^{\circ}\mathrm{C}$ [159]. The formation of these proto-carbons is likely due to condensation of HMF molecules or other derivatives to form oligosaccharides [139]. *Patil and Lund* postulate that the formation mechanism is a reaction of five HMF molecules and 2,5-dioxo-6-hydroxy-hexanal that releases four water molecules [141]. At a certain point, the oligomer ceases to be soluble under the HCW conditions, likely driven by HCW chemistry (e.g. pH, ionic product), resulting in a phase separation of these oligomers, and the formation of proto-carbon. These nanocarbons then undergo a growth stage (Figure 3.4). To date, no *in-situ* measurements of HTC nucleation and growth have been conducted. It is possible that *in-situ* small/wide angle X-ray scattering could be used to provide significant insight into the mechanisms governing hydrothermal carbon growth as has been done in other systems [160]. Two mechanisms for the growth of hydrothermal carbon have been proposed in former studies: LaMer growth and hydrophobic ripening.

**LaMer Growth Model** Initial reports of the growth stage of hydrothermal carbon suggested a LaMer type growth [148, 149]. The LaMer model is widely cited in colloid science to explain the formation of monodisperse particles from saturated solutions [161, 162]. Briefly, a rapid increase in the concentration of free monomers in solution leads to a burst-type nucleation, significantly reducing the concentration of the monomers in solution. In HTC of carbohydrates, this critical stage is thought to be the point of maximum HMF concentration, which has been observed as an orange/red mixture of oligosaccharides within the reactor [151]. Following nucleation, growth is limited by the diffusion of the monomer through the solution. it involves the increase in concentration of a dissolved species until a critical point is reached. Beyond this critical point, a rapid "burst" type nucleation from the monomer and any co-monomers occurs. Homogeneous nucleation stage growth occurs by heterogeneous nucleation as monomers bond to pre-existing seeds [163]. The final growth stage determines the the final number of particles and their subsequent size. The hydrophobicity of the growing

proto-carbon is likely to have a significant effect on the aggregation of proto-spheres, resulting in the reported feedstock-dependent monodispersed or polydispered carbon morphology.

**Growth by Hydrophobic Ripening** More recently, *Zhang et.al.* postulated an alternative HTC growth mechanism to LaMer growth. The authors measured the decline of the HMF concentration in HTC process water as a function of process time and concluded that it conflicts with a discrete nucleation mechanism [159]. Instead, the authors postulate a hydrophobic ripening model. Hydrophobic ripening is a subset of Ostwald ripening, which is critical in the study of emulsions and other phase-separated interfaces. Ostwald ripening is caused by the change in solubility of nanoparticles dependent on their size. Smaller nanoparticles with high solubility and low surface energy redissolve, resulting in the growth of phase-separated components at the expense of smaller nanoparticles. Full and detailed reviews of Ostwald ripening are available elsewhere [164, 165]. For hydrothermal carbon, condensation of the HMF monomer leads to the nucleation of a 3D cross-linked furanic structure with a highly hydrophillic surface due to the presence of carboxyl end-units. As the reaction goes on, a phase-separation process occurs when condensation reactions lead to the formation of a more hydrophobic structure. At this point, proto-carbon nucleation occurs. Instead of a "burst" of nucleation as in the LaMer model, hydrophobic ripening occurs due to the continuous removal of carboxyl end-units as nearby proto-carbons coalesce. Secondary observation of coalescence has been found in kinetic models, which appear to support this growth model [139].

### 3.2.3 Shell-Core Model of Carbohydrate-Derived Hydrothermal Carbon

A shell-core structure of hydrothermal carbon was first postulated in early studies [148]. Since then, a LaMer growth mechanism with a core-shell structure has been widely cited throughout the literature [138, 149, 155, 166]. Direct measurement of chemical differences between the shell and core of hydrothermal carbon have proved challenging. Bulk elemental analysis of hydrothermal carbon from carbohydrates has shown that these materials have consistent bulk O:C ratios of between 0.23 - 0.33 [139, 149, 166]. Evidence for a shell-core model of hydrothermal carbon was given *via* indirect observation of small differences between oxygen to carbon (O:C) atomic ratios observed using surface-biased XPS and bulk elemental analysis [138, 149]. *Fuertes et.al.* performed a comparison of XPS and elemental analysis, and observed that the O:C

atomic ratios in the core and in the shell of the particles are quite similar. However, despite the similar O:C values, the authors hypothesised that: *"the oxygen groups in the inner part of the hydrothermal carbon particles likely differ from those in the shell"* [149]. High resolution C1s XPS spectra appear to support the presence of carboyxlic groups on the carbon surface by the presence of a a shoulder in the $288\,\mathrm{eV}$. However no direct experimental evidence for a core-shell structure has been found.

**Chemistry of the Hydrothermal Carbon Shell/Surface**

Fourier-Transform Infrared (FTIR) spectroscopy has shown the presence of aliphatic and carboxyl carbon functionalities [143, 155]. XPS on the other hand, is highly sensitive to the surface chemistry of carbonaceous materials. High resolution XPS of the Carbon 1s region have commonly been split into three regions: (A) $285\,\mathrm{eV}$ (C-C, C=C), (B) $286.6\,\mathrm{eV}$ (C-O-H (hydroxyl)) and (C) $288\,\mathrm{eV}$ (carbonyl). Results from several authors show relatively high intensity of peaks B and C, indicating a considerable amount of oxygenated surface functionality, which is in good agreement with FTIR studies [143, 167]. Thermal analyses using thermogravimetric methods in combination with GC-MS techniques have also shown the levulinic acid and carboxyl species are present within hydrothermal carbon, most likely at the surface [143]. NEXAFS spectroscopy at the Carbon and Nitrogen *K*-edges has also been applied to nitrogen doped hydrothermal carbons from sucrose [168]. The measurement was performed at the Australian synchrotron using partial electron yield detection, which is surface sensitive to $\sim 50\,\mathrm{nm}$ [169]. A feature at $286.6\,\mathrm{eV}$ was attributed to the C−O bond in furan structure, as well as a feature at $288\,\mathrm{eV}$, which was attributed to surface carbonyl functionality in good agreement with other studies. TEM imaging of a shell-core structure was achieved by *Yao et.al.* [170].

**Chemistry of the Hydrothermal Carbon Core/Bulk**

As an amorphous material primarily composed of carbon and oxygen, hydrothermal carbon presents a significant challenge in terms of bulk spectroscopy. Confirmation of the amorphous nature of carbohydrate derived hydrothermal carbon was given by powder XRD measurements. XRD shows broad features for the inter-layer {0 0 2} and intra-layer {1 0 0} graphite reflections, confirming that hydrothermal carbon is a highly amorphous, disordered carbon

system [143]. The first bulk carbon spectroscopy for hydrothermal carbon was performed using solid $^{13}C$ nuclear magnetic resonance (NMR) spectroscopy [142]. A full description of solid state $^{13}C$ – NMR is beyond the scope of this review, but may be found in Ref. [171]. Conventional solid state NMR gives limited information about the structure of hydrothermal carbon, due to the relatively low (< 1%) natural abundance of the isotope $^{13}C$. Isotopic enrichment of hydrothermal carbon was performed by *Baccile et.al.* to gain the necessary resolution. Early models of the structure of hydrothermal carbon were aromatic in nature, consisting of small clusters of arene functionality with an oxygenated surface [149, 172]. A revised model of the structure of bulk hydrothermal carbon from carbohydrates was given by isotopically enriched, advanced solid state NMR measurements, which clearly showed that the structure was principally furanic in nature with some aromatic functionality [142, 173]. Furthermore, as previously discussed, it was shown that there were differences in the ratios of aromatic to furanic carbon between those produced from C5 and C6 sugars, with the former being more aromatic in nature [142]. The authors proposed that C5 sugars were more aromatic due to the principal monomer being furfural rather than HMF. Finally solid state $^{13}C$ – NMR was used to show that hydrothermal carbons produced from cellulose and lignocellulosic biomass, was similar in bulk carbon chemistry to that of those prepared from carbohydrates [136]. A final note on the bulk chemistry of hydrothermal carbon must be made regarding the use of X-ray spectroscopy. Conventional X-ray absorption spectroscopy must be performed in the soft X-ray regime, where measurements must be performed under vacuum and only provide surface information. However, as will be discussed in Chapter 4, X-ray Raman scattering spectroscopy may be used to probe soft X-ray photoabsorption edges using hard X-rays for bulk chemical insight with some key advantages over solid state $^{13}C$ – NMR [111].

## 3.3 Aim

The aim of this study was to the provide the first direct experimental evidence for a core-shell type structure in hydrothermal carbon using a synergistic TEM imaging and STXM spectromicroscopy approach. Previously reported measurements have not, as yet, provided direct experimental evidence of differing carbon chemistry between a shell and core in carbohydrate derived hydrothermal carbon. Formation of hydrothermal carbon is a phase separation

process under HCW conditions [139]. Hence, studying chemical alterations between the hydrothermal carbon interface, bulk material and surrounding aqueous environment is perhaps the most likely route to elucidate reaction pathways that underpin hydrothermal carbon formation and growth. In this study STXM, a synchrotron-based spectromicroscopy technique, is applied to a thin FIB-prepared cross-section of a single glucose derived hydrothermal carbon spherule. STXM, as discussed in Section 2.7.4, allows for the collection of spatially resolved XAS spectra, and has been applied to a variety of similar carbonaceous macromolecules (e.g. soils [115, 174], humic acids [117, 118], soot [119] and polymers [120]). Differences in surface and bulk carbon chemistry have also been identified in carbonaceous interfaces and thin films [175–178] and in pyrolysis carbons [179] using similar approaches to the one applied here.

## 3.4 Experimental Techniques

### 3.4.1 HTC of Glucose

HTC was performed as described in Section 2.3 at $200\,^{\circ}\mathrm{C}$ and $250\,^{\circ}\mathrm{C}$ under autogenous pressure. For each batch carbonisation, $20\,\mathrm{g}$ of glucose ($\leq$99.5 %, Sigma Aldrich) was dissolved in $200\,\mathrm{ml}$ of ultra-pure ($\geq 18\,\mathrm{M\Omega\,cm}$) water. The prepared 20 %w/v glucose solution, when completely dissolved, was loaded into the autoclave in an acid-washed quartz liner. After the reaction the resulting carbons, HTC-GLC-200 and HTC-GLC-250 produced at $200\,^{\circ}\mathrm{C}$ and $250\,^{\circ}\mathrm{C}$ respectively, were recovered by filtration (Whatman, Grade 3) without a solvent wash. A solvent wash, or soxhlet extraction was not performed in order to (i) reduce the risk of introducing erroneous features into the C *K*-edge X-ray spectroscopy arising from the presence of organics used for extraction and (ii) to avoid removing chemically-relevant macromolecules.

### 3.4.2 SEM

A few milligrams of powdered sample were affixed to a sticky carbon pad onto an aluminium SEM stub (Agar Scientific, UK). Excess sample was removed by compressed air. A $5\,\mathrm{nm}$ iridium sputter coating was applied to the prepared resin block using a high-resolution sputter coater (Agar Scientific, UK). Imaging was performed using the same FEGSEM used for FIB lift-out (see Section 2.5.3), using a voltage of $5\,\mathrm{kV}$ to provide good surface contrast.

### 3.4.3 S/TEM

FIB prepared lamellae were imaged using a FEI Titan$^3$ Themis G2 scanning transmission electron microscope (S/TEM). The field emission gun was operated at $80\,\mathrm{kV}$ in order to reduce knock-on damage to the sample during imaging. Images were processed in Gatan Microscopy Suite and the FIJI distribution of ImageJ [180].

### 3.4.4 Powder XRD fitting

XRD patterns were performed in triplicate using the method discussed in Section 2.6.1. The resulting patterns were averaged, and then smoothed using a Savitzky-Golay filter (window size 51 points, third order). Non-Linear least-squares regression fitting was performed using the LMFIT software [181]. Gaussian fitting was performed with two Gaussian functions and a

power law background model (order = -0.25), in order to find the approximate centre of the {0 0 2} interlayer carbon spacing.

### 3.4.5 STXM Data Analysis

Post-experiment treatment of the STXM-NEXAFS data was initially performed using the Mantis spectromicroscopy software. Mantis was used to normalise the carbon *K*-edge spectra, subtract dark current and correct for spatial drift in the image [182]. The Mantis software was also used to conduct a principal component (PCA) and cluster (CA) analysis, whereby a set of eigenimages and eigenspectra from the data covariance matrix are classified into clusters of pixels of similar spectral response. Further details on the workflow and analysis performed using Mantis may be found in the publication by *Lerotic et.al.* [182]. Extracted NEXAFS spectra were subsequently fit using a Gaussian fitting approach, which has been widely applied to carbon *K*-edge spectra to investigate local structural changes in similar materials [115, 174, 183]. Details of the Gaussian fitting approach applied throughout this thesis are shown in Appendix A. For reference, a table of the Gaussian peak locations used in this work, with relevant references, are shown below in Table 3.1.

TABLE 3.1: Summary of Gaussian peak locations and functional group assignment for carbon *K*-edge NEXAFS spectra.

| **Transition Energy (eV)** | **Interpretation** | **Electron Transition** | **Ref.** |
|---|---|---|---|
| 284.8 | C=C aromatic [benzene-type building blocks] | 1s-$\pi^*$ | [168, 174, 183–185] |
| 285.3 | C=C-X Aryl-linked group [X = O, C] | 1s-$\pi^*$ | [183, 186, 187] |
| 286.6 | C=C-O furan | 1s-$\pi^*$ | [123, 168, 183, 188] |
| 287.5 | C-H aliphatic | 1s-$\sigma^*$ | [188, 189] |
| 288.2 | C=O-OH carboxyl, C=O aldehyde | 1s-$\pi^*$ | [174, 174, 183] |

## 3.5 Hydrothermal Carbon Structure & Elemental Analysis

This section covers the morphology and chemistry of the two glucose derived hydrothermal carbons discussed in this chapter. Hydrothermal carbon produced at a process temperature of 200 °C and 250 °C are labelled at HTC-GLC-200 and HTC-GLC-250 respectively.

### 3.5.1 Morphology

High resolution, secondary electron, SEM images of HTC-GLC-200 and HTC-GLC-250 are shown in Figure 3.5. As per other studies, the morphology of the produced hydrothermal carbon is typically spherical and monodispersed in nature, with some larger dumbbell-like clusters forming by aggregation.

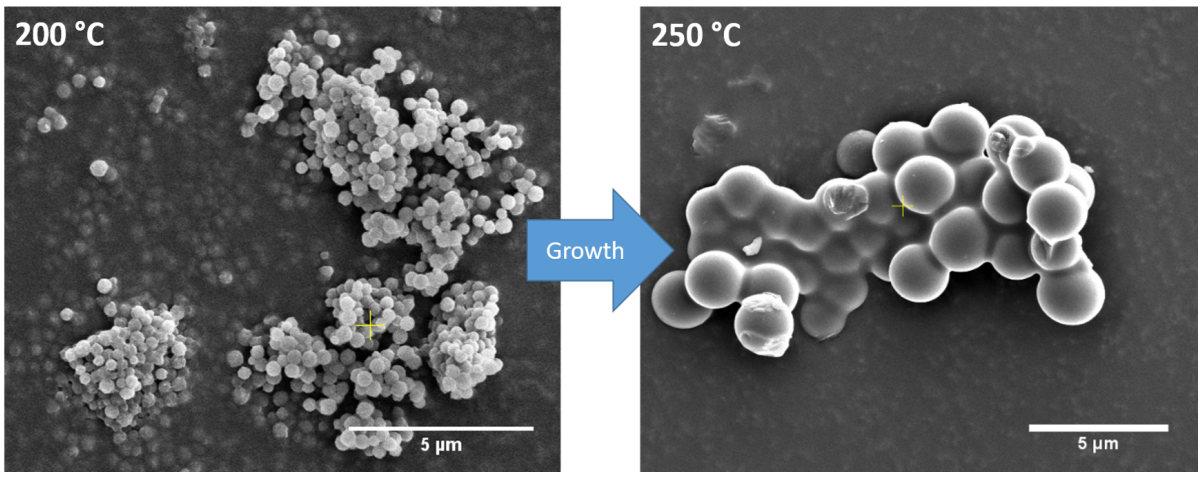


FIGURE 3.5: FEGSEM images collected at 5 kV. HTC-GLC-200 (left) and HTC-GLC-250 (right) from this study. The increase in size with process temperature is visible.

The average primary diameter of the produced spherules was found to increase with process temperature, from ~500 nm at 200 °C to ~3 µm at 250 °C. These results are similar to those of other glucose-derived hydrothermal carbons [136]. Laser diffraction analysis was used to quantify the change in mean particle size. Laser diffractometry measures the size of particle clusters formed by aggregation, whilst SEM imaging was used to measure the primary diameter of formed carbons. For samples of HTC-GLC-250, the correlation between laser diffractometry and SEM measurements were reasonable, approximately $7.5 \pm 0.4$ µm. For HTC-GLC-200 the volume-weighted mean diameters were much larger ($12.8 \pm 1.2$ µm) than SEM measurements.

### 3.5.2 Bulk Structural Disorder

The degree of structural order within HTC-GLC-200 and HTC-GLC-250 was investigated using powder XRD. The {0 0 2} and {1 0 0} reflections were fitted using Gaussian functions (Figure 3.6). The centroid of the {0 0 2} reflection was found to be at $21.4°$ and $21.0°$ $2\theta$ fo HTC-GLC-200 and HTC-GLC-250 respectively. The broad nature of the reflections suggests that the materials have very disordered and amorphous structures as reported elsewhere [143].

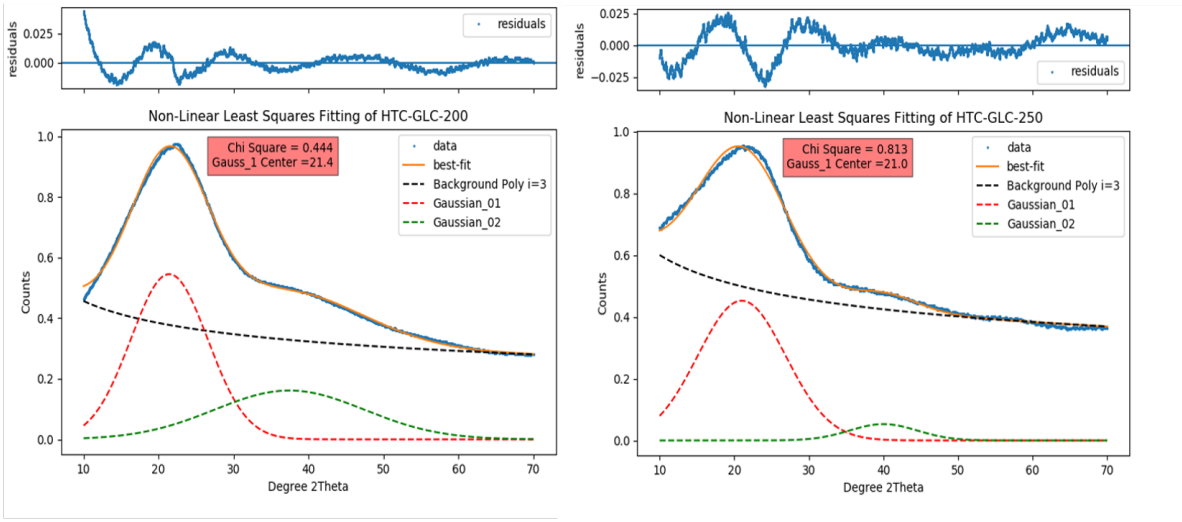


FIGURE 3.6: Non-linear least squares fitting of HTC-GLC-200 and HTC-GLC-250 XRD patterns ($\lambda$ =1.54 Å). The {0 0 2} and {0 0 1} reflections are fitted using two Gaussian functions.

### 3.5.3 Surface Carbon Chemistry

Changes in oxygen to carbon ratio (O:C) between the surface and bulk of HTC-GLC-200 and HTC-GLC-250 were investigated by comparison of XPS (~10 nm penetration depth) and traditional bulk elemental analysis. Significant changes in O:C would indicate changes in carbon chemistry between the surface and bulk of the hydrothermal carbons. In turn, such chemical changes may be used to infer a shell-core structure. This has been the only experimental evidence presented for a shell-core model of hydrothermal carbon [149]. Bulk O:C ratios for HTC-GLC-200 and HTC-GLC-250 are shown in Table 3.2. The O:C for HTC-GLC-200 and HTC-GLC-250 were found to be $0.28 \pm 0.04$ and $0.22 \pm 0.02$ respectively, and are consistent with other literature studies of glucose-derived hydrothermal carbon [139].

TABLE 3.2: Results of elemental analyses (C,H,N & O) for HTC-GLC-200 and HTC-GLC-250

| Sample | Component (wt %) | | | | | Atomic Ratio | |
|---|---|---|---|---|---|---|---|
| | Pc.Yield | C | H | N | O | H:C x10 | O:C |
| HTC-GLC-200 | 55.4 % | $61 \pm 2$ | $4.1 \pm 0.2$ | $1.21 \pm 0.07$ | $17.0 \pm 0.4$ | $0.7 \pm 0.6$ | $0.28 \pm 0.04$ |
| HTC-GLC-250 | 60.5 % | $66.2 \pm 0.7$ | $3.97 \pm 0.09$ | $1.14 \pm 0.04$ | $14.6 \pm 0.2$ | $0.6 \pm 0.2$ | $0.22 \pm 0.02$ |

XPS, as discussed in Section 2.6.2, was conducted at near-ambient pressure to reduce any loss of surface-carbon functional groups due to volatilisation. For this reason, high resolution C 1s spectra, which were recorded using a high-vacuum instrument are not reported here. Fitting of the near ambient pressure XPS data for HTC-GLC-250 gave a surface O:C of $0.22 \pm 0.01$, which is within standard error of the recorded bulk value from elemental analysis (Figure 3.7), as reported by previous studies [138]. Although the similar O:C ratios between the surface and the bulk of HTC-GLC-250 suggest broad similarity in the overall abundance of O and C throughout the structure, it does not provide information regarding chemical speciation and bonding within HTC-GLC-250. Carbon moieties at the surface could differ from the bulk of the material while maintaining similar O:C ratios.

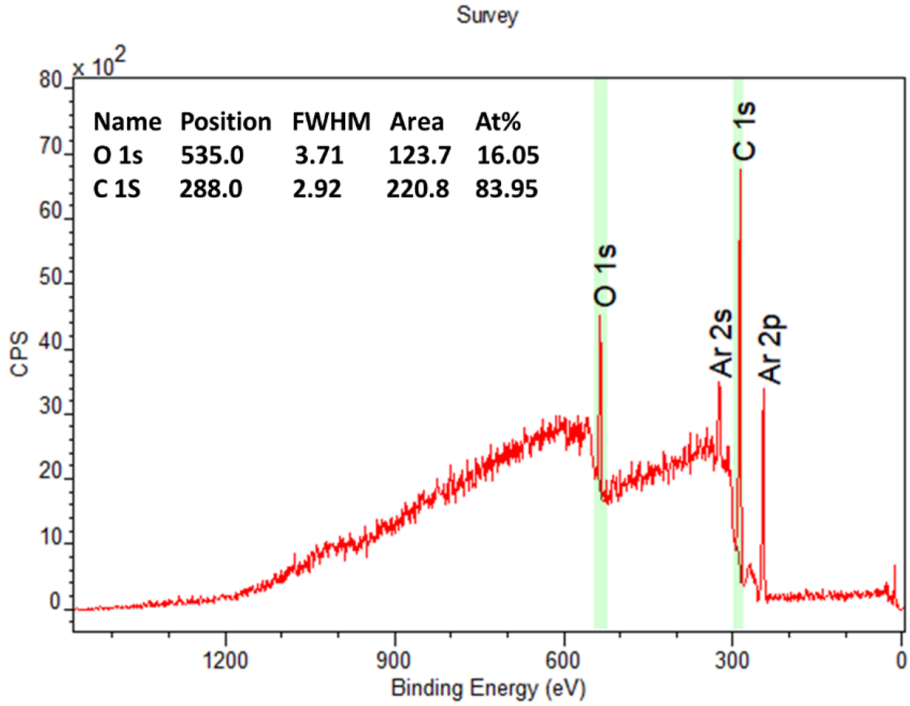


FIGURE 3.7: Near ambient pressure XPS survey spectrum for HTC-GLC-250 with C 1s and O 1s regions overlaid. $^{48}$Ar gas was used for charge neutralisation purposes.

### 3.5.4 Ethanol Extraction and Pyrolysis GC-MS

The presence of physisorbed organic species (e.g. levulinic acid), have been shown to be present on the surface of hydrothermal carbon [143]. As discussed in Section 3.4.1, a solvent wash was not performed in order to avoid the introduction of erroneous signals from physisorbed solvent or to remove important macromolecules from the hydrothermal carbon surface. In order to investigate the species present on the surface of hydrothermal carbon, a solvent extraction in ethanol was performed. The result of the soxhlet extraction was a tar-like substance, indicating the presence of high-molecular weight components. The candidate credits Jeanine Williams for performing the pyrolysis GC-MS experiment.

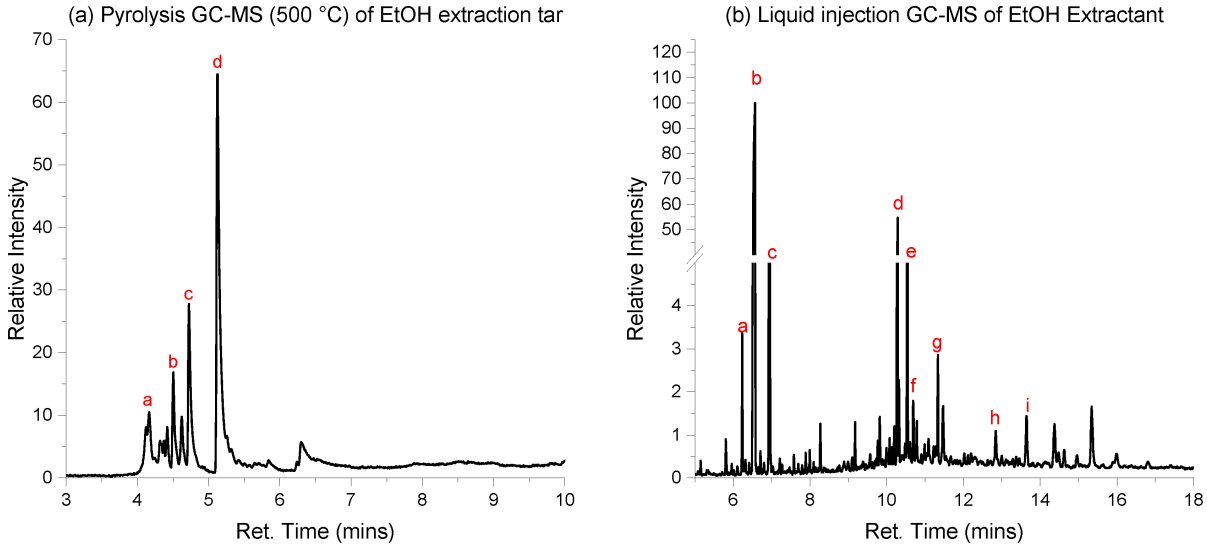


FIGURE 3.8: (A) Pyrolysis GC-MS (500 °C) of residue after soxhlet extraction – peaks: (a) 4.17 mins, 1,3-Butadiene; (b) 4.62 mins, 3-Penten-1-yne; (c) 4.72 mins Methyl-oxirane; (d) 5.12 mins, 2-methyl-furan. (B) Liquid injection GC-MS of extractant (in EtOH) after soxhlet extraction – peaks: (a) 6.23 mins, Levulinic acid (methyl ester); (b) 6.56 mins, Levulinic acid (ethyl ester); (c) 6.96 mins, 2,5-hexanedione; (d) 10.28 mins, Hexadecanoic acid (ethyl ester); (e) 10.54 mins, Levulinic acid; (f) 10.69 mins, 2,2'-methylenebis[5-methyl-Furan]; (g) 11.33 mins, Octadecanoic acid (ethyl ester); (h) 12.84 mins, 2,2'-methylenebis-Furan; (i) 13.65 mins, 3,4,8,8a-tetrahydro-8a-methyl-1,6(2H,7H)-Naphthalenedione.

Pyrolysis GC-MS was performed on the tarry residue after soxhlet extraction in ethanol (Figure 3.8a). The main resulting volatile components from the tar were found to be 1,3-Butadiene, 3-Penten-1-yne, Methyl-oxirane and 2-methyl-furan, which gave the highest intensity peak. These results are consistent with the proposed furanic network of hydrothermal carbon. Furthermore, it was shown that there were a considerable amount of high molecular weight components, with a very broad and continuous signal after 6 minutes on the column. Liquid

injection GC-MS was also performed on the Ethanol extractant prior to evaporation to the tar (Figure 3.8b). The results confirm the observations from pyrolysis GC-MS, but also provide further evidence for much higher molecular weight components such as long-chain aliphatic molecules (e.g. Octadecanoic acid [g]), linked furan species (e.g. Furan, 2,2'-methylenebis- [h]) and polyaromatic hydrocarbons. These results confirm that an ethanol extraction would remove species, especially larger macromolecules, from the surface of the hydrothermal carbon likely to be important for its surface chemistry. Furthermore the character of the molecules removed from the surface suggest that (i) hydrothermal carbon is furanic in nature (ii) long chain aromatic and linked furan species are present at the surface and (iii) levulinic acid is present.

## 3.6 X-ray and Electron Imaging

Bulk scale analyses showed no significant change in O:C between the surface and bulk of HTC-GLC-200 and HTC-GLC-250. Therefore, nanometre-scale imaging (TEM and STXM) were conducted on a FIB-section of a single spherule of the same material to investigate the presence of a core-shell structure.

### 3.6.1 TEM Imaging

TEM imaging of the produced lamellae for HTC-GLC-200 and HTC-GLC-250 is shown in Figure 3.9. The profiles of the thin cross sections can be seen embedded in the matrix.

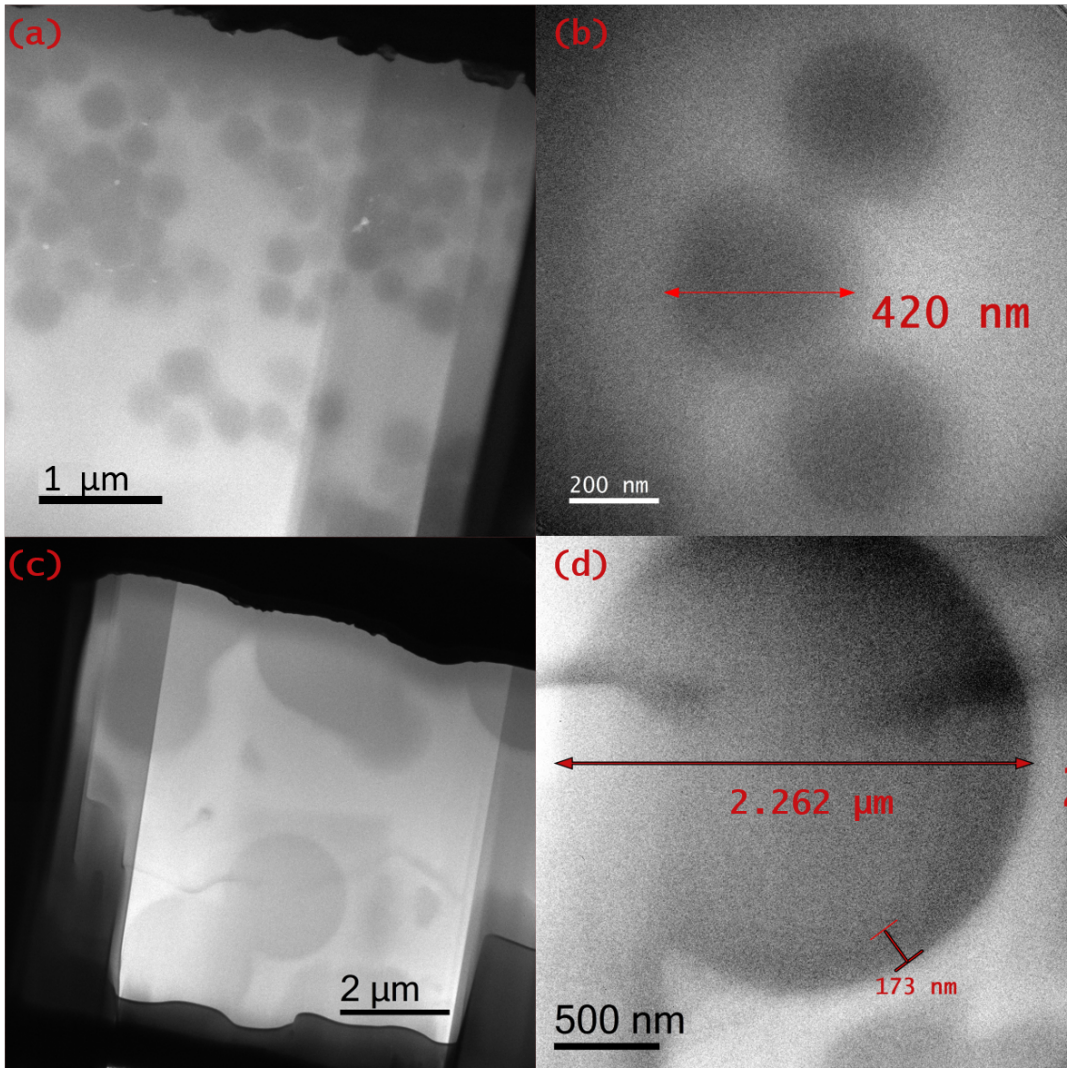


FIGURE 3.9: Brightfield TEM imaging of the prepared FIB lamellae for HTC-GLC-200 (a & b) and HTC-GLC-250 (c & d).

TEM imaging is consistent with the observation that the sizes of the carbon spherules increase with process temperature, as recorded in the SEM and laser diffraction experiments. A randomly selected slice of a HTC-GLC-200 spherule has a size of $420\,\mathrm{nm}$ compared to that of the much larger $2.3\,\mu\mathrm{m}$ HTC-GLC-250 counterpart. A faint outer shell may be observed in HTC-GLC-250 ($173\,\mathrm{nm}$ marked in Figure 3.9d), similar to that reported by *Yao et.al.* [170]. However the contrast between the carbon sphere and the resin carbon background does not allow for a satisfactory identification of a core-shell structure, nor does it provide any information regarding a difference in chemistry. A future experiment could attempt to utilise a polymeric sulphur resin to address this issue [187]. An attempt at EEL spectroscopy was made, but failed due to electron induced sample damage. As previously discussed, the dose rate in EEL spectroscopy may be up to 100 times more than in the equivalent X-ray spectroscopy [119]. However, TEM spatial resolution exceeds that of X-ray imaging, therefore TEM was used to provide some evidence the presence of a shell.

### 3.6.2 STXM Imaging

STXM imaging was used to study differences in carbon chemistry between the surface and bulk of HTC-GLC-250. HTC-GLC-200 was not suitable for STXM imaging because the spatial resolution was not sufficient to confidently identify a shell structure. Therefore from here on this chapter focuses on the chemistry of HTC-GLC-250. STXM images from the collected stack at $284.9\,\mathrm{eV}$ and $286.6\,\mathrm{eV}$ are shown in Figure 3.10.

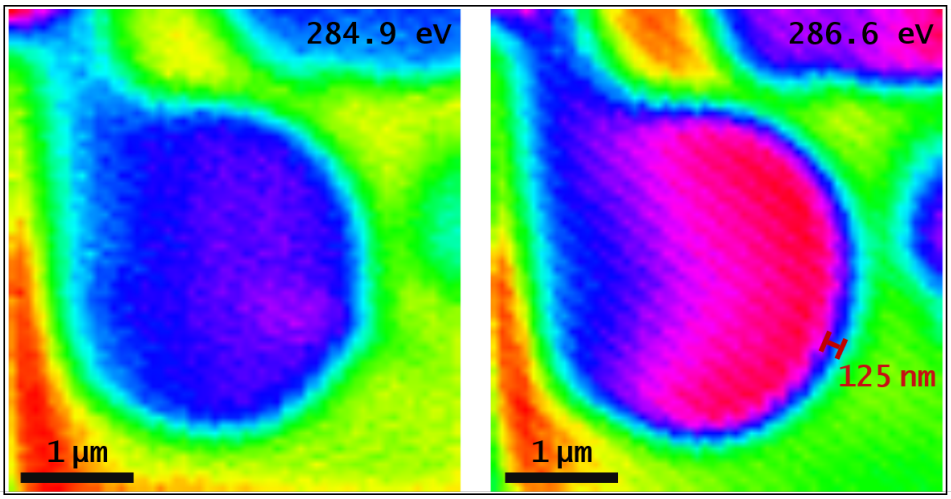


FIGURE 3.10: STXM image collected at $284.9\,\mathrm{eV}$ (left) and $286.6\,\mathrm{eV}$ (right) taken from the collected stack.

The STXM image collected at an X-ray energy of $286.6\,\mathrm{eV}$ achieved the highest contrast between the surface and bulk of the HTC-GLC-250 lamella, whilst the image collected at $284.9\,\mathrm{eV}$ shows the thin-section of the sphere distinct from the resin matrix. A clear shell-core type structure can be seen in the stack image collected at $286.6\,\mathrm{eV}$. In the carbon *K*-edge, $286.6\,\mathrm{eV}$ corresponds to the 1 s-$\pi^*_{\mathrm{C{=}\underline{C}-O}}$ furan transition energy (Table 3.1). Interestingly, in both the STXM and TEM images an outer shell was observed and measured to be approximately $125\,\mathrm{nm}$ to $175\,\mathrm{nm}$ in size (Figure 3.10). In the TEM image, the shell appears darker than the core, this result combined with the presence of this region in both the STXM and TEM images indicate that the shell is not simply a thickness artefact in the STXM optical density map.

## 3.7 STXM Analysis

### 3.7.1 Spectral Deconvolution and Principal Component Analysis

The observation of a core-shell type structure for HTC-GLC-250 led to an investigation of changes in carbon speciation between the core and shell. In order to investigate these differences, principal component analysis (PCA) and cluster analysis (CA) were performed on the STXM stack. PCA is a method of reducing the dimensionality of a large multidimensional data set to a small set of important variables, based on the correlation between the input variables and a principal component. The principal component represents the largest percentage variance in the dataset's covariance matrix, which is an orthogonal, zero-centred matrix composed of the variances between the large multidimensional data set [190]. In the case of STXM, this multidimensional dataset is composed of the energy, position and intensity recorded during the experiment. The covariance matrix may be understood as a set of eigenvectors and eigenvalues, which represent the mathematical route from the original dataset to the covariance matrix. The result of PCA is an ordered list of eigenvalues for each eigenvector from highest to lowest. The highest value represents the first principal component which accounts for the largest percentage of variance within the dataset, the second highest accounting for the second largest percentage variance and so on. Excellent reviews on the subject of PCA can be found elsewhere [191]. In this case, PCA was performed using the MANTIS software; the analysis approach used in MANTIS is discussed in Ref. [182].

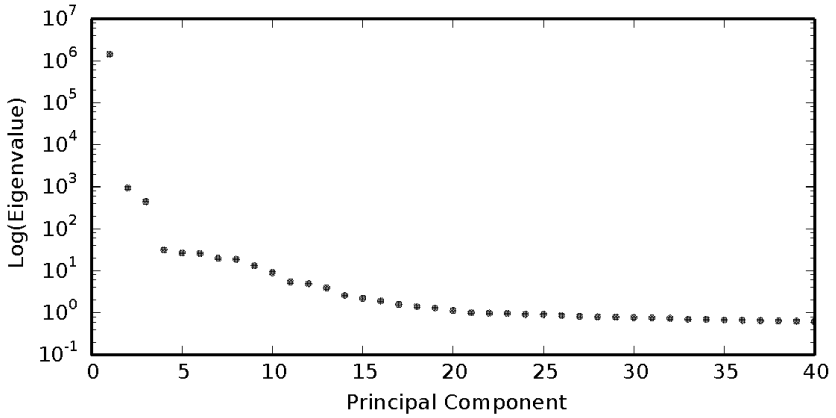


FIGURE 3.11: Scree plot produced from principal component analysis of STXM stack for HTC-GLC-250.

The results of the PCA performed on the STXM stack for HTC-GLC-250 are shown in Figure 3.11. This representation of the data as an ordered list of the eigenvalues is called a scree plot. Typically, the inflection point of the scree plot represents the fewest number of components which satisfactorily describe the data. Here, four components are found to satisfactorily represent the data. This number of points was then used to perform a cluster analysis, which separates out regions in the image with a similar spectral response (or similar eigenvalue/vector set) and also takes account of any thickness effects present in the spectra [182]. These components represent the following regions in the image: (i) core (ii) shell (iii) resin background (iv) thick region (Figure 3.12).

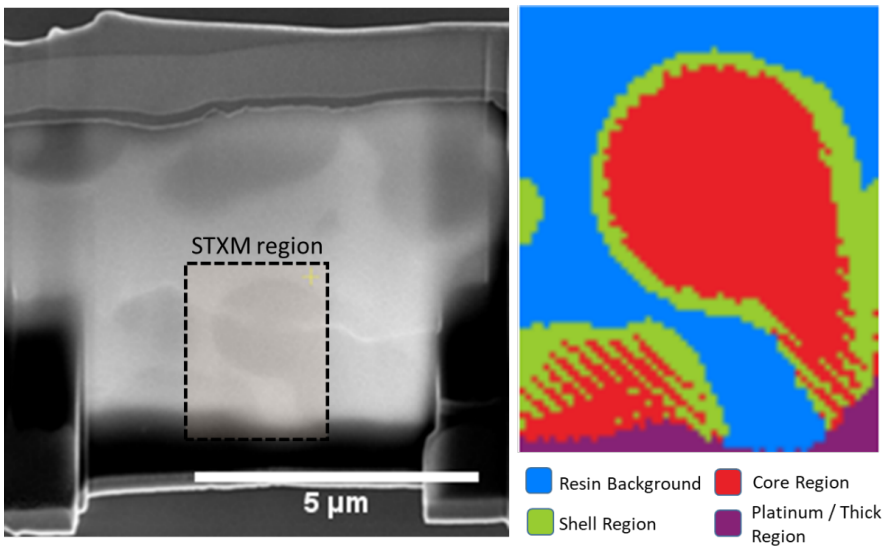


FIGURE 3.12: Result of Cluster Analysis. (left): FIBSEM image of the HTC-GLC-250 lamella with STXM region of interest highlighted (right): STXM cluster analysis result with the four components of the analysis labelled (image has been reflected in x and y to match the FIBSEM image orientation).

### 3.7.2 C *K*-edge NEXAFS Spectroscopy

The results of the cluster analysis clearly show a shell and core structure to HTC-GLC-250, and represent the first direct experimental evidence for this structure in hydrothermal carbon [111]. Since STXM is a spectromicrocsopy technique, C *K* NEXAFS may be produced for each pixel in the image. By averaging the spectra for those pixels in the core and shell regions, it is possible to reconstruct NEXAFS spectra for both the core and shell regions, and compare differences in carbon chemistry. The resulting core and shell NEXAFS spectra can be seen in Figure 3.13. Pixels in blue represent the core region of the hydrothermal carbon lamella, and pink pixels represent the shell region.

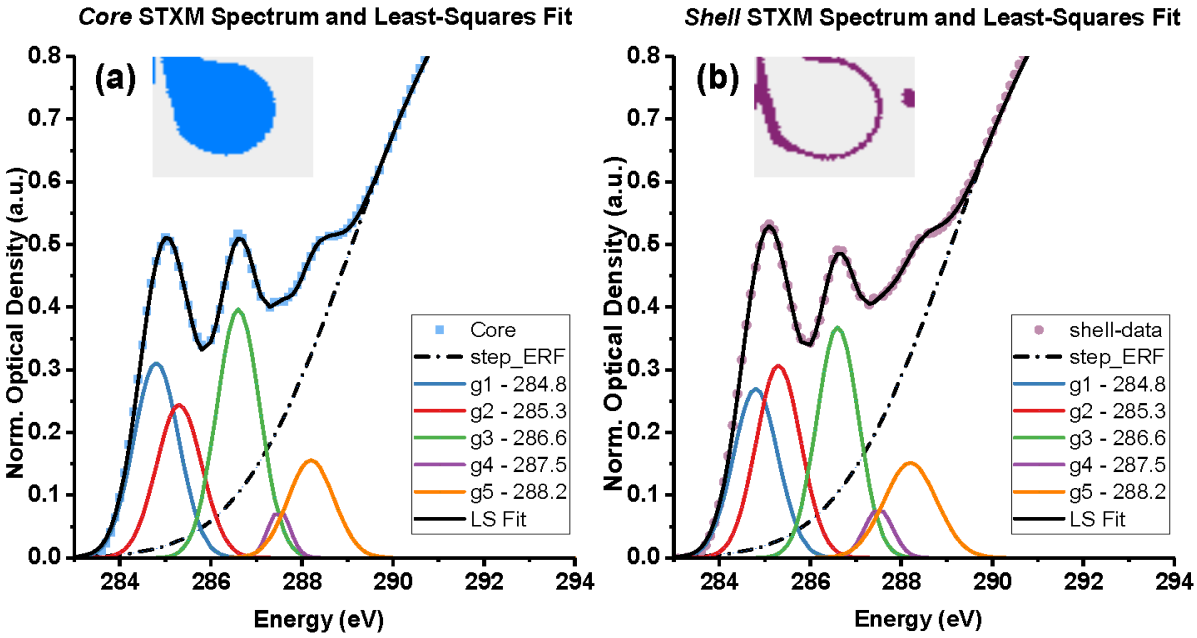


FIGURE 3.13: STXM generated NEXAFS spectra with the five components of Gaussian deconvolution and the corresponding fit for both (a) the core (blue) and (b) the shell (purple). Inset is the result of the cluster analysis and corresponding core/shell regions.

NEXAFS spectra for the corresponding shell and core regions exhibit three main peaks at 285 eV, 287 eV and 288 eV (Figure 3.13). The relatively small spectral changes between core and shell are expected, since these changes occur across a single HTC sphere. Neither the core nor the shell NEXAFS spectra exhibit a 1 s-$\pi^*_{\underline{C}OO-}$ transition (~290.3 eV) indicating an absence of both carbonate and residual carbohydrate (e.g. glucose) species in the HTC-GLC-250 lamella. The combination of (i) a lack of fine structure at the aromatic 1 s-$\sigma^*_{\underline{C}=C}$ transition (~292 eV) and

(ii) the broad nature of the corresponding XRD pattern for HTC-GLC-250 (Figure 3.6) suggest that no ordered polyaromatic component is present in either the core or shell. This result is contradictory to more aromatic models of hydrothermal carbon proposed in the literature [149, 166]. Significant chemical differences are observed between the surface and bulk regions of STXM image. Using known electron transitions (Table 3.1), the three main differences between the surface and bulk regions of HTC-GLC-250 are:

i. A broader 1 s-$\pi^*_{\underline{C}=C}$ (~285.0 eV) aromatic peak in the core spectrum.

ii. A change in peak area ratios between the 1 s-$\pi^*_{\underline{C}=C}$ (~285.0 eV) aromatic and 1 s-$\pi^*_{C=\underline{C}-O}$ (~286.6 eV) furan transitions.

iii. A broader 1 s-$\pi^*_{\underline{C}=O}$ (~288.2 eV) aldehyde/carboxyl shoulder in the shell spectrum.

To quantify these observations, Gaussian spectral deconvolution was performed. Gaussian fitting has been widely applied for studying the C *K*-edge in NEXAFS experiments [168, 185]. The results of the spectral deconvolution of the core and shell spectra were achieved with reduced $\chi^2$ values of 0.029 and 0.021 respectively (Figure 3.13). Resultant peak areas and FWHM are shown in Table 3.3. Three key changes moving from the core to shell spectra are observed and each of these is identified and discussed in the following sections.

TABLE 3.3: Peak areas and FWHM from the Gaussian spectral deconvolution of the principal components (core and shell) of HTC-GLC-250 with standard error.

| Transition | Centroid Position (eV) | Core | | Shell | |
|---|---|---|---|---|---|
| | | FWHM (eV) | Area (a.u.) | FWHM (eV) | Area (a.u.) |
| 1 s-$\pi^*_{\underline{C}=C}$ - Aromatic; | 284.8 | 1.17±0.03 | 0.31±0.01 | 1.15±0.03 | 0.27±0.01 |
| 1 s-$\pi^*_{\underline{C}=C-X}$ - Aryl | 285.3 | 1.17±0.03 | 0.24±0.02 | 1.15±0.03 | 0.31±0.02 |
| 1 s-$\pi^*_{C=\underline{C}-O}$ - Furan | 286.6 | 1.12±0.05 | 0.40±0.01 | 1.08±0.05 | 0.36±0.01 |
| 1 s-$\sigma^*_{C-CH}$ - Aliphatic | 287.5 | 0.57±0.08 | 0.06±0.02 | 0.73±0.10 | 0.08±0.01 |
| 1 s-$\pi^*_{\underline{C}-OOH}$ - Carboxyl<br>1 s-$\pi^*_{H\underline{C}-O}$ - Aldehyde | 288.2 | 1.19±0.08 | 0.16±0.01 | 1.36±0.07 | 0.15±0.01 |

### 3.7.3 285 eV: Core Condensation

The first of the three key changes observed between the core and shell STXM NEXAFS spectra is broadening of the lowest energy feature at ~285 eV (Figure 3.13). This feature may be interpreted as two distinct, yet highly correlated carbon moieties: aromatic C=C groups (284.8 eV) and heteroatomic-aryl C=C−X groups (285.3 eV). The interpretation of this feature as two overlapping functionalities is guided by previous experimental NEXAFS studies and dynamic

functional theory (DFT) calculations [186, 188, 192]. Since HTC-GLC-250 is formed primarily from C and O, and since C−O electron transitions occur at higher energies in the C *K*-edge (Table 3.1), the heteroatomic-aryl functionalities indicated by the 285.3 eV peak are assigned to aryl C=$\underline{C}$−C groups.

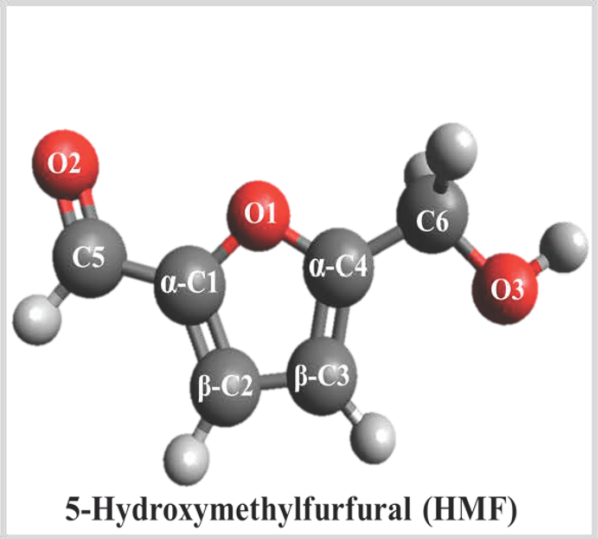


FIGURE 3.14: Structure of Hydroxymethylfurfural (HMF) with $\alpha$ and $\beta$ carbon positions labelled.

During the first stages of hydrothermal carbon growth, condensation reactions dominate [139, 149]. Dehydration reactions result in the formation of three dimensional oligomers with a furanic local structure linked at either the $\alpha$ or $\beta$ carbon positions on the furan ring (Figure 3.14) [142, 157]. In the spectral deconvolution, a 23% decrease in the 1 s-$\pi^*_{\text{C=}\underline{\text{C}}-\text{X}}$ (285.3 eV) aryl transition peak area between the shell and core of HTC-GLC-250 is observed (Table 3.3). The reduced total peak area at the 1 s-$\pi^*_{\text{C=}\underline{\text{C}}-\text{C}}$ transition in the core spectra indicates a loss of aryl functionality between the surface and bulk. This result suggests that aryl functionality is initially present at the hydrothermal carbon surface, but is removed during growth. It is possible that this aryl functionality is linked to long-chain surface carbon functionalities, such as those observed during ethanol extraction of the hydrothermal carbon surface (Section 3.5.4).

The observed loss in aryl functionality from shell to core is also concomitant with a 13% enhancement in aromatic 1 s-$\pi^*_{\text{C=}\underline{\text{C}}}$ (284.8 eV) peak area. This result indicates that the hydrothermal core region is more aromatic than the shell, and provides evidence for initial surface formation, followed by a series of condensation reactions during growth. Moieties linked at the $\beta$ carbon atom result in an increase in the peak amplitude at the 1 s-$\pi^*_{\text{C=}\underline{\text{C}}}$ (284.8 eV) transition.

Therefore, condensation is likely occurring *via* the shortening or removal of $\alpha$ carbon linking units. The bulk chemistry of hydrothermal carbon therefore contains small clusters of arene functionality, but remains predominantly furanic [136, 141, 173].

### 3.7.4 285 eV to 287 eV: Inhomogeneous Distribution of Furan Species

The second of the three changes observed in the core to shell spectra is a change in peak ratio between the 1 s-$\pi^*_{\underline{C}=C}$ (284.8 eV) aromatic transition and the 1 s-$\pi^*_{C=\underline{C}-O}$ (286.6 eV) furan transition peak areas in the experimental (non-deconvoluted) data (Figure 3.13). Although furan units are known to be present in both the surface and bulk of hydrothermal carbon, the distribution of furan units within a single spherule remains unknown [142]. HMF is the principal monomer in hydrothermal carbon formation and it has previously been assumed that furan-type C=C−O carbon is uniformly distributed within hydrothermal carbon [173]. However, here the spectral deconvolution shows a 10% decrease in the amplitude of the furan C=C−O transition between the core and shell NEXAFS spectra (Table 3.3). The inhomogeneous distribution of furan moieties between shell and core is incongruous with the hydrophobic ripening mechanism proposed by *Zhang et.al.*, since the authors state that *"the local structure of the primary particles and the carbonaceous spheres is expected to be globally uniform"* [159]. Dehydration reactions are likely the principal pathway in the core of the hydrothermal carbon spherule. Nonetheless, the lower abundance of furan functionality at the shell indicates an, as of yet unknown, intermediate reaction pathway at the water-carbon interface.

### 3.7.5 288.2 eV: the water-carbon interface

Broadening of the 1 s-$\pi^*_{\underline{C}-O}$ (288.2 eV) (aldehyde/carboxyl) transition peak is observed in the spectral deconvolution (Table 3.3). Previous literature suggests that intermediate pathways at the hydrothermal carbon surface may include aldol condensation reactions and acid-catalysed ring opening [141]. Such pathways lead to the production of reactive, dehydrated, carboxylic acid and aldehyde functionalities under HCW conditions. Changes in aldehyde and carboxylic functionality are known to result in changes at the 1 s-$\pi^*_{\underline{C}-O}$ (aldehyde/carboxyl) transition in the 288 eV region (Table 3.1).

The Gaussian deconvolution of the core and shell spectrum for HTC-GLC-250 show an increased FWHM at the 1 s-$\pi^*_{\underline{C}-O}$ (aldehyde/carboxyl) transition in the shell region (Table 3.3). The observed broadening of the 1 s-$\pi^*_{\underline{C}-O}$ transition suggests an increased distribution of aldehyde C – OH (287.5 eV) and carboxyl C – OOH functionalities at the hydrothermal carbon surface. Although caution must be exercised in attributing an increased distribution of aldehyde/carboxyl surface functionality to a single pathway, aldol condensation reactions are possibly responsible for producing an increased distribution of aldehyde/carboxyl functionalities [151, 193]. It is likely that the increased distribution of surface aldehyde/carboxyl functionality at the hydrothermal carbon surface is involved in hydrothermal growth by binding with local aqueous monomers (e.g. HMF).

## 3.8 Chapter Summary

The formation mechanism for hydrothermal carbon has been widely postulated [149, 157, 159, 194]. Experimental evidence for a growth mechanism has been impeded by a lack of direct spectroscopic techniques able to spatially resolve carbon functionality within hydrothermal carbon particles [131]. Previous TEM and $^{13}$C – NMR studies have found that initial hydrothermal carbon growth is from oligomers formed from condensation of HMF in HCW [142]. Phase separation of nascent hydrothermal carbon from the process water likely occurs by the formation of a hydrophobic core due to condensation of HMF. The synergistic TEM and STXM results presented here provide clear evidence for a core-shell model with different carbon chemical bonding environments for a glucose-derived hydrothermal carbon produced at 250 °C. NEXAFS spectroscopy here highlights a hydrothermal carbon core with increased aromatic and furanic functionality, presenting a more condensed, hydrophobic core. The shell displays a broader distribution of carboxylic and/or aldehyde functionality and is less aromatic. Using this information, a mechanism for hydrothermal carbon growth can be put forward. A schematic illustrating these findings is presented in Figure 3.15.

The proposed growth mechanism of glucose derived hydrothermal carbon is by hydrophobic-ripening and this is supported by kinetic modelling in other studies [139]. In contrast to the hydrophobic ripening mechanism presented by *Zhang et.al.* (Ref. [159]), the evidence from

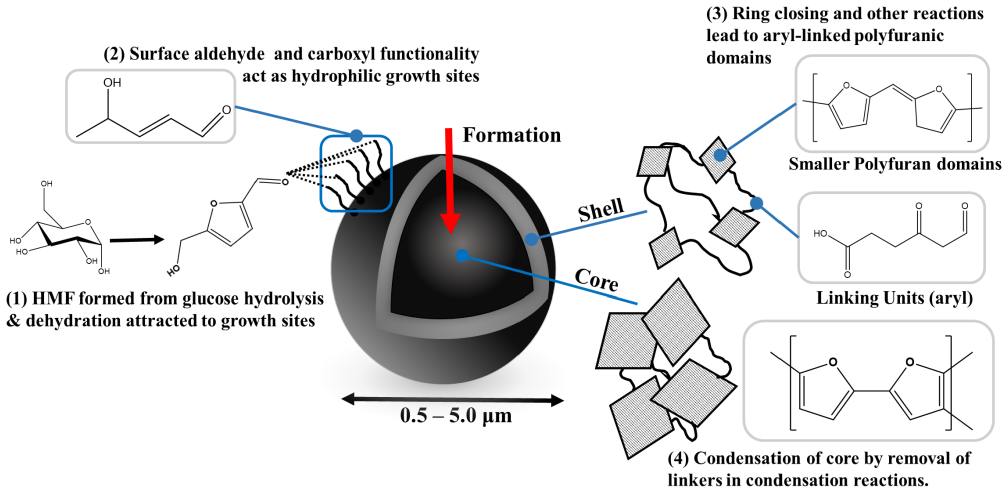


FIGURE 3.15: Schematic depiction of proposed formation mechanism from this study.

STXM suggests that (i) a shell is present and (ii) growth does not occur *via* cleavage of the carboxyl terminal unit in HMF. Our results suggest that nucleation and growth can be described in four stages: **Stage 1** – HMF is produced from the dehydration of glucose in HCW and acts as the key monomer for hydrothermal carbon growth. **Stage 2** – A carboxyl/aldehyde rich shell layer is observed, likely produced by the acid-catalysed ring opening of local HMF monomers or through aldol condensation of local carboxylic acids, which may act as a binding site for local HMF. **Stage 3** - As the hydrothermal carbon grows, the shell layer undergoes dehydration and condensation reactions (e.g. Diels-Alder reactions). **Stage 4** - In the core, condensation reactions dominate and led to the removal or shortening of HMF $\alpha$-carbon aryl linking units.

### 3.8.1 Further Work

It is important to note that the chemistry underpinning these reactions is highly complex, and that it is likely that different chemical pathways exist for other carbohydrate derived carbons. HTC-GLC-250 was produced under relatively severe conditions (250 °C, 1 h) and might only represent the final stage of growth. Further STXM studies are required at different stages of HTC formation, especially for other model carbohydrates over a range of reaction temperatures. Furthermore the NEXAFS spectra presented here only offer a snap-shot of hydrothermal formation. Future *in-situ* studies must be performed to monitor hydrothermal carbon from carbohydrates, possibly using X-ray Raman scattering spectroscopy [195].

# Chapter 4

# Bulk Structural Insight for Sustainable Carbon by X-ray Raman Scattering

## 4.1 Introduction

Building on the work of the previous chapter, this chapter investigates the chemistry of sustainable carbon materials from oak wood (*Quercus Ilex*) biomass received from an industrial pyrolysis facility. In terms of HTC chemistry, this chapter introduces the complexities of biomass-derived carbon (e.g. primary and secondary carbon formation) and investigates the primary furanic structures which underpin its chemistry. The carbon chemistry and local structure of hydrothermal carbon is then contrasted with that of pyrolysis carbon from the same biomass. Pyrolysis carbons, as discussed in Section 1.4, are non-graphitising microporous carbons produced by heating a feedstock under anoxic conditions. Pyrolysis carbons are commonly used to produce industrial activated carbon for use in filtration, energy storage and soil amendment [38]. Both hydrothermal carbon and pyrolysis carbon produced from biomass are highly heterogenous materials, which have been shown to have differing surface to bulk chemistry [111, 179]. The heterogeneity of these biomass-derived sustainable carbons makes investigating their bulk local chemistry challenging. This chapter demonstrates X-ray Raman scattering spectroscopy (XRSS) as a technique for investigating the bulk carbon chemistry of these materials. Comparison of two pyrolysis temperatures (450 °C and 650 °C) highlights the development of an increasingly condensed carbon structure. The results set out in this chapter are used to propose a semi-quantitative route to measure the total degree of aromatic condensation in pyrolysis carbons.

Production of value-added biorenewable materials and chemicals from lignocellulosic biomass has regained significant attention over the last decade as a way to move away from petroleum-derived carbon products. Underpinning this assessment is the availability of lignocellulosic biomass as an untapped resource of sustainable carbon. As an example, the UK forestry thinnings resource, which is primarily composed of soft wood biomass from the non-destructive management of the UKs forests, was on the order of $1.95$ million green tonnes of wood in 2017 [196]. This figure equates to an annual extraction rate of approximately $1.22\,\mathrm{t\,ha^{-1}\,yr^{-1}}$ of wood thinnings, and it is likely that an increase in forest area and financial input could increase this to around $5\,\mathrm{t\,ha^{-1}\,yr^{-1}}$ [196]. Forestry thinnings represent only a small proportion of the total lignocellulosic biomass produced in the UK. Biowastes from wood, wood derived fuel, fuel crops and agricultural by-products are all possible starting feedstocks. This large biomass resource makes the production of chemical and materials from biomass feasible in the UK. The global interest in producing chemicals and materials from biomass rather than fossil resources is driven by two key factors: (i) the economic necessity to use renewable carbon sources to reduce global reliance on fossil fuels and (ii) the need to decrease greenhouse gas (GHG) emissions by reducing the use of fossil resources [197, 198]. This concept of producing materials and chemicals from lignocellulosic biomass in order to reduce the global anthropogenic impact of sustaining or increasing the production of materials and fuels is called the *Biorefinery Principle* [25, 31, 199].

### 4.1.1 Lignocellulosic Biomass

The biorefinery principle encompasses a wide range of technologies able to separate lignocellulosic biomass resources into their constituents (e.g. cellulose, lignin) and convert these to value-added products, biofuels and chemicals [31]. The production of sustainable carbon materials from biomass revolves around the thermochemical decomposition of the biomass. However, lignocellulosic biomass presents a significant challenge in terms of understanding the chemistry of both pyrolysis and hydrothermal treatment. The major structural components of biomass represent the majority of the plant vascular structure and may be split into three key biopolymers: cellulose, hemicellulose and lignin. The ratios of these biopolymers vary between biomass type, species, growth season and location (Table 4.1). Biomass feedstocks can even be heterogeneous within the same plant (e.g. Table 4.1 Oak stem/branch/root).

TABLE 4.1: Lignocellulosic values for some key lignocellulosic biomass types. Lignocellulosic values for UK-grown oak (*Quercus Robus*) wood for stem, branch and root demonstrate the potential heterogeneity of a feedstock even within a single plant.

| **Biomass** | **Carbon (wt%)** | **Cellulose (wt%)** | **Hemicellulose (wt%)** | **Lignin (wt%)** | **Ref.** |
|---|---|---|---|---|---|
| Coconut Shell | 52.8 | 33.6 | 25.0 | 38.4 | [200] |
| Olive Stones | 46.0 | 14.0 | 15.0 | 42.0 | [201] |
| Gen. Hardwood | - | 43-47 | 25-35 | 16-24 | [202] |
| Gen. Softwood | - | 40-44 | 25-29 | 25-31 | [202] |
| Oak Stem | 47.1 | 50.8 | 20.3 | 24.7 | [196] |
| Oak Branch | 47.3 | 46.5 | 17.9 | 29.6 | [196] |
| Oak Root | 45.2 | 47.6 | 18.3 | 26.8 | [196] |

### Lignin

Lignin is an essential component of all vascular plants, and acts to bind the core components of lignocellulosic biomass, giving mechanical and chemical stability. Lignin itself is a complex, amorphous material built mainly of three repeating propylphenol units called monolignols: paracoumaryl alcohol, coniferyl alcohol and sinapyl alcohol (Figure 4.1).

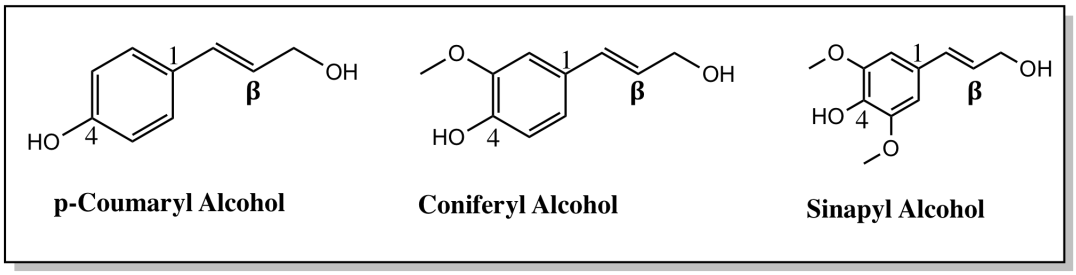


FIGURE 4.1: Monolignols - the common polyphenol units of which most lignin is composed. Lignin itself is a complex high molecular weight biopolymer with no fixed structure.

The variability of lignin is evident between soft and hardwood species, and is dictated by changes in the fractional content of the three polyphenol units. Softwood lignin consists predominantly of guaiacyl units, produced from the coniferyl monolignol. In comparison, hardwood species contain syringyl, formed from sinapyl alcohol, which alongside guaiacyl constitute the main constituents of hardwood lignin [202]. Lignin is the most chemically stable & recalcitrant component of lignocellulosic biomass. Lignin is a high molecular weight material, with approximate masses of $5000\,\mathrm{g\,mol^{-1}}$ to $15\,000\,\mathrm{g\,mol^{-1}}$ [203]. During both pyrolysis and hydrothermal treatment, lignin is the last component to carbonise, if it is carbonised at all. Lignin composes the rigid physical structures of plant biomass, which are commonly retained even after carbonisation [204, 205].

**Cellulose**

Cellulose is the main structural fibre of which lignocellulosic biomass is composed. The polymer acts as a tough fibrous support unit for the rigid plant cell wall. Cellulose is a well-defined long-chain unbranched polysaccharide, composed of $\beta$-D-glucopyranose units linked by (1-4) glycosidic bonds (Figure 4.2). The singular cellulose chains accumulate within the cell walls of woody-biomass, collectively referred to as microfibrils, which in turn comprises between $40\,\%$ to $50\,\%$ (by mass) of the total material [135]. Cellulose may either be in the crystalline or amorphous form. The amorphous form of cellulose appears to be more favoured in nature, however there is some debate about the actual degree of crystallinity within plant cellulose [135]. The fibrillar structure of plant cellulose has been investigated using molecular dynamics simulations to understand its bonding with lignin and its breakdown by enzymatic degradation [206, 207]. Cellulose acts as fibres holding the plant together, supported by a lignin superstructure [208].

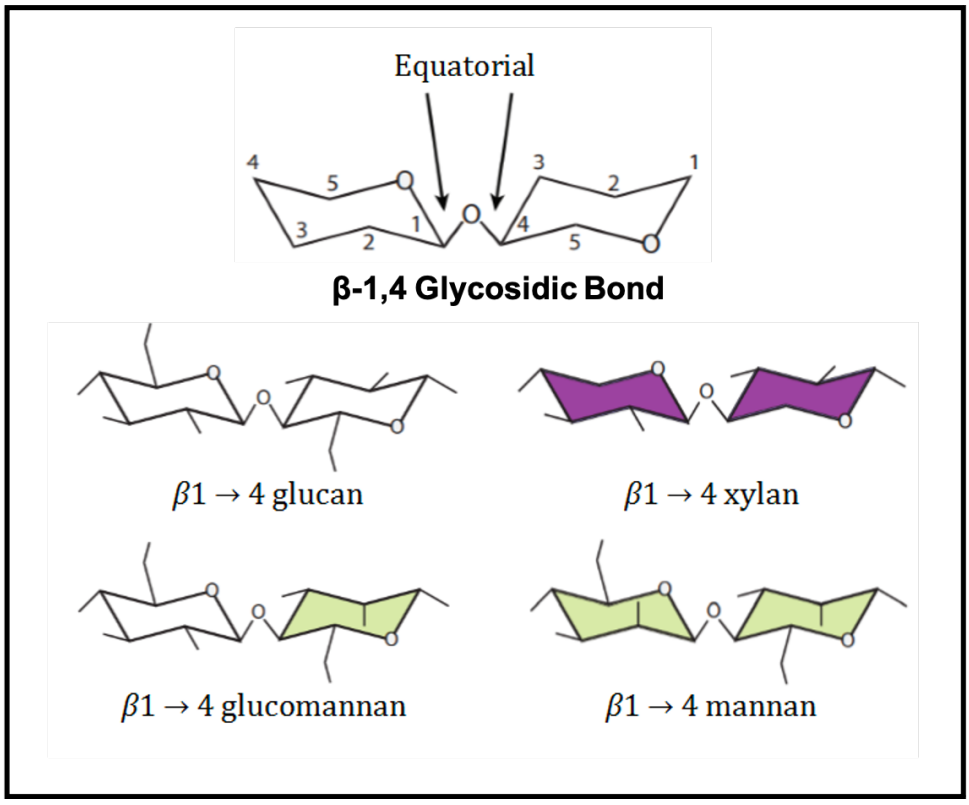


FIGURE 4.2: Hemicelluloses are characterised by equatorial $\beta$-(1,4)-linked bonding.

**Hemicellulose**

Hemicellulose acts in a similar way to cellulose, binding together the main structure of the cell wall. However, unlike cellulose which is reasonably well-defined polymer of glucose, hemicellulose is a complex mixture of heterogeneous soluble polysaccharides (e.g. mannose, galactose). Hemicellulose is an important component of most woody biomass and accounts for ~25% of the dry weight of wood, and is more abundant in hardwood species [202]. Hemicellulose is characterised by $\beta$-(1,4)-linked C1 and C4 carbons within polysaccharides (Figure 4.2). This also identifies some of the main disaccharides that are included within hemicellulose; other polysaccharides that are often grouped with these include galactans, arabinans and arabinogalactans, which are closely associated with pectin molecules.

**Extractives and Inorganics**

Other than the structural biomass components (lignin, cellulose, hemicellulose), biomass also contains extractives which are non-structural and may be extracted using a solvent wash [209]. Biomass additionally contains inorganics, which may be extracted through acid digestion. The extractive components of wood represent a diverse group of organic components. Extractives include a variety of saccharides, proteins, phenols and aromatics, while gums, tannins and flavonoids may also be present. Extractives in lignocellulosic biomass are highly dependent on species and have been shown to directly influence pyrolysis chemistry [210]. The inorganic materials contained within lignocellulosic biomass are predominantly mineral based. Inorganics are often important micronutrients for plant growth and function, and include: calcium (Ca), potassium (K) and magnesium (Mg) salts. It is important to note however that inorganic minerals may include a wide array of other elements, including transition metals (e.g. Fe, Mn, Cu) which have been shown to influence both hydrothermal carbonisation and pyrolysis chemistry [211].

### 4.1.2 Biomass-Derived Hydrothermal Carbon

As discussed in Chapter 3, simple monosacharides and other carbohydrates have been effectively employed as model feedstocks to monitor hydrothermal carbon chemistry. The chemical understanding of carbohydrate HTC is now at a stage where control over HTC products is possible, even though a full understanding is not yet established. This has resulted in the scale-up of HTC for waste management, as well as the design and manufacture of successful HTC-derived products, including a variety of energy storage devices [50, 133]. The ultimate goal for HTC is to utilise biomass-derived carbon for producing devices, minimising their environmental impact and reducing dependence on fossil resources. In order to achieve this, further understanding of the HTC of lignocellulosic biomass is required.

#### Primary and Secondary Char

Hydrothermal carbon is the water insoluble phase of the HTC reaction. During the HTC reaction, as discussed in Section 1.3.2, the feedstock remain in intimate contact with HCW. Due to the complex structure, chemical stability and relative insolubility of ligninocellulosic biomass, intimate contact between the lignocellulosic feedstock and HCW is often not achieved. This results in the formation of *primary char*, which contains pyrolysed biomass from solid-solid reactions and high molecular weight fragments from the initial feedstock [139, 212]. Secondary char is the most commonly reported form of hydrothermal carbon and forms from the thermochemical breakdown of carbohydrates, as discussed in Chapter 3.

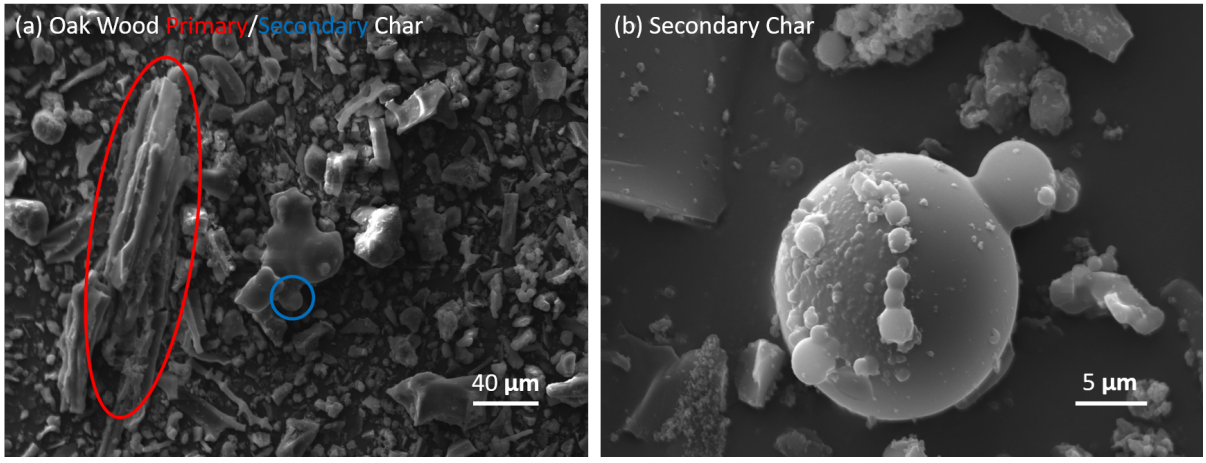


FIGURE 4.3: SEM secondary electron images of hydrothermal carbon produced at 250 °C from Oak wood. (a) A mixture of primary and secondary char. (b) Secondary char present in the same sample.

Secondary char has a spheroidal morphology, whilst primary char retains the original morphology of the starting biomass. Reports have shown that secondary char does not form on lignocellulosic biomass until hydrothermal treatment is performed above 180 °C [135]. When biomass is hydrothermally treated at higher temperatures (e.g. ≥220 °C), the firbrous cellulose network is disrupted, resulting in the formation of secondary char (Figure 4.3). However, complete breakdown of hemicellulose and cellulose in HCW conditions has been shown to occur only under more severe conditions, in the range of 250 °C to 280 °C for hemicellulose and cellulose respectively [213]. The chemistry of the primary char has not yet been completely understood, but seems to result in a more aromatic carbon [214].

**Differences in Carbon Chemistry between Biomass and Carbohydrate Derived Hydrothermal Carbon**

One of the main advantages of HTC is that it can successfully exploit cheap and renewable biomass as a carbon precursor. However, current research into the production of hydrothermal carbon for devices has so far been restrained to using carbohydrates as a precursor [50]. As discussed in Chapter 3, carbohydrate HTC has now been well-established due to a more complete understanding of HTC chemistry for carbohydrates than biomass. This is principally due to the structural and chemical complexity of lignocellulosic biomass as a precursor. However, it should be stressed that some experiments show advantages to using biomass as a carbon precursor which go beyond those of increased sustainability. Hydrothermal carbonisation of lignocellulosic biomass has been shown to produce: (i) excellent fuels with low propensity for slagging and fouling even when produced from high-ash feedstocks (i.e. high inorganic content) [137, 214] (ii) a route to physically activated aerogels from biomass [215] and (iii) ultrahigh surface area materials for energy storage devices (although these have not been implemented yet) [216, 217].

Whilst the current understanding of HTC has been set out in Chapter 3, there are some important differences between carbohydrate and biomass-derived hydrothermal carbon chemistry. Like the carbohydrate derived char, lignocellulosic biomass derived carbons have been shown to be composed of furanic polymers by solid-state $^{13}C$ – NMR [136]. *Falco et.al.* also observed that increasing the HTC temperature leads to a hydrothermal carbon with a higher degree of aromatisation and a larger proportion of condensed aromatic species than in an equivalent

carbohydrate derived hydrothermal carbon. When cellulose is treated under HCW conditions above 180 °C, its fibrous network is disrupted. Under these conditions, cellulose undergoes hydrolysis of the glycosidic bond (Figure 4.2), which then form carbohydrates that subsequently form the secondary char observed during carbohydrate HTC [218, 219]. It has been recorded, that the presence of hemicellulose and cellulose in HTC results in the formation of a wider variety of oligosaccharide products and organic acids in the process water after reaction completion [50]. This is likely due to longer chain components of cellulose hydrolysis undergoing side-reactions during HTC. The lignin fraction of the biomass is altered only slightly during HTC, remaining stable until above 250 °C. The main changes in the structure of lignin (extracted from the Kraft paper pulping process) are demethylation and dealkylation reactions, which result in a stable lignin-like primary char with similar morphology to the starting biomass [220]. The inorganic component of biomass is a complex factor in the HTC reaction. Inorganics such as calcium hydroxide and iron oxides are know to accelerate the formation of hydrothermal carbon, as well as influence the size of formed spherules in carbohydrate HTC [221]. However, a complete understanding of the effects of inorganics in biomass HTC is currently lacking [137]. Finally, hydrothermal carbons derived from biomass present larger surface areas than those from carbohydrates. Higher surface areas in biomass-derived hydrothermal carbon is likely due to the retained, richly textured "lignin-rich skeleton" [211].

### 4.1.3 Biomass-Derived Pyrolysis Carbon

As discussed in Section 1.4, pyrolysis carbon is a non-graphitising, microporous carbon produced by heating a feedstock in an anoxic environment (typically between 300 °C to 1000 °C). The resulting carbonaceous product is typically amorphous, containing a high fraction of $sp^2$ hybridised carbon atoms in tangled graphene ribbon-like structures. The properties of pyrolysis carbon production from biomass have been reviewed extensively elsewhere [84, 222]. It is understood that hemicellulose is the first lignocellulosic component to degrade at temperatures less than or equal to 250 °C. Depolymerisation of hemicellulose primarily results in the formation of syngas products (e.g. $CO_2$, $H_2$, $CH_4$). Cellulose and Lignin are the primary routes for the formation of pyrolysis carbon. The decomposition of cellulose has been reviewed by *Paris et.al.* and occurs at temperatures between 250 °C to 350 °C [223]. Between these temperatures cellulose is strongly degraded, resulting in the formation of volatile intermediates, which

decompose to form syngas or volatalise to form volatile organic compounds [224]. This leads to substantial mass loss and changes in the physical structure.

The formation of pyrolysis carbon from cellulose is often split into three distinct processes: (i) depolymerisation (ii) fragmentation and (iii) char formation. During depolymerisation, the monomer units of cellulose are broken by thermolysis, most likely at the glycosidic bonds discussed in Section 4.1.1. This results in the formation of levoglucosan (1,2-anhydro-$\alpha$-D-glucopyranose, $C_6H_{10}O_5$) via a chain-end depolymerisation reaction [225]. Cellulose depolymerisation, which typically occurs between $250\,^{\circ}\mathrm{C}$ to $350\,^{\circ}\mathrm{C}$, also results in the formation of a range of furanic and aldehyde species including both 5-HMF and hydroxy-acethaldeyde [223]. Depolymerisation of lignin is more complex and less well-understood, since lignin may vary significantly between plant species. However, it has been found that depolymerisation to Guaiacols and other aromatic species is favoured [226]. After depolymerisation, the resulting macromolecular species undergo fragmentation, forming incondensable gases [227]. Fragmentation results in the cleavage of covalent bonds in macromolecules from the starting biomass, producing syngas and a diverse range of volatile organic compounds. Fragmentation is favoured at temperatures above $500\,^{\circ}\mathrm{C}$ and may also result in the "cracking" of the organic compounds produced during depolymerisation, resulting in significant mass loss.

Pyrolysis carbon formation occurs over a wide range of temperatures, starting at about $350\,^{\circ}\mathrm{C}$. Char formation results in the formation of pyrolysis carbon with varying degrees of condensation. Intra- and intermolecular rearrangement reactions of depolymersation products, result in the production of more condensed species which tend to have higher thermal stability [227]. The main steps of this pathway are the formation of benzene rings and the combination of these rings in a polycyclic structure. Char formation appears to be the preferred route for lignin pyrolysis since, in general, higher lignin feedstocks result in higher yields of pyrolysis carbon. The higher char yield for lignin, rather than cellulose, may be explained by the propensity of monolignols to undergo secondary pyrolysis reactions, particularly polymerisation reactions [226]. From $380\,^{\circ}\mathrm{C}$ to $400\,^{\circ}\mathrm{C}$, the remaining cellulosic structure changes dramatically. The conversion of pyran ring structures formed during depolymersation is almost complete at $320\,^{\circ}\mathrm{C}$ [224, 227]. The concentration of furan species progressively increases until $350\,^{\circ}\mathrm{C}$ [227]. By $400\,^{\circ}\mathrm{C}$ the aromatic nature of the produced pyrolysis carbon becomes predominant

[228]. Significant mass loss is observed as material is removed from around micropores present within the starting biomass, producing large micrometre to millimetre sizes pores. This particle shrinkage has recently been studied *in-situ*, occurring primarily above 350 °C (after the degradation of cellulose) and is dependent on the properties of the starting biomass [229]. Aromatic and aliphatic species are progressively removed with increasing process times at temperatures, above 400 °C, predominantly by demethylation and condensation reactions [227]. However, it is known that pyrolysis conditions (e.g. residence time, heating rate, atmosphere composition, biomass composition etc) can have a significant effect on the final produced carbon [84, 222]. Thorough reviews on biomass pyrolysis are available elsewhere [230–232].

### Aromaticity and Degree of Aromatic Condensation

As discussed in Section 1.4, pyrolysis carbons are microporous, non-graphitising materials. Determining the structure of non-graphitising carbons (e.g. charcoal, pyrolysis carbon) is arguably one of the grand challenges of carbon science, and remains unknown. However the local structure of pyrolysis carbon has been shown to have a significant impact on its properties [205]. A common method of assessing the chemistry of pyrolysis carbons is by their bulk hydrogen to carbon, H:C, and oxygen to carbon, O:C, ratios by elemental analysis.

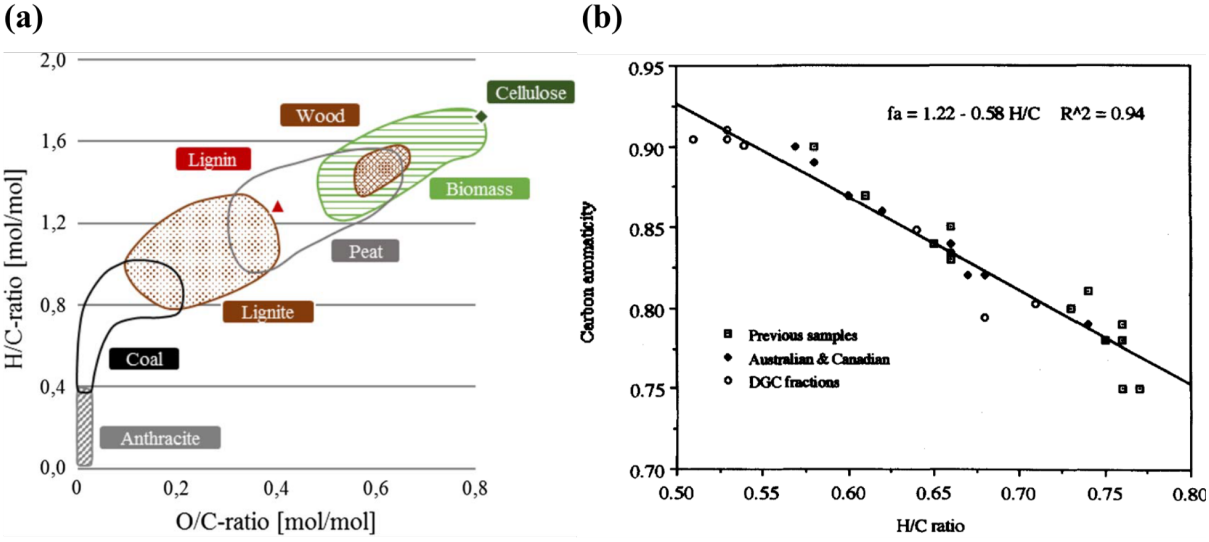


FIGURE 4.4: (a) Van Krevlen diagram [222]. (b) Plot of aromaticity against H:C ratio for a series of standard coals. Taken with permission from Elsevier [233]

In the 1950s, van Krevelen developed a graphical representation of macro-elemental ratios to evaluate the origin and chemical evolution of coals (Figure 4.4a) [234]. The van Krevlen

diagram has since been widely used to classify pyrolysis carbons and other biomass-derived materials [235]. The H:C and O:C values for pyrolysis carbons are now widely reported and form part of both the UC Davis Biochar and Phyllis2 databases [222]. These large datasets of pyrolysis carbon metrics have since been used to demonstrate a statistically-relevant link between H:C atomic ratios and the aromaticity of pyrolysis carbon [222, 236].

Aromaticity is a simplified model of aromatic structure, which considers the theory of aromaticity of benzenoids, which are the typical chemical example of systems with delocalised aromatic bonding - this model is more fully described elsewhere [237, 238]. In practice, aromaticity describes the local structural ordering of a sample in comparison to graphite, where graphite has a perfect aromaticity of 1.0. Measurement of aromaticity was first performed to describe the local structure of coal using FTIR [239], XRD [240] and, more commonly, by measuring relative chemical shifts in $^{13}C$ – NMR spectra [241]. In NMR, as aromaticity increases, the chemical shift of key aromatic peaks are moved to lower ppm values [242]. As shown in Figure 4.4b, the H:C atomic ratio of coals, and subsequently pyrolysis carbons, have been shown to be directly linear with measured values of aromaticity using $^{13}C$ – NMR [233, 236]. More recently the degree of aromatic condensation, a second measure of biochar aromatic chemistry, has been used to measure the average size of the fused aromatic structures present in pyrolysis carbon [243]. The concepts of aromaticity (the total proportion of aromatic C including both the disordered and ordered phases) [244] and degree of aromatic condensation (the proportion of the condensed aromatic C only) relate to a model of carbon with an ordered and a disordered phase as discussed in Section 1.4 [245, 246]. A quantitative understanding of both aromaticity and aromatic condensation are useful, since they may be used to predict the physicochemical properties of carbons, including chemical stability [125, 247], sorbtion capacity [248] and functionality [205, 243]. However, $^{13}C$ – NMR measurements of both aromaticity and the degree of aromatic condensation are limited by the ability to solubilise samples and can be impacted by the presence of magnetic inorganic components [249]. A recent review on experimental techniques to measure aromaticity and total aromatic condensation highlighted the challenges in repeatability between techniques, especially for measurements of total aromatic condensation [245].

### 4.1.4 Characterisation of Carbon Functionality in Sustainable Carbons

The characterisation of carbon functionalities in sustainable carbon materials is often complex, with no single technique providing a complete picture. Instead, analytical techniques must be applied in a synergistic approach in order to provide an accurate picture of sustainable carbon chemistry [250]. Important considerations for the selection of an appropriate technique include:

i. What is the spectral resolution and signal to noise ratio of the technique?

ii. Is the technique, and subsequent analysis, quantitative or qualitative?

iii. Does the technique provide *in-situ* or *ex-situ* information?

iv. Is the technique surface biased, or a bulk measurement?

v. Does the technique provide spatial resolution?

vi. Is the sample damaged during measurement?

vii. Is the technique element selective?

Such considerations are vital in the selection of appropriate techniques for measuring carbon chemistry in sustainable carbons. In this section, the most commonly applied analytical spectroscopy techniques (FTIR, $^{13}$C NMR, NEXAFS, XPS) will be briefly discussed and compared. This section will focus on the use of spectroscopy and will not cover other important techniques such as: Boehm titration, potentiometric titration, thermal analysis, elastic X-ray scattering (e.g. XRD, SAXS, WAXS) or electrochemical techniques. Thorough reviews of these techniques for carbon materials can be found in review articles [144, 230, 250, 251].

#### Common Spectroscopies for Sustainable Carbon Materials

**Fourier Transform Infrared Spectroscopy (FTIR)** FTIR methods have become popular and widely applied characterisation techniques for sustainable carbon materials. Transmission FTIR, attenuated total reflectance (ATR-) FTIR and diffuse reflectance FTIR (DRIFTs) are a set of techniques which measure the transmission and reflectance of infrared light from a sample. They measure the absorbance of infrared light in a sample, which produces absorption bands due to molecular vibration and stretching. These bands are used to fingerprint for specific

carbon functionalities. For example the band between $1600\,\mathrm{cm}^{-1}$ to $1550\,\mathrm{cm}^{-1}$ corresponds to aromatic functionality, and the band between $1250\,\mathrm{cm}^{-1}$ to $1230\,\mathrm{cm}^{-1}$ corresponds to C–O groups. FTIR methods provide good signal to noise ratios and can be measured within minutes. Measurements using transmission and ATR-FTIR are usually performed *ex-situ*, however DRIFT spectroscopy has been used successfully for *in-situ* measurements of pyrolysis [252, 253]. Whilst FTIR is a powerful tool for monitoring carbon functionality, IR spectroscopy does not provide quantitative information, and is typically limited to fingerprinting alone since absorption bands often overlap. Furthermore, infrared spectroscopy is a surface technique and does not provide information regarding bulk carbon chemistry, nor is the technique element sensitive.

**Raman Spectroscopy (optical)** Much like infrared spectroscopy, optical Raman spectroscopy relies upon the inelastic scattering of infrared photons to study the vibrational and rotational states of the sample. Raman spectroscopy analysis is well suited for the analysis of sustainable carbon materials. Spectra from sustainable carbons exhibit two main overlapping bands around $1350\,\mathrm{cm}^{-1}$ to $1370\,\mathrm{cm}^{-1}$ and $1580\,\mathrm{cm}^{-1}$ to $1600\,\mathrm{cm}^{-1}$, commonly called the "D" and "G" bands. The D band corresponds to in-plane vibrations of $sp^2$ -bonded carbon structures with structural defects. The G band corresponds to the in-plane vibrations of the $sp^2$ -bonded graphitic ordered structure. Analysis of Raman spectroscopy is qualitative, and may be used to identify certain carbon functionalities, as in infrared spectroscopy, and may also be performed *in-situ*. For example, a study by *Yao et.al.* used Raman spectroscopy to follow the growth in intensity of the $C{=}C_{aromatic}$ bond stretching mode *in-situ*, providing the first measurements of the early stages of the fructose ring dehydration [170].

**X-ray Photoelectron Spectroscopy (XPS)** XPS is a non-destructive soft X-ray technique that provides information on the chemical state and local environment of an atom on the surface of a sample. XPS has been widely used to study the carbon C 1s feature, which may be used to semi-quantitatively model for the presence of other carbon functionalities, which have known binding energies. However, XPS is also an element-specific spectroscopy, meaning that it is possible to selectively measure spectra for elements other than carbon (e.g. O, N, S). XPS is conventionally performed using a lab source of X-rays from a rotating anode. X-ray absorbed by carbon produce a photoelectron of energy $285\,\mathrm{eV}$. Due to the use of soft X-rays, XPS is

highly surface sensitive. Whilst XPS can be a convenient way of investigating the surface functionalities of sustainable carbons, the technique does have some important drawbacks. Due to the use of soft X-rays, XPS is commonly performed under ultra-high vacuum resulting in limitations on sample environment, making *in-situ* studies uncommon. This surface limitation also makes separating signals from surface hydrocarbon contamination and those from the sample challenging. Furthermore, sustainable carbons are most commonly insulators, resulting in sample charging. Charge compensation is possible in XPS, but may result in changes to peak shapes and make a full quantitative analysis challenging.

**Near-edge X-ray Absorption Spectroscopy (NEXAFS)** Recent studies have shown NEXAFS to be a powerful tool for element-specific characterisation of local structure and chemistry in disordered carbon materials [168, 183, 188, 254]. For studies of carbon and heteroatoms (mainly N *K*-edge, ~410 eV & O *K*-edge, ~543 eV), NEXAFS operates in the soft X-ray regime. As with XPS, the use of soft X-rays results in sub-micrometre path-lengths and a larger interaction cross-section, increasing radiolysis and producing highly surface sensitive measurements. Surface sensitivity is problematic since both hydrothermal and pyrolysis carbons have been shown to display different bulk to local-surface chemistry [111, 179]. The use of soft X-rays in NEXAFS and XPS also results in difficult sample preparation and challenging high-vacuum sample environments, which render *in-situ* studies impractical [213].

**Solid State $^{13}$C – NMR** NMR, is commonly associated with organic chemistry where all analyses are typically performed in the liquid state. Solid state NMR suffers from lower signal to noise ratios and broadening of features due to chemical shift anisotropy, when compared to its liquid counterpart. A full description of the techniques and challenges found in solid state $^{13}$C – NMR is beyond the scope of this section and is well discussed in several reviews [233, 255]). Currently $^{13}$C – NMR is the only route to bulk spectroscopy of sustainable carbons, and has provided the first evidence for a furanic substructure in hydrothermal carbon [142] and a measure of total aromatisation in pyrolysis carbon [242]. As discussed, however $^{13}$C – NMR suffers from inherent low sensitivity. Poor signal-to-noise ratios are due to (i) the low natural abundance of the isotope $^{13}$C ( 1.1% n.a) and (ii) because large relaxation times are required to generate quantitative spectra. Pulse sequencing, isotopic enrichment and correlation spectroscopy (e.g. INEPT & DQ-SQ) in solid state $^{13}$C – NMR have been successfully applied

to enhance spectral resolution, but such experiments require long measurement times and introduce significant experimental complexity [173, 224, 243]. Furthermore, *in-situ* experimental studies using NMR are uncommon and highly challenging. X-ray spectroscopy (NEXAFS, XPS), infrared spectroscopy FTIR or optical Raman spectroscopy, provide higher-resolution spectroscopic information than $^{13}$C – NMR .

**Benefits and Drawbacks of X-ray Raman Scattering Spectroscopy**

This chapter sets out the first application of XRSS to sustainable carbon materials. What makes XRSSunique with respect to the other spectroscopies set out in this chapter is the ability to obtain soft X-ray absorption spectra, analogous to that of NEXAFS, whilst using hard X-rays. Elements that can be measured using this approach include the *K*-edges of second-row elements, *L* and *M*-edges of 3d transition metals, all the way to O-edges of the rare-Earth elements and actinides [256]. It is because of this, that XRSS can be used to study the X-ray absorption spectra of low-Z elements critically important to sustainable carbon chemistry (e.g. C, N, O) using hard X-rays. In comparison to soft X-ray spectroscopy (e.g. NEXAFS, XPS), the use of hard X-rays allows experiments to be performed under ambient conditions without the need for vacuum environments. The use of ambient conditions allows for a wide variety of sample environments, such as the use of diamond anvil cells for the study of low atomic mass elements under high pressure [108]. Ambient conditions also allow XRSS to be used for *in-situ* experiments. For example, XRSS has been used to follow the carbon chemistry of X-ray induced dimerisation in real time [110]. In the future it may be possible to perform both pyrolysis and hydrothermal carbonisation *in-situ*. The smaller interaction cross-section of the hard X-rays used in XRSS also allows for bulk spectroscopy to be collected under ambient conditions. The result of this is that both solid state $^{13}$C – NMR and XRSS are the only element-specific spectroscopies which may be used to study carbon chemistry in bulk. Whilst both $^{13}$C – NMR and XRSS are, in principle, non-destructive, environmental samples for $^{13}$C – NMR are typically treated using highly concentrated acids (e.g. HF) to remove mineral impurities which can interfere magnetically with the measurement (e.g. pyrite). Such aggressive treatment of the sample, which may well alter carbon functionalities, is not required for XRSS measurements. This advantage has meant that, for more fragile environmental samples (e.g. fossilised pigments), XRSS has been shown to be superior to $^{13}$C – NMR [109, 257]. Furthermore, XRSS holds improved resolution in terms

of aromatic carbon functionalities which commonly overlap in $^{13}C$ – NMR spectroscopy. For this reason, and because of the challenges of studying oils and liquids under vacuum conditions, XRSS has been used to study condensed aromatic carbon species, such as polyaromatic hydrocarbons [258–260]. However, XRSS does also present some limitations. XRSS requires brilliant synchrotron sources to produce large enough flux to generate statistically significant signal within a reasonable scan time, especially for low-concentration samples. Furthermore, the lower energy resolution of XRSS when compared to NEXAFS measurements leads to a direct trade-off between energy resolution against penetration depth, sample environment and dose. Until recently, these drawbacks restricted the application of XRSS but third generation synchrotron facilities with high brilliance are changing this. The low sensitivity issue is easily overcome for sustainable carbon, since these materials are typically 60-90 wt/% carbon.

## 4.2 Aim

The aim of this chapter is to present XRSS as a technique for studying the bulk carbon chemistry of both HTC and pyrolysis. Both hard (XRSS) and soft (NEXAFS) X-ray spectra are compared for the same pyrolysis and hydrothermal carbons in order to highlight the differences between surface and bulk functionalities. Hydrothermal carbon produced at $250\,^{\circ}C$ (HTC-Oak-250) and pyrolysis carbon produced at $450\,^{\circ}C$ (Pyro-Oak-450) from oak wood (*Quercus Ilex*), display significantly different bulk carbon chemistry between each other despite having similar weight percentage of carbon. *Ab-initio* calculations using a modern density functional theory (DFT) code are performed for a suspected furanic sub-unit of hydrothermal carbon, highlighting recent advances in calculating XRS spectra. XRS spectra of two pyrolysis carbons (Pyro-Oak-450, Pyro-Oak-650), produced from the same feedstock at a moderate and severe process temperature, $450\,^{\circ}C$ and $650\,^{\circ}C$ respectively, highlight a potential route to a quantitative measurement of aromatic condensation. Comparison of NEXAFS and XRSS collected for these materials highlights the advantages of XRSS with respect to differences in penetration depth and lack of thickness effects. Finally, this chapter suggests ways that XRSS could bring unparalleled new chemical insight for sustainable carbons.

## 4.3 Experimental Techniques

### 4.3.1 Hydrothermal Carbonisation (HTC)

HTC of the oak wood biomass feedstock was performed in a modified two litre high-pressure batch autoclave (Parr, USA). The larger volume autoclave, in comparison to the method described in Section 2.3, was chosen to represent a more scalable product, however the rest of the described method remained the same. A 10% solid loading rate was used ($96\,\mathrm{g}$ biomass) with a combined mass of $1000\,\mathrm{g}$ per run. Once sealed, the autoclave was heated $250\,^{\circ}\mathrm{C}$, then held for $1\,\mathrm{h}$. Solid and liquid products from the reaction were separated using qualitative filter paper (Grade 3 Whatman, UK).

### 4.3.2 Pyrolysis of Oak Wood Biomass

Pyrolysis of the initial woody biomass feedstock was performed using the modified vertical tube furnace described in Section 2.2. The reactor was heated at $8\,^{\circ}\mathrm{C\,min^{-1}}$ to the desired temperature ($450\,^{\circ}\mathrm{C}$ or $650\,^{\circ}\mathrm{C}$), then maintained for a residence time of $1\,\mathrm{h}$ under nitrogen gas flow ($130\,\mathrm{ml\,min^{-1}}$). After the residence time had expired, the reactor was allowed to cool naturally before the samples were removed, weighed and stored in glass vials.

### 4.3.3 NEXAFS

Carbon *K*-edge NEXAFS data were collected using a $120\,\mathrm{nm}$ sized beam at beamline I08 of Diamond Light Source (Oxfordshire, UK). I08 is a scanning transmission X-ray microscopy (STXM) beamline, which also allows large spot sizes for NEXAFS measurements (i.e. STXM beam sizes are typically ~$20\,\mathrm{nm}$). Samples of hydrothermal and pyrolysis carbon were prepared by drop-casting a few milligrams of cryogenically-milled (Retsch, Ger) sample, well-dispersed in ultra-pure water, onto $75\,\mathrm{nm}$ thick $Si_3N_4$ windows. Image stacks (4x4 $\mu\mathrm{m}$) were acquired with $10\,\mathrm{ms}$ dwell time and $0.15\,\mathrm{eV}$ step-size over the main C *K*-edge features ($283\,\mathrm{eV}$ to $300\,\mathrm{eV}$), and a step-size of $0.5\,\mathrm{eV}$ in the energy regions below ($280\,\mathrm{eV}$ to $283\,\mathrm{eV}$) and above ($300\,\mathrm{eV}$ to $320\,\mathrm{eV}$) the NEXAFS region. As-received signals were converted to optical density using incident signal ($I_0$) measurements from an adjacent, empty region of the image. Spectra were averaged over a user-defined region-of-interest in the MANTIS software [182].

### 4.3.4 X-ray Raman Scattering Spectroscopy

XRSS was performed using the lower-energy resolution inelastic X-ray scattering (LERIX) spectrometer at sector 20-ID of the Advanced Photon Source (APS) as described in Section 2.7.3. Data were analysed programmatically using a python script written by the author as a module for the XRStools software [256]. The data presented in this study were taken from the first 7 analysers ($9°$ to $63°$), representing an average momentum transfer of $4.5\,\text{Å}^{-1}$. The energy resolution of the averaged signals from the first 7 analysers ($9°$ to $63°$) were calculated by quadrature from the resolution of the individual analysers for each scan. The average energy resolution of the collected data was $0.63\,\text{eV}$. Background subtraction of energy-loss spectra was carried out in XRStools using paramterised Pearson VII functions guided by a Hartree-Fock calculated core atomic carbon *K*-edge profile (Appendix B) [256, 261].

## 4.4 Computational Methods

In order to connect structural models with measured XRS spectra, electronic structure calculations were performed [262]. Due to the fast interaction process core-excited spectra (e.g. XAS, XRSS) reflect the instantaneous electronic structure of the probed system [113]. Excited state Density Functional Theory (DFT) calculations were performed to generate theoretical C *K*-edge XAS spectra; these spectra are compared with experimental data in Section 4.7. The discussed calculations were performed in collaboration with Dr. C.J.Sahle[1], who performed the DFT calculations using optimised, relaxed structures produced by the author. High performance computing resources were required to complete these calculations. This work was undertaken using High Performance Computing facilities at the University of Leeds, UK (ARC3) and the ESRF, FR (RNICE).

### 4.4.1 Selected Molecular Structures

Theoretical XRS spectra were calculated for a series of furfuryl-furan moieties (structure00, structure01 & structure02) and levulinic acid (Figure 4.5). The three structural motifs were chosen to represent structures thought to describe the local structure of hydrothermal carbon [173, 184]. Condensed furfuryl bonding (Structure00), furan bonding at the $\alpha$ carbon position

[1] Beamline ID20, European Synchrotron Radiation Facility

(Structure01) and furan bonding at the $\beta$ carbon position (Structure02) were each chosen for comparison to the experimental data. Structure00, Structure01 and Structure02 are not sufficiently stable in a non-polymerised, non carboxylic form in nature. Therefore, levulinic acid was calculated both as a known important product of HTC and potential structural component of hydrothermal carbon [143], but also as a reference structure.

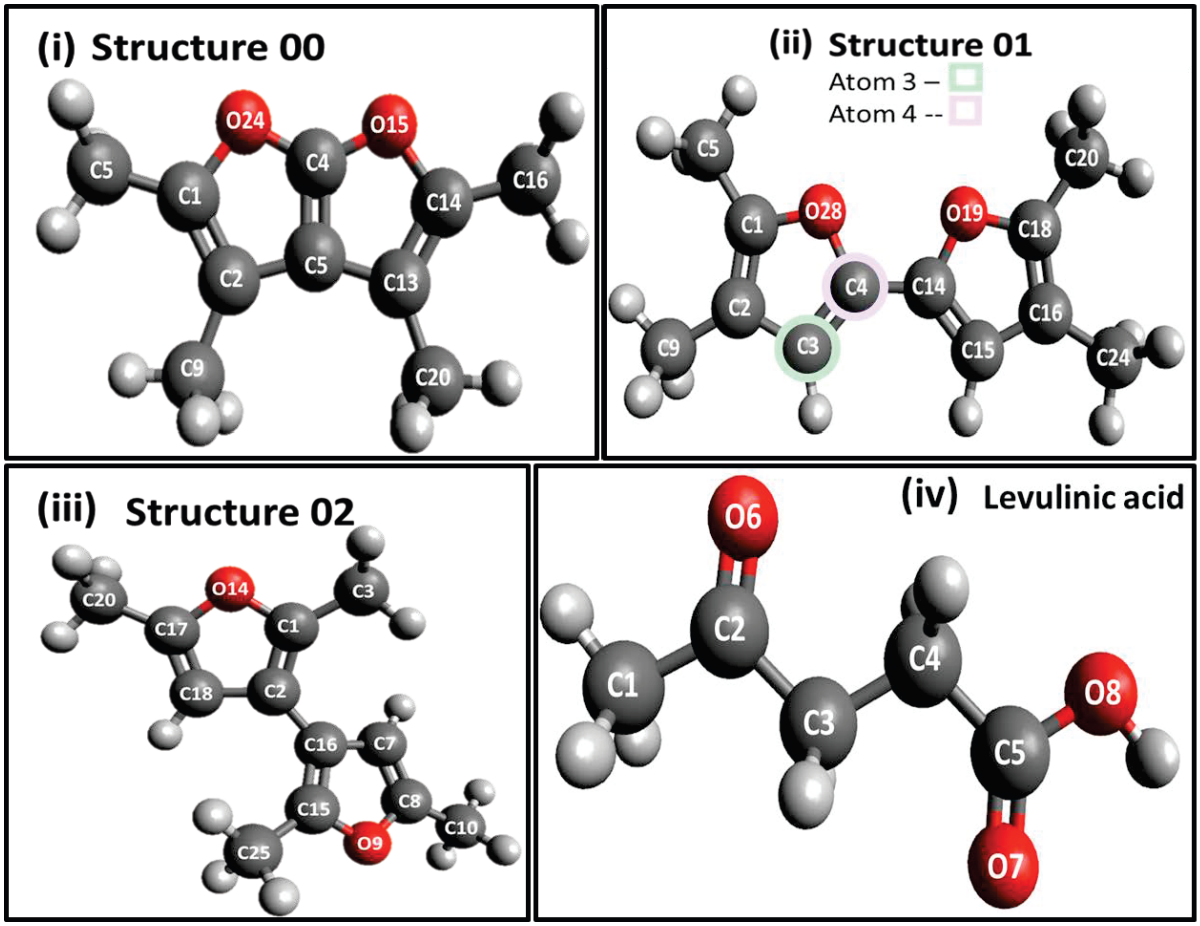


FIGURE 4.5: Four calculated molecular structures: (i) Structure 00: a condensed furan-type unit. (ii) Structure 01: an $\alpha$ carbon linked furan-furfuryl moiety (atoms 3 ($\alpha$-C) and 4 ($\beta$-C) highlighted) (iii) Structure 02: a furan-furfuryl moiety linked at the $\beta$ carbon position (iv) Levulinic acid. [Hydrogen; grey, Carbon; black, Oxygen; red].

### 4.4.2 Geometry Optomisation of Selected Structures (ORCA)

Molecular structures were initially constructed in Avogadro 1.1.1 [263]. Ground state geometry optimisation calculations for these structures were subsequently carried out using the ORCA 4.0 code with a B3LYP functional, def2-SVP basis set [264] and third order dispersion correction with Becke-Jones damping (D3BJ) [265, 266]. The selected functional, basis set and dispersion correction regime have been shown to be robust and accurate for other condensed

carbon systems [222, 267]. To reduce computational expense, the RIJCOSX approximation was used with appropriate def2-SVP/J basis sets [268]. Frequency calculations were run on the optimised structures to ensure that they corresponded to the global energy minimum.

### 4.4.3 Density Functional Calculations (ERKALE)

Using the open-source ERKALE software[2], DFT calculations were performed to produce theoretical XRS spectra [269]. For all atoms, other than the absorbing atom, triple-$\zeta$ basis functional calculations were applied. For the absorbing carbon atom, augmented IGLO-III basis functions were applied (1 DFT calculation per absorber) [270]. Spectra were calculated for the average experimental momentum transfer: $q$=4.5 Å$^{-1}$. The DFT calculations result in inaccurate absolute transition energies due to the shortcomings of DFT in accurately estimating the potentials close to the nucleus which results in 1s core level orbitals' energies appearing relatively higher than the valence orbitals' energies. Due to the inherent inaccuracy of calculating the absolute energy position of the calculated spectra, all spectra were shifted onto a relative energy scale using the delta Kohn-Sham correction scheme. An additional rigid shift of $+0.46\,\mathrm{eV}$ was used in order to match the energy scale of the experimental spectra. A Gaussian broadening scheme was applied to the computed spectra to mimic the continuum states [107].

### 4.4.4 Evaluating Calculated Structures & The Effects of Momentum Dependence

In order to test the accuracy of the DFT calculations discussed in Section 4.7, calculated spectra for Levulinic acid were compared to an experimentally collected standard. The XRS spectrum collected for levulinic acid and its calculated spectrum are shown in Figure 4.6a.

After the application of a rigid shift of $+0.46\,\mathrm{eV}$ the calculated spectra for levulinic acid displays three main features at $286.8\,\mathrm{eV}$, $288.6\,\mathrm{eV}$ and $288.9\,\mathrm{eV}$. The relative energy positions of these features correspond well to the collected experimental data, validating the selected calculation approach. However, it can be seen that the relative intensities of the calculation do not match experiment. This is common within DFT simulations of core electron transitions [262]. Currently, quantitative analysis by fitting of Gaussian functions to experimental data is still preferred over the use of component analyses using simulated spectra from DFT calculations. A potential reason for differences in ratios between the calculated XRS spectrum for levulinic

[2]https://github.com/susilehtola/erkale

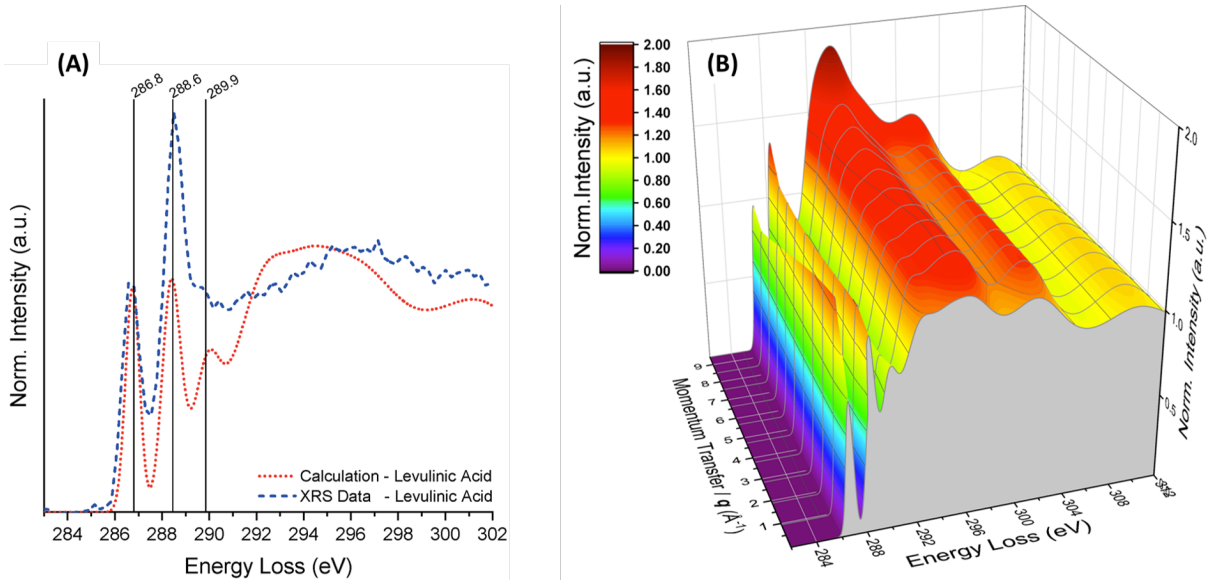


FIGURE 4.6: (a) Normalised experimental XRS spectrum for Levulinic acid (blue, dashed) and average calculated spectra for levulinic acid (red, dotted). (b) Calculated Levulinic acid spectrum over a range of momentum transfer (q).

acid is the effects of momentum transfer dependence. ERKALE is able to simulate the effects of momentum transfer. Using this ability, Figure 4.6b shows calculations of momentum transfer dependence were performed for Levulinic acid over a range of momentum transfer values (0.02, 0.94, 1.89, 2.83, 3.78, 4.72, 5.67, 6.61, 7.56, 8.50, 9.45 $Å^{-1}$). The results are congruous with momentum transfer results from experimental data (not shown), and highlight the flexibility of calculations for core-level XRSS using modern DFT codes.

## 4.5 Bulk Chemical Differences between Hydrothermal and Pyrolysis Carbon Chemistry

In order to demonstrate the sensitivity of XRSS to differences in bulk carbon chemistry between pyrolysis carbon and hydrothermal carbon, a comparison was made between HTC-Oak-250 and Pyro-Oak-450. Despite their remarkably different morphologies (Figure 4.7), these materials were chosen because of their similar carbon content and relative degree of carbonisation (Table 4.2). HTC-Oak-250, as shown in Figure 4.7a and reported in other lignocellulosic biomass derived hydrothermal carbons, shows the formation of both primary and secondary char [43]. HTC-Oak-250 displays some remaining cellulosic structure due to primary char formation, however this structure has been disrupted, resulting in smoothed edges and a loss of macroporosity. In contrast, in Figure 4.7b, Pyro-Oak-450 retains the structure of the starting biomass, with a well developed macroporous structure.

TABLE 4.2: Yield and Elemental Analysis of produced carbons.

| Sample | Component (wt %) | | | | | Atomic Ratio | |
|---|---|---|---|---|---|---|---|
| | Pc.Yield | C | H | N | O | H:C x10 | O:C |
| Oak Wood | - | 48.9 | 7.8 | 1.1 | 37.7 | 1.6 | 0.8 |
| HTC-Oak-250 | 42.7 % | 64.0 | 4.4 | 1.6 | 23.0 | 0.7 | 0.4 |
| Pyro-Oak-450 | 57.4 % | 65.7 | 2.7 | 0.6 | 8.9 | 0.4 | 0.1 |
| Pyro-Oak-650 | 25.8 % | 76.5 | 1.4 | 0.8 | 7.0 | 0.2 | 0.1 |

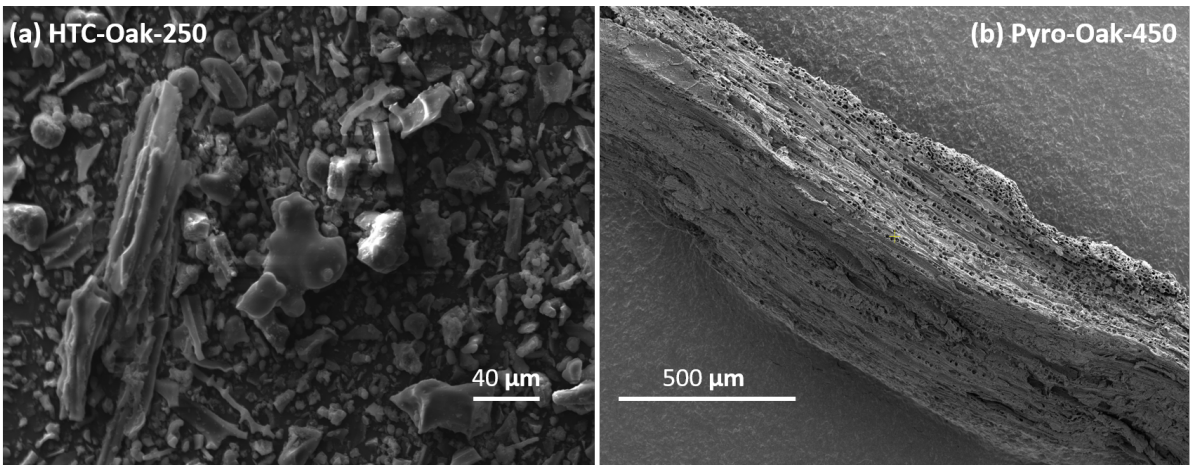


FIGURE 4.7: Secondary SEM images of (a) HTC-Oak-250 and (b) Pyro-Oak-450.

Figure 4.8 shows the normalised XRS spectra for Pyro-Oak-450, HTC-Oak-250 and their corresponding difference spectrum (HTC sub. Pyro). Carbon core electron transitions are also highlighted (Appendix A). From an initial assessment it is clear that, despite their similar carbon content, HTC-Oak-250 and Pyro-Oak-450 display different carbon chemistry. A comparison of pyrolysis carbon and hydrothermal carbon using bulk-sensitive, solid state $^{13}$C NMR has been performed using lignocellulosic components (i.e. cellulose, starch) [173]. However, previous studies have not made a direct comparison between chars produced from real lignocellulosic biomass. The lack of comparative, bulk-sensitive spectroscopy between lignocellulosic biomass derived chars is most likely due to the difficulties of $^{13}$C enrichment and the presence of interfering inorganic species (e.g. magnetite). In order to address the lack of a comparison of real-world pyrolysis and hydrothermal carbons, this section compares some of the key features in the C *K*-edge spectra of HTC-Oak-250 and Pyro-Oak-450.

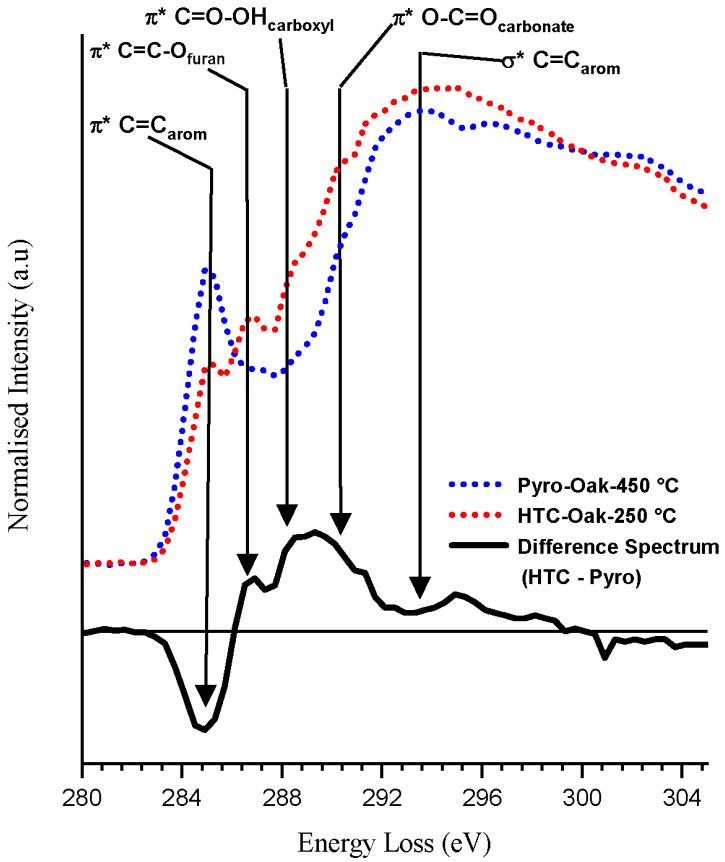


FIGURE 4.8: Background corrected and normalised XRS spectra of Pyrolysis (blue dashed) and hydrothermal (red dashed) carbon. Difference spectrum shown in solid black.

### 4.5.1 Aromatic Substructure (285.0 eV and 292-295 eV)

In both spectra (Figure 4.8), the lowest energy feature is the aromatic 1 s-$\pi^*_{\underline{C}=C}$ transition (285.0 eV), where an amplitude loss between Pyro-Oak-450 and HTC-Oak-250 is observed in the difference spectrum. The presence of the aromatic 1 s-$\pi^*_{\underline{C}=C}$ transition in both experimental XRS spectra confirms that Pyro-Oak-450 and HTC-Oak-250 contain bulk aromatic substructure, which has been reported for other pyrolysis and hydrothermal carbons [173, 188, 242]. The FWHM for the Gaussian fit of the aromatic 1 s-$\pi^*_{\underline{C}=C}$ transition (285.0 eV) in Pyro-Oak-450 (Table 4.3) was found to be $1.85 \pm 0.04$ eV using Gaussian fitting (see Section 4.8) and indicates a broad range of aromatic functionality [258]. In contrast, HTC-Oak-250 shows a smaller amplitude and FWHM ($1.24 \pm 0.02$ eV) for the same 1 s-$\pi^*_{\underline{C}=C}$ transition. The smaller amplitude and FWHM suggests that the bulk aromatic substructure is less well developed in hydrothermal carbon. Furthermore, Pyro-Oak-450 displays increased spectroscopic structure at the 1 s-$\sigma^*_{\underline{C}=C}$ transition (292 eV to 295 eV), which has been shown to indicate more ordered, polyaromatic structures such as polyaromatic hydrocarbons (PAHs) [258]. Taken together, the broader FWHM of the Pyro-Oak-450 1 s-$\pi^*_{\underline{C}=C}$ transition, and the increased structure at the 1 s-$\sigma^*_{\underline{C}=C}$ , suggests that pyrolysis carbon contains a continuum of condensed aromatic functionality, most likely due to the formation of ordered sextet carbon. This understanding is supported by chemical extractions of pyrolysis carbons performed by *Keiluweit et.al.*, which show high levels of extractable PAHs for pyrolysis carbons produced under similar conditions to Pyro-Oak-450 [271]. Increased structure at the 1 s-$\sigma^*_{\underline{C}=C}$ transition is absent in HTC-Oak-250 which, combined with the smaller FWHM of the 1 s-$\pi^*_{\underline{C}=C}$ transition, is indicative of fewer aromatic bonding positions and greater structural disorder.

### 4.5.2 Feature at 286.6 eV

From the difference spectrum (Figure 4.8), the most significant spectral change between Pyro-Oak-450 and HTC-Oak-250, other than the 1 s-$\pi^*_{\underline{C}=C}$ transition, is a significant peak at 286.6 eV, which is present in HTC-Oak-250 but absent from Pyro-Oak-450. A previous NEXAFS study of nitrogen modified hydrothermal carbons, attributed this feature to the presence of furan species, which had initially been proposed using $^{13}$C NMR [136, 167]. This feature is further discussed in Section 4.7.

### 4.5.3 Carboxylic Functionality and Lignocellulosic Recalcitrance (288.9 - 290.3 eV)

In Figure 4.8, the shoulder at ($\sim$288.9 eV), representing carboxylic functionalities, is present in HTC-Oak-250 but significantly reduced in Pyro-Oak-450. Lower amplitude in the 287 eV to 290 eV region, suggests that Pyro-Oak-450 has significantly less carboxylic functionality than the hydrothermal carbon. The XRS spectra for both HTC-Oak-250 and Pyro-Oak-450 also exhibit a shoulder at $\sim$290.3 eV, which is assigned to the 1 s-$\pi^*_{\underline{C}=O}$ carboxyl transition. This feature is most likely due to remaining bulk cellulosic functionality from the starting lignocellulosic biomass [183]. Since XRSS is sensitive to changes in bulk chemistry, due to the use of hard X-ray photons, a complimentary comparison with surface-sensitive, soft X-ray NEXAFS spectroscopy was conducted.

## 4.6 Comparison of NEXAFS and XRSS

In order to qualify the differences between XRSS and soft X-ray absorption spectroscopy, NEXAFS and XRS were performed for both pyrolysis carbons Pyro-Oak-650, Pyro-Oak-450 and the hydrothermal carbon HTC-Oak-250.

### 4.6.1 Pyro-Oak-450 and Pyro-Oak-650

Figure 4.9 shows both NEXAFS and XRS spectra for Pyro-Oak-650, Pyro-Oak-450 and HTC-Oak-250. These spectra were unit normalised over the whole range of the C *K*-edge, with the post-edge subtraction region extending from 320 eV to 340 eV. Whilst the produced NEXAFS and XRS spectra for the pyrolysis carbons are similar, there are some key differences. In Pyro-Oak-650 the 1 s-$\pi^*_{\underline{C}=C}$ transition ($\sim$285 eV) is reduced in magnitude in the NEXAFS compared to the bulk-sensitive XRS spectrum. This is in contrast to Pyro-Oak-450, where the NEXAFS and XRS spectra display similar magnitude at the 1 s-$\pi^*_{\underline{C}=C}$ transition. As will be discussed further in Section 4.8, the FWHM for the aromatic 1 s-$\pi^*_{\underline{C}=C}$ transition has been shown to be linked with the total aromatic condensation of polyaromatic and other condensed aromatic systems (e.g. asphaltenes) [272]. Reduced amplitude and FWHM at the NEXAFS 1 s-$\pi^*_{\underline{C}=C}$ transition for Pyro-Oak-650 highlights a more disordered surface layer, with a reduced polyaromatic component compared to the bulk material. The similar XRSS and NEXAFS intensities for Pyro-Oak-450 may also indicate a similar level of aromatisation throughout the material.

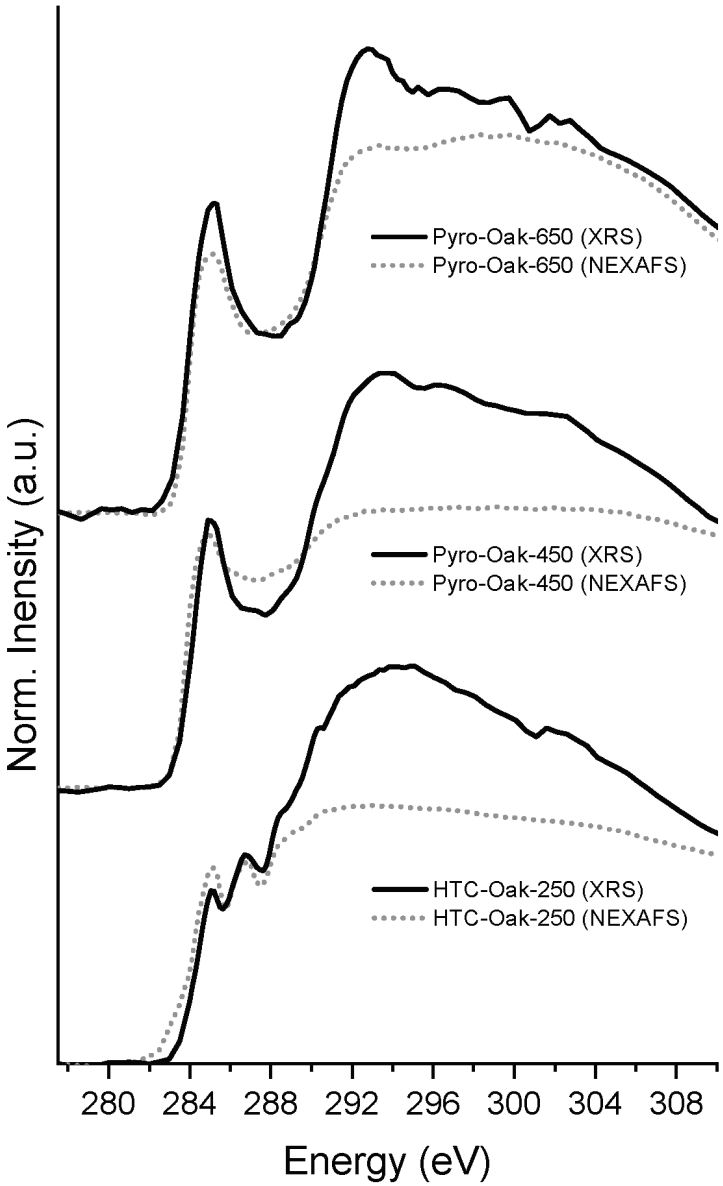


FIGURE 4.9: Background subtracted and normalised soft X-ray NEXAFS (grey, dashed) and hard XRSS (black, solid) for Pyro-Oak-650 (top), Pyro-Oak-450 (middle) and HTC-Oak-250 (bottom).

At the aromatic 1 s-$\sigma^*_{\underline{C}=C}$ transition (~292 eV), increased structure and intensity in the NEXAFS spectrum for Pyro-Oak-650 relative to Pyro-Oak-450 is observed. This is evidence that Pyro-Oak-650 contains more long-range graphitic-type ordering, as expected [188]. Relative to the XRS spectrum, the NEXAFS spectrum for Pyro-Oak-450 displays an increase in intensity in the C-O region (1 s-$\pi^*_{\underline{C}=O}$ , 286 eV to 289 eV). This is likely due to the surface of Pyro-Oak-450 containing more oxygenated functionalities, not present in the bulk material. Increased C-O functionality is not observed in the Pyro-Oak-650 NEXAFS spectrum. It is likely that oxygenated surface functionalities are removed at higher pyrolysis temperatures through decarboxylation

reactions. The XRS spectrum for Pyro-Oak-450 also exhibits a shoulder at $\sim 290.3\,\mathrm{eV}$, which is assigned to the $1\,\mathrm{s}$-$\pi^*_{\underline{\mathrm{C}}=\mathrm{O}}$ transition. This shoulder is known to be present in lignocellulosic materials, and is not present in the NEXAFS for either Pyro-Oak-450 or Pyro-Oak-650. The lack of a shoulder at $\sim 290.3\,\mathrm{eV}$ in the NEXAFS indicates that lignocellulosic functionality remains in the bulk, despite the surface being fully carbonised.

### 4.6.2 HTC-Oak-250

Figure 4.9 also shows the NEXAFS spectrum for HTC-Oak-250 which displays increased amplitude in the $1\,\mathrm{s}$-$\pi^*_{\underline{\mathrm{C}}=\mathrm{C}}$ aromatic region compared to the XRS spectrum. The differences in bulk and surface carbohydrate-derived char are discussed in Chapter 3. The conclusion of that work is that, for carbohydrate derived carbon, the surface region displays more oxygenated functionality with a more condensed furanic core. The result that the surface-biased NEXAFS spectra for HTC-Oak-250 here shows higher amplitude than the bulk XRSS measurement might therefore seem erroneous. However it is likely that the additional formation of primary char, which is known to be more aromatic in nature, is influencing this result.

### 4.6.3 Possible Spectral Distortion

Qualitative trends between the NEXAFS and XRS spectra clearly show potential differences between the carbon chemical signature of the surface compared with the bulk. However, the possibility of spectral distortions arising from thickness artefacts commonly observed in transmission mode NEXAFS may not be ruled out. Therefore, no quantification of the NEXAFS results in comparison to the XRS spectra is performed here. Transmission artefacts in transmission NEXAFS is due to the homogeneity of these samples. However, comparisons of different regions in the measured samples (Figure 4.10) show no significant spectral variation, and the XRS resolution is sufficient to resolve all major features over the spectral region. Therefore spectral distortion, whilst present, would not significantly influence the conclusions made here.

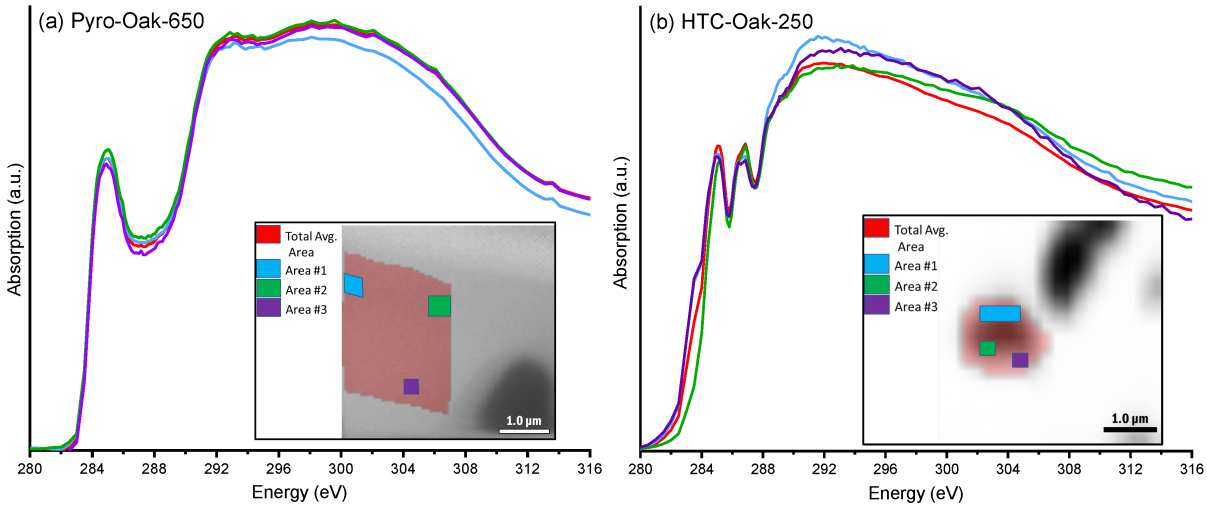


FIGURE 4.10: Scanning transmission X-ray microscopy images of (a) Pyro-Oak-650 and (b) HTC-Oak-250 with three areas and their corresponding average spectra highlighted in blue, green and purple. The average NEXAFS spectra used in this study and its corresponding selected area are shown in red.

## 4.7 Hydrothermal Carbon - *In-Silico* Simulations of Relevant Structures

From the difference spectrum shown in Section 4.5 (Figure 4.8), the most obvious XRS spectral change between Pyro-Oak-450 and HTC-Oak-250 is the addition of a significant peak at 286.6 eV in HTC-Oak-250 that is absent from Pyro-Oak-450. This feature has been reported for carbohydrate derived hydrothermal carbon using NEXAFS, where it was attributed to the presence of furan functionality [168]. The presence of furan species within the structure of carbohydrate derived hydrothermal carbon had previously been identified by solid-state $^{13}C$ – NMR , and is attributed to the nucleation of secondary char from HMF during HTC [43, 142, 173]. Solid-state $^{13}C$ – NMR collected for carbohydrate-derived hydrothermal carbons led *Baccile et.al.* to suggest several different furan-furfuryl units may be present in the structure [142]. However, the limitations of $^{13}C$ – NMR in terms of isotopic enrichment, spectral resolution and sample preparation have meant that no studies have been able to provide evidence for the major structural motif within hydrothermal carbon. Advances in modern DFT codes now allow for accurate *ab-initio* simulation of XRS spectra for low-Z structures. Such computational approaches now provide a route to modelling bulk local chemical motifs. In this section, simulated XRS spectra for three furan-furfuryl structures (Structure00, Structure01, Structure02) are compared to bulk experimental XRSS in order to: i) understand the

bulk chemical information obtained from XRSS, ii) compare those with published results using $^{13}C$ – NMR and surface-limited soft X-ray spectroscopy, and iii) highlight the importance of using DFT to simulate theoretical XRS spectra for an unambiguous assignment of peaks from experiment.

### 4.7.1 Comparison of Modelled Structures

Figure 4.11 shows the calculated structures (structure00, structure01 & structure02) plotted with the experimental XRS spectrum collected for HTC-Oak-250.

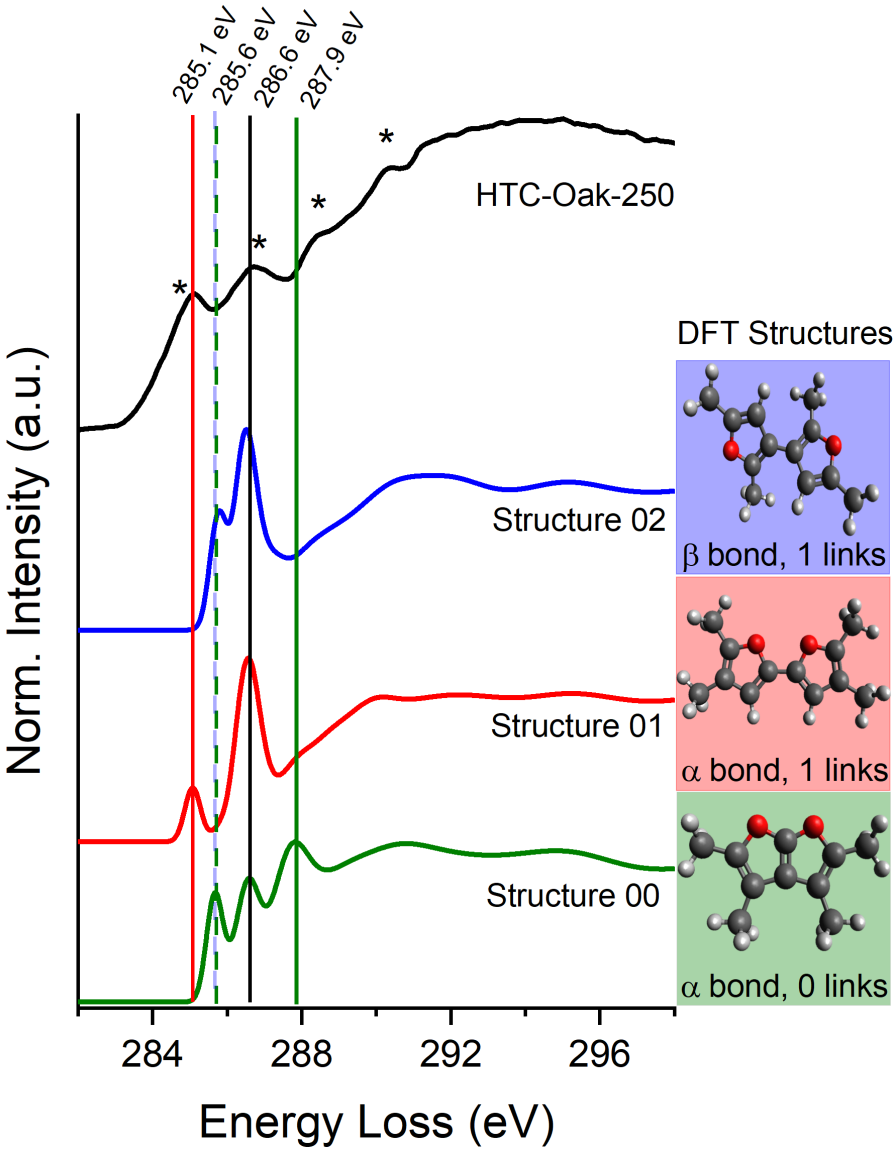


FIGURE 4.11: Experimental XRS spectrum for HTC-Oak-250 and average calculated spectra for: structure00, sturcture01 and structure02. Features in the experimental data are highlighted with asterisks.

The experimental data for HTC-Oak-250 displays four clear spectral features (highlighted with asterisks) at: $285.0\,\mathrm{eV}$, $286.6\,\mathrm{eV}$, $288.9\,\mathrm{eV}$ and $290.3\,\mathrm{eV}$. These features correspond to the aromatic $1\,\mathrm{s}$-$\pi^*_{\underline{\mathrm{C}}=\mathrm{C}}$ , furan $1\,\mathrm{s}$-$\pi^*_{\mathrm{C}=\underline{\mathrm{C}}-\mathrm{O}}$ , carboxyl $1\,\mathrm{s}$-$\pi^*_{\underline{\mathrm{C}}=\mathrm{O}}$ and carbonate $1\,\mathrm{s}$-$\pi^*_{\underline{\mathrm{C}}=\mathrm{O}}$ functionalities respectively. The furan $1\,\mathrm{s}$-$\pi^*_{\mathrm{C}=\underline{\mathrm{C}}-\mathrm{O}}$ transition in the experimental data is well matched by each of the spectra for the potential calculated structures, as expected. The calculated structures do not show features at $288.9\,\mathrm{eV}$ and $290.3\,\mathrm{eV}$ since these correspond to carbon functionalities not present within the calculated structures.

**Structure00**

Structure00 displays a low energy feature at $285.6\,\mathrm{eV}$ and a higher energy feature at $287.9\,\mathrm{eV}$. The relative energy difference between the lower energy peak at $285.6\,\mathrm{eV}$ and the furan transition ($286.6\,\mathrm{eV}$) in the calculated spectrum for Structure00 does not match the experimental data. Furthermore, the broad higher energy feature at $287.9\,\mathrm{eV}$ in Structure00 is not present in the experimental data. Combined, the differences between the calculation for Structure00 and the experimental data suggests that condensed furan units, without aryl linking units, are not common within the HTC-Oak-250 structure.

**Structure01**

The calculated spectrum for Structure01 has two features located at $285.1\,\mathrm{eV}$ and $286.6\,\mathrm{eV}$. These features correspond directly to those observed in the experimental data. The energy difference in the calculated spectrum matches the experiment well. This makes structure01 the most likely candidate of the modelled structures to be the main furan motif within HTC-Oak-250.

**Structure02**

The calculation for Structure02 displays two features at $285.6\,\mathrm{eV}$ and $286.6\,\mathrm{eV}$. The furan feature at $285.6\,\mathrm{eV}$, as discussed, matches the experimental data well. However, whilst the small shoulder at $285.6\,\mathrm{eV}$ in the calculation does not correspond well with the experimental feature at $285.1\,\mathrm{eV}$, there is still intensity in this region. This makes it possible that structure02 is present within hydrothermal carbon, but is unlikely to be the major structural motif.

### 4.7.2 The Structure01 Model

The experimental relative energy difference between the lower energy peak (285.1 eV) and furan peak (286.6 eV) in the experimental data is best matched by the calculation for structure01. Figure 4.12 displays the average calculated spectra and atom-wise calculated spectra for the $\alpha$-carbon (atom 4) and $\beta$-carbon (atom 3) atoms in the structure01 model (labelled atom positions shown in Figure 4.5).

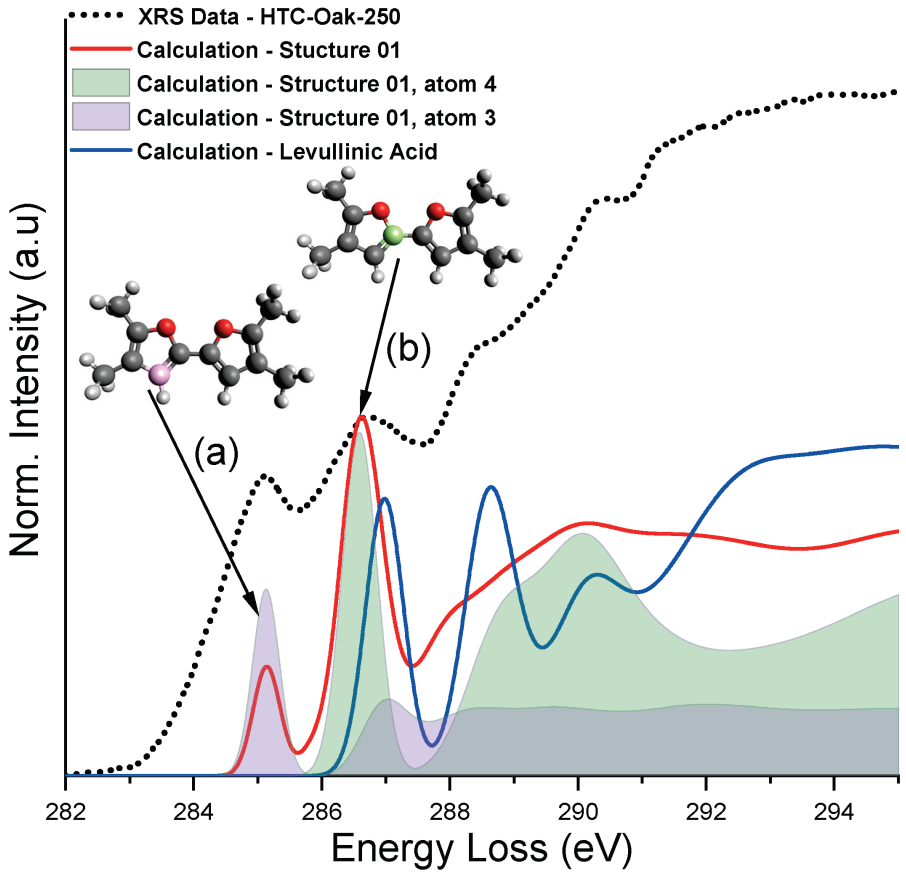


FIGURE 4.12: Experimental XRS spectrum for HTC-Oak-250 (black, dotted) and average calculated spectra for furan-furfuryl moiety: sturcture01 (red, solid) and Levulinic acid (blue, solid). Filled areas show calculated spectra for (a) structure01-atom 3 (green, fill) and (b) structure01-atom4 (pink, fill).

The spectra for structure01 (red, solid) is the average over all carbon atoms in the structure, including atoms 3 and 4. The $\alpha$-carbon (structure01, atom 4) component of the simulated XRS spectra has intensity at the furan 1 s-$\pi^*_{\underline{C}=\underline{C}-O}$ transition, but shows no amplitude in the aromatic region (285.0 eV). The aromatic 1 s-$\pi^*_{\underline{C}=C}$ transition is solely represented by the $\beta$-carbons in the structure01 model (e.g. structure01, atom 3). As previously discussed, the energy difference between the simulated $\beta$-carbon (285.0 eV) and $\alpha$-carbon (286.6 eV) transitions for structure01

matches the energy difference observed in the experimental data. The accurate representation of both the aromatic and furan transition peak positions by the structure01 model provides supportive evidence for the furan $1\,\mathrm{s}\text{-}\pi^*_{\mathrm{C=\underline{C}-O}}$ transition assignment made in soft NEXAFS measurements [168]. Therefore, it is possible to suggest that the bulk hydrothermal carbon (HTC-Oak-250) is built predominantly of furan units bridged at the $\alpha$-carbon atom. However, this does not rule out the presence of the other calculated structural motifs, since the resulting hydrothermal carbon is a complex amorphous material which is likely to contain a wide variety of different structural units, including Structure02. The calculation for levulinic acid (Figure 4.12, blue solid) also represents the experimental resonance at $286.6\,\mathrm{eV}$, as well as the feature at $288.9\,\mathrm{eV}$. The good fit between experiment and calculation provides supporting evidence for the role of levulinic acid and other organic acids in the bulk structure of hydrothermal carbon matrix. However, whilst the agreement between theory and experiment for the $\alpha$ carbon bridging model is compelling, the average XRS spectrum calculation of structure01 fails to reproduce the amplitude ratio between the experimental aromatic $1\,\mathrm{s}\text{-}\pi^*_{\mathrm{\underline{C}=C}}$ transition and furan $1\,\mathrm{s}\text{-}\pi^*_{\mathrm{C=\underline{C}-O}}$ transition peaks. Such differences are likely to be explained by the innate complexity of the material, the presence of additional aromatic functionalities and the associated structural disorder. The final experimental feature at $290.3\,\mathrm{eV}$ is not represented by these calculations, and is thought to be due to remaining lignocellulosic functionality within HTC-Oak-250 [254].

## 4.8 Evolution in Carbon Chemistry during Pyrolysis

In this section, XRSS is used to highlight differences in carbon functionality and to monitor changes in the total degree of aromatic condensation in two biomass-derived pyrolysis carbons produced under moderate (Pyro-Oak-450, $450\,^\circ\mathrm{C}$) and severe (Pyro-Oak-650, $650\,^\circ\mathrm{C}$) pyrolysis temperatures. Although previous NEXAFS studies have been performed on pyrolysis carbon and other black carbons [119, 187, 188], this section represents the first application of XRSS to pyrolysis carbons, and provides an understanding of chemical changes averaged over the entire bulk sample. XRSS is applied here to monitor the development of an increasingly condensed aromatic system in pyrolysis carbon and to propose a semi-quantitative description of pyrolysis condensation using previous measurements on polyaromatic carbons.

### 4.8.1 Local Structural Changes in Pyrolysis Carbon due to Process Temperature

Figure 4.13 shows normalised XRS spectra for Pyro-Oak-450 and Pyro-Oak-650. Details of XRS data treatment and background subtraction are shown in Appendix B. The figure also highlights the corresponding difference spectrum and electron transitions for the carbon functionalities shown in Table 4.3. An initial assessment suggests three main spectral differences between Pyro-Oak-450 and Pyro-Oak-650: (i) increased amplitude and broadening of the aromatic 1 s-$\pi^*_{\underline{C}=C}$ transition in Pyro-Oak-650 relative to Pyro-Oak-450 (285 eV, Figure 4.13-inset), (ii) inhibition of transition amplitudes in the C-O spectral region (286 eV to 290 eV) in Pyro-Oak-450 relative to Pyro-Oak-650 and (iii) increased fine structure in the 1 s-$\sigma^*_{\underline{C}=C}$ transition region (292 eV) in Pyro-Oak-650 .

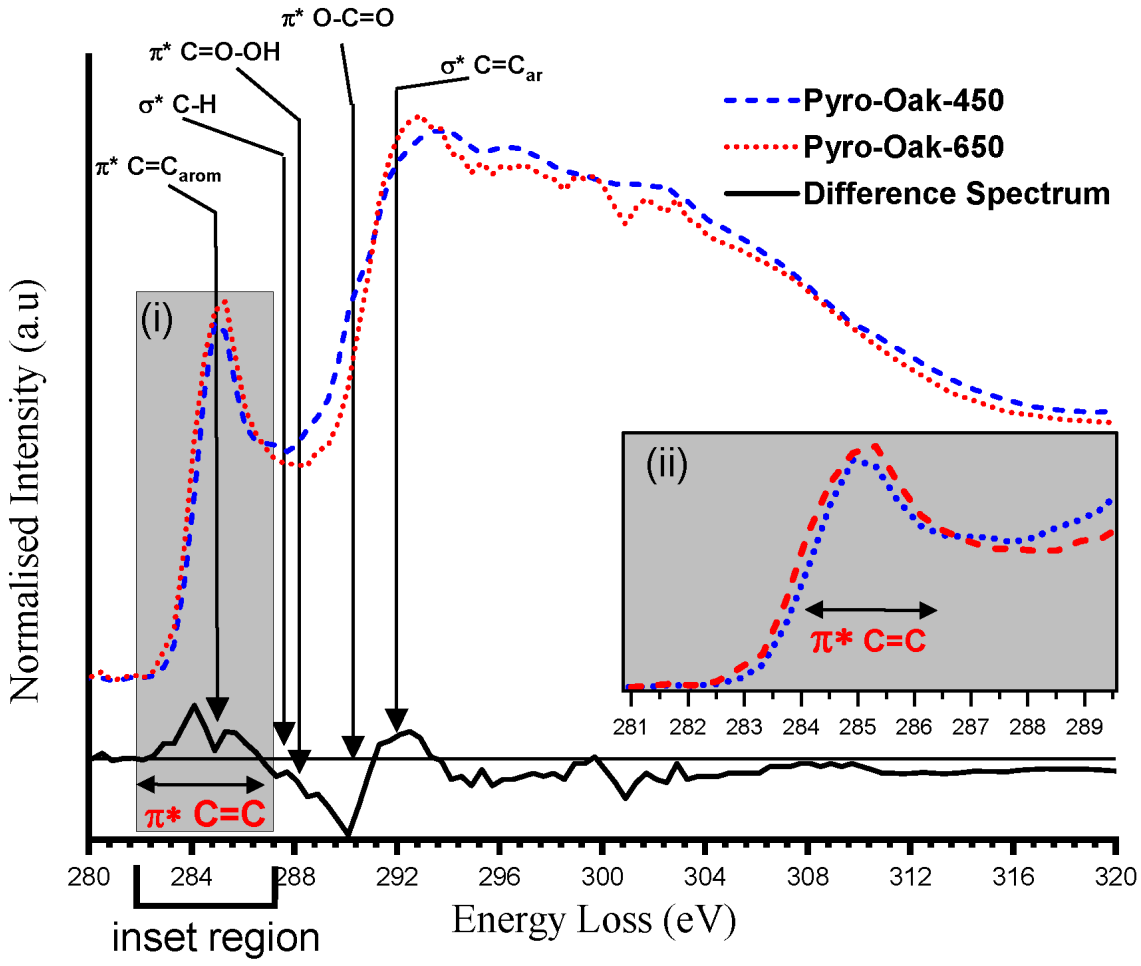


FIGURE 4.13: Background subtracted and normalised XRS spectra of Pyrolysis carbon produced at two temperatures (450 °C and 650 °C) are shown with electron transitions highlighted. Difference spectrum shown below in solid black. Region (i) shows the 1 s-$\pi^*_{\underline{C}=C}$ transition region. A magnification of this region is shown inset (ii).

In order to investigate the three discussed differences between the spectra for Pyro-Oak-450 and Pyro-Oak-650 in a semi-quantitative manner, Gaussian spectral fitting was performed. Spectral fitting has been routinely applied to NEXAFS of pyrolysis carbons [115, 187, 188, 273]. Gaussian spectral deconvolution is performed by fitting Gaussian functions at known electron transitions for functionalities within the sample. Here, six key electron transitions were used to describe the chemistry of the sample: G1: aromatic 1 s-$\pi^*_{\underline{C}=C}$ (285.0 eV), G2: furan/phenolic 1 s-$\pi^*_{C=\underline{C}-O}$ (286.6 eV), G3: aliphatic 1 s-$\sigma^*_{\underline{C}-H}$ (287.5 eV), G4: carboxyl 1 s-$\pi^*_{\underline{C}=O}$ (288.9 eV), G5: carbonate/carbonyl 1 s-$\pi^*_{O-\underline{C}=O}$ (290.3 eV), G6: aromatic 1 s-$\sigma^*_{\underline{C}=C}$ (292 eV). These transition energies were taken from previous studies of standards, pyrolysis carbons and similar materials and were fixed at these energy positions whilst the FWHM and amplitude of these peaks were allowed to vary. As well as the Guassian functions an atomic background error function and a series of asymmetric Gaussian functions were used to describe the edge step and fine structure and were fixed during the fit. Further details on the fitting approach used here can be found in Appendix A. Results of the Gaussian fitting are shown in Table 4.3.

TABLE 4.3: Results of non-linear least squares fitting. Peak area ($A_g$) and FWHM for each of the six pre-ionisation potential carbon functionalities are shown.

| Sample | G1 285.0 eV | | G2 286.6 eV | | G3 287.5 eV | | G4 288.9 eV | | G5 290.3 eV | | G6 292.0 eV | |
|---|---|---|---|---|---|---|---|---|---|---|---|---|
| | $A_g$ | FWHM | $A_g$ | FWHM | $A_g$ | FWHM | $A_g$ | FWHM | $A_g$ | FWHM | $A_g$ | FWHM |
| Pyro-Oak-450 | $2.17 \pm 0.04$ | $1.85 \pm 0.04$ | $0.66 \pm 0.08$ | $1.48 \pm 0.08$ | $0.61 \pm 0.03$ | 1.62 (fixed) | $0.42 \pm 0.01$ | 1.62 (fixed) | $0.46 \pm 0.02$ | 1.62 (fixed) | $1.48 \pm 0.05$ | $2.43 \pm 0.05$ |
| Pyro-Oak-650 | $2.62 \pm 0.07$ | $2.10 \pm 0.06$ | $0.63 \pm 0.09$ | $1.42 \pm 0.09$ | $0.61 \pm 0.04$ | 1.62 (fixed) | $0.28 \pm 0.02$ | 1.62 (fixed) | - | - | $1.95 \pm 0.03$ | $2.81 \pm 0.05$ |

Figure 4.14 shows the results of the non-linear least-squares Gaussian fitting for Pyro-Oak-450 and Pyro Oak-650. FWHM and peak areas ($A_g$) of the fitted Gaussian transitions are highlighted in Table 4.3. Fitting was performed using 188 data points, with $\chi^2$ values of 0.116 and 0.237 for the fits for Pyro-Oak-450 and respectively.

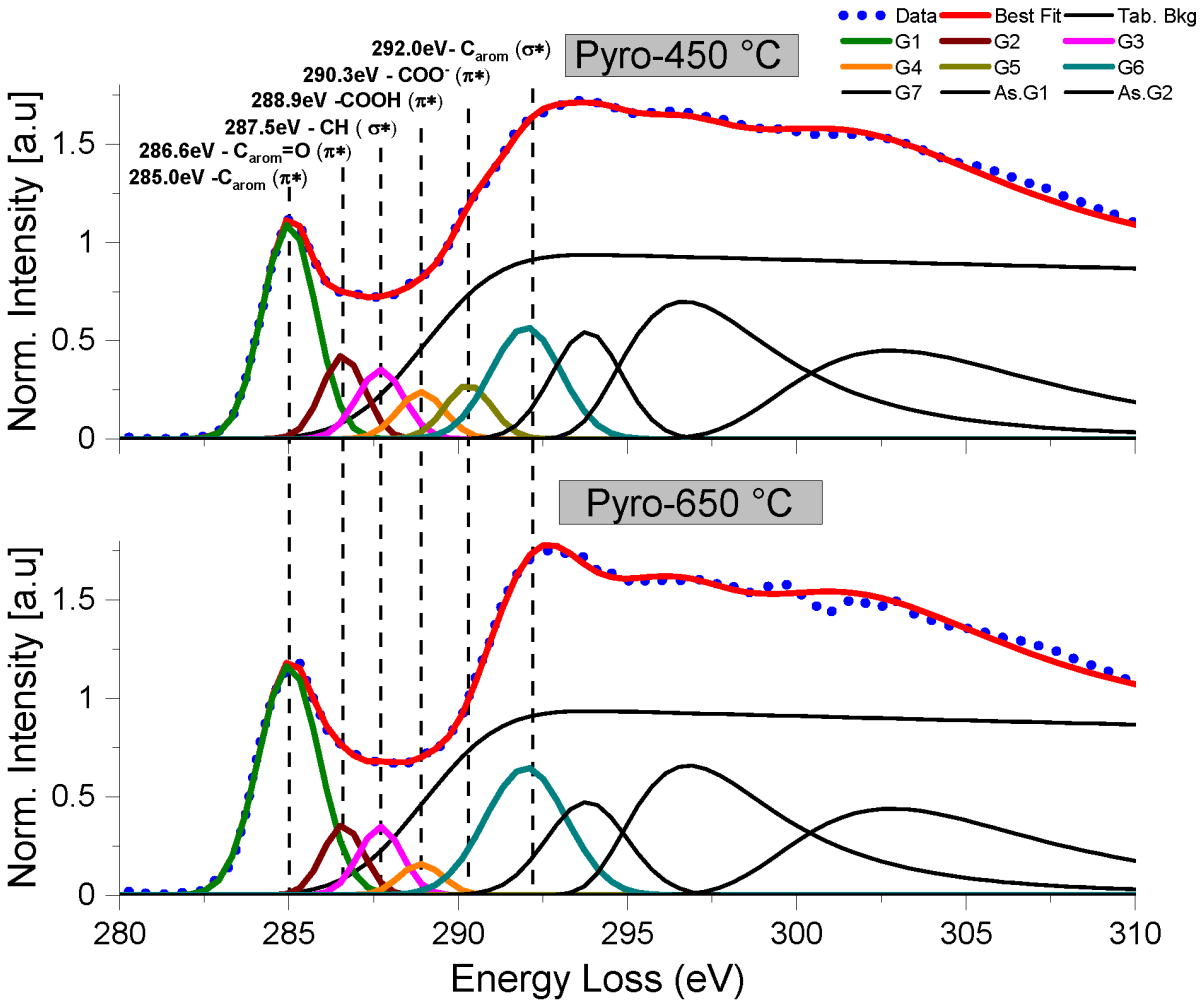


FIGURE 4.14: XRS Spectral fitting of two pyrolysis carbons produced at 650 °C (Pyro-Oak-650) and 450 °C (Pyro-Oak-450) using non-linear least-squares fitting. The pre-ionisation potential (pre-IP) region is represented using six Gaussian functions, the IP is represented using a decaying step function, and the post-IP region is represented using two asymmetric functions and one symmetric Gaussian function.

From Table 4.3, there is a $33 \pm 7\%$ decrease in $A_g$ at the carboxyl transition (G4, 288.9 eV) between Pyro-Oak-450 and Pyro-Oak-650. This large decrease in peak G4 intensity with respect to pyrolysis temperature, indicates decarboxylation reactions to be the dominant mechanism during pyrolysis as suggested by other studies [227]. The large reduction in the shoulder at G4 contrasts with previous NEXAFS studies of pyrolysis carbons, which show a significant peak at the 1 s-$\pi^*_{\underline{C}=C}$ transition, even at pyrolysis temperatures greater than 500 °C [271]. The retention

of peak G4 in soft X-ray NEXAFS studies and its reduced intensity in this XRS study suggests that carboxyl groups are principally found at the surface of the pyrolysis carbon. Spectral fitting also highlights the complete removal of the carbonyl 1 s-$\pi^*_{\text{O}-\underline{\text{C}}=\text{O}}$ transition (G5, 290.3 eV) going from Pyro-Oak-450 to Pyro-Oak-650. As previously discussed, the carbonyl 1 s-$\pi^*_{\text{O}-\underline{\text{C}}=\text{O}}$ transition is a feature present in the spectrum of raw cellulose and other carbohydrates. The removal of peak G5 from the fit indicates complete removal of cellulosic functionality during pyrolysis between $450\,^{\circ}\text{C}$ and $650\,^{\circ}\text{C}$. NEXAFS collected here, as well as literature NEXAFS, indicates complete removal of initial cellulosic functionality by $400\,^{\circ}\text{C}$ at the surface, however this does not seem to be the case in these bulk XRSS measurements [183]. It may well be that the removal of cellulosic functionality begins at the surface, leaving some of this functionality still present in the core of pyrolysis carbons at higher temperatures. There appears to be little change in both the furan (G2, $286.6\,\text{eV}$) and aliphatic (G3, $287.5\,\text{eV}$) region of the spectrum between Pyro-Oak-450 and Pyro-Oak-650. It is likely that beyond $450\,^{\circ}\text{C}$ any changes in these types of functionalities has already occurred, has reached a stable state or has been completely removed.

### 4.8.2 Potential Application of XRSS for Quantification of Aromatic Condensation

As discussed in Section 4.1.3 non-graphitising carbons, including pyrolysis carbons, may be considered as two principle aromatic carbon phases: (i) an amorphous carbon phase composed of randomly organised aromatic structures and (ii) a highly ordered crystallite phase, comprised of well organised sheets of aromatic 'graphene' layers [70, 274]. Aromaticity is a measure of both the disordered and ordered phases, where a perfect aromaticity value of 1.0 would represent the graphite lattice. An alternate measurement is the degree of aromatic condensation, which estimates the average size of the crytallite phase (i.e. ring conjugation).

#### Aromaticity

The difference in aromaticity between Pyro-Oak-450 and Pyro-Oak-650 was measured here using the method set out in previous studies [243, 245]. The relative increase in amplitude ($A_g$) in the 1 s-$\pi^*_{\underline{\text{C}}=\text{C}}$ transition between the two pyrolysis carbons was measured. The fit shows an increase in peak area ($A_g$), and therefore aromaticity, of $20.7 \pm 6.0$ %. This increase in aromaticity is similar to the total increase in percentage carbon between the two carbons (Table 4.2).

### Degree of Aromatic Condensation

The degree of aromatic condensation in polyaromatic systems may be considered as the average size of condensed ring systems in the carbon. Here, XRSS is suggested as an alternate route to measuring the degree of aromatic condensation in sustainable carbons. XRSS is more sensitive to the highly delocalised, poly-condensed $\pi$ electron systems in pyrolysis carbons than $^{13}C$ – NMR and may be performed without complex sample preparation [113]. In order to study the bulk degree of condensation in pyrolysis carbons, the Clar model is used [237]. In the Clar model, $\pi$ bonding in condensed systems is considered as a superposition of aromatic sextets (AS) and isolated double bonds (IDB) [238, 275]. AS contain electrons fully delocalised over the arene ring and are highly condensed, stable systems; AS may be considered as equivalent to the crystalline phase of the pyrolysis carbon model. Whilst IDB may be considered as the disordered aromatic phase. It is possible to directly quantify the degree of average bulk condensation for a material in terms of the ratio between IDB and AS (IDB:AS).

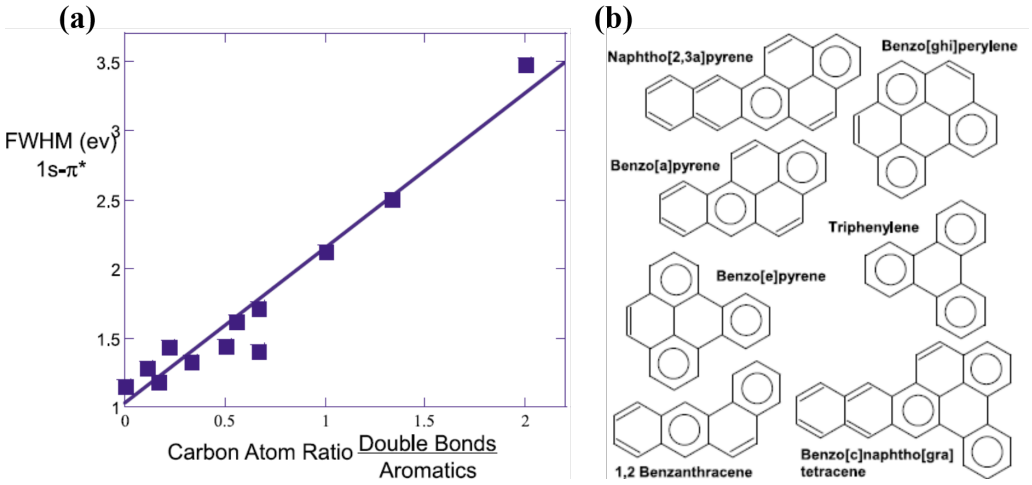


FIGURE 4.15: (a) The correlation of the 1 s-$\pi^*_{\underline{C}=C}$ FWHM with the ratio of sextet-type carbon and double-bond carbon atoms for the polyaromatic hydrocarbons in (b). The large variation in FWHM is directly correlated with PAH carbon type lending strong support for the corresponding fundamental description of polyaromatic hydrocarbons. Taken from [272] with permission from Elsevier.

XRSS has been shown to be an effective tool for measuring the ratio of isolated double bonds and aromatic sextets [276]. For a series of standard polyaromatic hydrocarbon materials, *Bergmann et.al.* demonstrated direct proportionality between IDB:AS and the FWHM of the 1 s-$\pi^*_{\underline{C}=C}$ (G1, 285 eV) transition (Figure 4.15) [258, 272]. In the fitting presented in Table 4.3, the FWHM of Pyro-Oak-450 and Pyro-Oak-650 were found to be 1.85 eV and 2.10 eV respectively.

By plotting these values onto Figure 4.15a, the IDB:AS ratios for Pyro-Oak-450 and Pyro-Oak-650 were estimated to be approximately 0.7 and 1.0 respectively [258, 272].

TABLE 4.4: Calculated ratio of aromatic carbon type vs FWHM for the 1 s-$\pi^*_{\underline{C}=C}$ peak. Taken from [272] with permission from Elsevier.

| Compound | IDB:AS Ratio | FWHM 1 s-$\pi^*_{\underline{C}=C}$ |
|---|---|---|
| Benzene | 0.0000 | 1.148 |
| Triphenylene | 0.0000 | 1.151 |
| Benzo[e]pyrene | 0.11100 | 1.282 |
| Phenanthrene | 0.16700 | 1.187 |
| Benzo[ghi]perylene | 0.22200 | 1.438 |
| Coronene | 0.33300 | 1.328 |
| 1,2-Benzanthracene | 0.50000 | 1.441 |
| Benzo[c]naphtho[gra]tetracene | 0.55500 | 1.623 |
| Benzo[a]pyrene | 0.66700 | 1.716 |
| Naphthalene | 0.66700 | 1.411 |
| Naphtho[2,3a]pyrene | 1.0000 | 2.123 |
| Anthracene | 1.3330 | 2.502 |
| 2,3-Benzanthracene (tetracene) | 2.0000 | 3.479 |

This suggests an average condensed ring system similar to Napthalene for Pyro-Oak-450 and to Naptho[2,3a]pyrene for Pyro-Oak-650. Through this method, XRSS offers an alternative route to measure aromaticity in complex, disordered carbonaceous materials, including those which are not suitable for $^{13}C$ – NMR . XRS data supports interpreting the NMR data with a model that weighs circularly condensed structures more heavily than linearly condensed structures. This XRSS approach needs further validation, but has been applied for other condensed aromatic systems [276].

## 4.9 Chapter Summary

XRSS is a powerful *bulk* spectroscopy technique capable of investigating disordered carbonaceous materials. Here XRSS has been applied to two complex, biomass-derived, amorphous sustainable carbon systems: hydrothermal and pyrolysis carbon. The hydrothermal carbon, HTC-Oak-250 displays less well-developed aromatic substructure than either Pyro-Oak-450 or Pyro-Oak-650. This chapter demonstrates that pyrolysis carbon is likely to be a continuum of aromatic moieties unlike hydrothermal carbon which exhibits higher local structural disorder. Using the ERKALE DFT code, experimental data were compared with three different molecular structures thought to be present in hydrothermal carbon. Comparison of calculation and experiment indicates that (i) the previous assignment of the $286.6\,\mathrm{eV}$ furan transition

is likely correct, (ii) hydrothermal carbon is primarily built of furan structures linked *via* the $\alpha$-carbons, and (iii) that carboxylic functionality (e.g. levulinic acid) is contained within the bulk hydrothermal carbon structure. Comparison of NEXAFS and XRSS supports the presence of an enriched aromatic layer on the surface of hydrothermal carbon.

Pyrolysis carbons produced at a moderate ($450\,^{\circ}\mathrm{C}$) and a severe ($650\,^{\circ}\mathrm{C}$) pyrolysis temperature were compared using XRSS. XRS spectral fitting suggests that decarboxylation appears to be the dominant mechanism between the two pyrolysis temperatures, and that bulk cellulosic functionality present at $450\,^{\circ}\mathrm{C}$ is removed by $650\,^{\circ}\mathrm{C}$. These finding were also confirmed through a comparison of NEXAFS and XRSS. NEXAFS highlighted a more disordered surface layer in Pyro-Oak-650 with limited oxygenated functionalities, this is in contrast to Pyro-Oak-450, which displays a more oxygenated surface layer. Together the XRSS fitting to the bulk local structure and the more surface-sensitive NEXAFS data suggest that the oxygenated surface layer in Pyro-Oak-450 is removed through decarboxylation reactions during pyrolysis at $650\,^{\circ}\mathrm{C}$. When compared to NEXAFS the three key advantages of XRSS are: (i) bulk sensitivity (ii) absence of spectral saturation due to self-absorption and (iii) increased experimental versatility.

### 4.9.1 Further Work

Comparison of NEXAFS and XRS C *K*-edge spectra offers an exciting route to study differences between surface and bulk carbon functionality. An initial attempt to study these differences using transmission X-ray spectroscopy (STXM) in ancient heritage materials has been performed [257]. However, other modes of NEXAFS spectroscopy (e.g. total electron yield), may produce better spectra with lower artefacts from heterogeneity in the sample. Future comparison of these techniques would likely yield significant results for pyrolysis carbon produced from a series of different biomass for example. Secondly, the key advantage of XRSS is the ability to perform measurements without complex sample environments or preparation required for other bulk techniques (e.g. $^{13}$C – NMR ). Further work is now required to explore systems where XRSS can provide key insight. An example of this would be in hydrothermal carbonisation, where *in-situ* measurements of carbon chemistry have, so far, not been possible.

# Chapter 5

# Reductive Recovery of $Au^{III}$ Chloride by Oak-Derived Pyrolysis Carbon

One of the most widely investigated and successful applications of pyrolysis carbon has been for the recovery of aqueous organic and inorganic species from soils and water [277]. Many studies have focussed on the uptake and kinetics of inorganic species onto pyrolysis carbon. However the mechanisms governing adsorption onto pyrolysis carbon are not well understood. Whilst a range of mechanisms are thought to be important for recovery onto carbons (e.g. ion exchange, physisorption), the reduction of inorganic species onto pyrolysis carbon has been the most commonly cited.

Due to the relatively low redox potential of $[Au^{III}Cl_4]^-$ (+0.8 V against a saturated calomel/-graphite electrode), the reduction of $Au^{III}$ to metallic $Au^0$ onto pyrolysis carbon was selected as a proxy for studying available reduction pathways. This chapter reports a multi-length scale microscopy and spectroscopic approach to understand the pathways enabling reduction of $Au^{III}$ onto oak-derived pyrolysis carbon (Pyro-Oak-650). This chapter demonstrates the capacity of Pyro-Oak-650 for $Au^{III}$ recovery. Reduction occurs onto the carbon surface, forming nanoparticulate $Au^0$ as well as micrometre-sized clusters. The average $Au^0$ particle size is shown to be proportional to the initial $Au^{III}{}_{(aq)}$ concentration. A maximum average $Au^0$ size is reached between $13\,mg\,g^{-1}$ to $26\,mg\,g^{-1}$ gold:char ratio, above this, ultrafine ($< 5\,nm$) Au nanoparticles form. Reduction is primarily driven by naturally occurring mixed $Fe^{II/III}$ oxides within the oak-derived pyrolysis carbon. Secondary reduction sites are proposed to consist of both condensed aromatic and sulfhydryl groups.

## 5.1 Introduction

Pyrolysis carbons may be treated using thermochemical processes (e.g. acid treatment, steam treatment) to produce activated carbons with tailored properties (e.g. ultra-high porosities). Activated carbons have been widely produced and applied in industrial processes since the 1980s [38]. Studies on the production, activation and subsequent performance of activated carbons from biomass such as coconut shell and apricot stones are well documented, with numerous literature reviews and books on the subject [38, 40, 278, 279]. However, in the late 1990s and early 2000s, new techniques and approaches to the study of carbon led to the advent of nano-carbon materials, resulting in the discovery of fullerenes, nanotubes, graphene and, at the micro/macro scale, hydrothermal carbon [280]. Nano-carbon development has led to the addition of a number of novel nano-structured carbon sorbents. More significantly, the nano-carbon age has fostered new development concepts and methodologies for producing materials with novel and controllable architectures and functionality. This revival has led to new approaches towards pyrolysis carbon adsorbents and a re-visiting of previous literature [278]. Modern studies are now beginning to consider the nano-scale structure and function within carbons, and are attempting to produce industrially relevant materials, whilst also complying with the principles of green chemistry and the biorefinery.

Biomass-derived pyrolysis carbons are being reassessed as a low-cost, but highly effective, route for the removal or recovery of pollutants and resources from aqueous media [150, 281–286]. This reassessment is being driven by an iterative process of identifying important mechanisms using modern spectroscopy, then developing 'engineered' carbons to improve their effectiveness. However the mechanisms governing these adsorption studies using pyrolysis carbon are often not reported. This is due to the difficulty of measuring the effects of carbon functionality, inorganic functionality and carbon macroscopic and microscopic structure on adsorption. Whilst some studies have tackled the adsorption mechanisms of inorganic species onto pyrolysis carbon, more work is required [287–289]. This chapter focuses on understanding the potential routes governing the reduction of inorganic species onto pyrolysis carbon before modification. It is hoped that through this understanding, a better approach to engineered carbons can be developed. This section briefly reviews the preparation of engineered

pyrolysis carbons for the recovery of inorganics, including the pathways for reduction of inorganic species onto pyrolysis carbons, before considering the reduction of $Au^{III}$ as a practical application and useful proxy for understanding such pathways.

### 5.1.1 Production of "Engineered Pyrolysis Carbons" - Activation Approaches

Engineered pyrolysis carbons are highly porous carbon materials designed and modified to fulfil a particular purpose or application, in this way they may be considered as activated carbons. Modification of pyrolysis carbons is carried out through either thermal or chemical treatment applied pre-pyrolysis or post-pyrolysis. Figure 5.1 shows a schema for the production of modified pyrolysis carbons. Modifications are generally performed to either: (i) increase porosity of the final carbon or (ii) increase or introduce new functionalities [61, 281].

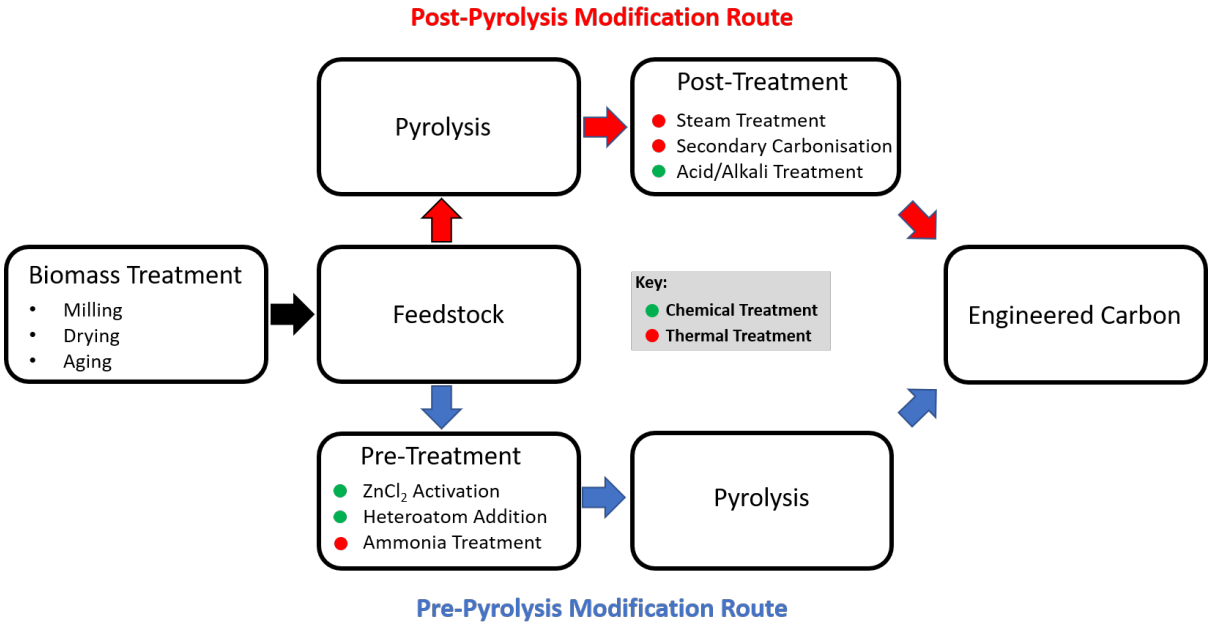


FIGURE 5.1: Schema for the pre/post modification routes to engineered pyrolysis carbons using chemical and thermal treatments.

#### Thermal Modification

Thermal modification is generally performed to develop porosity and increase surface area within the carbon [80]. An initial pyrolysis stage is performed, usually at lower temperatures than an unmodified pyrolysis carbon, before a second stage gasification, performed under oxidising conditions (e.g. by addition of $O_2, CO_2$), is performed.

**Carbonisation** Heat treatment of biomass-derived pyrolysis carbon has been shown to produce a surface that is more basic and hydrophobic because of the removal of oxygenated surface groups. Pyrolysis carbon precursors are typically heated to between 600 °C to 1000 °C [290]. Thermal treatment involves a loss of material, resulting in decreased yields.

**Steam and Carbon Dioxide Treatment** During the secondary thermal treatment stage, oxidising gases such as steam or $CO_2$ may be introduced into the reactor [291]. The introduction of oxidising gases results in the generation of oxygenated carbon functionalities, which are subsequently incorporated into the carbon structure. Surface carbon oxide species have been shown to be of critical importance for binding polar compounds through charged surface functional groups, which helps to immobilise both organic and inorganic onto its surface [292]. Steam and $CO_2$ treatments have traditionally been used to activate carbons for use as sorbents. Like all thermal modification methods, steam and $CO_2$ treatment suffer from "burn-off", reducing carbon yield. However, steam/$CO_2$ treatment provides a higher yield of carbon compared with secondary carbonisation, with low environmental risk and may be performed as a continuous process [293]. The introduction of steam or $CO_2$ during thermal treatment produces a significant increase in sorption capacity [294]. Steam activation results in the volatilisation of bio-oil produced during pyrolysis, increasing macro-porosity [295]. However the process reduces aromaticity in the final carbon, which can reduce adsorbtion performance in some cases [296].

**Templating** A more recent approach to the production of ultra-porous carbon sorbents is templating. Templating may be categorised as either soft or hard. During hard templating, a carbon precursor is soaked into the pore structure of an inorganic sacrificial template. The mixture is pyrolysed at high temperatures, before the template is subsequently removed. Hard-templating has led to the generation of ordered mesoporous carbons, with highly controlled pore size distributions [297]. However, hard templating requires the removal of the inorganic template, using hazardous chemicals such as hydroflouric acid. Soft templating addresses this issue by generating a cooperative assembly of structure-directing agents able to form a lyotropic phase, negating the need for acids to remove an inorganic hard template [298]. Both soft and hard templating allow remarkable control over the porosity and pore sizes of produced carbons, with the expense of more challenging synthesis.

### Chemical Activation & Modification

**Acid & Alkali Treatment** Acid and alkali treatment may be applied pre or post pyrolyis. Acid treatment is performed by refluxing the carbon in strong acids between 25 °C to 120 °C, promoting microporosity and increasing oxygen functionalities at the carbon surface [296, 299]. In the pre-pyrolysis approach, treatment of acids removes latent biopolymers on the carbon precursor surface, as well as removing some inorganic species which may later block pores during pyrolysis [281, 300]. Post-pyrolysis acid treatment may be applied to promote oxygen functionalities at the carbon surface. Alkali modification of biomass-derived carbon precursors typically utilises either KOH or NaOH, and can increase the surface pH as well as increase the available oxygen functionality in the char, but has been shown, under certain conditions, to reduce the porosity of the starting carbon [301]. Both acid and alkali treatment have been shown to increase the adsorption of certain potentially toxic inorganics by two or three times, and have shown changes in the pH behaviour of adsorption [300].

**Heteroatom Functionalisation** The introduction of heteroatoms (i.e. atoms which may replace carbon with cyclic structures) into pyrolysis carbon can induce new functionalities and catalytic sites [302]. Common heteroatoms for introduction into pyrolysis carbons include N, S, or P. Heteroatom functionalisation changes the available surface functional groups of the produced carbon and can yield increased performance in terms of chemo-selective adsorption and total adsorption capacity [303, 304]. Furthermore, the introduction of nitrogen in combination with transition metals (e.g. Fe, Ni), has been shown to be highly effective for catalysis purposes, such as applications within supercapacitors and oxygen reduction reaction catalysts [305]. A post-pyrolysis approach to heteroatom functionalisation is commonly applied to pyrolysis carbons and is performed by soaking either the starting biomass or precursor char in a chemical bath before drying or a further chemical modification step. A good example of this are pyrolysis carbons functionalised with sulphur [302]. Recent work has shown that sulphur doped pyrolysis carbons show a large increase in the remediation of a range of heavy metals from the aqueous environment [302]. The effect of sulphurisation on adsorption performance of pyrolysis carbon is most pronounced on mercury, where adsorption has been shown to occur at an order of magnitude higher than in untreated pyrolysis carbon [306].

**Impregnation** Impregnation is the loading of an inorganic phase onto the surface of the pyrolysis carbon matrix, typically in order to act as a redox-active site for complexation or nucleation. The most common *in-situ* method of preparing impregnated biomass-derived activated carbon is by soaking the precursor biomass in a concentrated solution of the compound desired. The prepared/soaked biomass is then pyrolysed, forming an oxide of the inorganic species on the surface of the char. A good example of this is the preparation of manganese oxide ($MnO_x$) impregnated pyrolysis carbons, which have been shown to increase the adsorption of lead, atrazine, phosphorous and mercury [307, 308]. However, other impregnated systems have also been prepared including calcium modified pyrolysis carbon which showed increased adsorption capacities for P, As and Cr respectively [309]. Another route to the production of activated carbons is by impregnating them with compounds that give the activated-carbon a magnetic quality. It has been shown that by impregnating chars with transition metal oxides with a significant magnetic moment (e.g. Fe, Mn, Co, Ni), it is possible to produce a char with significantly improved adsorption properties as well as being recoverable by magnetic separation [281, 300]. This yields real-world applications for recoverable remediation from the aqueous environment. Independent reports have shown that a magnetic pyrolysis carbon produced by soaking the starting biomass feedstock in concentrated iron chloride solution, results in magnetite formation in one-step [284, 310]. These magnetic pyrolysis carbons have also been shown to be able to increase adsorption capacity for both arsenic and crystal violet which is an organic synthetic dye which is carcinogenic [309, 311]. The work on this area is very rapidly evolving and both [281, 300] give a good review on the current status of chemical modification of pyrolysis carbons.

### 5.1.2 Mechanisms for Inorganic Adsorption onto Pyrolysis Carbon

Pyrolysis carbons have been widely studied and applied to remove potentially toxic inorganic species from the environment and also to recover valuable aqueous resources. The principle mechanisms for the removal of inorganic cations or anions from aqueous solution are thought to be physisorption, precipitation, ion-exchange and redox reactions (Figure 5.2). Other indirect mechanisms for the removal of inorganics onto pyrolysis carbon have also been observed, such as changes in pH or precipitation. Few studies have focused directly on understanding the, often complex, mechanisms that result in the inorganic adsorption from the aqueous environment. This section briefly reviews the main pathways for inorganic adsorption onto pyrolysis carbon as proposed by a series of literature reviews on the subject [277, 281, 292, 312–314]

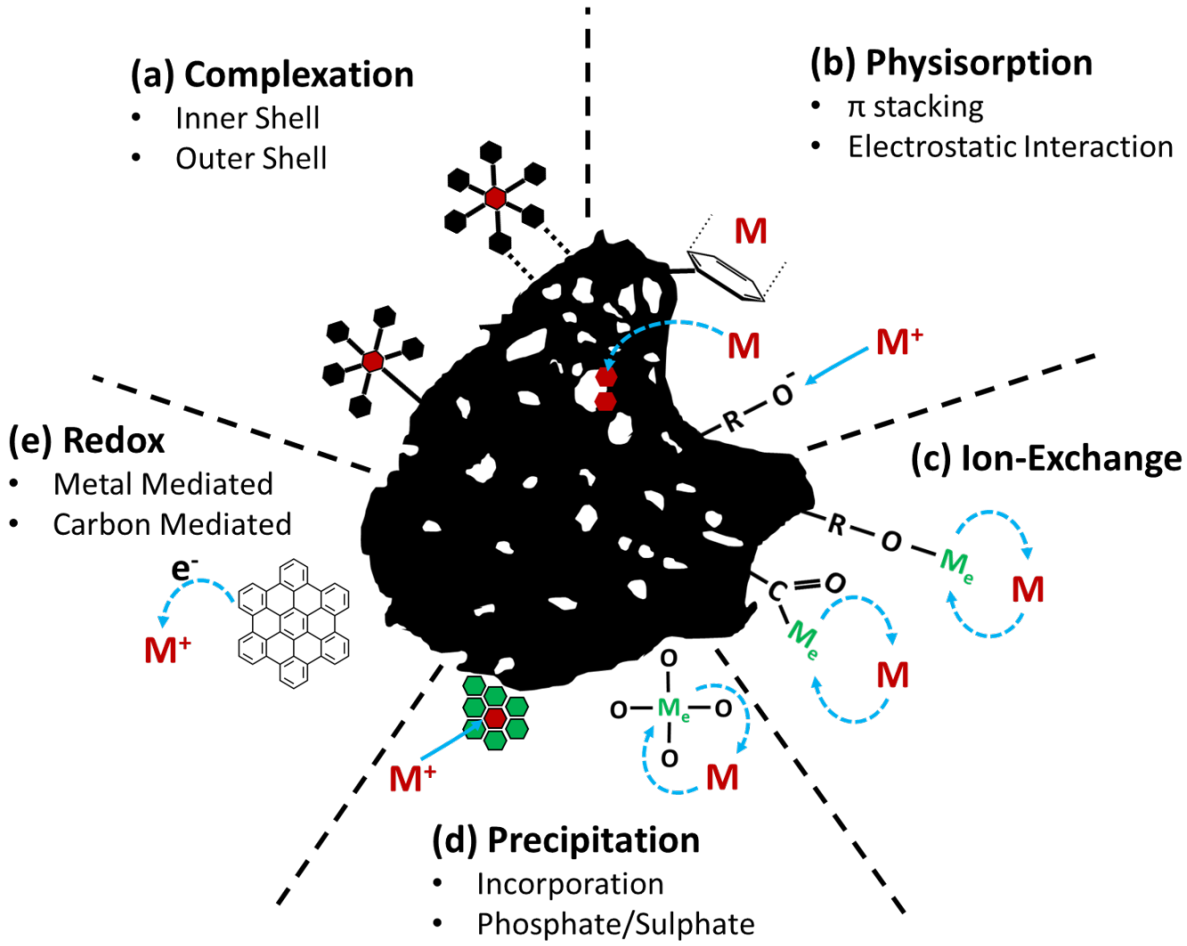


FIGURE 5.2: Diagram summarising the principle mechanisms governing the reduction of aqueous inorganic species onto microporous carbon (shown in black).

**Complexation**

Complexation involves the formation of multi-atom species with specific metal-ligand interactions [314]. Complexes formed on the surface of pyrolysis carbon are separated into inner-sphere and outer-sphere complexes. An inner-sphere complex is formed when no water molecule is present between the metal ion (or ions in binuclear complexes) and the surface functional group to which it is bound (e.g. direct bonding). Inner-sphere complexes can be either monodentate or bidentate, in ligands which donate either a single or double pair of electrons to the metal ion respectively. Examples of monodentate ligands include hydroxide, cyanide and chloride. Outer-sphere complexes form when there is an indirect, coulombic attraction between the metal ligand and a pyrolysis carbon surface species. The inner-sphere complexation of transition metals with partially filled d-orbitals is common, since many 3d species readily form ligands with surface carbon oxides [251]. A good example of this is the adsorption of $Ni^{II}$ and $Zn^{II}$ onto pyrolysis carbon derived from straw and wood, which form inner-sphere complexes with carboxyl and hydroxyl surface species [288]. Similarly, $Cr^{VI}$ was shown to form inner-sphere complexes with surface carbon oxide groups [315]. The adsorption of $Cr^{VI}$ is a useful tool for understanding the complexity of adsorption onto pyrolysis carbons. $Cr^{VI}$ may form an inner-sphere complex, but is also reduced to $Cr^{III}$ on the pyrolysis carbon surface; $Cr^{III}$ species are less soluble than $Cr^{VI}$, and readily precipitate as a solid [287]. The competition between complexation and reduction for $Cr^{VI}$ is likely to be highly dependent on indirect factors such as carbon feedstock, modification or pH [315, 316]. In order to study the complexation of inorganic species onto pyrolysis carbon, surface complexation modelling in tandem with Boehm titration has been widely applied. Surface complexation models are chemical models that can account for the effects of variable chemical conditions, such as pH, on adsorption reactions, and in combination with other spectroscopic techniques (e.g. XANES) can be highly illuminating. Double layer complexation models have been successfully applied to several potentially toxic elements (e.g. Pb, Zn, Cr) and actinide species (e.g. $U^{VI}$) [289, 317]. These models have demonstrated that surface carbon oxide functional groups (carboxyl, phenolic, and lactonic) in pyrolysis carbons are effective in binding inorganic species *via* complexation [312].

**Physisorption**

Physisorption is the physical adsorption of the sorbate by electrostatic/coloumbic interactions between the inorganic species and the pyrolysis carbon surface. These interactions may occur between carbon oxide species, or directly onto the condensed aromatic species of which pyrolysis carbon is principally composed. Physisorption is directly influenced by the total porosity and surface area of the carbon. Pyrolysis carbons produced at higher temperatures offer more condensed aromatic species and a large relative proportion of microporosity ($< 2\,\mathrm{nm}$), making physisorption favoured at higher temperatures [318]. The surfaces of pyrolysis carbons are amphoteric, meaning that they are capable of reacting chemically either as an acid or a base. Currently it is understood that the nature of the pyrolysis carbon-metal interactions is dictated by the ratio between acidic (e.g. carboxyl) and basic functional (e.g. quinonic) groups. The theory underpinning this is called the hard and soft acids and bases (HSAB) concept and is more completely discussed elsewhere [251, 319]. Higher temperature pyrolysis carbons have reduced concentrations of oxygenated functionalities, and are therefore more likely to be dominated by soft Lewis base functional groups. The presence of basic surface functionalities in pyrolysis carbons results in dipole-dipole interactions such as cation-$\pi$ bonding. For example, $Cd^{II}$ has been shown to form $\pi$ bonding with electron-rich domains on aromatic structures in higher temperature pyrolysis carbon [320].

**Ion-Exchange**

Ion-exchange occurs between the aqueous inorganic ion and a correspondingly charged ion on the surface of pyrolysis carbon. Cation exchange stems from the presence of mineral components containing the ions potassium (K), calcium (Ca), magnesium (Mg), and phosphorus (P) in pyrolysis carbon. These cations are thought to readily exchange with inorganic cations in aqueous solution [321]. Measuring the cation exchange in pyrolysis carbons is very challenging, and literature reports often vary for similar materials [322]. A common metric for understanding the relative availability of such cations for exchange is called: the cation exchange capacity (CEC). CEC is relative to the pH at which it is determined, since pH has a large effect on the availability of counter-ion exchange. The higher the value of CEC, the greater the potential for the removal of inorganic species [323]. It has been reported that pyrolysis carbon produced from rice husk showed greater affinity for $Hg^{II}$ and $Zn^{II}$ because of a high CEC

resulting from the high mineral loading from the rice husk [324]. Anion exchange is also possible, where positively charged sites at mineral surfaces develop due to the dissociation of $OH^-$ ions from local acidic groups or by the presence of basic functional groups on the pyrolysis carbon surface. Little is understood about anion exchange capacities of pyrolysis carbons and this is an area for further review [321].

**Precipitation**

The adsorption of inorganic species onto pyrolysis carbon may occur through a reduction in solubility, resulting in the formation of a precipitate on the carbon surface [323]. Precipitation may occur through the reduction or complexation of an inorganic species, or through other indirect mechanisms (e.g. changes in surface pH). An example of precipitation is lead ($Pb^{II}$), which has been shown to form the mineral cerussite and its hydrated form, hydrocerussite, on the surface of pyrolysis carbon after initially forming an outer-sphere complex with surface oxides [133]. In the presence of phosphate minerals on the surface of pyrolysis carbons from dairy manures, $Pb^{II}$ may also precipitate as lead phosphates such as pyromorphite and hydropyromorphite [325]. In pyrolysis carbons derived from high-sulphur feedstocks, the presence of both reduced sulphydryl and sulphate species is common. $Hg^{II}$ is known to precipitate onto the surfaces of such carbons by initial reduction to less soluble $Hg^{I}$ species by sulphur functionalities [326, 327]. The incorporation of aqueous inorganic species into minerals may also occur. This is common with disordered mineral species such as iron-oxyhydroxides which transforms arsenate and chromate species into schwertmannite ($Fe_8O_8(OH)_x(SO_4)_y \cdot nH_2O$), but has not yet been observed in pyrolysis carbons [328].

**Reduction-Oxidation**

The reduction of inorganic aqueous species onto pyrolysis carbon is a common pathway for adsorption [312]. Metallic species in the aqueous environment are typically cations, that are reduced onto the pyrolysis carbon surface *via* three main redox pathways: (i) oxygenated surface functionalities (ii) electron-donating condensed aromatic species and (iii) inorganic surface functionalities (e.g. oxides). Oxygenated carbon functionalities may act as both electron donators or acceptors. Carboxyl and phenolic groups present within pyrolysis carbons present

a significant source of electron donating capacity (EDC) especially in lower temperature carbons (i.e. $< 500\,^{\circ}C$) [321, 329]. A recent study has demonstrated that woody-biomass derived pyrolysis carbon can donate one order of magnitude more electrons than they can accept, potentially favouring surface reduction of inorganic species [330]. However, the same study also points out that the reaction kinetics for the EDC in pyrolysis carbon are relatively sluggish compared to other redox active species present in carbons, which may be favoured. At higher pyrolysis temperatures, carbons tend to become more condensed, as discussed in Section 4.8. This condensation leads to the formation of highly conjugated $\pi$-electron systems and basic surface oxide functional groups (e.g. quinone / hydroquinone moieties) as observed by NEXAFS spectroscopy [188, 271]. These species have been shown to provide a significant electron accepting capacity (EAC) in higher temperature pyrolysis carbons [329]. In either case, pyrolysis carbon presents a significant concentration of 'electron-shuttling' functionalities to aqueous inorganic species which are likely to play a significant role in redox reactions. To the author's knowledge, no direct experimental evidence for the reduction of inorganic aqueous species by organic pyrolysis carbon functionality has been observed. However, the ready reduction of $Cr^{VI}$ to $Cr^{III}$ on pyrolysis carbon has long been associated with surface electron donating carbon oxide functionalities and FT-IR results by *Xu et.al.* suggest that lactone functional groups may be one route for Cr reduction [331]. As well as its organic chemistry, pyrolysis carbon from biomass contains a wide variety of naturally-occurring mineral functionalities and oxides which offer a significant redox potential [312]. In particular, manganese and iron oxide impregnation of pyrolysis carbons has been used to increase the adsorption capacities [312, 332]. Increased adsorption due to the addition of metal oxide species is thought to be due to their acting as electron donors.

### 5.1.3 Motivations for Studying Aqueous Gold Recovery

#### Mechanistic Insights

Despite many publications investigating the adsorption of metallic species onto the surface of pyrolysis carbon, the mechanisms governing adsorption are not well understood. Studies typically focus on the adsorption kinetics and maximum recovery values of pyrolysis carbon rather than the mechanisms governing adsorption. In particular, the reduction and redox chemistry of pyrolysis has not yet been fully explored. Studies on the organic species deemed likely to

act as a source of EDC have made significant progress, but are yet to define clear species or mechanisms for how reduction of inorganic species occurs [329]. Even less is known about mechanisms governing metal oxide species which may act as electron donors on pyrolysis carbon. This is despite evidence that iron-oxide modified pyrolysis carbon is highly redox-active and effective in its use as a sorbent for toxic elements (e.g. As, Cd) amongst a wide range of other applications [61, 332, 333].

As a metal, gold is unreactive in water and over a a wide pH range. Under very acidic conditions and/or under oxidising conditions gold may either form the trivalent gold ($Au^{III}$ ) or monovalent gold ($Au^{I}$ ) species. However, gold is rapidly oxidised to $Au^{III}$ rather than monovalent gold because of the low reduction potential of the trivalent species [334]. Gold may form complexes with both cyanide (e.g. $CN^-$, $SCN^-$) and halide (e.g. $Cl^-$, $Br^-$, $I^-$) species. Gold chloride is able to form both the monovalent ($[AuCl_2]^-$) and the trivalent ($[AuCl_2]^-$) chloride complex, however the trivalent species is more common [334]. The key benefit for the use of gold chloride for studying the reduction mechanisms at play during inorganic reduction onto pyrolysis carbon is the low reduction potentials of both the trivalent and monovalent gold chloride species (Equations. 5.1 and 5.2).

$$AuCl_2^- + e^- \rightleftharpoons Au + 2\,Cl^-; \qquad E^0 = 1.113\,V \tag{5.1}$$

$$AuCl_4^- + 3\,e^- \rightleftharpoons Au + 4\,Cl^-; \qquad E^0 = 0.994\,V \tag{5.2}$$

The low redox potential of gold chloride species results in a simple reduction onto the surface of pyrolysis carbon. Previous studies have shown that the reduction of gold chloride onto pyrolsyis carbon occurs readily, forming metallic gold on the surface of the carbon [335–338]. However, an understanding of the reduction mechanisms governing gold reduction onto activated carbon is not currently available [339].

**Metallurgical Importance**

To date, the majority of gold enters the market from mining, rather than from recycled sources. The demand for gold is increasing; the majority of gold is used for either financial investment and the production of jewellery (Figure 5.3a). The increasing proportion of gold used in

technology and electronic goods is also of cause for concern, since the time between use and disposal is much shorter than for the other applications of metallic gold.

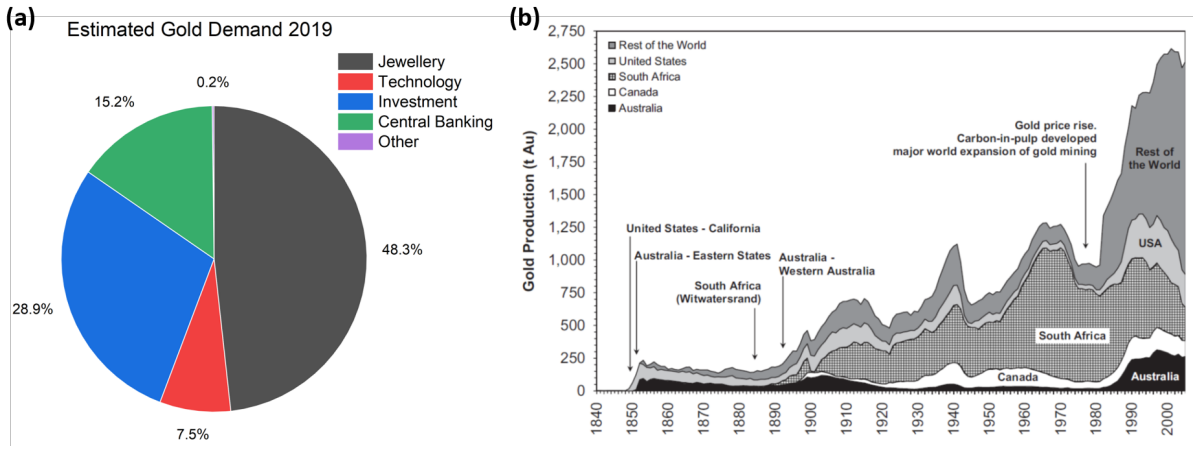


FIGURE 5.3: (a) Gold in 2019 as a percentage of total demand: 4388 tonnes. Sources: ICE Benchmark Administration, Metals Focus, Refinitiv GFMS, World Gold Council. Data harvested December 2020. (b) World gold production 1840-2005. Taken from [340] with permission from Elsevier.

The increasing value of gold in the markets, combined with sustained value for use in jewellery and a growing use in consumer electronics, has caused a significant increase in gold demand and gold production (Figure 5.3b). Gold is a finite and non-renewable resource and long-term gold production trends include declining ore grades, resulting in increasing solid wastes (tailings, waste rock) and, environmentally damaging, open cut mining. Recovery of gold from mining tailings is performed industrially using the leaching process. A leaching agent is used to form a soluble gold complex which is subsequently recovered. Cyanides and thiocyanides have traditionally been used as the leaching agent, since the formed gold cyanide complex ($[Au(CN)_2]^-$) is relatively stable, effective for gold dissolution and is low cost [334]. However cyanidation, whilst effective, is controversial due to the repeated accidental release of potentially toxic elements, as well as toxic cyanide waste into the environment [341, 342]. Alternative approaches and leaching agents have been widely researched. There are now a large number of technological approaches for the recovery of gold from secondary sources [342, 343]. These include pyrolysis of ground electronic waste, hydro-technologies, biological recovery using hyper-accumulating species and a wide variety of novel non-cyanide leaching agents. Alternative leaching agents include thiourea, thiosulphate and halides, which all form stable gold complexes in aqueous solution [344]. The use of halide species for recovery of gold is re-emerging as an alternative to cyanide for the leaching of gold from ore. Furthermore,

the recovery of gold from the leachate is typically performed using (steam) activated pyrolysis carbons through the carbon in pulp (CIP) and carbon in leachate (CIL) processes [345]. Therefore, understanding the mechanisms governing the reduction of $[Au^{I}Cl_2]^-$ complexes onto pyrolysis carbon is extremely relevant for future gold recovery techniques.

### 5.1.4 Halide Leaching and Pyrolysis Carbon Recovery

#### Halide Leaching

Hydrochloric acid and/or Aqua Regia are common in both industrial gold recovery from mine tailings, but also in the artisinal recovery of gold from electronic wastes. The use of HCl for recovery offers an economic fast reaction rate, which is not common for other approaches such as biological recovery or leaching using thiourea or thiosulphate [343]. In chloride gold leaching, gold may form aqueous monovalent cyanide $[Au^{I}(CN)_2]^-$ and chloride $[Au^{I}Cl_2]^-$ complexes as well as trivalent complexes (e.g. $[Au^{III}Cl_4]^-$). EXAFS studies on gold chloride have shown that the stable aqueous state of gold chloride various with pH [346]. At pH 6, aqueous gold chloride remains in its $Au^{III}$ state as the planar $[Au^{III}Cl_4]^-$ anion, but above pH 6 $Au^{III}$ may also coordinate with oxygen species to form mixed Cl, O square-planar complexes (e.g. $[Au^{III}(O,Cl)_x]$) [346, 347]. Gold chloride leaching is economical and widely practised, but is also more difficult to apply than cyanide leaching. This difficulty is due to corrosion of ducting by the acidic halide species and hazards resulting from the potential production of toxic chlorine gas. However, recent work has show that chloride gold leaching could be combined with ozone ($O_3$) or hypochlorite to reduce the concentration of required HCl making the process potentially less hazardous [348, 349].

#### Recovery of Gold from Leachate

**Non-Carbon Methods** Recovery after lixiviation may be achieved *via* several processes, such as: cementation, solvent extraction and through ion-exchange resins or biosorpents. Cementation, commonly known as the "Merille-Crowe process" involves adding powdered Zn to the leachate solution, reducing gold to $Au^0$ and forming $[Zn(CN)_4]^{2-}$ ions. Cementation was widely used prior to the 1980s, however the use of activated carbon became more widespread due to its lower cost and faster recovery times [334]. Another option is solvent extraction.

Solvent extraction is not widely practised, however organophosphorous species (e.g. tetrabutylphosphorous) may be used to compete with gold cyanide and gold chloride complexes, freeing the gold as $Au^0$ . Recent studies into the use of solvent extraction for recovery of gold from chloride solutions have shown the technique to be highly effective for gold recovery, and also highly selective at low concentrations [350, 351]. Similarly ion-exchange resins, which typically use organosulphur type resins are highly selective for gold recovery from leachate. Recovery occurs *via* the formation of intermediate $Au^I$ -SH complexes. While the use of traditional sorbents and ion-exchange resins is effective due to the ease of reduction of $Au^{III}$ to $Au^0$ , there are concerns regarding the leaching of toxic organic and organo-sulphur species from ion-exchange resins, as well as the sustainability and effectiveness of such sorbents [342]. Biosorption and phyto-recovery are also potential, low-yield alternatives to hydrometallurgical processes. X-ray absorption spectroscopy (XAS) was used to determine that $Au^{III}$ was reduced to form metallic gold colloids on Alfalfa biomass, which varied in size depending on the pH of the initial solution [352]. Other studies on the adsorption of $Au^{III}$ onto biomass include egg-shells, collagen and chitosan [353].

**Recovery using Pyrolysis Carbons** Due to their low-cost and effectiveness, lignocellulosic derived pyrolysis carbons have emerged as the primary sorbent for gold (and other precious metals) from leachate solutions. However, the nature of the species adsorbed on the carbon surface has proved difficult to resolve [38]. The $[Au^{III}Cl_4]^-$ anion is readily reduced to $Au^0$ on the surface of pyrolysis carbons, forming large grains of metallic gold on the outer surface of pyrolysis carbon. Studies have reported on sorption capacities [336, 338, 354, 355] and kinetics [335, 356] of pyrolysis carbon in dilute gold chloride systems under different chemical conditions, temperatures and pHs. These studies have shown that the adsorption of gold chloride onto pyrolysis carbon follows a first order rate and is highly dependent on the mass-transfer of the aqueous leachate into the carbon pore matrix [338]. However the mechanisms governing the adsorption of $Au^{III}$ onto pyrolysis carbon are not well understood. Studies from the 1980s and 1990s focussed on cation exchange, resulting in stable $[Au^{III}Cl_4]^-$ complexes of Ca, Mg or K on the surface of the carbons. *McDougall and Hancock* emphasised that the reduction of gold chloride ($[Au^{III}Cl_4]^-$) onto activated pyrolysis carbon was simply due to the high electron donating capacities of activated carbons in comparison with the relatively low redox potential

of $[Au^{III}Cl_4]^-$ (+0.8 V to 1.2 V against a saturated calomel/graphite electrode) [357]. The authors of the study do not suggest any species likely to cause this reduction, but the electron donating capacities of other non-activated carbons have been shown to be remarkably high and often underestimated in the past [330]. Surface carbon species responsible for electron donation in lignocellulose derived pyrolysis carbons are understood to be primarily quinone species or polyaromatic condensed carbon species. Some indirect evidence for these species playing a role during $Au^{III}$ chloride reduction onto activated carbon was presented using XPS [338]. However, beyond this, no experimental evidence for the reduction mechanisms governing gold chloride reduction onto carbons are known.

## 5.2 Aim

In this study, wet chemical batch sorption experiments have been integrated with a multi-length scale microscopy and spectroscopic approach to elucidate the recovery mechanisms of gold by a woody biomass-derived pyrolysis carbon. Gold uptake experiments followed by transmission electron microscopy (TEM), X-ray absorption near edge spectroscopy (XANES) at the Fe, S, and Au ionisation edges and extended X-ray absorption fine structure (EXAFS) measurements at the Au $L_3$-edge have been used to highlight the formation mechanism and size distribution of nanoparticulate gold recovered by the pyrolysis carbon. X-ray microtomography ($X\mu T$ ) illustrates that agglomerations of gold nanoparticles form micrometre-scale $Au^0$ particles at the outer surface of the pyrolysis carbon. High resolution scanning transmission electron microscopy (HR-STEM) with dual electron energy loss spectroscopy (EELS) highlights the role of naturally occurring, redox-active iron species within the pyrolysis carbon in promoting formation of nanoparticulate gold. EXAFS analysis of the reduced gold atom coordination number suggests that nanoparticulate gold, forms directly on the pyrolysis carbon matrix, and only dominates at an initial aqueous gold loading above 100 ppm ($13\,mg\,g^{-1}$). These insights into the reaction mechanisms occurring in the recovery of gold by pyrolysis carbon should lead to an optimised recovery pathway, possibly resulting in more environmentally and economically sustainable processes.

## 5.3 Experimental Techniques

### 5.3.1 Batch Uptake Experiments

$150\,\mathrm{mg}$ of Pyro-Oak-650 (see Section 4.3.2) was suspended in a pH 6 acetic acid buffer solution in polypropylene centrifuge tubes. The buffer-pyrolysis carbon suspension was left to equilibriate for 1 hour before being brought to a final pH of $6.0 \pm 0.4$ (2 SD, n=30) using small volumes of 1 M sodium hydroxide and acetic acid in order to correct for basic inorganic surface functional groups present on the pyrolysis carbon. The correction of surface pH is conventional for pyrolysis carbon uptake experiments [358]. Blank samples containing only the buffered gold solution (described below) across the measured concentration range, were prepared according to the same protocol. The acetic acid buffer was found to maintain the model $Au^{III}$ chloride standard in solution at pH 6 at all concentrations. As discussed, at pH 6, aqueous gold chloride remains in its $Au^{III}$ state as the planar $[Au^{III}Cl_4]^-$ anion [346]. Uptake experiments were carried out in triplicate, with acid-washed glassware (2 %v/v $HNO_3$) using ultrapure water ($> 18\,\mathrm{M\Omega\,cm}$). After the pyrolysis carbon suspension had stabilised at pH 6, the volume was made up to $20\,\mathrm{mL}$ (solid-to-solution ratio: $7.5\,\mathrm{g\,L^{-1}}$) and brought to the desired Au concentration (10 – 1000 ppm) using a 10,000 ppm gold chloride stock solution (Alfa Aesar). Uptake was performed on a lateral shaker at 150 rpm for 6 hours, with regular pH checks at thirty-minute intervals during the first $3\,\mathrm{h}$. No significant changes in pH were observed during uptake. After equilibration, samples were centrifuged for 15 min at 3000 g. The supernatant was filtered through a $0.2\,\mu\mathrm{m}$ cellulose acetate syringe filter, then acidified with 2 %v/v $HNO_3$ for analysis. The solid phase retained in the vials after centrifugation was washed twice with $10\,\mathrm{mL}$ of ultrapure water, then dried overnight at $40\,^\circ\mathrm{C}$. $Au^{III}$ uptake was determined by difference using a flame atomic absorption spectrophotometer (AAS). Standard additions of both the supernatant samples and reagent blanks were performed using an external standard (1000 ppm Au, Alfa Aesar). Further information regarding the batch uptake experiment, and issues with gold reduction in a Good's buffer can be found in Appendix C.

### 5.3.2 Inorganic Analysis

The concentrations of certain inorganic constituents (Al, Fe, Mg, Mn) in the starting biomass were determined by flame AAS. Dry oak biomass used for the preparation of Pyro-Oak-650

was cryogenically milled (Retsch, UK), then digested in $10\,\mathrm{ml}$ 70%, trace metal grade $HNO_3$ (Fisher Scientific, UK) using a microwave digestor. The resulting aliquot was diluted gravimetrically using ultrapure water to a total volume of $50\,\mathrm{ml}$. The flame AA spectrometer (Varian FS-240) was fitted with a semi-automatic sample dilution system (SIPS-20, Varian). The AAS was calibrated using ICP-MS standard solutions (Alfa Aesar) to element-specific calibration ranges (Mn: 0-5 ppm, Fe: 0-15 ppm, Mg: 0-20 ppm, Al: 0-200 ppm). Measurements were performed in triplicate using an air/acetylene flame, except for Al, where a nitrous oxide/acetylene flame was used to reduce possible matrix effects.

### 5.3.3 Electron Imaging and Spectroscopy

Samples for TEM were prepared by dispersing the pyrolysis carbon in ethanol *via* sonication, before drop casting onto amorphous carbon holey support films on copper grids (Agar, UK) and mounting onto a double-tilt analytical TEM holder (FEI, UK). HAADF and EDX measurements were performed using an FEI Titan$^3$ Themis G2 scanning transmission electron microscope (S/TEM) operating at $300\,\mathrm{kV}$ with an FEI Super-X energy dispersive X-ray EDX system. The same microscope was also fitted with a monochromator ($\Delta$E ~$0.4\,\mathrm{eV}$) and a Gatan Quantum 965 ER energy filter to collect dual EEL spectroscopy measurements at the Fe $L_{3,2}$ edges and zero loss (elastic) peak. Dual EEL spectroscopy allows for simultaneous collection of core and elastic electron loss spectra for absolute energy-loss calibration.

STEM-EDX mapping was performed on a small isolated region adjacent to a gold nanoparticle. On a pixel basis, the signal to noise ratio for STEM-EDX data is not sufficient to produce an accurate EDX spectrum with sufficient statistical confidence. Therefore, pixel-wise data were rebinned by a factor of four, reducing spectral resolution from $5\,\mathrm{eV}$ to $20\,\mathrm{eV}$. Principal component analysis was performed to de-noise the EDX spectrum. Hyperspy, a python-based software for hyperspectral data analysis was used to perform the principal component analysis through the built-in "decomposition" method [359]. Principal component analysis finds linear combinations of components in the raw data which best match the co-variance matrix. Using the de-noised EDX spectrum, peak intensity values were extracted.

### 5.3.4 X-ray Absorption Spectroscopy

**APS - 10-BM** Gold $L_3$-edge EXAFS was acquired at sector 10 of the Advanced Photon Source (APS) using an ion-chamber in standard transmission geometry. Samples of Pyro-Oak-650 after the batch uptake experiments were prepared by mounting cryogenically-milled powder (sieved through $100\,\mu m$) in a slotted, thin Teflon holder sealed with kapton film. Rejection of higher-order beam harmonics was performed by de-tuning the cryogenically-cooled, Si(111) monochromator by 50%. No harmonic rejection mirror is available at 10-BM [360]. Energy calibration was performed using a standard gold foil in the reference position of the standard transmission geometry. Four scans were averaged in order to produce the presented data.

**APS - 20-BM** Iron *K*-edge XANES were acquired at beamline 20-BM using an ion-chamber in standard transmission geometry. 20-BM utilises a cryogenically cooled Si (111) double-crystal monochromator and a toroidal focusing mirror, which was used to reject higher-order harmonics of the desired energy. Transmission mode spectra were collected using the standard geometry, with a metallic iron foil collected simultaneously as a reference. Samples were prepared as cryogenically milled powder (passed $100\,\mu m$ sieve) spread thinly onto Kapton tape. Three scans were averaged in order to produce the presented data. XANES data were treated using the XAS-viewer application as part of Larch (v0.9.46) [361]. Pre-edge subtraction and unit normalisation was performed using the MBACK function [362]. Energy calibration was performed against the first maximum of the derivative spectrum of an iron foil standard.

**APS - 13-IDE** Sulphur *K*-edge XANES spectra for Pyro-Oak-650 were acquired at beamline 13-ID-E using an energy-dispersive Vortex ME4 silicon drift diode array detector in fluorescence mode. Samples of Pyro-Oak-650 were prepared by mounting powder onto sulphur-free tape. Harmonic rejection was performed by using a Si mirror. XANES measurements were performed in a He atmosphere bag. Five scans were averaged to produce the presented spectra. Commercially synthesised sulphur compounds (cysteic acid, pyrite and cysteine) were used as reference standards. XANES data were treated using the XAS-viewer application as part of Larch (v0.9.46). Pre-edge subtraction and unit normalisation was performed using the MBACK function [362]. Energy calibration was performed by setting the maximum of the white line of the spectrum for a sulphate tape to $2480\,eV$.

## 5.4 Reduction of $Au^{III}$ and Microscopic Distribution of $Au^0$

### 5.4.1 Uptake Isotherm

An uptake isotherm was collected at pH 6 in order to determine the uptake capacity of Pyro-Oak-650 for aqueous $Au^{III}$ chloride (Figure 5.4). The concentration of $Au^0$ in the pyrolysis carbon phase increased directly with the initial aqueous gold concentration. Fitting these data using a Langmuir function suggested that the maximum projected uptake of the char was $391 \pm 25\,\mathrm{mg\,g^{-1}}$. This result and the Langmuir fitting approach used is similar to those of other pyrolysis carbon kinetics studies with $Au^{III}$ [354]. Further details regarding the uptake experiment and subsequent Langmuir fit may be found in Appendix C.

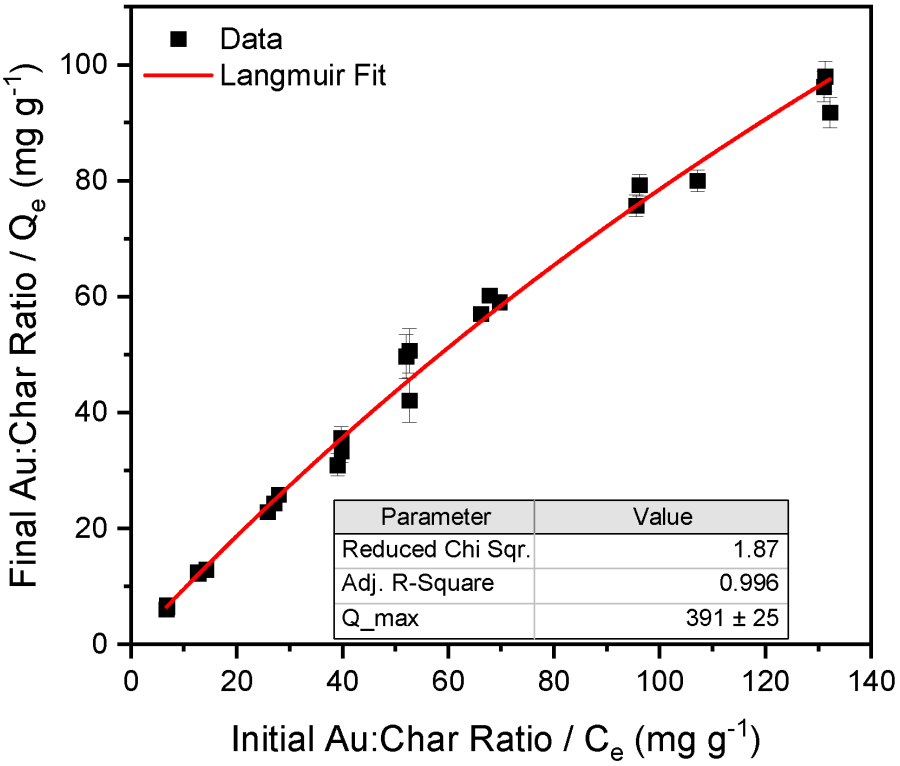


FIGURE 5.4: Adsorption isotherm for $[Au^{III}Cl_4]^-$ adsorption onto Pyro-Oak-650 at pH 6.

### 5.4.2 Identification and Distribution of nAu

As previously discussed, the reduction of $Au^{III}$ chloride to metallic gold onto pyrolysis carbon has been well established, despite no complete understanding of the reduction mechanism [335, 357]. TEM imaging and electron diffraction demonstrate the complete reduction of aqueous $Au^{III}$ to nanoparticulate $Au^0$ (nAu) at all initial gold concentrations (Figure 5.5).

The formed nanoparticulate, colloidal gold (nAu) was polycrystalline, with the characteristic lattice spacing for Au {1 1 1} (0.235 nm) being observed. The sizes of observed nAu varied between sub-10 nm to micrometre sized metallic gold.

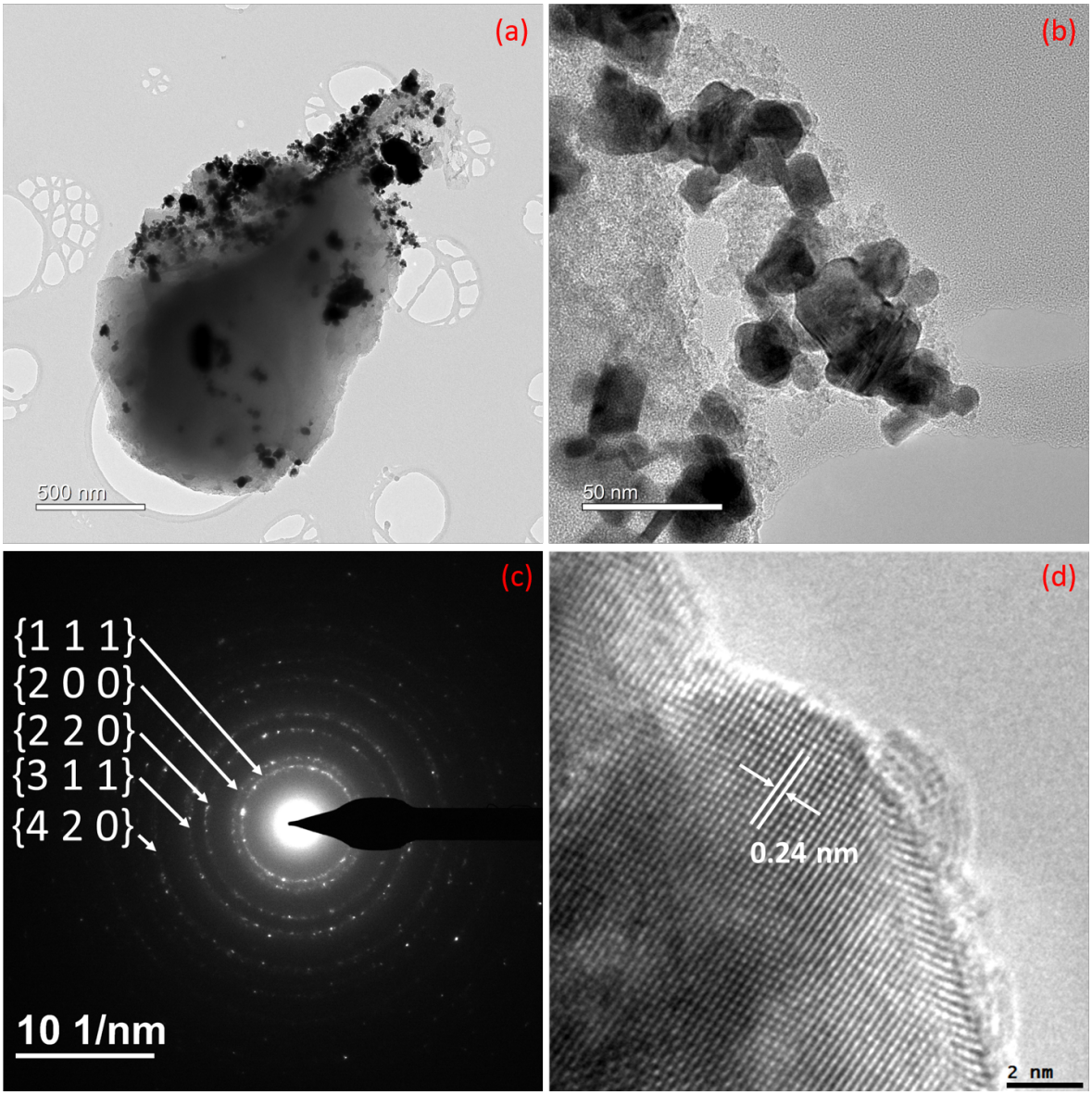


FIGURE 5.5: (a) Bright field TEM image of a Pyro-Oak-650 particle with formed nAu both internally and externally. (b) Zoomed bright field TEM image of image (a) showing faceted $Au^0$ colloids. (c) SAED pattern which is indexed as metallic gold. (d) High-resolution image of the gold lattice with a fringe spacing of 0.24 nm - identified as the gold {1 1 1} spacing (0.235 nm).

The large variation in size of reduced $Au^0$ was apparent from TEM imaging. TEM studies are not well suited for measuring large clusters of heterogeneous inorganic materials. Furthermore, the preparation of the sample for TEM imaging disturbed the original microstructure of Pyro-Oak-650. Pyrolysis carbon microstructure is well-known to affect the diffusive transport,

and hence adsorption pathways, of aqueous species [248, 363]. However, the distribution of the adsorbate is rarely discussed. Therefore X$\mu$T was used here to non-destructively observe the location and distribution of $Au^0$ at the micrometre-scale. Synchrotron X-ray microtomography has been applied to pyrolysis carbons, and is well-suited for measuring a wide range of macroporous structure, which is challenging to interpret using other techniques (e.g. 2-D electron microscopy, SEM, BET) [229, 364]. Figure 5.6a shows a reconstructed slice from an intact sample of Pyro-Oak-650 after gold uptake at an initial aqueous gold concentration of 1000 ppm ($133\,\mathrm{mg\,g^{-1}}$).

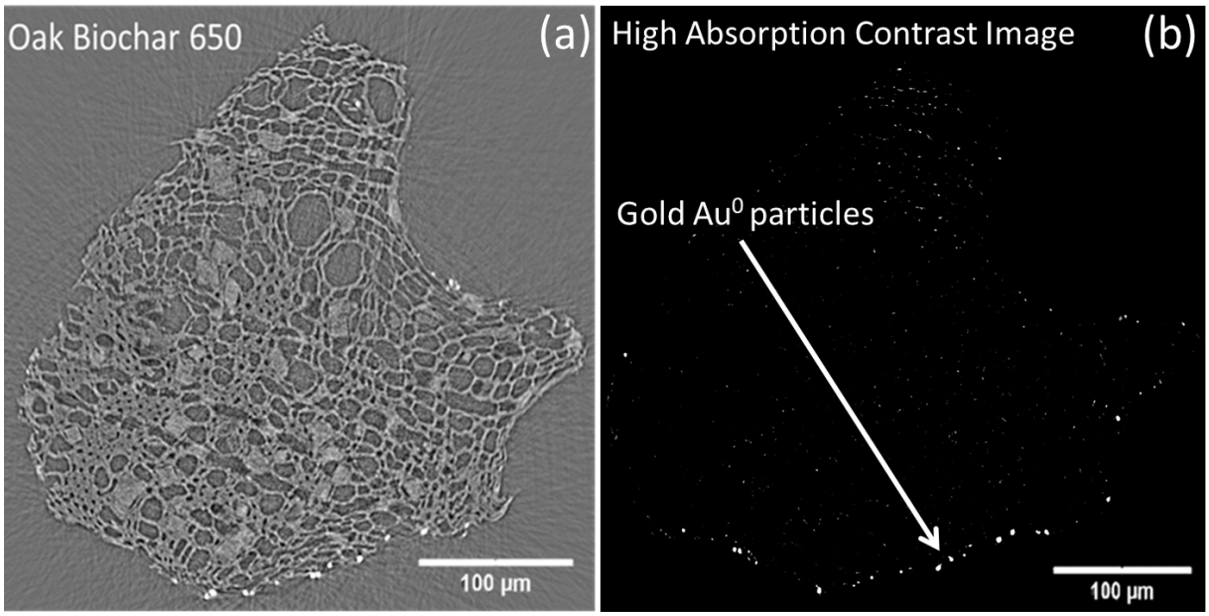


FIGURE 5.6: X-ray micro-tomogram of Pyro-Oak-650 after gold uptake at 1000 ppm. (a) is an absorption contrast tomogram collected at an energy above the Au $L_2$-edge at $19\,\mathrm{keV}$ and (b) the same tomogram slice after subtraction of a tomogram collected at an energy below the $L_2$-edge and digitally modified for enhanced contrast.

In order to investigate the distribution of the reduced $Au^0$ species, chemical contrast was given to gold by subtraction of tomograms collected $40\,\mathrm{eV}$ above and below the $L_2$-edge. By subtraction of the tomograms collected above and below the $L_2$-edge, chemical contrast is given to areas containing gold. This method of difference micro-tomography has been discussed and performed elsewhere [365]. The result of this subtraction is shown in Figure 5.6b after contrast enhancement. Whilst gold clusters are clearly visible in the image without contrast enhancement, Figure 5.6b has been digitally altered to enhance bright spots (white) on the printed page. As in the non-chemical absorption-contrast image $Au^0$ particles, several micrometres

in size, primarily form at the outer surface of the pyrolysis carbon. However, with added chemical contrast, much smaller gold particles, such as those observed in Figure 5.5b, are seen deeper within the pyrolysis carbon matrix with sizes on the order of the pixel resolution of the detector ($0.325\,\mu m$). The concomitant reduction in average size of gold particles with respect to the distance from the outer surface of the pyrolysis carbon is likely due to interpore diffusion of aqueous gold into the pyrolysis carbon matrix. Several studies have highlighted the importance of physical structure in the reduction of aqueous metals onto pyrolysis carbon [312, 366]. Knowledge of the underlying mechanisms of fluid-flow through the pyrolysis carbon matrix is nascent, but recent studies suggest that fluid-flow through macropores is crucial for the transport of aqueous reactants to active-sites [367]. This suggests that the size of the formed gold particles is dependent on how the aqueous $Au^{III}$ solution diffuses deeper into the pyrolysis carbon matrix, where further redox sites would be available after redox sites on the surface are spent.

## 5.5 Potential Reduction Pathways

### 5.5.1 Condensed Aromatic Species

As discussed in Section 5.1.2, surface carbon oxides and condensed aromatic species within pyrolysis carbon offer a significant source of EDC [329]. As shown in Chapter 4, Pyro-Oak-650 does not contain a significant proportion of bulk oxygenated functionality. In turn, this makes the likelihood of carboxyl or phenolic groups acting as significant sources of EDC quite low. The low concentrations of oxygenated surface functionalities are also demonstrated in the surface NEXAFS spectra for Pyro-Oak-650 in comparison to Pyro-Oak-450 (Figure 4.9). However, Pyro-Oak-650 is highly aromatic and the C *K*-edge XRSS demonstrates significant aromtic ordering and the presence of condensed aromatic phases (Section 4.8). It is likely that polyaromatic species and quinone-like functionalities within Pyro-Oak-650 play a significant role during the direct reduction of aqueous gold onto a pyrolysis carbon surface. In a similar study by *Wojnicki et.al.*, it was suggested that phenolic species are primarily responsible for the reduction of aqueous $Au^{III}$ *via* a coupled redox transformation with phenolic electron donating species [338]. However, direct experimental evidence for such redox interactions within pyrolysis carbon have not yet been reported.

### 5.5.2 Sulphur Species

Heteroatomic functionalities provide pathways for both complexation and redox in pyrolysis carbon [146]. Of the heteroatomic species present in pyrolysis carbon, nitrogen and sulphur species appear to be the most active [368]. Pyrolysis carbons modified through chemical addition of sulphur species are commonly reported as having high electron donating capacities, and have been shown to reduce potentially toxic elements (e.g. Cd) to less-toxic sulphides [369]. However, pyrolysis carbon sulphur chemistry has been only sparingly investigated despite its important role in active redox functionality. A study on pyrolysis carbon sulphur speciation by *Cheah et.al.* found the presence of both sulfhydryl and sulphate groups present within pyrolysis carbon derived from Oak wood and corn stover [370].

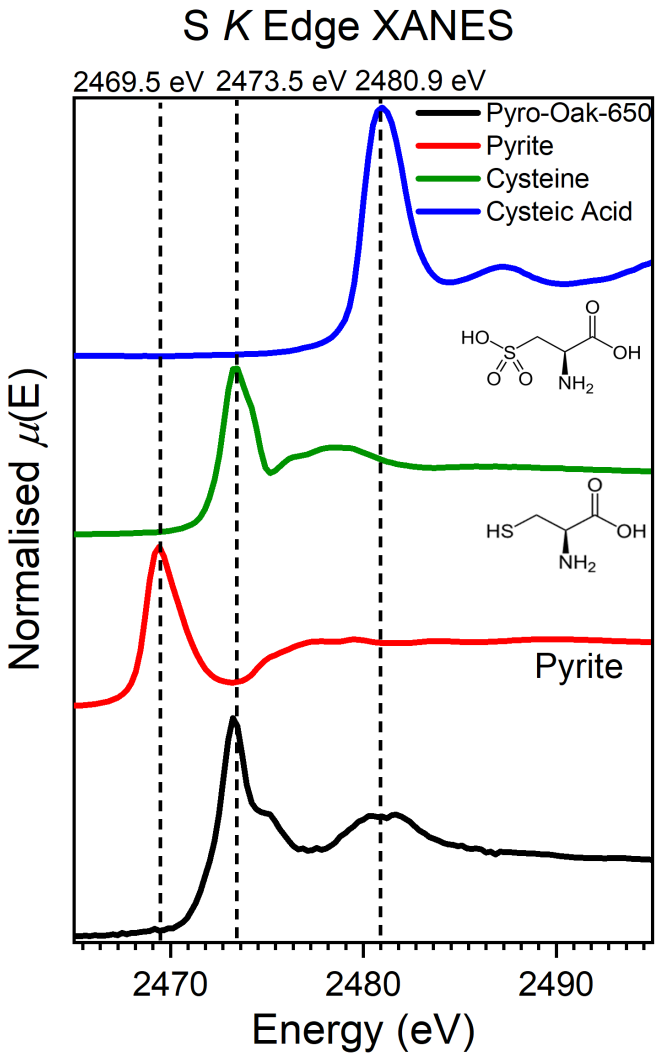


FIGURE 5.7: Sulphur *K*-edge XANES spectra of Pyro-Oak-650 with chemical state reference standards

Figure 5.7 shows the S *K*-edge XANES for Pyro-Oak-650. Principal component analysis demonstrates that Pyro-Oak-650 is primarily composed of reduced sulfhydryl functionality, with only a limited contribution from sulphate groups (< 10%). The lower concentration of sulphate groups in Pyro-Oak-650, when compared to the aforementioned study by *Cheah et.al.*, may be due to the formation of sulphates by ingress of oxygen during pyrolysis, or by slow oxidation of reduced sulphur groups in the pyrolysis carbon. Regardless, the significant presence of sulfhydryl groups in Pyro-Oak-650 offers an intermediate reduction pathway for the formation of nanoparticulate $Au^0$ *via* an initial $Au^I-S$ reduction step. The reduction of aqueous $Au^{III}-Cl$ to $Au^I-S$ has been observed for algal biomass, where sulfhydryl sites were found to be the principal reduction pathway [371]. In this case, Au $L_3$-edge EXAFS of Pyro-Oak-650 post-uptake (discussed later in Section 5.7) provides no evidence for $Au^I-S$ species; instead $Au^{III}$ was completely reduced to $Au^0$ .

### 5.5.3 Iron Oxides

Transition metals and their oxides have been shown to act as highly effective redox agents within pyrolysis carbon. Increasing the concentration of iron oxides within pyrolysis carbon by chemical impregnation has been shown to dramatically increase the ability of pyrolysis carbon to recover emerging contaminants, as well as provide magnetic properties for more straightforward recovery [60, 286, 310]. Furthermore, recent work has shown that chemical impregnation using iron precursors may yield significant improvements in pyrolysis gas yields and gas energy content, lowering the potential energy costs of scaled-up production [372]. Many lignocellulosic feedstocks are naturally high in micronutrients, including iron, without the need for doping or further modification. In these feedstocks, transition metal oxides are formed from naturally occurring iron within the biomass feedstock [301]. During pyrolysis, naturally occurring iron is likely reduced to magnetite, as observed for Fe-modified pyrolysis carbons [372]. The ratio of $Fe^{II}$:$Fe^{III}$ in the formed magnetite, has been found to have a direct effect on the rate and extent of reduction of other aqueous metal species (e.g. $Hg^{II}$) onto pyrolysis carbon sorbents [373]. Here, flame AAS was performed to determine the concentrations of iron, as well as some other relevant oxide-forming metals in the oak biomass used to produce Pyro-Oak-650.

TABLE 5.1: Major Inorganics present within Oak Wood as determined by flame AAS. Estimated concentration of inorganic concentration in Pyro-Oak-650 by percentage yield.

| **Element** | **Conc. in Biomass** ($\mathrm{mg\,kg^{-1}}$) | **Conc. in Pyro-Oak-650** ($\mathrm{mg\,kg^{-1}}$) |
|---|---|---|
| Aluminium (Al) | $11 \pm 3$ | $40 \pm 12$ |
| Iron (Fe) | $40 \pm 1$ | $156 \pm 5$ |
| Magnesium (Mg) | $480 \pm 15$ | $1880 \pm 62$ |
| Manganese (Mn) | $19 \pm 1$ | $75 \pm 3$ |

Inorganic content for Al, Fe, Mg and Mn in the raw biomass are shown in Table 5.1, which also shows approximate concentrations of (Al, Fe, Mg, Mn) in Pyro-Oak-650. Since total digestion of the sample was not possible in $HNO_3$, the concentrations for Pyro-Oak-650 were calculated from the pyrolysis percentage yield (Table 4.2). This analysis is considered to be valid since none of the selected inorganic constituents are known to volatilise at or below $650\,^{\circ}\mathrm{C}$. The concentration of iron in Pyro-Oak-650 was found to be $156 \pm 5\,\mathrm{mg\,kg^{-1}}$.

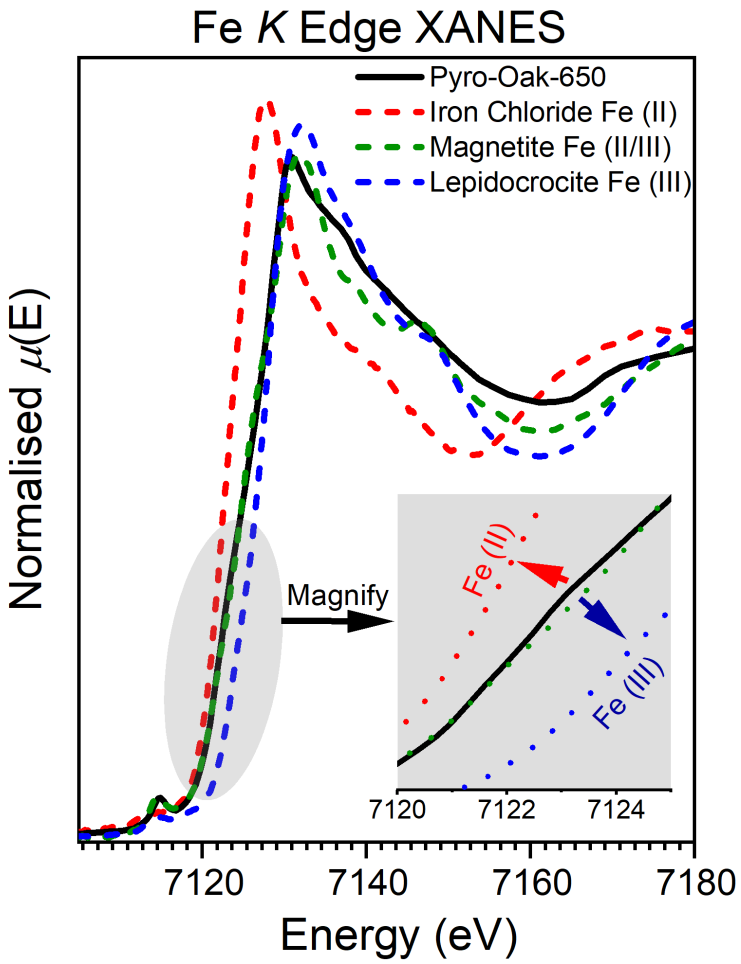


FIGURE 5.8: Iron *K*-edge XANES spectra of Pyro-Oak-650 with chemical state reference standards.

Fe *K*-edge XANES of Pyro-Oak-650 was performed to assess the chemical state of the iron within Pyro-Oak-650 before gold adsorption (Figure 5.8). The result is consistent with a mixed magnetite-like $Fe^{II}$:$Fe^{III}$ valence state. Linear combination fitting of Pyro-Oak-650 Fe *K*-edge XANES against $Fe^{II}$ and $Fe^{III}$ standards ($Fe^{II}Cl_2$ and Lepidocrocite respectively), gave a ratio of 14% $Fe^{II}$ and 86% $Fe^{III}$, similar to that reported in Ref. [372]. These results support the idea that Fe exists in a solid solution between magnetite $Fe_3O_4$ ($Fe^{II}$:$Fe^{III}$ = 0.5) and maghemite $\gamma$-$Fe_2O_3$, which each have an inverse spinel structure. The complex chemistry of iron in environmental samples makes a positive identification of magnetite challenging. However, as will be discussed in Section 5.6, the identification of single crystalline lattice of iron oxide, in conjunction with the evidence presented here, makes magnetite the most likely phase of iron oxide present in Pyro-Oak-650 before gold uptake. The potential for the iron content of Pyro-Oak-650 to be involved in the reduction of aqueous gold to nanoparticulate gold onto the pyrolysis carbon was further investigated using analytical electron microscopy (Section 5.6).

## 5.6 Role of Mixed Valence Iron Oxide in Aqueous gold Reduction

### 5.6.1 Co-location of Iron Oxide and $Au^0$

Fe $K-$edge XANES was conducted post-uptake, but did not show any significant change in bulk iron speciation or valence when compared to the spectra for pre-uptake Pyro-Oak-650, and is therefore not shown. However, STEM imaging showed a lower atomic contrast thin film formed around nAu in Pyro-Oak-650 after uptake (Figure 5.9a).

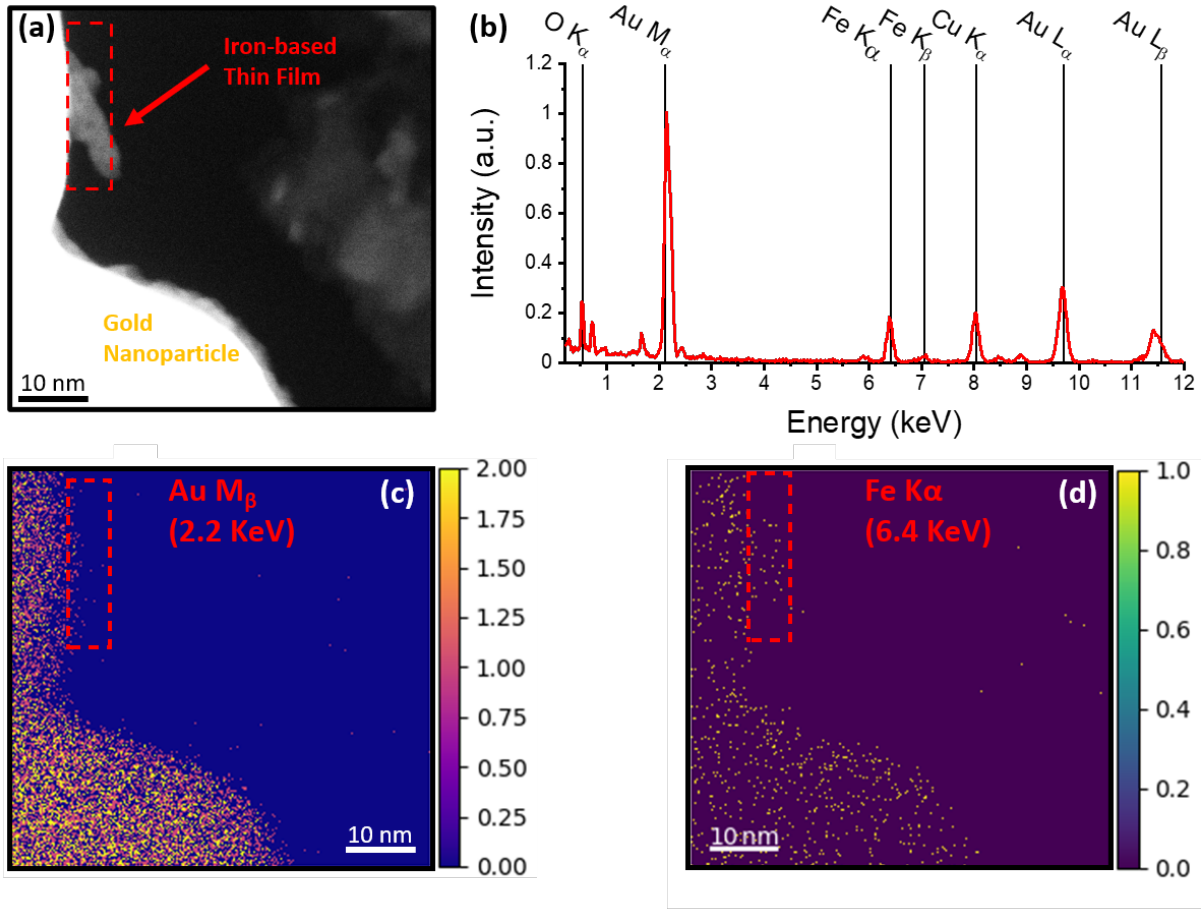


FIGURE 5.9: (a) HAADF-STEM image of nAu in post-uptake Pyro-Oak-650 with a crystalline thin film (highlighted red-dashed) around the nanoparticle edge. (b) STEM-EDX spectrum shows the presence of Fe and O within the highlighted region. Corresponding STEM-EDX maps at the (c) Au $M_\beta$ (d) Fe $K_\alpha$.

STEM mode, high-angle annular dark field (HAADF) imaging shows an isolated, lower atomic mass contrast, crystalline film around a gold nanoparticle within the Pyro-Oak-650 carbon matrix after gold uptake at 500 ppm ($67\,\mathrm{mg\,g^{-1}}$). STEM EDX was collected for an isolated region of the crystalline film (Figure 5.9b). The spectrum shows the presence of gold from the

nanoparticle surface, as well as both iron and oxygen (the Cu peak is due to the copper support grid). The corresponding EDX maps for gold and iron (Figure 5.9c & Figure 5.9d respectively) clearly show that the isolated region is an iron rich lattice and is most likely some form of iron oxide. An attempt to index the lattice of the isolated crystalline iron-containing phase to a specific iron oxide was made (Figure 5.10).

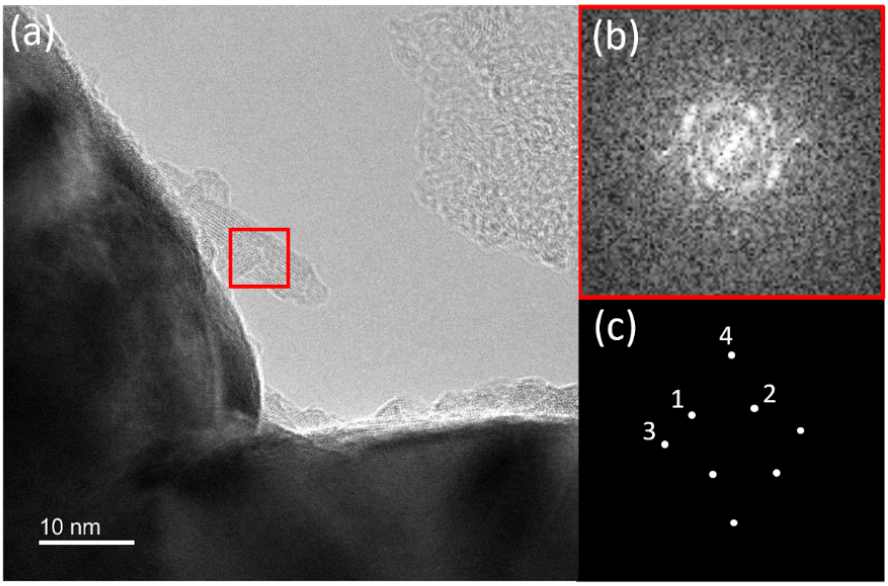


| Spot pair Number | $((2d_{hkl})^{-1})$ / $nm^{-1}$ | $d_{hkl}$ / Å |
|---|---|---|
| 1 | 7.87 | 2.54 |
| 2 | 6.63 | 3.08 |
| 3 | 11.89 | 1.68 |
| 4 | 13.80 | 1.44 |

FIGURE 5.10: (a) HRTEM image of iron oxide film surrounding nAu (b) Fast Fourier transform of highlighted region. (c) lattice spots from (b), with their corresponding spacings shown in the table below.

The isolated iron oxide region identified by HAADF-STEM (Figure 5.9a), can be seen as a crystal in the HR-TEM image in Figure 5.10a. A fast Fourier transform (FFT) was performed on the lattice image region highlighted in red. The power spectrum produced from the FFT is shown in Figure 5.10b. By indexing the power spectrum, it is possible to identify lattice planes and zone axes of nanoparticles. Further details on indexing electron diffraction patterns are available [374]. Using the Gatan Microscopy Suite software, a line intensity profile of the individual spots identified by FFT were used to measure the spot spacings; these are shown in the inset table within Figure 5.10. Using the results of the EDX, which identify this particle as an iron oxide, several likely iron oxide lattices were compared to the FFT spot spacings

(i.e. Wustite, Magnetite, Ferrihydrite). Unfortunately, no exact solutions to the spacing and orientation of the spots were found. It is possible that the iron oxide here displays some form of defect ordering, resulting in a misleading diffraction image. A disordered iron oxide lattice is supported by the FFT, which shows significant 'blurring' of the lattice spots. Several papers have reported faulting and highly disordered iron oxides using electron microscopy [375–377]. It is also possible that due to the very thin crystal, forbidden diffraction spots may become visible due to a lack of destructive interference. Interestingly *Alam et.al.* report the formation of a disordered iron oxide phase after the reduction of $Cr^{VI}$ onto a magnetite modified pyrolysis carbon. However, the authors were unable to identify the crystalline phase to either magnetite or maghemite using a combination of electron microscopy and mossbauer techniques [378]. It is possible the imaged isolated crystalline phase of iron oxide co-located with the reduced $Au^0$ may be evidence of such a disordered phase.

### 5.6.2 Role of Surface Iron Oxide Species in Au Reduction

The presence of both Fe and O in the EDX, combined with the bulk Fe *K*-edge XANES measurements, provides strong evidence that the crystalline film around the gold nanoparticle is some form of magnetite-like iron oxide. Having established the presence of iron oxides at the surface of the pyrolysis carbon, it was presumed likely that iron oxide was one significant mechanism for the reduction of $Au^{III}$ onto pyrolysis carbon. It is also worth noting that the iron species present within Pyro-Oak-650 were naturally occurring, rather than introduced through a chemical modification stage. In order to investigate whether iron oxides in Pyro-Oak-650 were a direct pathway for $Au^{III}$ reduction, STEM dual-EELS measurements were performed on Pyro-Oak-650 post uptake. EEL spectroscopy allows for spatially-resolved core electron spectra to monitor changes in chemical speciation. Dual EEL spectroscopy provides higher energy resolution than traditional EEL. This is achieved through absolute energy alignment by subtracting the elastic energy ($\Delta E \sim 0$) peak of the scattered electrons produced by a monochromated electron source [379]. Using dual-EEL spectroscopy, it is possible to resolve two sub-peaks within the acquired Fe $L_3$-edge EEL spectra: one centred at $709.0\,\mathrm{eV}$ and the other at $710.8\,\mathrm{eV}$). The Fe $L_2$-edge is centred around $721\,\mathrm{eV}$. Resolving the two subpeaks in the Fe $L_3$-edge spectra allows one to monitor the ratio between $Fe^{II}$ and $Fe^{III}$ for a nanometre-scale region of interest [380].

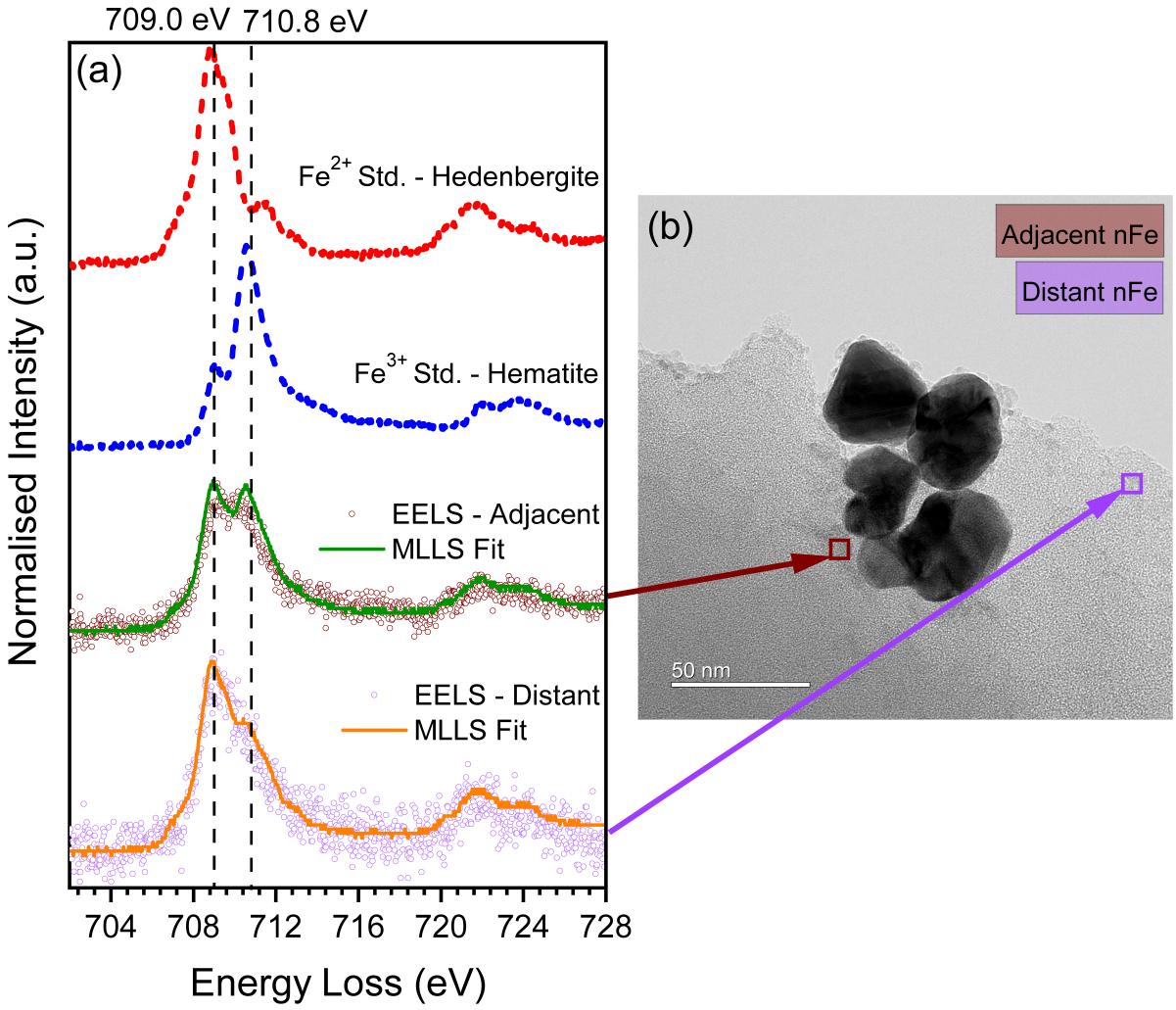


FIGURE 5.11: Spatially-resolved Fe $L_{3,2}$-edge EEL spectra for iron oxide nanoparticles adjacent to (maroon circles) and distant from (purple circles) nAu within Pyro-Oak-650 post-uptake. EEL spectra for Fe$^{II}$ and Fe$^{III}$ standards are also shown.

Dual EELS was applied here to monitor the valence of nanoparticulate iron oxide adjacent to an Au$^0$ nanoparticle on the Pyro-Oak-650 surface. Dual EEL spectra (Figure 5.11a) were collected for isolated iron oxide nanoparticles within the pyrolysis carbon matrix at locations adjacent to, and distant from a cluster of gold nanoparticles (Figure 5.11b). The Fe$^{II}$ and Fe$^{III}$ edges from monovalent mineral reference spectra are located at 709.0 eV and 710.8 eV respectively. Least-squares fitting of the Fe $L_3$ and Fe $L_2$ edges by linear combination of the Fe$^{II}$ and Fe$^{III}$ reference spectra (Hedenbergite and Hematite respectively) was performed. The fit shows that the iron oxide nanoparticle adjacent to the reduced Au$^0$ nanoparticle was *more oxidised* than the distant iron oxide nanoparticle (Table 5.2).

TABLE 5.2: $Fe^{II/III}$ ratio generated by linear combination fitting of EELS Fe $L_{3,2}$-edge data for iron oxide nanoparticles adjacent to and distant from a $Au^0$ nanoparticle within the pyrolysis carbon matrix (Figure 5.11).

| **Position** | **Hedenbergite Std. ($Fe^{II}$)** | **Hematite Std. ($Fe^{III}$)** |
|---|---|---|
| Adjacent | 44% | 52% |
| Distant | 67% | 38% |

Collectively, the co-location of mixed Fe oxides with the gold nanoparticle shown in Figure 5.11, and the $Fe^{III}$-rich nanoparticles adjacent to $Au^0$ provide strong evidence for the role of mixed iron oxides in the reduction of aqueous $Au^{III}$ onto the surface of Pyro-Oak-650. Other inorganic species, especially other transition metal oxides, are likely present within the pyrolysis carbon matrix. Flame AAS measurements carried out on a sample of the initial woody feedstock for Pyro-Oak-650 show trace quantities of several transition metals as well as iron (Table 5.1). It is possible that naturally occurring oxides of these metals are formed during pyrolysis. However, no evidence for this was observed.

## 5.7 Size Distribution of Nanoparticulate Gold within Pyro-Oak-650

Figure 5.12 shows SEM back-scattered electron imaging and X-ray microtomography of Pyro-Oak-650 post-uptake at 1000 ppm initial Au loading. Both imaging modalities clearly show the formation of larger clusters ($500\,\mathrm{nm}$ to $1000\,\mathrm{nm}$) of reduced metallic gold on the carbon surface. At the same time, TEM imaging has identified the presence of reduced nanoparticulate gold within the pyrolysis carbon matrix. As discussed in Section 5.4.2, X-ray tomography shows that nanoparticulate gold forms further within the carbon matrix, whilst larger clusters are predominantly present at the surface only. It seems likely that the reduction of $Au^{III}$ occurs primarily at the carbon surface, before diffusing into the highly porous carbon network. Understanding the formation and growth of nanoparticulate gold within Pyro-Oak-650 as a function of initial $Au^{III}$ concentration is important for identifying possible reduction mechanisms and designing effective gold recovery strategies. For example, finding the concentration at which the average gold cluster size is largest may allow for more effective recovery of gold chloride. Understanding the relative changes in gold nanoparticle size may also help identify the pathways by which gold, and other aqueous inorganics, are reduced onto the surface.

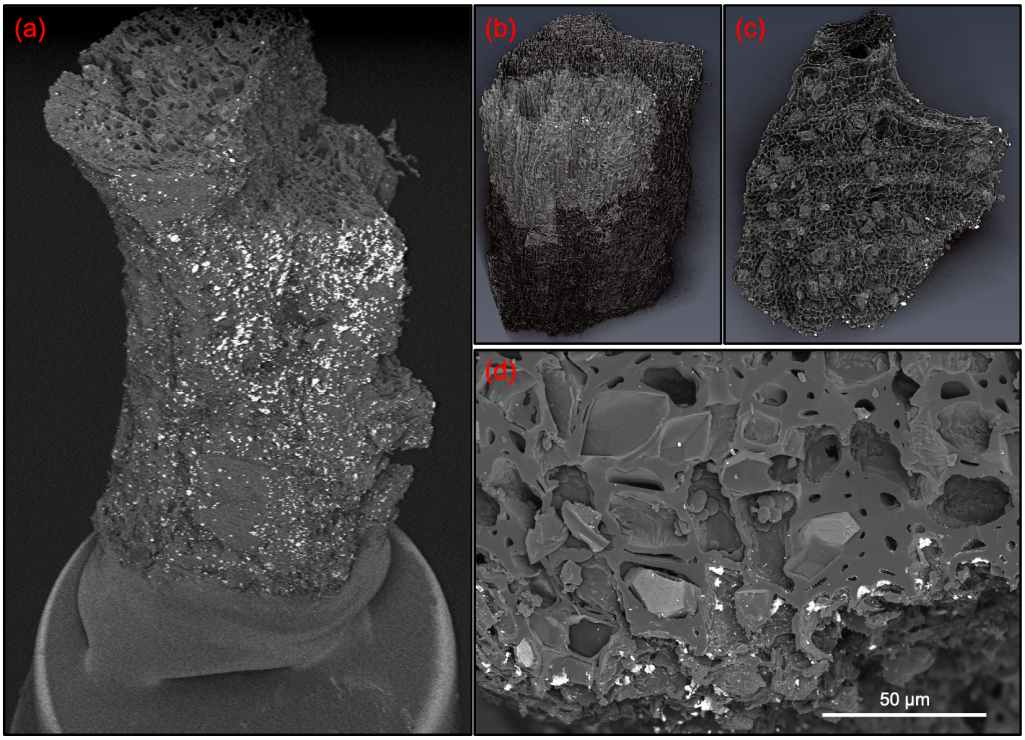


FIGURE 5.12: (a) FEG-SEM back-scattered electron image of Pyro-Oak-650 after 1000ppm gold uptake. The same sample was reconstructed using X$\mu$T which is shown from two angles in (b) and (c). (d) FEG-SEM image of the carbon surface of the same sample, showing small gold clusters.

### 5.7.1 EXAFS Fitting

EXAFS is a powerful tool for measuring coordination numbers, bond lengths and structural disorder in nanoparticles [381]. By using the known face centred cubic structure of metallic gold, it is possible to model changes in the coordination number (i.e. the number of adjacent gold atoms) within a sample. Lower coordination numbers are directly correlated with reduced nanoparticle sizes since, on average, every gold atom has fewer nearest neighbours. In this way, changes in average coordination number can be measured using EXAFS to estimate average nanoparticle size [381–383].

EXAFS fitting was initially performed by finding the amplitude reduction factor ($S_0^2$) for a reference gold foil by fixing the coordination number to 12 - the coordination number of the gold atoms in the face-centred cubic (FCC) lattice. Throughout the fitting the input parameter determining the maximum frequency of the background, $R_{bkg}$, was set to $1.5$ Å. The data range used for Fourier transforming the EXAFS $\chi(k)$ data was $2.5$ Å$^{-1}$ to $10$ Å$^{-1}$. A Hanning window with a $\delta k$ value of $2.0$ Å$^{-1}$ was used for each fit. Fitting of each dataset was performed with a k weighting of 2 over the first coordination shell ($1.5$ Å to $3.6$ Å).

TABLE 5.3: Results of EXAFS fitting for gold foil reference standard.

| **Sample** | **Coordination Number, N** | **Amplitude Reduction Factor $S_0^2$** | **Radial Distance, R (Å)** | **$\sigma^2$** (Å$^2$) | **$\Delta E_0$** (eV) |
|---|---|---|---|---|---|
| Gold Foil | 12 (fixed) | $0.96 \pm 0.07$ | $2.85 \pm 0.04$ | $8.3 \pm 0.5$ | $2.2 \pm 0.2$ |

The fit of the gold foil standard was used to calibrate the amplitude reduction factor $S_0^2$. The absorption energy shift $\Delta E_0$, mean-squared relative displacement $\sigma^2$ and average interatomic distance (R) were also calibrated for fitting the experimental data. The results of fitting the gold foil are shown in Table 5.3. As expected, R was found to be $2.85 \pm 0.05$ Å - the average interatomic spacing in the gold lattice. The amplitude reduction factor was found to be 0.96±0.06. The values shown in Table 5.3 were used for subsequent fitting of the experimental data.

TABLE 5.4: Results of EXAFS fitting for Pyro-Oak-650 after gold uptake.

| **Initial $AuCl_3$ Conc. (ppm)** | **Coordination Number (N)** |
|---|---|
| 50 | $11.52 \pm 0.23$ |
| 100 | $11.87 \pm 0.24$ |
| 200 | $11.61 \pm 0.28$ |
| 500 | $10.20 \pm 0.32$ |
| 1000 | $9.71 \pm 0.36$ |

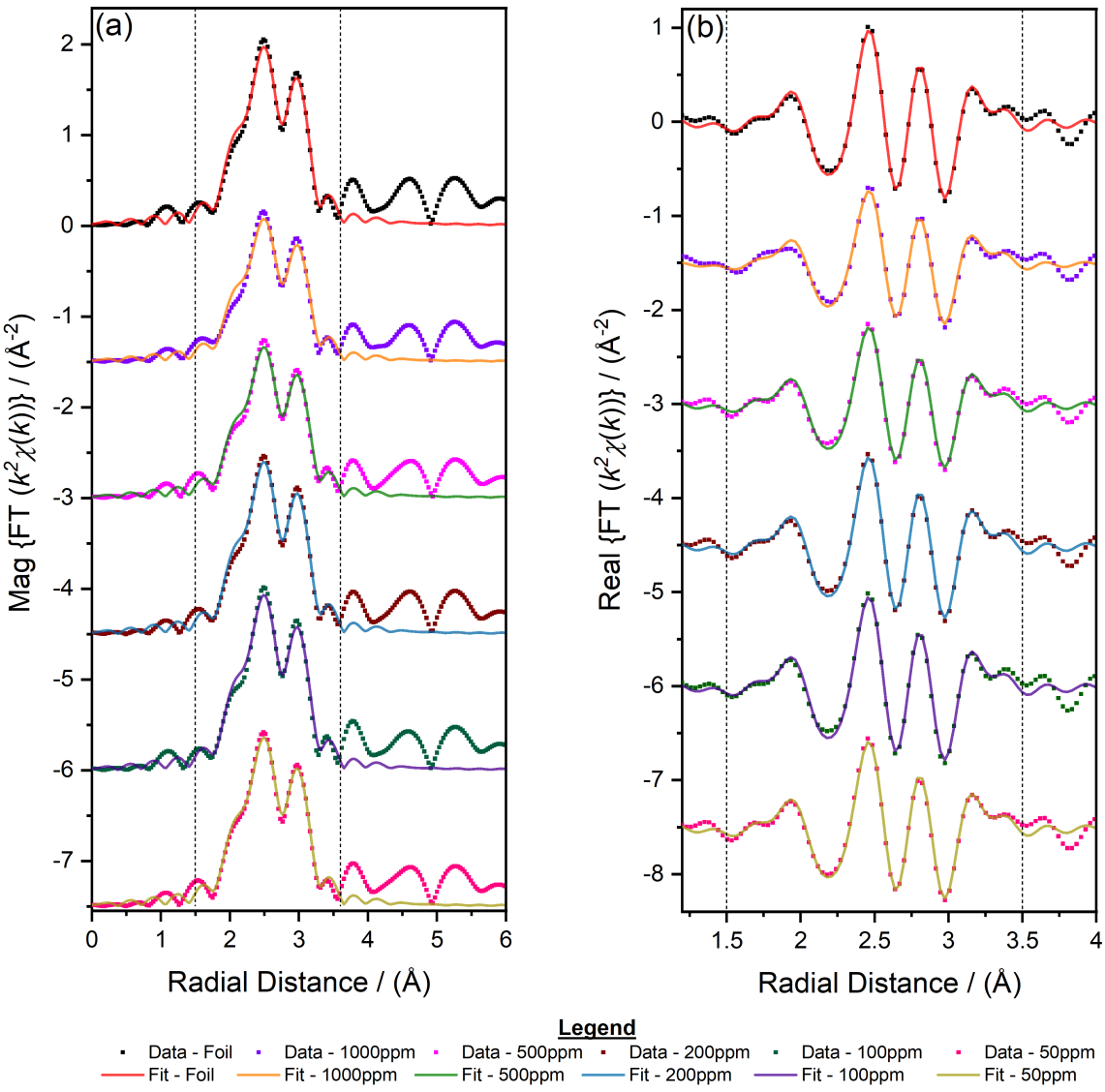


FIGURE 5.13: Au $L_3$-edge data and fits for: (a) the magnitude and (b) the real part of the Fourier Transform of the EXAFS data for the gold foil and Pyro-Oak-650 after batch gold absorption experiments at 50 ppm, 100 ppm, 200 ppm, 500 ppm and 1000 ppm. Dotted vertical lines represent the fitting region.

EXAFS fitting of the gold nanoparticles formed on the pyrolysis carbon post-uptake was performed simultaneously in order to reduce errors due to correlations within an individual fitting approach. The energy shift, $\Delta E_0$, interatomic distance, $R$, and mean-square displacement, $\sigma^2$, between gold atoms in the nanoparticle were refined but constrained to be the same in all samples. This approach carries the implicit assumption that $Au^0$ nanoparticles are formed within each sample, and only the coordination number of the produced nanoparticulate gold varies between the post-uptake pyrolysis carbon samples. This has been applied in several studies, as it is well known that reductions in coordination number strongly correlate with a reduction of average nanoparticle diameter [381, 382]. The fits for each sample are shown in Figure 5.13.

Phase-uncorrected Fourier-transformed EXAFS for the absorption isotherm series between 50-1000 ppm initial gold concentrations ($6.5\,\mathrm{mg\,g^{-1}}$ to $130\,\mathrm{mg\,g^{-1}}$ gold:char ratio) are shown in Figure 5.14a. Au $L_3$-edge EXAFS confirms the complete reduction of aqueous $Au^{III}$ to $Au^0$ across all concentrations, with no evidence of $Au^I$ species present.

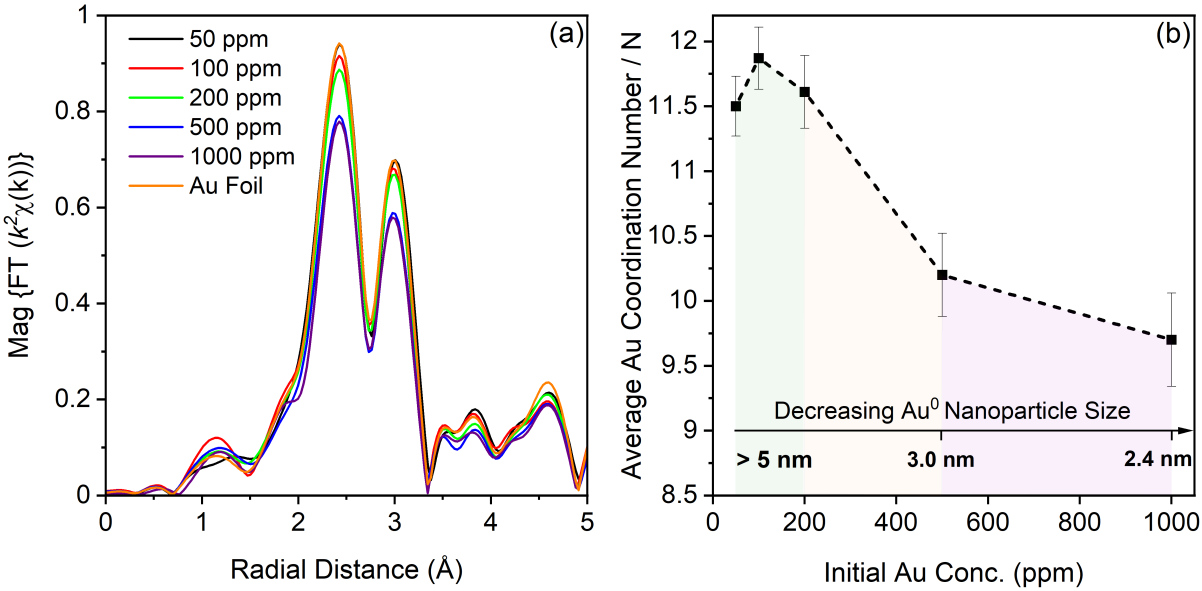


FIGURE 5.14: (a) Magnitude of Au $L_3$ EXAFS for the range of initial gold concentrations. (b) Change in the average coordination number of $Au^0$ nanoparticles against initial concentration.

The results of the first coordination shell EXAFS fitting from Table 5.4 are plotted in Figure 5.14b against the initial gold chloride concentration. The average gold atom coordination initially increases between 50 ppm and 100 ppm ($6.5\,\mathrm{mg\,g^{-1}}$ to $13\,\mathrm{mg\,g^{-1}}$), before decreasing from 12 at 100 ppm to 9.7 at 1000 ppm ($130\,\mathrm{mg\,g^{-1}}$). The average coordination number of nanoparticulate gold within the pyrolysis carbon after uptake at 1000 ppm is $9.7 \pm 0.3$. FEFF9, a self-consistent real space multiple-scattering code, was used to calculate average nanoparticle sizes for the observed $Au^0$ coordination numbers by building gold lattices with set diameters and subsequently calculating their corresponding EXAFS spectra [104]. Figure 5.14b shows that above 100 ppm, the average gold coordination number is significantly lower. At 500 ppm ($65\,\mathrm{mg\,g^{-1}}$) a coordination number of $10.2 \pm 0.3$ corresponds to an average gold nanoparticle size of $3.0 \pm 0.4$ nm, whilst at 1000 ppm a coordination number of $9.7 \pm 0.3$ corresponds to an average gold nanoparticle size of $2.4 \pm 0.2$ nm. At coordination numbers above 11, the average nanoparticle size exceeds 5 nm. At this point, the accuracy nanoparticulate $Au^0$ size

calculation using EXAFS measurements becomes unreliable. TEM, which provides better estimate of particle size above $5\,\mathrm{nm}$, has been used as a complementary technique to EXAFS for determining the particle size distribution of nanoparticulate $Au^0$ . TEM and FIB-SEM images clearly show the formation of larger micrometre-sized $Au^0$ (Figure 5.12), as well as $10\,\mathrm{nm}$ to $50\,\mathrm{nm}$ sized nanoparticles, at lower initial gold loading below 200 ppm ($26\,\mathrm{mg\,g^{-1}}$). EXAFS coordination numbers suggest largest $Au^0$ particle size to occur around 100 ppm gold loading. However, EXAFS coordination numbers between 50 – 200 ppm initial $Au^{III}$ loadings are the same within uncertainty, creating ambiguity for any significant differences in $Au^0$ in nanoparticle size. Above 200 ppm ($26\,\mathrm{mg\,g^{-1}}$), the observed reduction in average nanoparticle size is likely due to the formation of monoatomic or ultrafine gold nanoparticles. The dependence of reduced zerovalent gold cluster size on initial aqueous loading may be due to two primary reasons: (i) diffusion of gold chloride into the pyrolysis carbon pore matrix and (ii) the availability of redox active sites.

## 5.8 Chapter Summary

This chapter highlights the role of naturally occurring iron oxides, formed during pyrolysis, in the reduction of aqueous $Au^{III}$ onto oak-derived pyrolysis carbon. Analytical S/TEM with EEL spectroscopy and Fe *K*-edge XANES give evidence that mixed $Fe^{II/III}$ oxides act as nucleation sites for the reduction of aqueous $Au^{III}$ to $Au^0$ nanoparticles within the pyrolysis carbon matrix. During the reduction process, a film of iron oxide was observed to form around the gold nanoparticles between $10\,\mathrm{nm}$ to $50\,\mathrm{nm}$ in size. The average oxidation state of this iron oxide thin film was higher in proximity to $Au^0$ nanoparticles, thus providing direct evidence for the role of mixed valence iron oxides in reduction of $Au^{III}$ onto pyrolysis carbon. Such naturally occurring, mixed valence iron oxides are likely to act as primary sites for aqueous $Au^{III}$ reduction. At higher $Au^{III}$ concentrations, X$\mu$T shows the formation of micrometre-sized $Au^0$ particles at the surface of the pyrolysis carbon, as well as the extraordinary porosity of Pyro-Oak-650. It is proposed that aqueous $Au^{III}$ is initially reduced to $Au^0$ nanoparticles by primary sites, composed of heterogeneously distributed, highly redox-active species (e.g. iron oxides). At the surface of the pyrolysis carbon, $Au^0$ nanoparticles quickly grow to form the large micrometre-sized $Au^0$ particles observed using TEM and X$\mu$T . EXAFS suggests that the

maximum average size of the $Au^0$ particles in the pyrolysis carbon is reached between 100 – 200 ppm ($13\,mg\,g^{-1}$ to $26\,mg\,g^{-1}$). Beyond these concentrations 'primary sites' become spent, and other less potent redox-active sites, as well as sites physically located further within the pyrolysis carbon pore structure, become active. These secondary sites are likely to include quinonic and aromatic functionalities as well as other heteroatomic functionalities such as the sulfhydryl groups embedded in the pyrolysis carbon, as observed using XANES. At very high $Au^{III}$ concentrations EXAFS highlights the reduction of average $Au^0$ size, presumably due to the formation of nanoparticles less than $5\,nm$ in size at secondary sites within the pyrolysis carbon matrix.

Understanding routes for the reduction of aqueous gold onto pyrolysis carbon has important implications for the recovery of this precious metal from the environment. The use of pyrolysis carbon for gold recovery offers a cost-effective and renewably sourced route. In the future, pyrolysis carbon could be modified using magnetite, other oxides or zero-valent iron for improved performance in gold recovery – a practice which has already proved successful [301, 312, 321]. Reversible uptake and release of $Fe^{II}$ onto magnetite using only modifications in pH could also have an interesting application here for "re-charging" a magnetite-modified pyrolysis carbon sorbent [384]. Furthermore, larger $Au^0$ particles form at the outer surface of the pyrolysis carbon matrix at concentrations in the range of 100 – 100 ppm ($13\,mg\,g^{-1}$ to $26\,mg\,g^{-1}$). The mechanistic understanding presented here suggests that the aqueous gold stream should be conducted at these concentrations since larger $Au^0$ particles may be recovered more economically.

# Chapter 6

# Summary & Future Directions

## 6.1 Summary

The underlying motivation for this project has been the need to reduce global dependence on fossil fuels and develop sustainable materials for future technologies. This goal is fundamentally driven by the need to address the effects of anthropogenic activity on the biosphere. We are explicitly accountable for the environment we live in and the finite natural resources that we exploit. Irresponsible, profit-led exploitation of Earth's resources is unsustainable and will result in irreversible non-linear changes to both our climate and the wider biosphere. It is now clear that future development must be aligned with the compass of planetary and social responsibility discussed in Chapter 1. A planetary boundaries model is currently being implemented by relevant stakeholders to guide sustainable development whilst upholding human rights obligations (Figure 1.1, Chapter 1).

This thesis has developed the current understanding of sustainable carbon production from pyrolysis and hydrothermal carbonisation. Chapter 1 set out the background and goals of this thesis, discussing the need to address the production of materials from finite resources by building a sustainable bioeconomy. Both pyrolysis and hydrothermal carbonisation offer a sustainable carbon product which can be integrated within the biorefinery for treatment of lower-value biomass resources that are currently viewed as waste. The sustainable carbons produced through hydrothermal carbonisation and pyrolysis are now increasingly performant within a wide variety of applications including, but not limited to, soil amendment, energy storage and catalysis. Both hydrothermal carbonisation and pyrolysis offer a remarkable degree of structural and chemical tunability through careful control of both feedstock and process conditions.

However, in order to exploit this tunability to produce higher-performance carbons, it is crucial to understand the mechanisms underpinning carbonisation of the feedstock. This thesis has taken a reductionist approach to provide insight into both the local structure and the function of pyrolysis and hydrothermal carbon. This has involved the application and development of state-of-the-art synchrotron techniques. A brief theory and outline of these techniques was given in Chapter 2.

Hydrothermal carbonisation has emerged as a tunable and sustainable technique for carbon material formation, especially from wet feedstocks, giving comparatively higher carbon yields than pyrolysis. After re-emerging from scientific obscurity, hydrothermal carbonisation now represents a significant technology for utilisation within the biorefinery. Specifically, there is commercial interest in hydrothermal carbonisation for (i) the treatment of wastes to produce fuels or fertilisers and (ii) the production of high-technology carbons for energy storage devices or catalyst supports from waste, or low-carbon resources. Whilst a reasonably good understanding of the local structure of hydrothermal carbon now exists, the mechanisms governing its formation are not yet known. Biomass-derived hydrothermal carbon is formed from two components: primary and secondary char. Very little is know about primary char, which is thought to be formed from solid-solid interactions during carbonisation, the final product is a highly amorphous carbon with an irregular morphology. In contrast, the carbohydrate components of lignocellulosic biomass form the more well-studied secondary char which exhibits a spherical morphology. Carbohydrate-derived hydrothermal carbons are extremely tunable; remarkable control over carbon functionality, morphology and the final particle size has been achieved. For this reason, carbohydrate-derived hydrothermal carbon is the most likely initial starting point for high-technology carbon products.

Chapter 3 considers both the formation mechanism and local structure of hydrothermal carbon from a model carbohydrate - glucose. Previous TEM and $^{13}C$ – NMR studies have shown that hydrothermal carbon nucleates from oligomers formed during the condensation of 5-hydroxymethylfurfural under hot-compressed water conditions. Differences between surface and bulk carbon chemistry in hydrothermal carbon is a crucial factor for understanding the nucleation and growth since growth occurs under interface control. In particular, two main

growth mechanisms of secondary char have been proposed: (i) La-Mer growth and (ii) hydrophobic ripening. Whilst La-Mer growth supports a shell-core model of hydrothermal carbon, hydrophobic ripening does not. Therefore demonstrating a core-shell hydrothermal carbon structure has importance both in terms of understanding available surface functionality and for developing a analytical understanding of hydrothermal carbonisation. Unsuccessful attempts to verify the core-shell model have been conducted using TEM imaging and by making comparisons between bulk elemental analysis and surface XPS measurements. As in previous studies, Chapter 3 reports similar C:O results from elemental analysis and XPS. Chapter 3 is the first study to utilise STXM-NEXAFS to demonstrate that whilst the surface and bulk C:O ratios are similar, significant chemical differences between the core and shell exist. STXM-NEXAFS spectroscopy highlights a hydrothermal carbon core with increased aromatic and furanic functionality, providing evidence for a more condensed, hydrophobic core. The shell displays a broader distribution of carboxylic and/or aldehyde functionality and is less aromatic. This work provides the first experimental evidence for a core-shell model of hydrothermal carbon and is published in [111]. The study also demonstrates the effectiveness of STXM-NEXAFS of FIB-prepared hydrothermal carbon lamellae to provide nano-scale chemical information not available by other techniques.

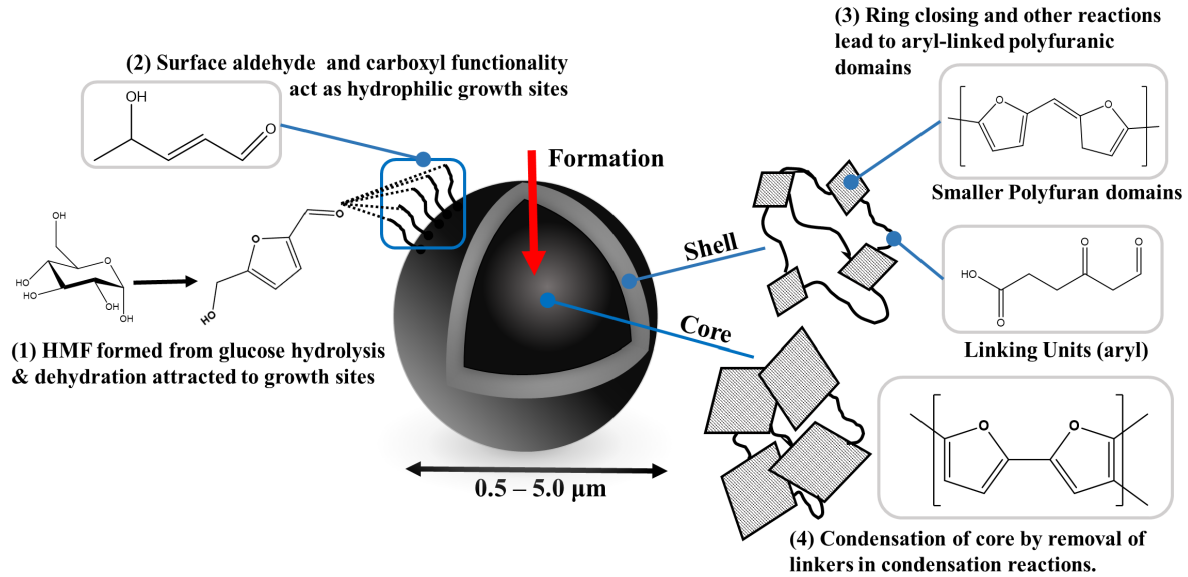


FIGURE 6.1: Schematic depiction of the proposed hydrothermal carbonisation mechanism discussed in Chapter 3.

The STXM-NEXAFS collected for the glucose-derived hydrothermal carbon enabled an alternative growth mechanism to be proposed. In this proposed mechanism, growth does not occur *via* cleavage of the carboxyl terminal unit in 5-hydroxymethylfurfural as proposed in prior work. Instead, growth is described in four stages (Figure 6.1): **Stage 1** – 5-hydroxymethylfurfural is produced from the dehydration of glucose in HCW and acts as the key monomer for hydrothermal carbon nucleation. **Stage 2** – A carboxyl/aldehyde rich shell layer is formed, likely due to acid-catalysed ring opening of local 5-hydroxymethylfurfural monomers or through aldol condensation of local carboxylic acids. The carbon oxide rich surface layer is likely to act as a binding site for local 5-hydroxymethylfurfural monomers. **Stage 3** - As the hydrothermal carbon grows, the shell layer undergoes dehydration and condensation reactions (e.g. Diels-Alder reactions). The shell layer also acts as a site for further carbon growth by reacting with local 5-hydroxymethylfurfural monomers and by aggregation with other nearby proto-spheres. **Stage 4** - In the core, dehydration and condensation reactions dominate which leads to the removal or shortening of these aryl linking units. The mechanism proposed in Chapter 3 is congruent with previously reported work, whilst also driving the study to a more comprehensive understanding. This mechanistic insight will likely have a significant impact within the community by providing the first experimental evidence for the long-held core-shell hypothesis. However, this information alone does not solve the mechanism of carbohydrate-derived hydrothermal carbon formation, nor does it address the complexities of biomass-derived hydrothermal carbon formation. Both of these challenges are likely to require a new approach. For carbohydrate-derived hydrothermal carbon, *in-situ* measurements of carbon and oxygen chemistry are required to isolate key functional stages during growth. Whilst, for biomass-derived hydrothermal carbon, the highly heterogeneous nature of the material demands bulk spectroscopy to better understand local structure without erroneous influences from surface-based chemistry or from single particle bias.

The challenge of gaining bulk carbon spectroscopy for heterogeneous carbons produced from biomass is primarily to overcome experimental limitations. Electron and soft X-ray spectroscopy are limited in penetration depth by the interaction cross-section of the electron/X-ray, whilst solid-state $^{13}C$ – NMR is limited by low signal-to-noise ratios and challenges due to isotopic enrichment and can be distorted by magnetic mineral components. This thesis has

identified and developed X-ray Raman scattering spectroscopy as a tool for studying sustainable carbon materials. Chapter 4 demonstrates the first application of XRSS for investigating the bulk local structure of sustainable carbons produced from lignocellulosic biomass. XRSS allows for the collection of soft X-ray absorption spectra for lower atomic mass elements using hard X-ray photons under environmental conditions. This makes the study of local structural changes within heterogeneous sustainable carbons more straightforward, without the need for complex high vacuum environments, with the added advantage of bulk sensitivity.

Chapter 4 utilises XRSS to investigate the local structure of both pyrolysis carbon and hydrothermal carbon produced from a common lignocellulosic biomass - Spanish holm oak wood (*Quercus Ilex*). By comparison of XRS spectra and density functional theory calculations, the local structure of oak wood-derived hydrothermal carbon is shown to be composed of furan structures linked *via* the $\alpha$-carbon position. This bulk understanding of the local-structure of hydrothermal carbon has not been previously reported. Further work is required to make comparisons between the local structure of lignocellulosic and carbohydrate derived hydrothermal carbons to assess potential differences in mechanisms.

Chapter 4 also applied XRSS to pyrolysis carbon derived from oak wood biomass. The results demonstrate that pyrolysis carbon is remarkably different from the furanic structure of hydrothermal carbon from the same feedstock. XRS spectra show that pyrolysis carbon is composed of a highly-defective condensed carbon structure. The pyrolysis process between $400\,^{\circ}\mathrm{C}$ and $600\,^{\circ}\mathrm{C}$ is driven by decarboxylation reactions, resulting in an increasingly condensed non-graphitic carbon structure. Gaussian fitting of the 1 s-$\pi^*_{\underline{C}=C}$ transition is used here as an alternative technique to quantify bulk aromatic condensation in non-graphitising carbons. The results clearly demonstrate the effectiveness of this approach, however further validation is required (e.g. by comparison with other measured standards and alternatives techniques such as optical Raman scattering). The surfaces of pyrolysis carbons are known to contain carbon oxide functionalities important for the final function of the carbon. A comparison of surface-biased soft X-ray NEXAFS and bulk XRS spectra was performed. The results demonstrate the difficulties of using soft X-rays to investigate such heterogeneous materials, with the presence of thickness effects evident within the NEXAFS data. However, a fingerprinting approach suggests that the surface of the lower temperature pyrolysis carbon (Pyro-Oak-450), contains a higher

proportion of surface oxide species than the higher temperature carbon produced at $650\,^{\circ}\mathrm{C}$, as expected. Surface oxides of this kind are relevant for a range of pyrolysis carbon applications, including adsorption of environment pollutants.

Pyrolysis carbons are now well-established as effective sorbents for potentially toxic aqueous inorganic species (e.g. Cr, Pb, Hg). Studies have extensively demonstrated that pyrolysis carbons offer remarkably high adsorbtion capacities and rates for such species. However the mechanisms by which adsorption occurs onto pyrolysis carbon have not been fully explored. Potential mechanisms such as ion-exchange, physisorption and complexation, have each been observed. An especially important mechanism for the immobilisation of inorganic species onto pyrolysis carbon is direct reduction. The direct reduction of inorganic species onto pyrolysis carbon is well-documented, often resulting in the precipitation of less toxic or less soluble species. Understanding the routes for inorganic species to be reduced onto the surface of pyrolysis carbon would be an important step to producing tailor-made pyrolysis-derived sorbents. Such tailored carbon sorbents could be engineered to produce increased sorbtion rates and capacities, whilst also offering routes for carbon regeneration or lower-energy synthesis. Chapter 5 used the absorption of gold chloride as a proxy to investigate the reductive recovery of gold species onto the surface of pyrolysis carbon, since the low reduction potential of $[Au^{III}Cl_4]^-$, results in a facile reduction of $Au^{III}$ to $Au^0$ onto the pyrolysis carbon surface. It is hoped that a better understanding of reduction for this system might be translatable to other inorganic systems also.

Reduced metallic $Au^0$ formed readily on the surface of the oak-derived pyrolysis carbon (Pyro-Oak-650). X-ray microtomography and SEM imaging clearly showed the presence of large clusters of $Au^0$ micro-particles at the carbon surface. TEM imaging and X-ray microtomography also show the presence of much smaller nanoparticulate gold within the porous carbon structure. Reductive pathways considered likely for the reduction of $[Au^{III}Cl_4]^-$ to metallic $Au^0$ included surface carbon oxides, heteroatomic species and highly redox-active iron oxide species. The previous chapter (Chapter 4) set out clear evidence for the existence of a highly oxidised carbon surface within the oak-derived pyrolysis carbon produced at both $450\,^{\circ}\mathrm{C}$ and $650\,^{\circ}\mathrm{C}$ using NEXAFS spectroscopy. Likewise, XRSS and Gaussian fitting highlighted the highly condensed carbon species found within Pyro-Oak-650. Both surface oxides

and the condensed aromatic network present within Pyro-Oak-650 are known to act as electron donors for reduction. However, in Chapter 5, no evidence of carbon acting as a pathway for direct reduction was observed. Similarly, it is known that heteroatomic species present within lignocellulose-derived pyrolysis carbons may act as a reduction pathway for inorganic species. Previous studies have highlighted organic and mineral sulphur species within grass-derived pyrolysis carbon as a reduction pathway for gold chloride [352]. S *K*-edge XANES showed that Pyro-Oak-650 primarily contains reduced sulfhydryl functionalities, with only a limited contribution from sulphate groups (< 10%). Au $L_3$-edge EXAFS showed no evidence of Au(I)-S species, though there activity is not totally ruled out here. High-resolution STEM imaging highlighted a thin film of an iron oxide in close proximity to a reduced gold nanoparticle. Iron within the pyrolysis carbon primarily exists as a magnetite-like mixed valence $Fe^{II/III}$ oxide. EEL spectroscopy, taken from iron oxide nanoparticles adjacent to and distant from a reduced $Au^0$ nanoparticle, showed a significant change in valence. The iron oxide particle next to the $Au^0$ precipitates had more ferric iron than the isolated iron oxide. Taken together the data presented in Chapter 5 present strong evidence for the role of iron species in the reduction of aqueous gold species (Figure 6.2). Fitting of Au $L_3$-edge EXAFS demonstrated a reduction in the average nanoparticle size as a function of initial gold loading concentration.

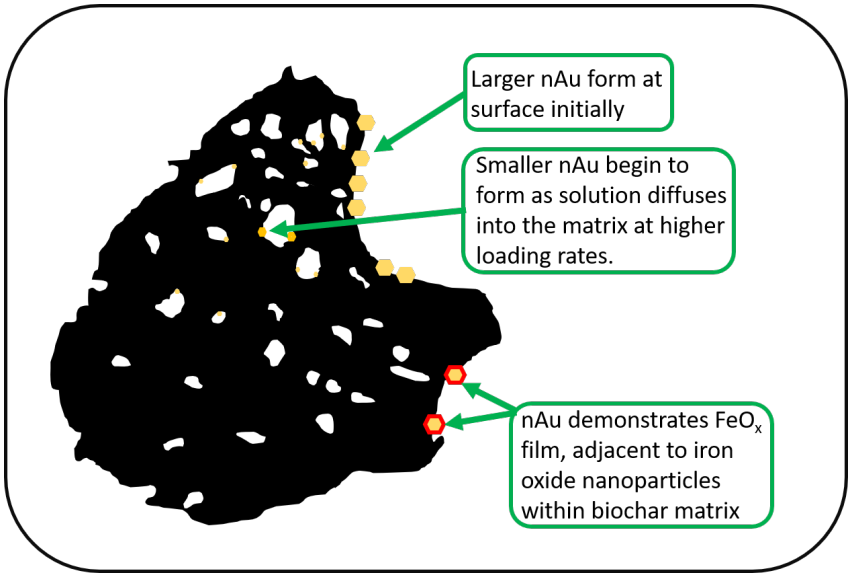


FIGURE 6.2: Schematic depiction of the proposed gold (III) chloride reduction mechanism discussed in Chapter 5

Combining this information, a reduction mechanism for $Au^{III}$ was proposed (Figure 6.2). $Au^{III}$

is initially reduced to $Au^0$ nanoparticles by primary sites, composed of heterogeneously distributed, highly redox-active species (e.g. iron oxides). At the surface of the pyrolysis carbon, $Au^0$ nanoparticles quickly grow to form the large micrometre-sized $Au^0$ particles observed by TEM and X-ray tomography. EXAFS suggests that the maximum average size of the $Au^0$ particles in the pyrolysis carbon is reached between 100 – 200 ppm ($13\,\mathrm{mg\,g^{-1}}$ to $26\,\mathrm{mg\,g^{-1}}$). Beyond these concentrations 'primary sites' become spent, and other less potent redox-active sites, as well as sites physically located further within the pyrolysis carbon pore structure, become active. Though no evidence for such sites was found here, secondary sites are likely to include quinonic and aromatic functionalities, as well as other heteroatomic functionalities such as the sulfhydryl groups observed using XANES. At very high $Au^{III}$ concentrations EXAFS highlights the progressive reduction of average $Au^0$ nanoparticle size. Nanoparticles less than $5\,\mathrm{nm}$ in size likely form at secondary sites within the pyrolysis carbon carbon matrix.

### 6.1.1 Conclusions

Sustainable carbon materials will inevitably play a significant role in the transition from fossil-produced materials. Sustainable carbon devices for energy storage, catalysis and waste management appear to be the closest in terms of technology-readiness. The results presented in this thesis provide significant insight into both the structure and function of hydrothermal carbon and pyrolysis carbon. Insights of this nature will guide the development of materials with enhanced properties (e.g. carbon functionality) for high performance devices. Furthermore, synchrotron X-ray spectroscopy is presented as a tool for gaining formerly unprecedented chemical and mechanistic information for carbons. Further technical developments will likely yield significant insight, especially for *in-situ* science. Key project results are summarised below:

**Technical Developments**

- The first experimental evidence for a core-shell model of hydrothermal carbon has been published. Evidence was collected by scanning transmission X-ray microscopy (STXM), in the first known application of this technique to hydrothermal carbon. STXM is shown to be an effective tool for studying the hydrothermal water-carbon interface.
- The demonstration and development of X-ray Raman scattering spectroscopy (XRSS) as a tool for studying the bulk local-structure of sustainable carbon materials. XRSS has significant potential for use in *in-situ* studies as well as studying heterogeneous materials.

**Sustainable Carbon Developments**

- A hydrothermal carbon nucleation and growth mechanism has been proposed. This model provides direct insight into hydrothermal carbon functionalities relevant for future sustainable carbon devices.
- The principle furanic repeating unit within hydrothermal carbon has been isolated by XRSS and DFT calculations. Experimental evidence for this structure provides important fundamental insight for future mechanistic developments.
- Comparison of two pyrolysis temperatures ($450\,^{\circ}\mathrm{C}$ & $650\,^{\circ}\mathrm{C}$) shows the development of an increasingly condensed carbon structure and removal of surface oxide species. Based on these results, a semi-quantitative route to pyrolysis condensation has been proposed.
- Naturally-occurring iron oxides have been identified as a key pathway for the reduction of gold species onto pyrolysis carbon.

## 6.2 Future Directions

This thesis has demonstrated the potential of synchrotron X-ray techniques for exploring both the structure and function of sustainable carbon materials. There is significant scope for building on the work undertaken during this doctoral project. This section outlines some potential directions for these studies and then finishes by discussing the specific aims of the EPSRC Doctoral Prize Fellowship awarded to the candidate.

### 6.2.1 Local Structural Implications of Pyrolysed Hydrothermal Carbons

As discussed in Chapter 3, there is an increasing body of work considering the application of hydrothermal carbons within energy storage devices [216]. For this purpose, it is now common to pyrolyse carbohydrate-derived hydrothermal carbon to increase porosity and conductivity in the final product [50]. Pyrolysis of hydrothermal carbon has also been used as to introduce heteroatomic species (typically N groups) as active sites for catalysis. Facile heteroatomic modification of hydrothermal carbons can be achieved by simply adding aqueous species directly to the process water prior to carbonisation. Subsequent pyrolysis of hydrothermal carbon has also been shown to remove polyaromatic and phenolic functionalities [385]. The removal of toxic polyaromatic and phenolic species from hydrothermal carbon makes the final product safer for disposal or for use as a soil amendment. The benefits of pyrolysing hydrothermal carbons have been demonstrated, but little is known about the local-structure of the final pyrolysed hydrothermal carbon (pyHTC).

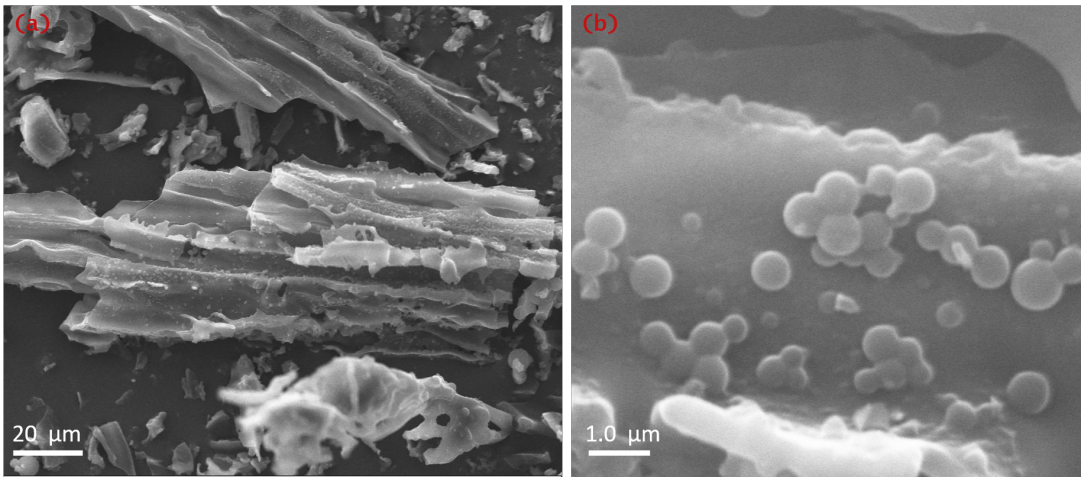


FIGURE 6.3: Secondary electron SEM images of pyHTC-Oak-250+450 (HTC at 250 °C followed by pyrolysis at 450 °C) showing the remaining (a) primary and (b) secondary char morphologies.

In order to study changes to hydrothermal carbon during pyrolysis and to understand the local structure of the final product, a preliminary XRSS study was performed. The experiment compared samples Pyro-Oak-450 and HTC-Oak-250 (from Chapter 4) against PyHTC-Oak-250+450 - a sample of HTC-Oak-250 which had subsequently been pyrolysed under the same experimental conditions as sample Pyro-Oak-450 (see Section 2.2). The resulting pyrolysed hydrothermal carbon (pyHTC) was produced with a yield of 55 wt% carbon after pyrolysis, resulting in a total process yield (both HTC and pyrolysis) of 24 wt% carbon. The total yield of pyHTC was therefore considerably less than direct pyrolysis (57 wt% carbon, see Table 4.2). However, for certain applications, this low yield may be acceptable due to increased material performance. PyHTC-Oak-250+450 retained the morphology of the starting HTC-Oak-250, with the features of primary and secondary charring clearly visible (Figure 6.3).

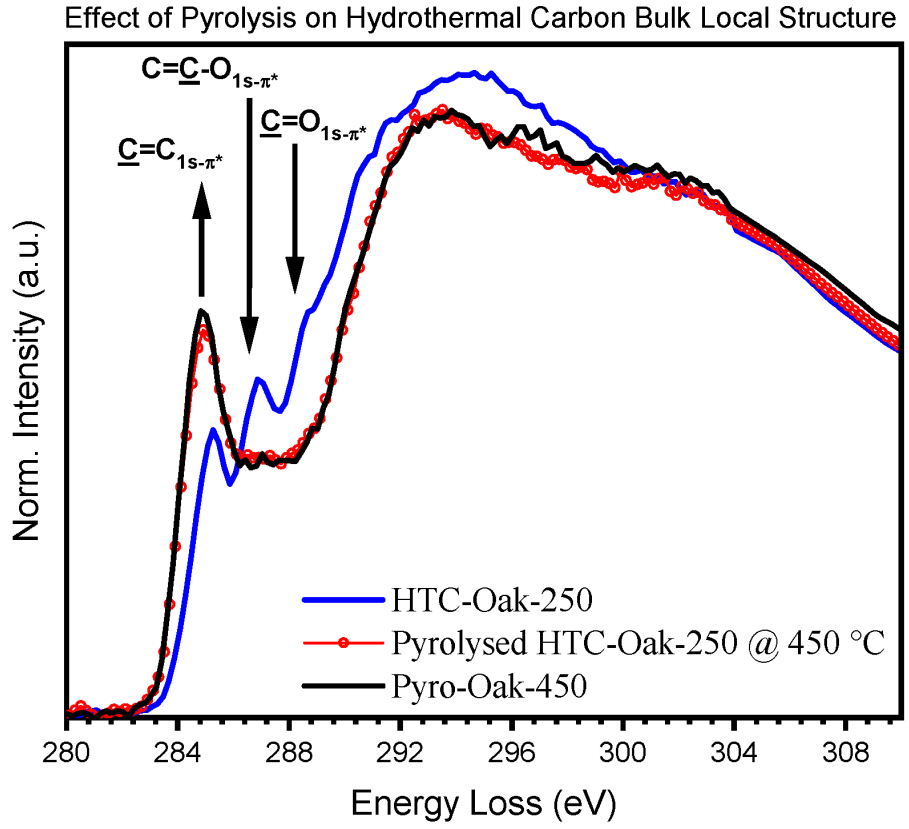


FIGURE 6.4: XRS spectrum showing the similar bulk local-structure between pyrolysed oak wood and pyrolysed oak-derived hydrothermal carbon.

From XRSS, the bulk local structure of PyHTC-Oak-250+450 is remarkably similar to pyrolysis carbon derived directly from the starting biomass - Pyro-Oak-450 (Figure 6.4). In order

to quantitatively assess the changes in carbon functionality produced during pyHTC, Gaussian fitting was performed. The fitted peak areas of the relevant carbon *K*-edge transitions are shown in Table 6.1 (full fit results are shown in Appendix D). It is clear that, during pyrolysis of HTC-Oak-250, the furanic sub-structure (shown to be present in Chapter 4) is almost completely destroyed. The 1 s-$\pi^*_{\underline{C}=C-O}$ peak at 286.6 eV (G2) shows an approximate 50% reduction in peak area. Similarly, the fitting suggests that carboxylic/aldehyde species (1 s-$\pi^*_{\underline{C}=C=O}$, G4 & G5) are almost completely removed, whilst more aliphatic species are produced (G3). The removal of oxygenated carbon functionalities is concomitant with a dramatic increase in the condensed aromatic 1 s-$\pi^*_{\underline{C}=C}$ peak (G1), yet still less than found in Pyro-Oak-450.

TABLE 6.1: Results of non-linear least squares fitting. Peak area ($A_g$) and FWHM for each of the six pre-ionisation potential carbon functionalities are shown.

| Sample | G1 285.0 eV | | G2 286.6 eV | | G3 287.7 eV | | G4 288.9 eV | | G5 290.3 eV | |
|---|---|---|---|---|---|---|---|---|---|---|
| | $A_g$ | FWHM | $A_g$ | FWHM | $A_g$ | FWHM | $A_g$ | FWHM | $A_g$ | FWHM |
| HTC-Oak-250 | 0.93 | 1.72 | 0.57 | 1.28 | 0.28 | 1.88 | 0.83 | 2.08 | 0.78 | 1.93 |
| PyHTC-Oak-250+450 | 1.35 | 1.78 | 0.31 | 1.47 | 0.54 | 2.38 | 0.08 | 2.33 | 0.14 | 2.05 |
| HTC-Oak-250 | 1.45 | 1.79 | 0.32 | 1.35 | 0.33 | 1.75 | 0.22 | 2.54 | 0.12 | 1.75 |

Overall, these preliminary data suggest that pyHTC-Oak-250+450 has remarkably similar bulk carbon chemistry to a directly-produced pyrolysis carbon. This bulk understanding of pyHTC carbon chemistry has not yet been reported and many articles appear to suggest that furanic functionality remains present in pyrolysed hydrothermal carbon - this is clearly not the case. This preliminary result might mean that hydrothermal carbonisation could act as an intermediate process in situations where direct pyrolysis may not be appropriate. Examples of this might include:

- The introduction of bulk heteroatomic functionalities, which is more straightforward with hydrothermal methods.
- Waste-management, where hydrothermal treatment of 'wet' biomass can be performed without costly drying methods. Hydrothermal carbon is much more hydrophobic than the starting biomass, meaning that drying of hydrothermal carbon prior to a secondary pyrolysis step may be more economic, with the added benefits of reduced phenolics/polyaromatic hydrocarbons.

Both the chemistry and implications for applications of pyHTC deserve further investigation and XRSS would likely be a powerful tool for such studies.

### 6.2.2 Carbohydrate Derived Hydrothermal Carbon - Bulk Local Structure and Effects of Pentose vs Hexose Starting Feedstocks

Another area of interest requiring further investigation is the effect of different carbohydrates on the formation of hydrothermal carbon. As discussed in Section 3.2, the morphology of the produced carbon remains as the familiar spherule shape, however the homogeneity and sizes of the produced carbons are remarkably different. *Titirici et.al.* described the carbons produced from pentoses (i.e. fructose, xylose) as dispersed spheres, whereas those produced from hexoses (i.e. glucose) as a mixture of interconnected particles below $200\,\mathrm{nm}$ in size and isolated spheres between $500\,\mathrm{nm}$ to $1000\,\mathrm{nm}$ [43]. The authors suggested that the differences in morphology between hexose and pentose sugars are due to a different formation pathway, postulating that C5 sugars proceed *via* polymerisation of furfural, whilst C6 sugars are formed by the polymerisation of 5-hydroxymethylfurfural [143]. In order to investigate any differences in bulk, local structure, carbons derived from fructose (C5), sucrose (mixed) and xylose (C6) were investigated using XRSS (Figure 6.5).

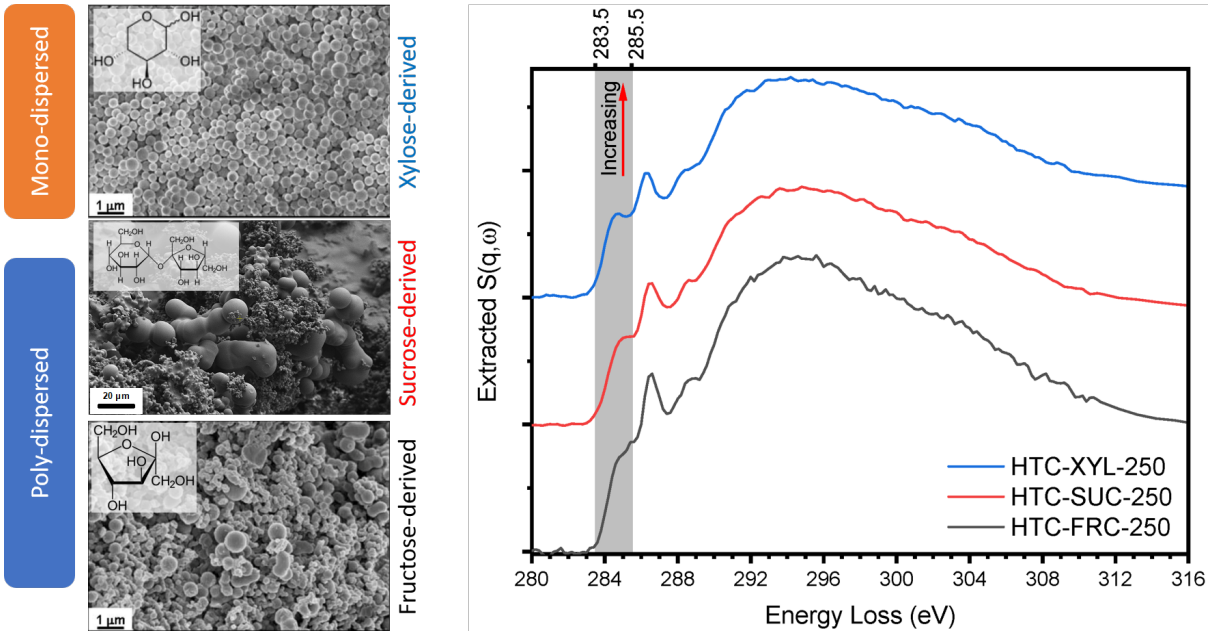


FIGURE 6.5: XRS spectra showing the different bulk local-structure between pyrolysed oak wood and pyrolysed oak-derived hydrothermal carbon.

SEM images show that both the fructose and sucrose derived hydrothermal carbons display significant poly-dispersed particle morphologies, whilst the xylose-derived carbon was mono-dispersed - as reported elsewhere [43]. The XRS spectra for the produced chars are also shown

in Figure 6.5. Whilst these data are preliminary, there is a significant increase in peak area beneath the $1\,s\text{-}\pi^*_{\underline{C}=C}$ transition from fructose to sucrose to xylose. This trend also appears to be reversed in the $1\,s\text{-}\pi^*_{C=\underline{C}-O}$ (286.6 eV) feature. These significant differences in carbon chemistry between hydrothermal carbons produced from different sugars have not been fully explained. Further work may include monitoring differences in the O *K*-edge to determine whether differences are due to changing oxygen chemistry, or by monitoring differences in surface and bulk chemistry by comparing XRSS with NEXAFS spectroscopy.

### 6.2.3 EPSRC Doctoral Prize Fellowship - *in-situ* XRSS and Device Development

The next stage in the development of sustainable carbon materials is the production of useful, sustainable devices from waste biomass. In order to achieve this goal, I intend to use an atoms-to-devices approach, building upon the mechanistic and technological advances discussed within this thesis. The awarded fellowship will be used to produce an effective energy storage device from a common waste biomass - coffee grounds. Hydrothermal carbonisation and heteroatom doping will be used to produce a sustainable carbon for the device, whilst an accurate model of how carbon and heteroatom chemistry impacts the device's performance will be investigated using a range of spectroscopy and imaging approaches.

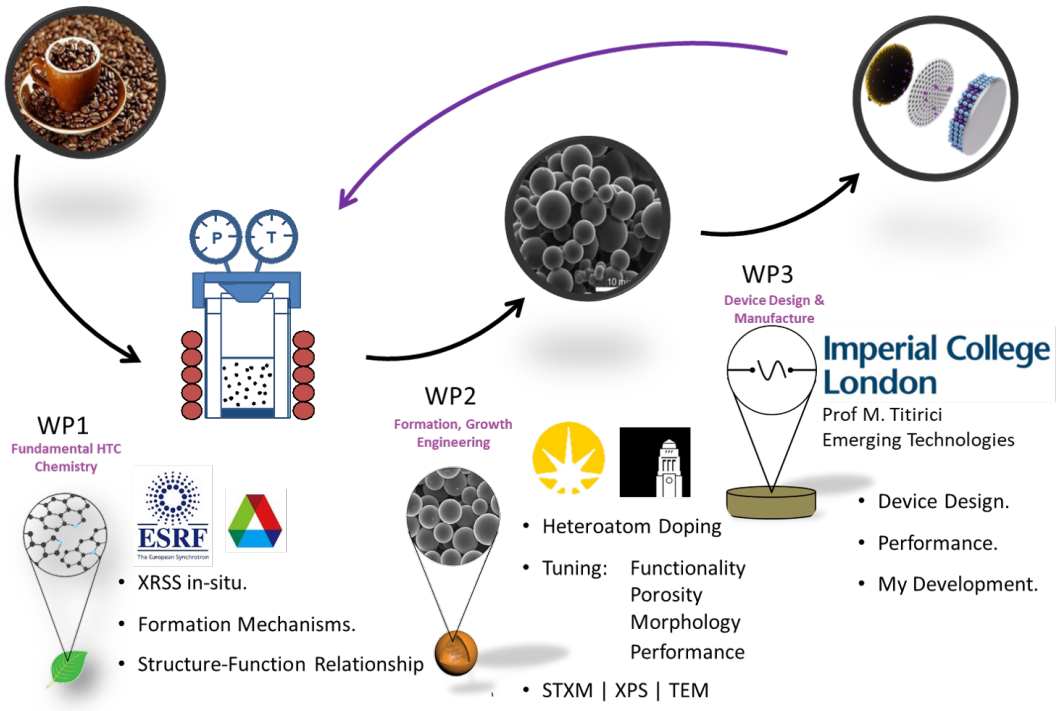


FIGURE 6.6: Schematic summarising workpackages within the awarded doctoral prize fellowship.

A workflow for the proposed project is shown in Figure 6.6. This fellowship will be undertaken as a series of workpackages (WPs). WP1 will be used to perform *in-situ* XRSS of hydrothermal carbonisation under hot compressed water conditions. This will extend my PhD collaboration with sector 20 of the European Synchrotron Radiation Facility (ESRF) by utilising beamline ID-20s detection capabilities to isolate inelastically-scattered photons from within an *in-situ* cell. *In-situ* XRSS will enable the study of oxygen and carbon bond development during hydrothermal carbonisation. The results from these *in-situ* experiments will link directly with the mechanism proposed in Chapter 3 and will be used to guide development of a suitable carbon for an energy storage device. For example, understanding changes in local chemistry during carbon formation in the autoclave can be used to more efficiently introduce heteroatomic functionalities for higher catalytic performance. Furthermore the behaviour of carbohydrates under hot compressed water conditions may have importance in other fields such as HTC for waste disposal or geochemistry.

Building on WP1, WP2 will be used to collect surface carbon and oxygen spectroscopy using bulk and spatially-resolved X-ray spectroscopy (NEXAFS and STXM) obtained at Diamond lightsource. WP2 will also utilise the experimental resources of the recently established Bragg centre at the University of Leeds (e.g. HRTEM, XPS). The experiments in workpackage 2 will be used to modify hydrothermal carbons using heteroatom functionalisation. In this way, it will be possible to produce a carbon with improved functionality. Secondary pyrolysis may also be used to increase conductivity and porosity. Finally, WP3 will focus on conducting electrocatalytic performance measurements on selected carbons conducted in collaboration with Prof. Titirici at Imperial College London. These measurements will demonstrate how bulk and surface functionality identified in WP 1 and 2 influence device performance. Project data will identify efficient hydrothermal carbonisation transformation pathways for energy storage device applications.

# Appendix A

# Carbon *K*-edge Fitting

Carbon *K*-edge spectra may be interpreted by monitoring changes in peak heights and ratios at certain energies corresponding to individual carbon functionalities. Gaussian fitting is currently the most reliable way to assess changes in carbon functionalities in NEXAFS spectra and has been applied extensively [386]. The curve fitting procedure is based upon deconvolving spectra using Gaussian functions at energies of known electron transitions. The energies of electron transitions for carbon functionalities have been investigated in NEXAFS and EELS studies of reference compounds. A list of electron transitions and references for the carbon functionalities described throughout this thesis are shown below in Table A1.

TABLE A1: Summary of Gaussian peak locations and functional group assignment for carbon *K* edge NEXAFS spectra.

| **Transition Energy (eV)** | **Interpretation** | **Electron Transition** | **Ref.** |
|---|---|---|---|
| 284.8 | C=C aromatic [benzene-type building blocks] | 1s-$\pi^*$ | [168, 174, 183–185] |
| 285.3 | C=C-X Aryl-linked group [X = O, C] | 1s-$\pi^*$ | [183, 186, 187] |
| 286.6 | C=C-O furan | 1s-$\pi^*$ | [123, 168, 183, 188] |
| 287.5 | C-H aliphatic | 1s-$\sigma^*$ | [188, 189] |
| 288.2 | C=O-OH carboxyl, C=O aldehyde | 1s-$\pi^*$ | [174, 174, 183] |
| 290.3 | O-C=O carbonate | 1s-$\pi^*$ | [174, 183, 188] |
| 292.0 | C=C aromatic [benzene-type building blocks] | 1s-$\sigma^*$ | [174, 183, 188] |

$$ERF = \frac{A \cdot \left(1 + erf\left[\frac{x-\mu}{\sigma}\right]\right)}{2 \cdot \exp\left[-d \cdot (x - \mu - \sigma)\right]} \tag{A1}$$

$$G = \frac{A}{\sigma\sqrt{2\pi}} \cdot \exp\left[-(x-\mu)^2/(2\sigma^2)\right] \tag{A2}$$

$$Asym.G = \frac{A}{\sigma\sqrt{2\pi}} \cdot \exp\left[-(x-\mu)^2/(\Gamma^2)\right] \quad ;\Gamma = (x \cdot m) - b \tag{A3}$$

Parameters: $x$ – Energy (eV); $A$ – Amplitude; $\mu$ – centroid position; $\sigma$ – sigma (width); $d$ - decay; $m$ - constant, 0.5; $b$ - constant, - 165 eV.

In this study, spectral deconvolution was performed by non-linear least squares fitting using LMFIT, a high-level interface to non-linear optimisation and curve fitting for Python [181]. Fitting was performed using a series of Gaussian functions with a step function to represent the ionisation potential. Here, instead of using a traditional step function for fitting the ionisation potential step, an exponentially modified error function was used (Equation A1) and is labelled in fits as "ERF".

The motivation for this choice is to better represent the non-linear decay of the *K*-edge after the ionisation potential and is discussed within Chapter 7 of in Ref. [387]. An exponential, defined by the variable $d$, was used to best simulate the decay of the edge after the ionisation potential and was initially allowed to vary before being set for the fit. Whilst the value of $d$ is not reported during fitting, it was typically found to be in the range of $0.05$ to $0.10$, whilst the centroid position $\mu$ and width $\sigma$ were set at $289\,\mathrm{eV}$ and $2.0\,\mathrm{eV}$ respectively.

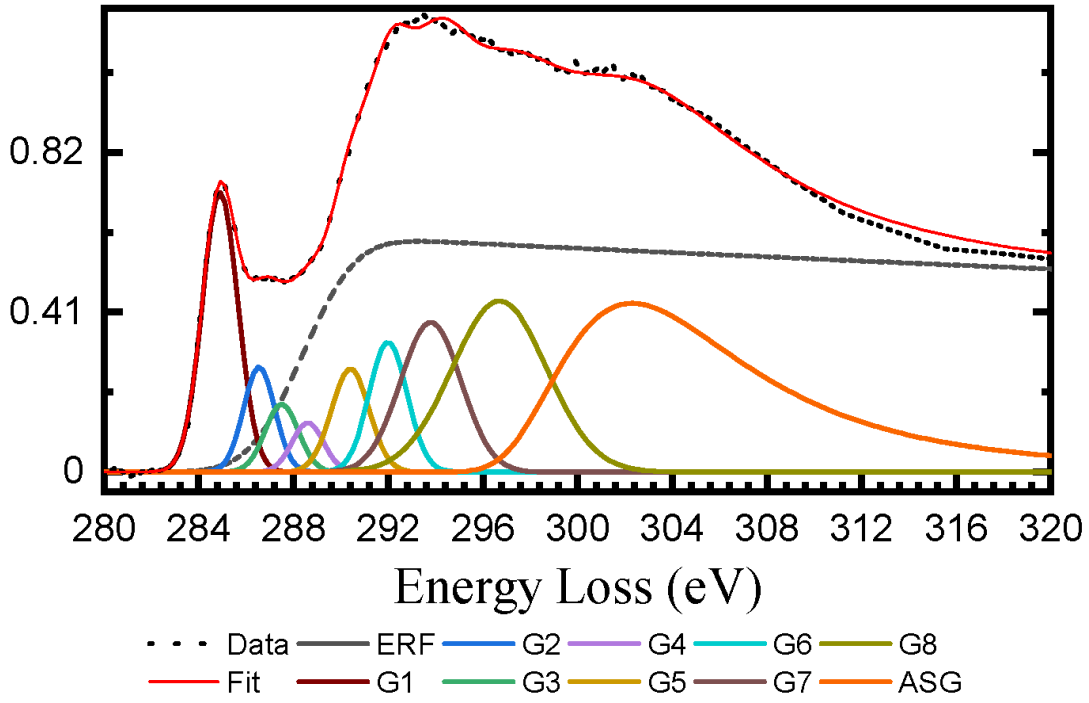


FIGURE A1: Example of Gaussian fitting for the C *K*-edge.

An example carbon *K*-edge fit is shown in Figure A1. The quantitative region of the spectrum, which contains all the chemical information relevant to this study lies in the region between

$284.8\,\mathrm{eV}$ to $292.0\,\mathrm{eV}$ (see Table A1). This region was typically fitted with five Gaussian functions at each of the energy positions $\mu$ in Table A1 except for the function at $285.3\,\mathrm{eV}$. The Gaussian function at $285.3\,\mathrm{eV}$ is only used in Chapter 3 to describe aryl-linked functionalities and is further discussed there. The full width half maximum (FWHM) of these Gaussian functions were considered as a convolution of experimental energy resolution and physical peak broadening due to the chemistry of the material. The Gaussian FWHM were initially set at $0.2\,\mathrm{eV}$, approximating the energy resolution of the instrument, then allowed to vary between $0.3\,\mathrm{eV}$ to $0.8\,\mathrm{eV}$. This fitting approach is set out by *Stohr et.al.* in Ref. [386]. Gaussian functions in this thesis are labelled G[No.] by their relative position in the spectrum and energy positions for the Gaussian functions are always highlighted in a corresponding table.

Beyond the quantitative region of the spectrum ($> 292\,\mathrm{eV}$) asymetric Gaussian functions (Equation A3) were used to simulate the structure of the edge beyond the ionisation potential. The asymmetric Gaussians used for this part of the spectrum were fixed at energy positions: $293.8\,\mathrm{eV}$ $296.7\,\mathrm{eV}$ and $302.3\,\mathrm{eV}$. The Asymmetric Gaussian function neatly describes the decay of the carbon *K*-edge beyond the ionisation potential, but does not carry any significant chemical information and once fitted, were left fixed so to not influence the statistics of the final result. The use of an asymmetric Gaussian function to describe this 'far' edge region is discussed in Refs. [386, 387].

# Appendix B

# LERIX Module for XRStools Software

XRStools is a python-based open source software for the ingest and treatment of X-ray Raman scattering data. The software has been written by *A. Mirone* and *C. Sahle* from the inelastic X-ray scattering beamline (ID-20) at the European Synchrotron Radiation Facility (ESRF). A brief description of the software has been published in Ref. [256]. This appendix describes the function of XRStools for extracting core-loss XRSS data and a module written by the candidate to input data from the LERIX spectrometer at the Advanced Photon Source (see Section 2.7.3).

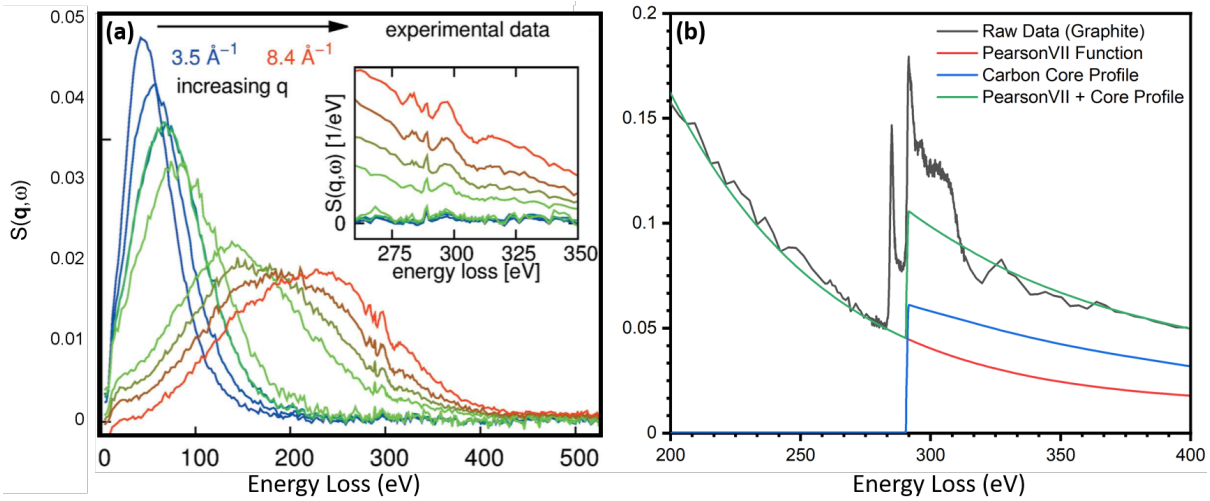


FIGURE B1: (a) Measured spectra for acetic acid (from Ref. [256] with permission), showing the valence Compton profile over a range of momentum transfer ($3.5\,\text{Å}^{-1}$ to $8.4\,\text{Å}^{-1}$). The core-loss region of the C *K*-edge ($285\,\text{eV}$) sits 'on top' of the valence Compton profile. (b) Extraction of core-loss region from Compton background using a combination of a Pearson VII and calculated core profile in XRStools.

XRStools is software originally designed as a utility for treating XRS data from beamline ID-20 at the ESRF. The principal benefit of the software is the ability to extract core-loss spectra

from raw data. As discussed in Section 2.7.3, XRSS measures non-resonant inelastic X-ray scattering (NRIXS). A significant part of the NRIXS profile is valence Compton scattering. The valence Compton profile is dependent on the momentum transfer of the scattered photon. In Figure B1a, the valence Compton profiles for an XRS spectrum of acetic acid is shown. At low momentum transfer, the Compton profile is sharp and remains at energies well below the carbon *K*-edge. At higher momentum transfer, the carbon *K*-edge rests 'on top' of the Compton profile. This makes the subtraction of the valence contribution from the total spectrum a possible source of spectral distortion and can complicate data analysis considerably. In order to perform a reliable extraction of core-loss edges from XRS data, XRStools uses a Pearson-VII function in combination with an atomic photoabsorption profile taken from tabulated Hartree-Fock data in Ref. [261]. As shown in Figure B1b, the Pearson-VII function successfully represents the 'tail' of the valence Compton profile, while the tabulate core absorption profile represents the edge region. This 'extraction' process allows for a reliable removal of the Compton background. Furthermore, the use of a quantitative Hartree-Fock core profile should, in theory, leave data on the same scale as the structure factor $S(\mathbf{q}, \omega)$.

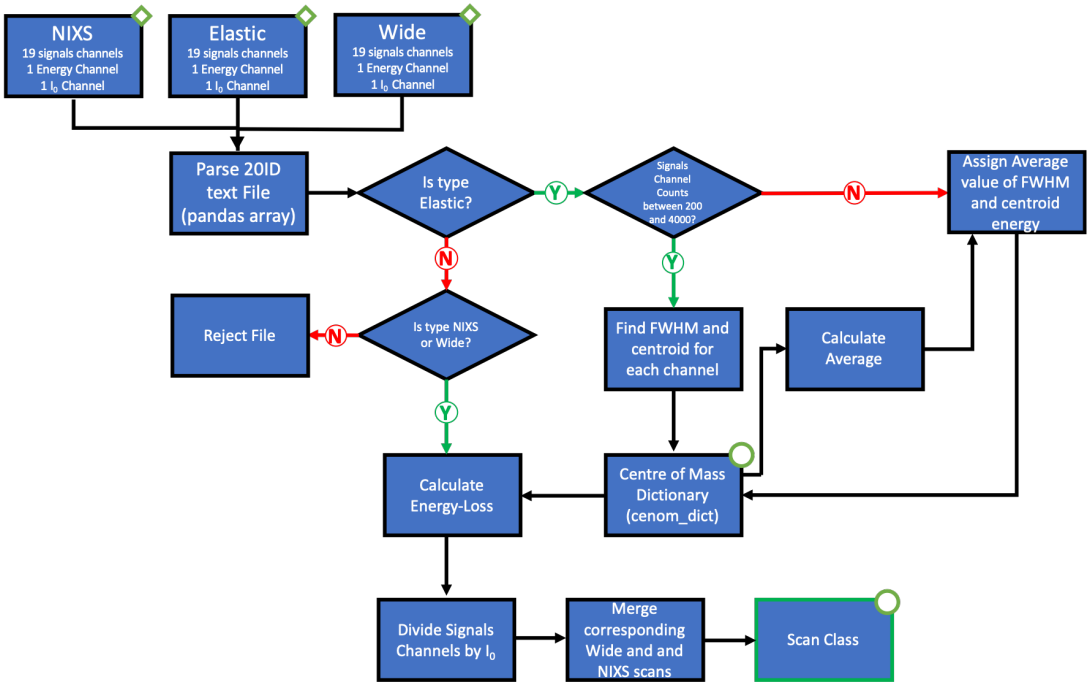


FIGURE B2: Logic flow diagram for the LERIX script written as a module for the XRStools software.

The extraction module, as well as other useful features beyond this discussion, within XRStools makes this code extremely useful for careful treatment of XRSS data. However, the python

code has been maintained for use with the ESRF ID-20 beamline only. In order to treat data from the LERIX beamline (20-ID) at APS using XRStools, a python module, xrs_read.read_lerix, was written by the candidate to parse and prepare LERIX data for analysis in XRStools.

Raw XRSS data at the LERIX beamline is typically received in ASCII format as three types: (i) elastic (ii) nixs and (iii) wide. ASCII files for each type contain a variety of scan configuration information (e.g. scan time, regions and motor positions) as well as the energy position, $I_0$ intensity and the detector values for each of the 19 crystal analysers [1]. The elastic file type contains data for the elastic X-ray scattering region, typically between $-3\,\mathrm{eV}$ to $3\,\mathrm{eV}$. The wide file type contains a low energy resolution scan over the whole energy region of interest (e.g. for the C *K*-edge: $3\,\mathrm{eV}$ to $450\,\mathrm{eV}$) and captures the Compton profile for extraction. The nixs file contains the core-loss region of the spectrum and is typically performed with better statistics (longer count times, higher resolution) than the wide region. The xrs_read.read_lerix module parses these three file types and treats the data so that it is ready for extraction using the XRStools.xrs_extraction module. A logic flow diagram for the xrs_read.read_lerix module is shown in Figure B2. The module treats the data by finding the FWHM and centroid position of the elastic profile for each analyser by Gaussian fitting. This information is then used to convert the raw monochromator energy value to the core-loss energy scale (i.e. $E = E_i - E_f$) for nixs and wide scans, and to report the resolution for each crystal analyser. The nixs and wide scans are then merged to produce the final raw data which can be analysed using XRStools. The treated data can be viewed graphically using the matplotlib library, and also has a user interface for exporting and saving the data for future use.

The full XRStools code with LERIX support is available on the candidate's github page, which also contains instructions for installation and example usage:

https://github.com/LJRH/XRStools

[1] Information regarding the LERIX beamline design can be found in Ref. [114]

# Appendix C

# Gold Uptake Experimental Details

A series of batch uptake experiments were conducted to quantify the adsorption of $Au^{III}$ chloride onto Pyro-Oak-650. Details of the uptake experiment are available in Section 5.3.1. This appendix contains details regarding the choice of pH buffer and the fitting of the uptake data. The results from the uptake experiment discussed in Chapter 5 are shown below in Table C1.

TABLE C1: Results of batch gold uptake experiment (pH 6).

| Initial Au Conc. $C_{init}$ ($\mathrm{mg\,l^{-1}}$) | Char Mass m (mg) | Final Conc. $C_f$ ($\mathrm{mg\,l^{-1}}$) | Dilution Factor/d | Initial Au:Char Ratio/$C_e$ ($\mathrm{mg\,l^{-1}}$) | Equilibrium Au:Char Ratio/$Q_e$ ($\mathrm{mg\,l^{-1}}$) | Std.Dev |
|---|---|---|---|---|---|---|
| 50 | 149.4 | 2.4 | 2 | 6.69 | 6.05 | |
| 50 | 146.4 | 1.5 | 2 | 6.83 | 6.42 | 0.26 |
| 50 | 148.4 | 0.2 | 2 | 6.75 | 6.69 | |
| 100 | 157.6 | 1.6 | 2 | 12.69 | 12.28 | |
| 100 | 158.3 | 0.7 | 2 | 12.63 | 12.46 | 0.25 |
| 100 | 140.7 | 4.7 | 2 | 14.21 | 25.82 | |
| 200 | 148.0 | 2.0 | 10 | 27.03 | 24.32 | 1.22 |
| 200 | 155.0 | 2.3 | 10 | 25.81 | 22.84 | |
| 300 | 153.7 | 6.2 | 10 | 39.04 | 30.97 | |
| 300 | 150.6 | 4.9 | 10 | 39.84 | 33.33 | 1.90 |
| 300 | 151.0 | 3.1 | 10 | 39.74 | 35.63 | |
| 400 | 152.0 | 8.0 | 10 | 52.63 | 42.11 | |
| 400 | 153.8 | 1.8 | 10 | 52.02 | 49.67 | 3.82 |
| 400 | 152.0 | 1.5 | 10 | 52.63 | 50.66 | |
| 500 | 147.5 | 5.6 | 10 | 67.80 | 60.20 | |
| 500 | 151.1 | 6.9 | 10 | 66.18 | 57.05 | 1.30 |
| 500 | 143.4 | 7.7 | 10 | 69.74 | 59.00 | |
| 750 | 157.0 | 7.8 | 20 | 95.54 | 75.67 | |
| 750 | 156.0 | 6.6 | 20 | 96.15 | 79.23 | 1.89 |
| 750 | 140.0 | 9.5 | 20 | 107.14 | 80.00 | |
| 1000 | 152.6 | 13.3 | 20 | 131.06 | 96.20 | |
| 1000 | 152.3 | 12.7 | 20 | 131.32 | 97.96 | 2.62 |
| 1000 | 151.3 | 15.3 | 20 | 132.19 | 91.74 | |

$$C_e = \frac{C_i \cdot V}{m} \cdot 100 \tag{C1}$$

$$Q_e = \frac{((C_i - C_f) \cdot d) \cdot V}{m} \tag{C2}$$

The initial gold:char ratio ($C_e$; $\mathrm{mg\,g^{-1}}$), the concentration prior to adsorption, was calculated using Equation C1. The equilibrium gold:char ratio ($Q_e$; $\mathrm{mg\,g^{-1}}$), the concentration of gold after adsorption, was calculated using Equation C2 using flame AAS. The $C_i$ ($\mathrm{mg\,l^{-1}}$) is the prepared initial Au concentration and $C_f$ ($\mathrm{mg\,l^{-1}}$) is the final Au concentration measured by flame atomic absorption spectrophotometry (AAS). The mass of biochar and the dilution factor used for AAS measurements are $m$ and $d$ respectively. The volume $V$ of solute used during AAS spectrophotometry was $20\,\mathrm{ml}$.

$$Q_e = \frac{(C_e \cdot kQ_{max})}{(1 + kC_e)} \tag{C3}$$

The gold adsorption isotherm was modelled using a Langmuir expression (Equation C3). The use of a Langmuir function has been shown to represent the adsorption of inorganic species onto pyrolsyis carbon well [388]. Fitting was performed in OrginPro2019 using Equation C3, where k ($\mathrm{mg^{-1}}$) is the Langmuir constant and $Q_{max}$ is the maximum uptake onto the biochar. The Langmuir model was used to estimate adsorption onto, an assumed, heterogeneous distribution of active sites on the biochar surface. Fitting was achieved with a $\chi^2_{reduced}$ of 1.8 and an adjusted R square value of 0.997, results are shown in Table C2.

TABLE C2: Results of Langmuir fit of batch uptake experiment.

| Fitting Variable | Fit Value | Standard Error |
|---|---|---|
| Qmax | 391 | 25 |
| k | 0.00251 | $1.8 \times 10^{-4}$ |

## Buffer Selection

An Acetic acid buffer was selected for the gold uptake experiment. The acetic acid buffer was prepared by adding $100\,\mathrm{ml}$ of 1 M NaOH to $0.6\,\mathrm{ml}$ of $CH_3COOH$ and making up to $500\,\mathrm{ml}$ volumetrically using high-purity water (>$18\,\mathrm{M\Omega\,cm}$). The selection of the acetic acid buffer was due

to a failed attempt using MOPS (3-(N-morpholino)propanesulfonic acid) buffer (Figure C1).

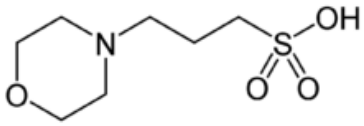


FIGURE C1: MOPS (3-(N-morpholino)propanesulfonic acid).

MOPS is standard Good's buffer and is frequently used as a buffering agent in biology and biochemistry in the presence of inorganic species. It is not known to form complexes with inorganic species and is highly effective at maintaining pH 7 in an aqueous environment. However, when MOPS was applied to the $[Au^{III}Cl_4]^-$ solution, it immediately formed a red/purple colour indicating the formation of gold nanoparticles (Figure C2). On further reading it was found that Good's buffers readily precipitate $Au^0$ from gold chloride solutions [389]. Further control experiments (without pyrolysis carbon) were conducted to demonstrate that the Acetic acid buffer did not lead to nanoparticulate formation at pH 6 (Figure C2).

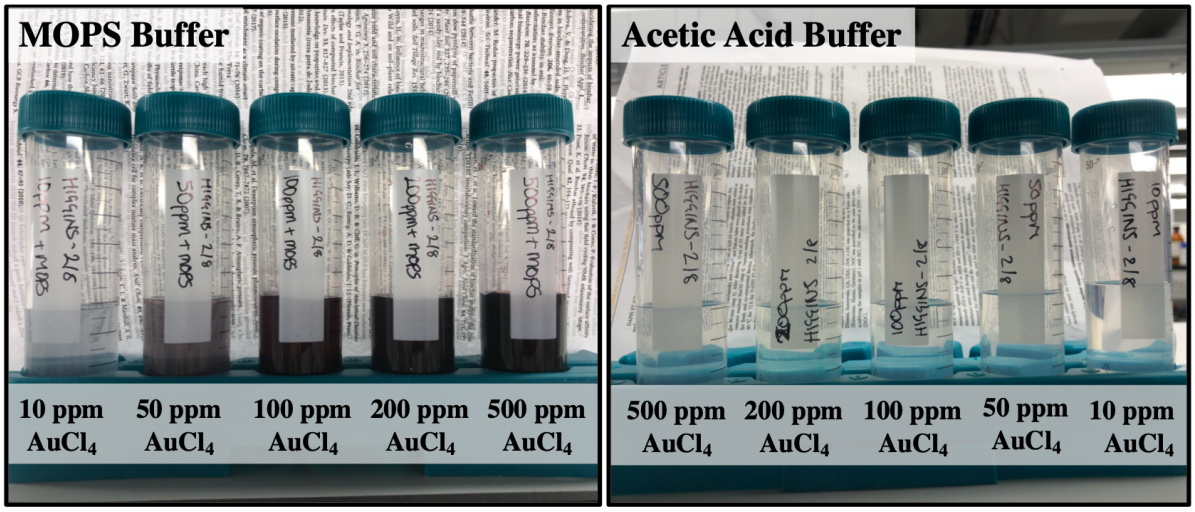


FIGURE C2: Photographs of a range of $[Au^{III}Cl_4]^-$ concentrations (10 - 500 ppm) buffered at pH 6 using MOPS buffer (left) and acetic acid buffer (right). MOPS buffer resulted in precipitation of nanoparticulate gold.

# Appendix D

# Pyrolysis of Hydrothermal Carbon - C *K*-edge Fitting

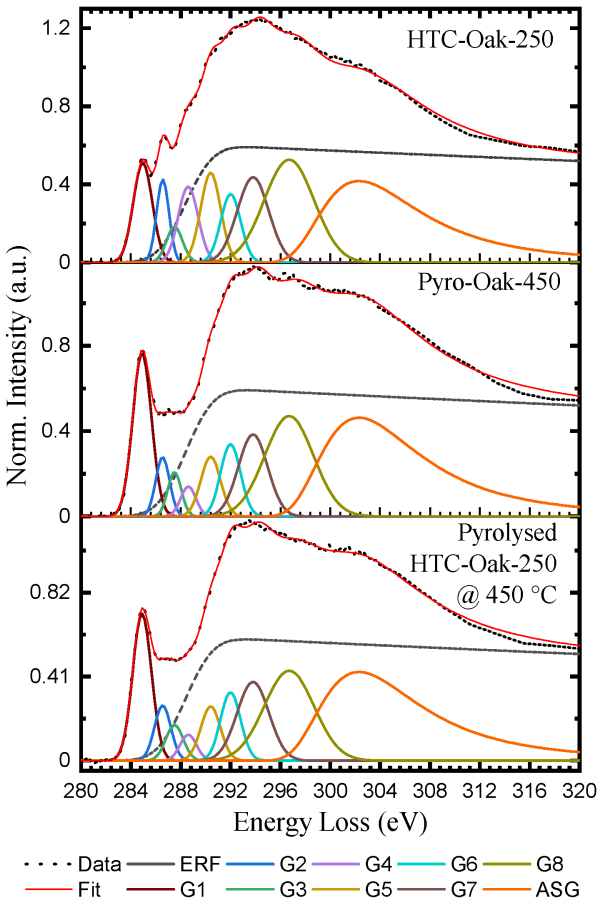


FIGURE D1: Results of Gaussian fitting for HTC-Oak-250, Pyro-Oak-450 and PyHTC-Oak-250+450.

# Bibliography


[1] Intergovernmental Panel on Climate Change (IPCC). IPCC Fifth Assessment Report (AR5) Observed Climate Change Impacts Database, Version 2.01, 2017.

[2] Intergovernmental Panel on Climate Change (IPCC). Global warming of 1.5 Celsius. Technical report, IPCC, 2018.

[3] Adrian E. Raftery, Alec Zimmer, Dargan M. W. Frierson, Richard Startz, and Peiran Liu. Less than 2 Celsius warming by 2100 unlikely. *Nature Climate Change*, 7(9):637–641, 9 2017.

[4] Kevin E. Trenberth, John T. Fasullo, and Theodore G. Shepherd. Attribution of climate extreme events. *Nature Climate Change*, 5(8):725–730, 8 2015.

[5] Carl-Friedrich Friedrich Schleussner, Joeri Rogelj, Michiel Schaeffer, Tabea Lissner, Rachel Licker, Erich M. Fischer, Reto Knutti, Anders Levermann, Katja Frieler, and William Hare. Science and policy characteristics of the Paris Agreement temperature goal. *Nature Climate Change*, 6(9):827–835, 9 2016.

[6] W. Dansgaard, S. J. Johnsen, H. B. Clausen, D. Dahl-Jensen, N. S. Gundestrup, C. U. Hammer, C. S. Hvidberg, J. P. Steffensen, A. E. Sveinbjörnsdottir, J. Jouzel, and G. Bond. Evidence for general instability of past climate from a 250-kyr ice-core record. *Nature*, 364(6434):218–220, 1993.

[7] Patrick Rioual, Valerie Andrieu-Ponel, Miri Rietti-Shati, Richard W Battarbee, Jacques-louis de Beaulieu, Rachid Cheddadi, Maurice Reille, Helena Svobodova, and Aldo Shemesh. High-resolution record of climate stability in France during the last interglacial period. *Nature*, 413(September):293–296, 2001.

[8] Stephen R. Carpenter and Elena M. Bennett. Reconsideration of the planetary boundary for phosphorus. *Environmental Research Letters*, 6(1):014009, 1 2011.

[9] Markus Reichstein, Michael Bahn, Philippe Ciais, Dorothea Frank, Miguel D. Mahecha, Sonia I. Seneviratne, Jakob Zscheischler, Christian Beer, Nina Buchmann, David C. Frank, Dario Papale, Anja Rammig, Pete Smith, Kirsten Thonicke, Marijn Van Der Velde, Sara Vicca, Ariane Walz, and Martin Wattenbach. Climate extremes and the carbon cycle. *Nature*, 500(7462):287–295, 2013.

[10] Linn M. Persson, Magnus Breitholtz, Ian T. Cousins, Cynthia A. de Wit, Matthew MacLeod, and Michael S. McLachlan. Confronting Unknown Planetary Boundary Threats from Chemical Pollution. *Environmental Science & Technology*, 47(22):12619–12622, 11 2013.

[11] S. E. Nelms, C. Coombes, L. C. Foster, T. S. Galloway, B. J. Godley, P. K. Lindeque, and M. J. Witt. Marine anthropogenic litter on British beaches: A 10-year nationwide assessment using citizen science data. *Science of the Total Environment*, 579:1399–1409, 2017.

[12] Joeri Rogelj, Michel Den Elzen, Niklas Höhne, Taryn Fransen, Hanna Fekete, Harald Winkler, Roberto Schaeffer, Fu Sha, Keywan Riahi, and Malte Meinshausen. Paris Agreement climate proposals need a boost to keep warming well below 2 Degrees Celsius. *Nature*, 534(7609):631–639, 2016.

[13] Simon L. Lewis and Mark A. Maslin. Defining the Anthropocene. *Nature*, 519(7542):171–180, 3 2015.

[14] J. Rockström, W. Steffen, K. Noone, Å. Persson, F. S. Chapin, E. F. Lambin, T. M. Lenton, M. Scheffer, C. Folke, H. J. Schellnhuber, B. Nykvist, C. A. de Wit, T. Hughes, S. van der Leeuw, H. Rodhe, S. Sörlin, P. K. Snyder, R. Costanza, U. Svedin, M. Falkenmark, L. Karlberg, R. W. Corell, V. J. Fabry, J. Hansen, B. Walker, D. Liverman, K. Richardson, P. Crutzen, and J. A. Foley. A safe operation space for humanity. *Nature*, 461(September):472–475, 2009.

[15] Will Steffen, Katherine Richardson, J. Rockstrom, Sarah E. Cornell, Ingo Fetzer, Elena M. Bennett, Reinette Biggs, Stephen R. Carpenter, Wim de Vries, Cynthia A. de Wit, Carl Folke, Dieter Gerten, Jens Heinke, Georgina M. Mace, Linn M. Persson, Veerabhadran Ramanathan, Belinda Reyers, S. Sorlin, Johan Rockström, Sarah E. Cornell, Ingo Fetzer, Elena M. Bennett, Reinette Biggs, Stephen R. Carpenter, Wim de Vries, Cynthia A. de Wit, Carl Folke, Dieter Gerten, Jens Heinke, Georgina M. Mace, Linn M. Persson, Veerabhadran Ramanathan, Belinda Reyers, and Sverker Sörlin. Planetary boundaries: Guiding human development on a changing planet. *Science*, 347(6223):1259855–1259855, 2 2015.

[16] Patricia M. Glibert, Roxane Maranger, Daniel J. Sobota, and Lex Bouwman. The Haber Bosch-harmful algal bloom (HB-HAB) link. *Environmental Research Letters*, 9(10), 2014.

[17] Kate Raworth. A Doughnut for the Anthropocene: humanity's compass in the 21st century. *The Lancet Planetary Health*, 1(2):e48–e49, 2017.

[18] Maarten Hajer, Måns Nilsson, Kate Raworth, Peter Bakker, Frans Berkhout, Yvo de Boer, Johan Rockström, Kathrin Ludwig, and Marcel Kok. Beyond Cockpit-ism: Four Insights to Enhance the Transformative Potential of the Sustainable Development Goals. *Sustainability*, 7(2):1651–1660, 2 2015.

[19] Daniel W. O'Neill, Andrew L. Fanning, William F. Lamb, and Julia K. Steinberger. A good life for all within planetary boundaries. *Nature Sustainability*, 1(2):88–95, 2 2018.

[20] J.-P. Gattuso, A. Magnan, R. Billé, W. W. L. Cheung, E. L. Howes, F. Joos, D. Allemand, L. Bopp, S. R. Cooley, C. M. Eakin, O. Hoegh-Guldberg, R. P. Kelly, H.-O. Pörtner, A. D. Rogers, J. M. Baxter, D. Laffoley, D. Osborn, A. Rankovic, J. Rochette, U. R. Sumaila, S. Treyer, and C. Turley. Contrasting futures for ocean and society from different anthropogenic CO 2 emissions scenarios. *Science*, 349(6243):45, 7 2015.

[21] International Energy Agency. The future of petrochemicals. Technical report, International Energy Agency, IEA-petrochemicals, 10 2018.

[22] Arne Kätelhön, Raoul Meys, Sarah Deutz, Sangwon Suh, and André Bardow. Climate change mitigation potential of carbon capture and utilization in the chemical industry. *Proceedings of the National Academy of Sciences*, 116(23):11187–11194, 6 2019.

[23] Pete Smith and John R. Porter. Bioenergy in the IPCC Assessments. *GCB Bioenergy*, 10(7):428–431, 2018.

[24] James H. Clark. Green biorefinery technologies based on waste biomass. *Green Chemistry*, 21(6):1168–1170, 2019.

[25] Arthur J. Ragauskas, Charlotte K. Williams, Brian H. Davison, George Britovsek, John Cairney, Charles A. Eckert, William J. Frederick, Jason P. Hallett, David J. Leak, Charles L. Liotta, Jonathan R. Mielenz, Richard Murphy, Richard Templer, and Timothy Tschaplinski. The Path Forward for Biofuels and Biomaterials. *Science*, 311(5760):484–489, 1 2006.

[26] Walter R. Stahel. The circular economy. *Nature*, 531(7595):435–438, 3 2016.

[27] Shikha Dahiya, A. Naresh Kumar, J. Shanthi Sravan, Sulogna Chatterjee, Omprakash Sarkar, and S. Venkata Mohan. Food waste biorefinery: Sustainable strategy for circular bioeconomy. *Bioresource Technology*, 248:2–12, 1 2018.

[28] WRAP (Waste Resources Action Programme). Action on food waste, 2021.

[29] Energy Department for Business and Industrial Strategy. 2019 UK Greenhouse Gas Emissions, Final Figures. Technical report, Department for Business, Energy and Industrial Strategy (UK Govt), 2021.

[30] Lucie A. Pfaltzgraff, Mario De Bruyn, Emma C. Cooper, Vitaly Budarin, and James H. Clark. Food waste biomass: a resource for high-value chemicals. *Green Chemistry*, 15(2):307, 2013.

[31] Francesco Cherubini. The biorefinery concept: Using biomass instead of oil for producing energy and chemicals. *Energy Conversion and Management*, 51(7):1412–1421, 2010.

[32] Paul Anastas and Nicolas Eghbali. Green Chemistry: Principles and Practice. *Chem. Soc. Rev.*, 39(1):301–312, 2010.

[33] Klaus Kümmerer, James H. Clark, and Vânia G. Zuin. Rethinking chemistry for a circular economy. *Science*, 367(6476):369–370, 1 2020.

[34] James H Clark. Green chemistry for the second generation biorefinery—sustainable chemical manufacturing based on biomass. *Journal of Chemical Technology & Biotechnology*, 82(7):603–609, 7 2007.

[35] Yuanyuan Ren, Miao Yu, Chuanfu Wu, Qunhui Wang, Ming Gao, Qiqi Huang, and Yu Liu. A comprehensive review on food waste anaerobic digestion: Research updates and tendencies. *Bioresource Technology*, 247:1069–1076, 1 2018.

[36] Yohanis Irenius Mandik, Benjamas Cheirsilp, Sirasit Srinuanpan, Wageeporn Maneechote, Piyarat Boonsawang, Poonsuk Prasertsan, and Sarote Sirisansaneeyakul. Zero-waste biorefinery of oleaginous microalgae as promising sources of biofuels and biochemicals through direct transesterification and acid hydrolysis. *Process Biochemistry*, 95(February):214–222, 8 2020.

[37] M. Fatih Demirbas. Biorefineries for biofuel upgrading: A critical review. *Applied Energy*, 86:151–161, 11 2009.

[38] Harry Marsh and Francisco Rodríguez-Reinoso. *Activated Carbon*. Elsevier, 2006.

[39] Henry M. Leicester. Tobias Lowitz—Discoverer of basic laboratory methods. *Journal of Chemical Education*, 22(3):149, 3 1945.

[40] S. J. Allen, L. Whitten, and G. Mckay. The Production and Characterisation of Activated Carbons: A Review. *Developments in Chemical Engineering and Mineral Processing*, 6(5):231–261, 5 2008.

[41] Li Li Zhang and X. S. Zhao. Carbon-based materials as supercapacitor electrodes. *Chemical Society Reviews*, 38(9):2520, 2009.

[42] Philippe Serp and Jośe Lúís Figueiredo, editors. *Carbon Materials for Catalysis*. John Wiley & Sons, Inc., Hoboken, NJ, USA, 12 2008.

[43] Maria-Magdalena Titirici, Markus Antonietti, and Niki Baccile. Hydrothermal carbon from biomass: a comparison of the local structure from poly- to monosaccharides and pentoses/hexoses. *Green Chemistry*, 10(11):1204, 2008.

[44] Maria-Magdalena Titirici, Robin J. White, Nicolas Brun, Vitaliy L. Budarin, Dang Sheng Su, Francisco del Monte, James H. Clark, and Mark J. MacLachlan. Sustainable carbon materials. *Chemical Society Reviews*, 44(1):250–290, 10 2015.

[45] Robin J. White, Vitaly Budarin, Rafael Luque, James H. Clark, and Duncan J. Macquarrie. Tuneable porous carbonaceous materials from renewable resources. *Chemical Society Reviews*, 38(12):3401, 2009.

[46] Gangaraju Gedda, Chun Yi Lee, Yu Chih Lin, and Hui Fen Wu. Green synthesis of carbon dots from prawn shells for highly selective and sensitive detection of copper ions. *Sensors and Actuators, B: Chemical*, 224:396–403, 2016.

[47] Shuyan Gao, Xiaoge Li, Lingyu Li, and Xianjun Wei. A versatile biomass derived carbon material for oxygen reduction reaction, supercapacitors and oil/water separation. *Nano Energy*, 33:334–342, 2017.

[48] Weixue Meng, Xue Bai, Boyang Wang, Zhongyi Liu, Siyu Lu, and Bai Yang. Biomass-Derived Carbon Dots and Their Applications. *ENERGY & ENVIRONMENTAL MATERIALS*, 2(3):172–192, 9 2019.

[49] V.L. Budarin, J.H. Clark, R Luque, D.J. Macquarrie, Robin. J. White, and R K Milkowski. PCT Int. Patent WO 2007104798 A2 20070920.

[50] Sabina A. Nicolae, Heather Au, Pierpaolo Modugno, Hui Luo, Anthony E. Szego, Mo Qiao, Liang Li, Wang Yin, Hero J. Heeres, Nicole Berge, and Maria Magdalena Titirici. Recent advances in hydrothermal carbonisation: From tailored carbon materials and biochemicals to applications and bioenergy. *Green Chemistry*, 22(15):4747–4800, 2020.

[51] Andrea Kruse, Axel Funke, and Maria Magdalena Titirici. Hydrothermal conversion of biomass to fuels and energetic materials. *Current Opinion in Chemical Biology*, 17(3):515–521, 2013.

[52] A. Chabbi, J. Lehmann, P. Ciais, H. W. Loescher, M. F. Cotrufo, A. Don, M. Sanclements, L. Schipper, J. Six, P. Smith, and C. Rumpel. Aligning agriculture and climate policy. *Nature Climate Change*, 7(5):307–309, 2017.

[53] Johannes Lehmann. A handful of carbon. *Nature*, 447(7141):143–144, 2007.

[54] Pete Smith. Soil carbon sequestration and biochar as negative emission technologies. *Global Change Biology*, 22(3):1315–1324, 3 2016.

[55] Shaon Kumar Das, R. K. Avasthe, Raghavendra Singh, and Subhash Babu. Biochar as carbon negative in carbon credit under changing climate. *Current Science*, 107(7):1090–1091, 2014.

[56] Paul T. Williams and Serpil Besler. The influence of temperature and heating rate on the slow pyrolysis of biomass. *Renewable Energy*, 7(3):233–250, 3 1996.

[57] A. V. Bridgwater. Review of fast pyrolysis of biomass and product upgrading. *Biomass and Bioenergy*, 38:68–94, 2012.

[58] S. Czernik and A. V. Bridgwater. Overview of Applications of Biomass Fast Pyrolysis Oil. *Energy & Fuels*, 18(2):590–598, 3 2004.

[59] Johannes Lehmann, Jose Pereira, Christopher Steiner, Thomas Nehls, Wolfgang Zech, and Bruno Glaser. Nutrient availability and leaching in an archaeological Anthrosol and a Ferralsol of the Central Amazon basin: fertilizer, manure and charcoal amendments. *Plant and Soil*, 249:343–357, 5 2003.

[60] Yunchao Li, Bo Xing, Yan Ding, Xinhong Han, and Shurong Wang. A critical review of the production and advanced utilization of biochar via selective pyrolysis of lignocellulosic biomass. *Bioresource Technology*, 312:123614, 2020.

[61] Wei-Hao Hao Huang, Duu-Jong Jong Lee, and Chihpin Huang. Modification on biochars for applications: A research update. *Bioresource Technology*, 319:124100, 1 2021.

[62] Maria-Magdalena Titirici, Arne Thomas, and Markus Antonietti. Back in the black: hydrothermal carbonization of plant material as an efficient chemical process to treat the CO2 problem? *New Journal of Chemistry*, 31(6):787, 6 2007.

[63] Anthony N. Stranges. Friedrich Bergius and the Rise of the German Synthetic Fuel Industry. *Isis*, 75(4):643–667, 12 1984.

[64] Friedrich Bergius. Beitraege zur Theorie der Kohleenstehung. *Naturwissenschaften*, 16:1–10, 1928.

[65] Kubilay Tekin, Selhan Karagöz, and Sema Bektaş. A review of hydrothermal biomass processing. *Renewable and Sustainable Energy Reviews*, 40:673–687, 2014.

[66] Eloise Bevan, Jile Fu, and Ying Zheng. Challenges and opportunities of hydrothermal carbonisation in the UK; Case study in Chirnside. *RSC Advances*, 10(52):31586–31610, 2020.

[67] E. Danso-Boateng, R. G. Holdich, S. J. Martin, G. Shama, and A. D. Wheatley. Process energetics for the hydrothermal carbonisation of human faecal wastes. *Energy Conversion and Management*, 105:1115–1124, 2015.

[68] R. E. Franklin. The structure of graphitic carbons. *Acta Crystallographica*, 4(3):253–261, 1951.

[69] J.D. Bernal. The structure of graphite. *Proceedings of the Royal Society of London. Series A*, 106(740):749–773, 12 1924.

[70] R. E. Franklin. Crystallite Growth in Graphitizing and Non-Graphitizing Carbons. *Proceedings of the Royal Society A: Mathematical, Physical and Engineering Sciences*, 209(1097):196–218, 1951.

[71] P.J.F. Harris. Rosalind Franklin's work on coal, carbon, and graphite. *Interdisciplinary Science Reviews*, 26(3):204–210, 2001.

[72] P. J. F. Harris. Structure of non-graphitising carbons. *International Materials Reviews*, 42(5):206–218, 1997.

[73] Erika Mészáros, Emma Jakab, Gábor Várhegyi, Jared Bourke, Merilyn Manley-Harris, Teppei Nunoura, and Michael Jerry Antal. Do All Carbonized Charcoals Have the Same Chemical Structure? 1. Implications of Thermogravimetry-Mass Spectrometry Measurements. *Industrial & Engineering Chemistry Research*, 46(18):5943–5953, 8 2007.

[74] J. Robertson. Amorphous carbon. *Advances in Physics*, 35(4):317–374, 1 1986.

[75] Peter J.F. Harris. New perspectives on the structure of graphitic carbons. *Critical Reviews in Solid State and Materials Sciences*, 30(4):235–253, 2005.

[76] Peter J. F. Harris. Fullerene-like models for microporous carbon. *Journal of Materials Science*, 48(2):565–577, 1 2013.

[77] P. J.F. Harris. Non-graphitizing carbon: Its structure and formation from organic precursors. *Eurasian Chemico-Technological Journal*, 21(3):215–226, 2019.

[78] Zhi Li Zhang, Rik Brydson, Zabeada Aslam, Sundeep Reddy, Andy Brown, Aidan Westwood, and Brian Rand. Investigating the structure of non-graphitising carbons using electron energy loss spectroscopy in the transmission electron microscope. *Carbon*, 49(15):5049–5063, 2011.

[79] Zhipeng Wang, Hironori Ogata, Gan Jet Hong Melvin, Michiko Obata, Shingo Morimoto, Josue Ortiz-Medina, Rodolfo Cruz-Silva, Masatsugu Fujishige, Kenji Takeuchi, Hiroyuki Muramatsu, Tae-Young Kim, Yoong Ahm Kim, Takuya Hayashi, Mauricio Terrones, Yoshio Hashimoto, and Morinobu Endo. Structural evolution of hydrothermal carbon spheres induced by high temperatures and their electrical properties under compression. *Carbon*, 121:426–433, 9 2017.

[80] Fernanda Gomes de Mendonça, Igor Tadeu da Cunha, Ricardo Reis Soares, Juliana Cristina Tristão, and Rochel Montero Lago. Tuning the surface properties of biochar by thermal treatment. *Bioresource Technology*, 246:28–33, 12 2017.

[81] H.P P. Boehm. Surface oxides on carbon and their analysis: a critical assessment. *Carbon*, 40(2):145–149, 2 2002.

[82] Harry Marsh. A tribute to Philip L. Walker. *Carbon*, 29(6):703–704, 1991.

[83] Nils Borchard, Brenton Ladd, Sita Eschemann, Dominik Hegenberg, Bodo Maria Möseler, and Wulf Amelung. Black carbon and soil properties at historical charcoal production sites in Germany. *Geoderma*, 232-234:236–242, 11 2014.

[84] Michael Jerry Antal and Morten Grønli. The Art, Science, and Technology of Charcoal Production †. *Industrial & Engineering Chemistry Research*, 42(8):1619–1640, 4 2003.

[85] G. B. Olson. Designing a New Material World. *Science*, 288(5468):993–998, 5 2000.

[86] Grant Bunker. *Introduction to XAFS*. Cambridge University Press, Cambridge, 2010.

[87] Antonella Balerna and Settimio Mobilio. Introduction to Synchrotron Radiation. In Settimio Mobilio, Federico Boscherini, and Carlo Meneghini, editors, *Synchrotron Radiation: Basics, Methods and Applications*, chapter 1, pages 3–28. Springer Berlin Heidelberg, Berlin, Heidelberg, 2015.

[88] ECN and TNO. Phyllis2 - Database for (treated) biomass, algae, feedstocks for biogas production and biochar, 2020.

[89] Aidan Mark Smith. *Fate and influence of inorganics and heteroatoms during the hydrothermal carbonisation of biomass*. PhD thesis, University of Leeds, 11 2018.

[90] Yasushige Mori, Hideto Yoshida, and Hiroaki Masuda. Particle size analysis by laser diffraction method using reference particles. *Advanced Materials Research*, 508:33–37, 2012.

[91] F. Haguenau, P. W. Hawkes, J. L. Hutchison, B. Satiat-Jeunema??tre, G. T. Simon, and D. B. Williams. Key events in the history of electron microscopy. *Microscopy and Microanalysis*, 9(2):96–138, 2003.

[92] D. B. Wittry, R. P. Ferrier, and V. E. Cosslett. Selected-area electron spectrometry in the transmission electron microscope. *Journal of Physics D: Applied Physics*, 2(12):1767–1773, 1969.

[93] R. M. Langford and C. Clinton. In situ lift-out using a FIB-SEM system. *Micron*, 35(7):607–611, 2004.

[94] Jian Li, T. Malis, and S. Dionne. Recent advances in FIB–TEM specimen preparation techniques. *Materials Characterization*, 57(1):64–70, 7 2006.

[95] Liping Zhong, Dingkai Chen, and Spyridon Zafeiratos. A mini review of in situ near-ambient pressure XPS studies on non-noble, late transition metal catalysts. *Catalysis Science & Technology*, 9(15):3851–3867, 2019.

[96] Klaus Wille. *Physik der Teilchenbeschleuniger und Synchrotronstrahlungsquellen*. Oxford University Press, Dortmund, Germany, 1996.

[97] M. Newville. Fundamentals of XAFS. *Reviews in Mineralogy and Geochemistry*, 78(1):33–74, 2014.

[98] Farrel W. Lytle. The EXAFS family tree: A personal history of the development of extended X-ray absorption fine structure. *Journal of Synchrotron Radiation*, 6(3):123–134, 1999.

[99] Annibale Mottana and Augusto Marcelli. The Historical Development of X-ray Absorption Fine Spectroscopy and of Its Applications to Materials Science. *History of Mechanism and Machine Science*, 27:275–301, 2015.

[100] Charles G. Barkla. The spectra of the fluorescent Röntgen radiations. *The London, Edinburgh, and Dublin Philosophical Magazine and Journal of Science*, 22(129):396–412, 1911.

[101] J.J. Rehr, S.I. Zabinsky, A. Ankudinov, and R.C. Albers. Atomic-XAFS and XANES. *Physica B: Condensed Matter*, 208-209(C):23–26, 3 1995.

[102] J. J. Rehr and A. L. Ankudinov. Progress in the theory and interpretation of XANES. *Coordination Chemistry Reviews*, 249(1-2):131–140, 2005.

[103] Yves Joly, Chiara Cavallari, Sergey A. Guda, and Christoph J. Sahle. Full-Potential Simulation of X-ray Raman Scattering Spectroscopy. *Journal of Chemical Theory and Computation*, 13(5):2172–2177, 2017.

[104] Kevin Jorissen and John J. Rehr. New developments in FEFF: FEFF9 and JFEFF. *Journal of Physics: Conference Series*, 430(1), 2013.

[105] R. de L. Kronig and W. G. Penney. Quantum Mechanics of Electrons in Crystal Lattices. *Proceedings of the Royal Society A: Mathematical, Physical and Engineering Sciences*, 130(814):499–513, 1931.

[106] Dale E. Sayers, Edward A. Stern, and Farrel W. Lytle. New technique for investigating noncrystalline structures: Fourier analysis of the extended x-ray-absorption fine structure. *Physical Review Letters*, 27(18):1204–1207, 1971.

[107] Iina Juurinen, Tuomas Pylkkänen, Kari O. Ruotsalainen, Christoph J. Sahle, Giulio Monaco, Keijo Hämäläinen, Simo Huotari, and Mikko Hakala. Saturation Behavior in X-ray Raman Scattering Spectra of Aqueous LiCl. *The Journal of Physical Chemistry B*, 117(51):16506–16511, 12 2013.

[108] C. Sternemann and M. Wilke. Spectroscopy of low and intermediate Z elements at extreme conditions: in situ studies of Earth materials at pressure and temperature via X-ray Raman scattering. *High Pressure Research*, 36(3):275–292, 2016.

[109] Rafaella Georgiou, Pierre Gueriau, Christoph J. Sahle, Sylvain Bernard, Alessandro Mirone, Romain Garrouste, Uwe Bergmann, Jean-Pascal Rueff, and Loïc Bertrand. Carbon speciation in organic fossils using 2D to 3D x-ray Raman multispectral imaging. *Science Advances*, 5(8), 2019.

[110] Juho Inkinen, Johannes Niskanen, Tuomas Talka, Christoph J. Sahle, Harald Müller, Leonid Khriachtchev, Javad Hashemi, Ali Akbari, Mikko Hakala, and Simo Huotari. X-ray induced dimerization of cinnamic acid: Time-resolved inelastic X-ray scattering study. *Scientific Reports*, 5(1):15851, 12 2015.

[111] Luke J.R. Higgins, Andy P. Brown, John P. Harrington, Andrew B. Ross, Burkhard Kaulich, and Bhoopesh Mishra. Evidence for a core-shell structure of hydrothermal carbon. *Carbon*, 161:423–431, 5 2020.

[112] D.S. Sivia. *Elementary Scattering Theory*. Oxford University Press, 1 2011.

[113] W Shülke. *Electron Dynamics by Inelastic X-Ray Scattering*, volume 7. Oxford University Press, Oxford, 7 edition, 2007.

[114] T. T. Fister, G. T. Seidler, L. Wharton, A. R. Battle, T. B. Ellis, J. O. Cross, A. T. Macrander, W. T. Elam, T. A. Tyson, and Q. Qian. Multielement spectrometer for efficient measurement of the momentum transfer dependence of inelastic x-ray scattering. *Review of Scientific Instruments*, 77(6):0–7, 2006.

[115] Karen Heymann, Johannes Lehmann, Dawit Solomon, Biqing Liang, Eduardo Neves, and Sue Wirick. Can functional group composition of alkaline isolates from black carbon-rich soils be identified on a sub-100nm scale? *Geoderma*, 235-236:163–169, 2014.

[116] Chunmei Chen, James J. Dynes, Jian Wang, Chithra Karunakaran, and Donald L. Sparks. Soft X-ray spectromicroscopy study of mineral-organic matter associations in pasture soil clay fractions. *Environmental Science and Technology*, 48(12):6678–6686, 2014.

[117] A. Naber, M. Plaschke, J. Rothe, H. Hofmann, and Th. Fanghänel. Scanning transmission X-ray and laser scanning luminescence microscopy of the carboxyl group and Eu(III) distribution in humic acid aggregates. *Journal of Electron Spectroscopy and Related Phenomena*, 153(3):71–74, 10 2006.

[118] Markus Plaschke, Jörg Rothe, Marcus Altmaier, Melissa A. Denecke, and Thomas Fanghänel. Near edge X-ray absorption fine structure (NEXAFS) of model compounds for the humic acid/actinide ion interaction. *Journal of Electron Spectroscopy and Related Phenomena*, 148(3):151–157, 9 2005.

[119] A. Braun, A. Kubatova, S. Wirick, and S. B. Mun. Radiation damage from EELS and NEXAFS in diesel soot and diesel soot extracts. *Journal of Electron Spectroscopy and Related Phenomena*, 170(1-3):42–48, 3 2009.

[120] A. P. Hitchcock, J. Li, S. R. Reijerkerk, P. Foley, H. D.H. Stöver, and I. Shirley. X-ray absorption spectroscopy of polyureas and polyurethanes and their use in characterizing chemical gradients in thin-walled polyurea capsules. *Journal of Electron Spectroscopy and Related Phenomena*, 156-158:467–471, 5 2007.

[121] Joan Vila-Comamala, Konstantins Jefimovs, Jörg Raabe, Tero Pilvi, Rainer H. Fink, Mathias Senoner, Andre Maaßdorf, Mikko Ritala, and Christian David. Advanced thin film technology for ultrahigh resolution X-ray microscopy. *Ultramicroscopy*, 109(11):1360–1364, 2009.

[122] Adam P. Hitchcock. Soft X-ray spectromicroscopy and ptychography. *Journal of Electron Spectroscopy and Related Phenomena*, 200:49–63, 4 2015.

[123] Dawit Solomon, Johannes Lehmann, Jennifer Harden, Jian Wang, James Kinyangi, Karen Heymann, Chithra Karunakaran, Yingshen Lu, Sue Wirick, and Chris Jacobsen. Micro- and nano-environments of carbon sequestration: Multi-element STXM-NEXAFS spectromicroscopy assessment of microbial carbon and mineral associations. *Chemical Geology*, 329:53–73, 2012.

[124] Junshan Xiu, Yunyan Liu, Benyi Wang, Yanling Xue, Min Chen, Te Ji, and Huiqiang Liu. Quantitative toxicological study of dose-dependent arsenic-induced cells: Via synchrotron-based STXM and FTIR measurement. *Analyst*, 145(13):4560–4568, 2020.

[125] J. Wang, C. Morin, L. Li, A. P. Hitchcock, A. Scholl, and A. Doran. Radiation damage in soft X-ray microscopy. *Journal of Electron Spectroscopy and Related Phenomena*, 170(1-3):25–36, 3 2009.

[126] M. Polacci, F. Arzilli, G. La Spina, N. Le Gall, B. Cai, M. E. Hartley, D. Di Genova, N. T. Vo, S. Nonni, R. C. Atwood, E. W. Llewellin, P. D. Lee, and M. R. Burton. Crystallisation in basaltic magmas revealed via in situ 4D synchrotron X-ray microtomography. *Scientific Reports*, 8(1):1–13, 2018.

[127] Johann Kastner, Bernhard Harrer, Guillermo Requena, and Oliver Brunke. A comparative study of high resolution cone beam X-ray tomography and synchrotron tomography applied to Fe- and Al-alloys. *NDT and E International*, 43(7):599–605, 2010.

[128] Gunjan Das, Anuradha Pallipurath, Joanna Leng, Kazimir Wanelik, John Mcginty, Russell Miller, Sin-yuen Chang, Laila H Al-madhagi, Shashidhara Marathae, Christoph Rau, Jan Sefcik, and L M Schroeder. Time-Resolved X-ray Phase-Contrast Imaging ( XPCI ) of Nucleation and Crystal Growth in the Anti-Solvent Crystallization of Lovastatin Time-Resolved X-ray Phase-Contrast Imaging ( XPCI ) of Nucleation and Crystal Growth in the Anti-Solvent Crystallization. *ChemRchiv*, pages 1–29, 2020.

[129] A. J. Bodey and C. Rau. Launch of the I13-2 data beamline at the Diamond Light Source synchrotron. *Journal of Physics: Conference Series*, 849(1), 2017.

[130] Doğa Dog˘a Gürsoy, Francesco De Carlo, Xianghui Xiao, and Chris Jacobsen. TomoPy: A framework for the analysis of synchrotron tomographic data. *Journal of Synchrotron Radiation*, 21(5):1188–1193, 9 2014.

[131] Ángel Fernández-Sanromán, Gabriela Lama, Marta Pazos, Emilio Rosales, Maria Ángeles Sanromán, and Maria Ángeles Sanromán. Bridging the gap to hydrochar production

and its application into frameworks of bioenergy, environmental and biocatalysis areas. *Bioresource Technology*, 320(September 2020):124399, 1 2020.

[132] Patrick Biller, Konstantinos Anastasakis, Aidan Smith, Juliano Souza Dos Passos, and Ib Johannsen. Hydrothermal liquefaction of organic waste streams on a continuous pilot scale reactor. In *Pyroliq 2019: Pyrolysis and Liquefaction of Biomass and Wastes*, 2019.

[133] Yafei Shen, Shili Yu, Shun Ge, Xingming Chen, Xinlei Ge, and Mindong Chen. Hydrothermal carbonization of medical wastes and lignocellulosic biomass for solid fuel production from lab-scale to pilot-scale. *Energy*, 118:312–323, 2017.

[134] Bo Hu, Kan Wang, Liheng Wu, Shu Hong Yu, Markus Antonietti, and Maria Magdalena Titirici. Engineering carbon materials from the hydrothermal carbonization process of biomass. *Advanced Materials*, 22(7):813–828, 2010.

[135] AC C O'Sullivan. Cellulose: the structure slowly unravels. *Cellulose*, 4(3):173–207, 1997.

[136] Camillo Falco, Niki Baccile, and Maria-Magdalena Titirici. Morphological and structural differences between glucose, cellulose and lignocellulosic biomass derived hydrothermal carbons. *Green Chemistry*, 13(11):3273, 2011.

[137] Aidan M. Smith, Surjit Singh, and Andrew B. Ross. Fate of inorganic material during hydrothermal carbonisation of biomass: Influence of feedstock on combustion behaviour of hydrochar. *Fuel*, 169:135–145, 2016.

[138] M. Sevilla and A. B. Fuertes. The production of carbon materials by hydrothermal carbonization of cellulose. *Carbon*, 47(9):2281–2289, 2009.

[139] Dennis Jung, Michael Zimmermann, and Andrea Kruse. Hydrothermal Carbonization of Fructose: Growth Mechanism and Kinetic Model. *ACS Sustainable Chemistry & Engineering*, 6(11):13877–13887, 11 2018.

[140] George Tsilomelekis, Michael J. Orella, Zhexi Lin, Ziwei Cheng, Weiqing Zheng, Vladimiros Nikolakis, and Dionisios G. Vlachos. Molecular structure, morphology and growth mechanisms and rates of 5-hydroxymethyl furfural (HMF) derived humins. *Green Chemistry*, 18(7):1983–1993, 2016.

[141] Sushil K.R. Patil and Carl R.F. Lund. Formation and growth of humins via aldol addition and condensation during acid-catalyzed conversion of 5-hydroxymethylfurfural. *Energy and Fuels*, 25(10):4745–4755, 2011.

[142] Niki Baccile, Guillaume Laurent, Florence Babonneau, Franck Fayon, Maria-Magdalena Titirici, and Markus Antonietti. Structural Characterization of Hydrothermal Carbon Spheres by Advanced Solid-State MAS 13 C NMR Investigations. *Journal of Physical Chemistry C*, 113(22):9644–9654, 2009.

[143] Linghui Yu, Camillo Falco, Jens Weber, Robin J White, Jane Y Howe, and Maria-Magdalena Titirici. Carbohydrate-Derived Hydrothermal Carbons: A Thorough Characterization Study. *Langmuir*, 28(33):12373–12383, 2012.

[144] Maria-Magdalena Titirici, editor. *Sustainable Carbon Materials from Hydrothermal Processes*. John Wiley & Sons, Ltd, Oxford, UK, 5 2013.

[145] Stephanie-Angelika Wohlgemuth, Filipe Vilela, Maria-Magdalena Titirici, and Markus Antonietti. A one-pot hydrothermal synthesis of tunable dual heteroatom-doped carbon microspheres. *Green Chemistry*, 14(3):741, 2012.

[146] Jens Peter Paraknowitsch and Arne Thomas. Doping carbons beyond nitrogen: an overview of advanced heteroatom doped carbons with boron, sulphur and phosphorus for energy applications. *Energy & Environmental Science*, 6(10):2839, 2013.

[147] Zhen Chen, Lijian Ma, Shuqiong Li, Junxia Geng, Qiang Song, Jun Liu, Chunli Wang, Hang Wang, Juan Li, Zhi Qin, and Shoujian Li. Simple approach to carboxyl-rich materials through low-temperature heat treatment of hydrothermal carbon in air. *Applied Surface Science*, 257(20):8686–8691, 2011.

[148] Xiaoming Sun and Yadong Li. Colloidal Carbon Spheres and Their Core/Shell Structures with Noble-Metal Nanoparticles. *Angewandte Chemie - International Edition*, 43(5):597–601, 1 2004.

[149] Marta Sevilla and Antonio B. Fuertes. Chemical and Structural Properties of Carbonaceous Products Obtained by Hydrothermal Carbonization of Saccharides. *Chemistry - A European Journal*, 15(16):4195–4203, 4 2009.

[150] Ana S. Mestre, Emil Tyszko, Marta A. Andrade, Margarida Galhetas, Cristina Freire, and Ana P. Carvalho. Sustainable activated carbons prepared from a sucrose-derived hydrochar: remarkable adsorbents for pharmaceutical compounds. *RSC Advances*, 5(25):19696–19707, 2015.

[151] A. Kruse and E. Dinjus. Hot compressed water as reaction medium and reactant. Properties and synthesis reactions, 1 2007.

[152] Michael Jerry Antal, William S.L. Mok, and Geoffrey N. Richards. Mechanism of formation of 5-(hydroxymethyl)-2-furaldehyde from d-fructose and sucrose. *Carbohydrate Research*, 199(1):91–109, 5 1990.

[153] Stephen J. Angyal. The Lobry de Bruyn-Alberda van Ekenstein Transformation and Related Reactions. In *Topics in Current Science*, volume 215, pages 1–14. Springer, 2001.

[154] Bernard M Kabyemela, Tadafumi Adschiri, Roberto M Malaluan, and Kunio Arai. Kinetics of Glucose Epimerization and Decomposition in Subcritical and Supercritical Water. *Industrial & Engineering Chemistry Research*, 36(5):1552–1558, 5 1997.

[155] Yujie Yang Qi, Mu Zhang, Lin Qi, and Yujie Yang Qi. Mechanism for the formation and growth of carbonaceous spheres from sucrose by hydrothermal carbonization. *RSC Advances*, 6(25):20814–20823, 2 2016.

[156] Paul Körner, Dennis Jung, and Andrea Kruse. Influence of the pH Value on the Hydrothermal Degradation of Fructose. *ChemistryOpen*, 8(8):1121–1132, 8 2019.

[157] Mu Zhang, Hong Yang, Yinong Liu, Xudong Sun, Dongke Zhang, and Dongfeng Xue. First identification of primary nanoparticles in the aggregation of HMF. *Nanoscale Research Letters*, 7:1–13, 2012.

[158] Xianghong Qian, Mark R. Nimlos, Mark Davis, David K. Johnson, and Michael E. Himmel. Ab initio molecular dynamics simulations of $\beta$-D-glucose and $\beta$-D-xylose degradation mechanisms in acidic aqueous solution. *Carbohydrate Research*, 340(14):2319–2327, 10 2005.

[159] Mu Zhang, Hong Yang, Yinong Liu, Xudong Sun, Dongke Zhang, and Dongfeng Xue. Hydrophobic precipitation of carbonaceous spheres from fructose by a hydrothermal process. *Carbon*, 50(6):2155–2161, 5 2012.

[160] Xuelian Chen, Jan Schröder, Stephan Hauschild, Sabine Rosenfeldt, Martin Dulle, and Stephan Förster. Simultaneous SAXS/WAXS/UV-Vis Study of the Nucleation and Growth of Nanoparticles: A Test of Classical Nucleation Theory. *Langmuir*, 31(42):11678–11691, 2015.

[161] Nguyen T K Thanh, N. Maclean, and S. Mahiddine. Mechanisms of nucleation and growth of nanoparticles in solution. *Chemical reviews*, 114(15):7610–30, 8 2014.

[162] Daniel B. K. Chu, Jonathan S. Owen, and Baron Peters. Nucleation and Growth Kinetics from LaMer Burst Data. *The Journal of Physical Chemistry A*, 121(40):7511–7517, 10 2017.

[163] Victor K. LaMer and Robert H. Dinegar. Theory, Production and Mechanism of Formation of Monodispersed Hydrosols. *Journal of the American Chemical Society*, 72(11):4847–4854, 11 1950.

[164] P. Taylor. Ostwald ripening in emulsions. *Advances in Colloid and Interface Science*, 75(2):107–163, 1998.

[165] P W Voorhees. The theory of Ostwald ripening. *Journal of Statistical Physics*, 38(1-2):231–252, 1 1985.

[166] Jihye Ryu, Young Woong Suh, Dong Jin Suh, and Dong June Ahn. Hydrothermal preparation of carbon microspheres from mono-saccharides and phenolic compounds. *Carbon*, 48(7):1990–1998, 2010.

[167] Kenneth G. Latham, Aditya Rawal, James M. Hook, and Scott W. Donne. Molecular structures driving pseudo-capacitance in hydrothermal nanostructured carbons. *RSC Advances*, 6(16):12964–12976, 2016.

[168] Kenneth G. Latham, Michela I. Simone, Wesley M. Dose, Jessica A. Allen, and Scott W. Donne. Synchrotron based NEXAFS study on nitrogen doped hydrothermal carbon: Insights into surface functionalities and formation mechanisms. *Carbon*, 114:566–578, 4 2017.

[169] Scott Calvin. *XAFS for Everyone*. CRC Press, 5 2013.

[170] Chunhua Yao, Yongsoon Shin, Li Qiong Wang, Charles F Windisch, William D Samuels, Bruce W Arey, Chongmin Wang, William M Risen, and Gregory J Exarhos. Hydrothermal dehydration of aqueous fructose solutions in a closed system. *Journal of Physical Chemistry C*, 111(42):15141–15145, 2007.

[171] K. Schmidt-Rohr and H. W. Spiess. *Multidimensional Solid-State NMR and Polymers*. Elsevier, 1994.

[172] Athika Chuntanapum and Yukihiko Matsumura. Formation of Tarry Material from 5-HMF in Subcritical and Supercritical Water. *Industrial & Engineering Chemistry Research*, 48(22):9837–9846, 11 2009.

[173] Camillo Falco, Fernando Perez Caballero, Florence Babonneau, Christel Gervais, Guillaume Laurent, Maria-Magdalena Titirici, and Niki Baccile. Hydrothermal Carbon from Biomass: Structural Differences between Hydrothermal and Pyrolyzed Carbons via 13 C Solid State NMR. *Langmuir*, 27(23):14460–14471, 12 2011.

[174] Dawit Solomon, Johannes Lehmann, Jian Wang, James Kinyangi, Karen Heymann, Yingshen Lu, Sue Wirick, and Chris Jacobsen. Micro- and nano-environments of C sequestration in soil: A multi-elemental STXM–NEXAFS assessment of black C and organomineral associations. *Science of The Total Environment*, 438:372–388, 11 2012.

[175] Brian A. Collins and Harald Ade. Quantitative compositional analysis of organic thin films using transmission NEXAFS spectroscopy in an X-ray microscope. *Journal of Electron Spectroscopy and Related Phenomena*, 185(5-7):119–128, 8 2012.

[176] Jian Li, Adam P Hitchcock, Harald D.H. Stöver, and Ian Shirley. A new approach to studying microcapsule wall growth mechanisms. *Macromolecules*, 42(7):2428–2432, 4 2009.

[177] Danielle Covelli, Daniel Hernández-Cruz, Brian M. Haines, Vincente Munoz, Oladipo Omotoso, Randy Mikula, and Stephen Urquhart. NEXAFS microscopy studies of the association of hydrocarbon thin films with fine clay particles. *Journal of Electron Spectroscopy and Related Phenomena*, 173(1):1–6, 6 2009.

[178] S. Bernard, K. Benzerara, O. Beyssac, G.E. Brown, L. Grauvogel Stamm, and P. Duringer. Ultrastructural and chemical study of modern and fossil sporoderms by Scanning Transmission X-ray Microscopy (STXM). *Review of Palaeobotany and Palynology*, 156(1-2):248–261, 7 2009.

[179] Nikolas Hagemann, Stephen Joseph, Hans-Peter Schmidt, Claudia I. Kammann, Johannes Harter, Thomas Borch, Robert B. Young, Krisztina Varga, Sarasadat Taherymoosavi, K. Wade Elliott, Amy McKenna, Mihaela Albu, Claudia Mayrhofer, Martin Obst, Pellegrino Conte, Alba Dieguez-Alonso, Silvia Orsetti, Edisson Subdiaga, Sebastian Behrens, and Andreas Kappler. Organic coating on biochar explains its nutrient retention and stimulation of soil fertility. *Nature Communications*, 8(1):1089, 12 2017.

[180] Johannes Schindelin, Ignacio Arganda-Carreras, Erwin Frise, Verena Kaynig, Mark Longair, Tobias Pietzsch, Stephan Preibisch, Curtis Rueden, Stephan Saalfeld, Benjamin Schmid, Jean-Yves Tinevez, Daniel James White, Volker Hartenstein, Kevin Eliceiri, Pavel Tomancak, and Albert Cardona. Fiji: an open-source platform for biological-image analysis. *Nature Methods*, 9(7):676–682, 7 2012.

[181] Matt Newville, Renee Otten, Andrew Nelson, Antonino Ingargiola, Till Stensitzki, Dan Allan, Austin Fox, Faustin Carter, Dima Pustakhod, Yoav Ram, Christoph Deil, Alexandre Beelen, Oliver Frost, Nicholas Zobrist, Gustavo Pasquevich, Allan L. R. Hansen, Tim Spillane, Shane Caldwell, Anthony Polloreno, Andrewhannum, Julius Zimmermann, Jose Borreguero, Jonathan Fraine, Benjamin F. Maier, Ben Gamari, and Anthony Almarza. Non-Linear Least-Squares Minimization and Curve-Fitting for Python. *Zenodo*, 9 2014.

[182] Mirna Lerotic, Rachel Mak, Sue Wirick, Florian Meirer, and Chris Jacobsen. Mantis: A program for the analysis of x-ray spectromicroscopy data. *Journal of Synchrotron Radiation*, 21(5):1206–1212, 9 2014.

[183] Dawit Solomon, Johannes Lehmann, James Kinyangi, Biqing Liang, Karen Heymann, Lena Dathe, Kelly Hanley, Sue Wirick, and Chris Jacobsen. Carbon (1s) NEXAFS Spectroscopy of Biogeochemically Relevant Reference Organic Compounds. *Soil Science Society of America Journal*, 73(6):1817–1830, 11 2009.

[184] Kenneth G. Latham, Wesley M. Dose, Jessica A. Allen, and Scott W. Donne. Nitrogen doped heat treated and activated hydrothermal carbon: NEXAFS examination of the carbon surface at different temperatures. *Carbon*, 128:179–190, 3 2018.

[185] George D. Cody, Robert E. Botto, Harald Ade, Sutinder Behal, Mark Disko, Susan Wirick, Sutinder Behai, Mark Disko, and Susan Wirick. Inner-Shell Spectroscopy and Imaging of

a Subbituminous Coal: In-Situ Analysis of Organic and Inorganic Microstructure Using C(ls)-, Ca(2p)-, and Cl(2s)-NEXAFS. *Energy and Fuels*, 9(3):525–533, 5 1995.

[186] Cheng-Cheng Tsai, Jien-Lian Chen, Wei-Ping Hu, Yi-Shiue Lin, Huei-Ru Lin, Tsai-Yun Lee, Yuan T. Lee, Chi-Kung Ni, and Chen-Lin Liu. Selectivity of peptide bond dissociation on excitation of a core electron: Effects of a phenyl group. *Chemical Physics Letters*, 660:60–68, 9 2016.

[187] Johannes Lehmann, Biqing Liang, Dawit Solomon, Mirna Lerotic, Flavio Luizão, James Kinyangi, Thorsten Schäfer, Sue Wirick, and Chris Jacobsen. Near-edge X-ray absorption fine structure (NEXAFS) spectroscopy for mapping nano-scale distribution of organic carbon forms in soil: Application to black carbon particles. *Global Biogeochemical Cycles*, 19(1):1–12, 2005.

[188] Karen Heymann, Johannes Lehmann, Dawit Solomon, Michael W.I. Schmidt, and Thomas Regier. C 1s K-edge near edge X-ray absorption fine structure (NEXAFS) spectroscopy for characterizing functional group chemistry of black carbon. *Organic Geochemistry*, 42(9):1055–1064, 10 2011.

[189] A. C. Scheinost, R. Kretzschmar, I. Christ, and Ch. Jacobsen. Carbon group chemistry of humic and fulvic acid: A comparison of C-1s NEXAFS and 13C-NMR spectroscopies. In *Humic Substances*, pages 39–48. Royal Society of Chemistry, Cambridge, 10 2001.

[190] Hervé Abdi and Lynne J. Williams. Principal component analysis. *Wiley Interdisciplinary Reviews: Computational Statistics*, 2(4):433–459, 7 2010.

[191] Ian T. Jolliffe and Jorge Cadima. Principal component analysis: a review and recent developments. *Philosophical Transactions of the Royal Society A: Mathematical, Physical and Engineering Sciences*, 374(2065):1–7, 4 2016.

[192] Balwant Singh, Yunying Fang, Bruce C.C. Cowie, and Lars Thomsen. NEXAFS and XPS characterisation of carbon functional groups of fresh and aged biochars. *Organic Geochemistry*, 77:1–10, 12 2014.

[193] Xiao Liang, Brian S. Haynes, and Alejandro Montoya. Acid-Catalyzed Ring Opening of Furan in Aqueous Solution. *Energy and Fuels*, 32(4):4139–4148, 4 2018.

[194] Andrea Kruse. Hydrothermal biomass gasification. *Journal of Supercritical Fluids*, 47(3):391–399, 2009.

[195] Luke J.R. Higgins, Christoph J Sahle, Mahalingam Balasubramanian, and Bhoopesh Mishra. X-ray Raman scattering for bulk chemical and structural insight into green carbon. *Physical Chemistry Chemical Physics*, 22(33):18435–18446, 2020.

[196] Douglas Phillips. *The UK ' s forest resource and its potential as a sustainable feedstock for bioenergy*. PhD thesis, University of Leeds, 2018.

[197] Jie. Chang. High value chemicals and materials production based on biomass components separation. *RSC Green Chemistry Series*, 27(Renewable Resources for Biorefineries):146–175, 2014.

[198] Pierre Gallezot. Conversion of biomass to selected chemical products. *Chemical Society Reviews*, 41(4):1538–1558, 2012.

[199] Sunil K. Maity. Opportunities, recent trends and challenges of integrated biorefinery: Part II. *Renewable and Sustainable Energy Reviews*, 43:1446–1466, 2015.

[200] S.J.T. Pollard, G.D. Fowler, C.J. Sollars, and R. Perry. Low-cost adsorbents for waste and wastewater treatment: a review. *Science of The Total Environment*, 116(1-2):31–52, 5 1992.

[201] Benoît Cagnon, Xavier Py, André Guillot, Fritz Stoeckli, and Gérard Chambat. Contributions of hemicellulose, cellulose and lignin to the mass and the porous properties of chars and steam activated carbons from various lignocellulosic precursors. *Bioresource Technology*, 100(1):292–298, 2009.

[202] N. S. David. *Chemical Modification of Lignocellulosic Materials*. Routledge, 9 2017.

[203] Tao Wang, Marta Camps-Arbestain, and Mike Hedley. Predicting C aromaticity of biochars based on their elemental composition. *Organic Geochemistry*, 62:1–6, 9 2013.

[204] Daegi Kim, Kwanyong Lee, and Ki Young Park. Upgrading the characteristics of biochar from cellulose, lignin, and xylan for solid biofuel production from biomass by hydrothermal carbonization. *Journal of Industrial and Engineering Chemistry*, 42:95–100, 2016.

[205] David W. Rutherford, Robert L. Wershaw, Colleen E. Rostad, and Charlene N. Kelly. Effect of formation conditions on biochars: Compositional and structural properties of cellulose, lignin, and pine biochars. *Biomass and Bioenergy*, 46:693–701, 2012.

[206] Carl J Houtman and Rajai H Atalla. Cellulose-Lignin Interactions (A Computational Study). *Plant Physiology*, 107(3):977–984, 3 1995.

[207] Gregg T. Beckham, Yannick J. Bomble, Edward A. Bayer, Michael E. Himmel, and Michael F. Crowley. Applications of computational science for understanding enzymatic deconstruction of cellulose. *Current Opinion in Biotechnology*, 22(2):231–238, 2011.

[208] Josh V. Vermaas, Loukas Petridis, Xianghong Qi, Roland Schulz, Benjamin Lindner, and Jeremy C. Smith. Mechanism of lignin inhibition of enzymatic biomass deconstruction. *Biotechnology for Biofuels*, 8(1):1–16, 2015.

[209] A Sluiter, R Ruiz, C Scarlata, J Sluiter, and D Templeton. Determination of Extractives in Biomass: Laboratory Analytical Procedure (LAP), NREL/TP-510-42619. Technical Report January, NREL, 2008.

[210] Xiu-juan GUO, Shu-rong WANG, Kai-ge WANG, Qian LIU, and Zhong-yang LUO. Influence of extractives on mechanism of biomass pyrolysis. *Journal of Fuel Chemistry and Technology*, 38(1):42–46, 2 2010.

[211] Catalina Rodriguez Correa, Tobias Hehr, Ariane Voglhuber-Slavinsky, Yannik Rauscher, and Andrea Kruse. Pyrolysis vs. hydrothermal carbonization: Understanding the effect of biomass structural components and inorganic compounds on the char properties. *Journal of Analytical and Applied Pyrolysis*, 140:137–147, 2019.

[212] Dragan Knežević, Wim Van Swaaij, and Sascha Kersten. Hydrothermal conversion of biomass. II. conversion of wood, pyrolysis oil, and glucose in hot compressed water. *Industrial and Engineering Chemistry Research*, 49(1):104–112, 2010.

[213] Roger Ibbett, Sanyasi Gaddipati, and Gregory Tucker. In-situ studies of hydrothermal reactions of lignocellulosic biomass using high-pressure differential scanning calorimetry. *Biomass and Bioenergy*, 121:48–55, 2 2019.

[214] Maurizio Volpe and Luca Fiori. From olive waste to solid biofuel through hydrothermal carbonisation: The role of temperature and solid load on secondary char formation and hydrochar energy properties. *Journal of Analytical and Applied Pyrolysis*, 124:63–72, 2017.

[215] Xi Lin Wu, Tao Wen, Hong Li Guo, Shubin Yang, Xiangke Wang, and An Wu Xu. Biomass-derived sponge-like carbonaceous hydrogels and aerogels for supercapacitors. *ACS Nano*, 7(4):3589–3597, 2013.

[216] Jie Wang, Ping Nie, Bing Ding, Shengyang Dong, Xiaodong Hao, Hui Dou, and Xiaogang Zhang. Biomass derived carbon for energy storage devices. *Journal of Materials Chemistry A*, 5(6):2411–2428, 2017.

[217] Noel Díez, Marta Sevilla, and Antonio B. Fuertes. Highly Packed Monodisperse Porous Carbon Microspheres for Energy Storage in Supercapacitors and Li-S Batteries. *ChemElectroChem*, 7(18):3798–3810, 2020.

[218] Axel Funke and Felix Ziegler. Hydrothermal carbonization of biomass: A summary and discussion of chemical mechanisms for process engineering, 2010.

[219] Akshay Jain, Rajasekhar Balasubramanian, and M. P. Srinivasan. Hydrothermal conversion of biomass waste to activated carbon with high porosity: A review. *Chemical Engineering Journal*, 283:789–805, 2016.

[220] Hanne Wikberg, Taina Ohra-Aho, Filoklis Pileidis, and Maria Magdalena Titirici. Structural and Morphological Changes in Kraft Lignin during Hydrothermal Carbonization. *ACS Sustainable Chemistry and Engineering*, 3(11):2737–2745, 2015.

[221] Junze Chen, Zhenhua Chen, Caihong Wang, and Xudong Li. Calcium-assisted hydrothermal carbonization of an alginate for the production of carbon microspheres with unique surface nanopores. *Materials Letters*, 67(1):365–368, 2012.

[222] Kathrin Weber and Peter Quicker. Properties of biochar. *Fuel*, 217(December 2017):240–261, 2018.

[223] Oskar Paris, Cordt Zollfrank, and Gerald A. Zickler. Decomposition and carbonisation of wood biopolymers - A microstructural study of softwood pyrolysis. *Carbon*, 43(1):53–66, 2005.

[224] Ivana Pastorova, Robert E. Botto, Peter W. Arisz, and Jaap J. Boon. Cellulose char structure: a combined analytical Py-GC-MS, FTIR, and NMR study. *Carbohydrate Research*, 262(1):27–47, 9 1994.

[225] Eliseo Ranzi, Alberto Cuoci, Tiziano Faravelli, Alessio Frassoldati, Gabriele Migliavacca, Sauro Pierucci, and Samuele Sommariva. Chemical kinetics of biomass pyrolysis. *Energy and Fuels*, 22(6):4292–4300, 11 2008.

[226] Haruo Kawamoto. Lignin pyrolysis reactions. *Journal of Wood Science*, 63(2):117–132, 4 2017.

[227] François-Xavier Collard and Joël Blin. A review on pyrolysis of biomass constituents: Mechanisms and composition of the products obtained from the conversion of cellulose, hemicelluloses and lignin. *Renewable and Sustainable Energy Reviews*, 38:594–608, 10 2014.

[228] Thomas E. McGrath, W.Geoffrey Chan, and Mohammad R. Hajaligol. Low temperature mechanism for the formation of polycyclic aromatic hydrocarbons from the pyrolysis of cellulose. *Journal of Analytical and Applied Pyrolysis*, 66(1-2):51–70, 1 2003.

[229] Meredith Rose Barr, Rhodri Jervis, Yeshui Zhang, Andrew J. Bodey, Christoph Rau, Paul R. Shearing, Dan J.L. Brett, Maria Magdalena Titirici, and Roberto Volpe. Towards

a mechanistic understanding of particle shrinkage during biomass pyrolysis via synchrotron X-ray microtomography and in-situ radiography. *Scientific Reports*, 11(1):1–13, 2021.

[230] Shurong Wang, Gongxin Dai, Haiping Yang, and Zhongyang Luo. Lignocellulosic biomass pyrolysis mechanism: A state-of-the-art review. *Progress in Energy and Combustion Science*, 62:33–86, 9 2017.

[231] Tao Kan, Vladimir Strezov, and Tim J. Evans. Lignocellulosic biomass pyrolysis: A review of product properties and effects of pyrolysis parameters. *Renewable and Sustainable Energy Reviews*, 57:1126–1140, 5 2016.

[232] Stylianos D. Stefanidis, Konstantinos G. Kalogiannis, Eleni F. Iliopoulou, Chrysoula M. Michailof, Petros A. Pilavachi, and Angelos A. Lappas. A study of lignocellulosic biomass pyrolysis via the pyrolysis of cellulose, hemicellulose and lignin. *Journal of Analytical and Applied Pyrolysis*, 105:143–150, 1 2014.

[233] M.Mercedes Maroto-Valer, Darrell N. Taulbee, John M. Andrésen, James C. Hower, and Colin E. Snape. Quantitative 13C NMR study of structural variations within the vitrinite and inertinite maceral groups for a semifusinite-rich bituminous coal. *Fuel*, 77(8):805–813, 6 1998.

[234] D van Krevelen. Graphical-Statistical Method for the Study of Structure and Reaction Processes of Coal. *Fuel*, 29:269–284, 1950.

[235] Albert Rivas-Ubach, Yina Liu, Thomas S. Bianchi, Nikola Tolić, Christer Jansson, and Ljiljana Paša-Tolić. Moving beyond the van Krevelen Diagram: A New Stoichiometric Approach for Compound Classification in Organisms. *Analytical Chemistry*, 90(10):6152–6160, 2018.

[236] Xin Xiao, Zaiming Chen, and Baoliang Chen. H/C atomic ratio as a smart linkage between pyrolytic temperatures, aromatic clusters and sorption properties of biochars derived from diverse precursory materials. *Scientific Reports*, 6(1):22644, 9 2016.

[237] Milan Randić. Aromaticity of Polycyclic Conjugated Hydrocarbons. *Chemical Reviews*, 103(9):3449–3606, 9 2003.

[238] D. J. Klein. Aromaticity via Kekule structures and conjugated circuits. *Journal of Chemical Education*, 69(9):691, 9 1992.

[239] Thieres M.C. Pereira, Gabriela Vanini, Emanuele C.S. Oliveira, Felipe M.R. Cardoso, Felipe P. Fleming, Alvaro C. Neto, Valdemar Lacerda, Eustáquio V.R. Castro, Boniek G. Vaz, and Wanderson Romão. An evaluation of the aromaticity of asphaltenes using atmospheric pressure photoionization Fourier transform ion cyclotron resonance mass spectrometry – APPI FT-ICR MS. *Fuel*, 118:348–357, 2 2014.

[240] Liming Lu, Veena Sahajwalla, and David Harris. Characteristics of Chars Prepared from Various Pulverized Coals at Different Temperatures Using Drop-Tube Furnace. *Energy & Fuels*, 14(4):869–876, 7 2000.

[241] G. D. Love, R. V. Law, and C. E. Snape. Determination of nonprotonated aromatic carbon concentrations in coals by single pulse excitation carbon-13 NMR. *Energy & Fuels*, 7(5):639–644, 9 1993.

[242] Anna V. McBeath, Ronald J. Smernik, Maximilian P.W. Schneider, Michael W.I. Schmidt, and Emma L. Plant. Determination of the aromaticity and the degree of aromatic condensation of a thermosequence of wood charcoal using NMR. *Organic Geochemistry*, 42(10):1194–1202, 11 2011.

[243] Anna V. McBeath, Ronald J. Smernik, Evelyn S. Krull, and Johannes Lehmann. The influence of feedstock and production temperature on biochar carbon chemistry: A solid-state 13C NMR study. *Biomass and Bioenergy*, 60:121–129, 1 2014.

[244] A. D. McNaught and A. Wilkinson. *IUPAC. Compendium of Chemical Terminology, 2nd ed. (the "Gold Book")*. Blackwell, Oxford, 1997.

[245] Daniel B. Wiedemeier, Samuel Abiven, William C. Hockaday, Marco Keiluweit, Markus Kleber, Caroline A. Masiello, Anna V. McBeath, Peter S. Nico, Lacey A. Pyle, Maximilian P.W. Schneider, Ronald J. Smernik, Guido L.B. Wiesenberg, and Michael W.I. Schmidt. Aromaticity and degree of aromatic condensation of char. *Organic Geochemistry*, 78:135–143, 1 2015.

[246] Milan Randić. Average carbon-13 chemical shifts in benzenoid dications. *Journal of Magnetic Resonance (1969)*, 59(1):34–40, 8 1984.

[247] Marco Keiluweit and Markus Kleber. Molecular-Level Interactions in Soils and Sediments: The Role of Aromatic $\pi$-Systems. *Environmental Science & Technology*, 43(10):3421–3429, 5 2009.

[248] Ke Sun, Marco Keiluweit, Markus Kleber, Zezhen Pan, and Baoshan Xing. Sorption of fluorinated herbicides to plant biomass-derived biochars as a function of molecular structure. *Bioresource Technology*, 102(21):9897–9903, 11 2011.

[249] Colin E. Snape, Axelson D, Botto R, Delpuech J, Tekeley P, Gerstein B, Pruskig Maciel M, and Wilson M. Quantitative reliability of aromaticity and related measurements on coals by 13C n.m.r. A debate. *Fuel*, 68(5):547–548, 5 1989.

[250] Thomas E Rufford, John Zhu, and Denisa Hulicova-Jurcakova. *Green carbon materials: advances and applications*. Jenny Stanford Publishing, 2014.

[251] H.P. Boehm. Some aspects of the surface chemistry of carbon blacks and other carbons. *Carbon*, 32(5):759–769, 1 1994.

[252] Minori Uchimiya, Alexander Orlov, Girish Ramakrishnan, and Karamat Sistani. In situ and ex situ spectroscopic monitoring of biochar's surface functional groups. *Journal of Analytical and Applied Pyrolysis*, 102:53–59, 2013.

[253] Erwei Leng, Yang Zhang, Yang Peng, Xun Gong, Ming Mao, Xiaomin Li, and Yun Yu. In situ structural changes of crystalline and amorphous cellulose during slow pyrolysis at low temperatures. *Fuel*, 216(November 2017):313–321, 2018.

[254] Adrian Gainar, Joanna S. Stevens, Cherno Jaye, Daniel A. Fischer, and Sven L. M. Schroeder. NEXAFS Sensitivity to Bond Lengths in Complex Molecular Materials: A Study of Crystalline Saccharides. *The Journal of Physical Chemistry B*, 119(45):14373–14381, 11 2015.

[255] David D. Laws, Hans-Marcus L. Bitter, and Alexej Jerschow. Solid-State NMR Spectroscopic Methods in Chemistry. *Angewandte Chemie International Edition*, 41(17):3096–3129, 9 2002.

[256] Ch.J. Sahle, A. Mirone, J. Niskanen, J. Inkinen, M. Krisch, and S. Huotari. Planning, performing and analyzing X-ray Raman scattering experiments. *Journal of Synchrotron Radiation*, 22(2):400–409, 2015.

[257] Pierre Gueriau, Jean-Pascal Rueff, Sylvain Bernard, Josiane A Kaddissy, Sarah Goler, Christoph J Sahle, Dimosthenis Sokaras, Roy A Wogelius, Phillip L Manning, Uwe Bergmann, and Loïc Bertrand. Noninvasive Synchrotron-Based X-ray Raman Scattering Discriminates Carbonaceous Compounds in Ancient and Historical Materials. *Anal. Chem. Anal. Chem*, 89(89):10819–10826, 2017.

[258] Uwe Bergmann, Henning Groenzin, Oliver C. Mullins, Pieter Glatzel, John Fetzer, and S. P. Cramer. X-ray Raman spectroscopy - A new tool to study local structure of aromatic hydrocarbons and asphaltenes. *Petroleum Science and Technology*, 22(7-8):863–875, 2004.

[259] Andrew E Pomerantz, Ethan Crace, Tsu Chien Weng, Dimosthenis Sokaras, and Dennis Nordlund. Carbon Core Electron Spectra of Polycyclic Aromatic Hydrocarbons. *Journal of Physical Chemistry A*, 122(26):5730–5734, 2018.

[260] Michelle L. Gordon, David Tulumello, Glyn Cooper, Adam P. Hitchcock, Pieter Glatzel, Oliver C. Mullins, Stephen P. Cramer, and Uwe Bergmann. Inner-shell excitation spectroscopy of fused-ring aromatic molecules by electron energy loss and x-ray Raman techniques. *Journal of Physical Chemistry A*, 107(41):8512–8520, 2003.

[261] F. Biggs, L.B. Mendelsohn, and J.B. Mann. Hartree-Fock Compton profiles for the elements. *Atomic Data and Nuclear Data Tables*, 16(3):201–309, 9 1975.

[262] Richard M Martin. *Electronic structure : basic theory and practical methods*. Cambridge University Press, Cambridge, 2004.

[263] Marcus D. Hanwell, Donald E. Curtis, David C. Lonie, Tim Vandermeerschd, Eva Zurek, and Geoffrey R. Hutchison. Avogadro: An advanced semantic chemical editor, visualization, and analysis platform. *Journal of Cheminformatics*, 4(8):17, 12 2012.

[264] Fabian Weber, Jian Ren, Tristan Petit, and Annika Bande. Theoretical X-ray absorption spectroscopy database analysis for oxidised 2D carbon nanomaterials. *Physical Chemistry Chemical Physics*, 21(13):6999–7008, 3 2019.

[265] Frank Neese. Software update: the ORCA program system, version 4.0. *WIREs Computational Molecular Science*, 8(1):1327, 1 2018.

[266] Stefan Grimme, Stephan Ehrlich, and Lars Goerigk. Effect of the damping function in dispersion corrected density functional theory. *Journal of Computational Chemistry*, 32(7):1456–1465, 5 2011.

[267] Julian Tirado-Rives and William L. Jorgensen. Performance of B3LYP density functional methods for a large set of organic molecules. *Journal of Chemical Theory and Computation*, 4(2):297–306, 2008.

[268] Florian Weigend. Accurate Coulomb-fitting basis sets for H to Rn. *Physical Chemistry Chemical Physics*, 8(9):1057–1065, 2 2006.

[269] Jussi Lehtola, Mikko Hakala, Arto Sakko, and Keijo Hämäläinen. ERKALE-A flexible program package for X-ray properties of atoms and molecules. *Journal of Computational Chemistry*, 33(18):1572–1585, 7 2012.

[270] Adam E. A. Fouda and Nicholas A. Besley. Assessment of basis sets for density functional theory-based calculations of core-electron spectroscopies. *Theoretical Chemistry Accounts*, 137(1):6, 1 2018.

[271] Marco Keiluweit, Peter S. Nico, Mark G. Johnson, and Markus Kleber. Dynamic molecular structure of plant biomass-derived black carbon (biochar). *Environmental Science and Technology*, 44(4):1247–1253, 2 2010.

[272] Uwe Bergmann, Henning Groenzin, Oliver C. Mullins, Pieter Glatzel, John Fetzer, and S.P. P Cramer. Carbon K-edge X-ray Raman spectroscopy supports simple, yet powerful description of aromatic hydrocarbons and asphaltenes. *Chemical Physics Letters*, 369(1-2):184–191, 2 2003.

[273] Fungai N. D. Mukome, Arthur L. D. Kilcoyne, and Sanjai J. Parikh. Alteration of Biochar Carbon Chemistry during Soil Incubations: SR-FTIR and NEXAFS Investigation. *Soil Science Society of America Journal*, 78(5):1632, 2014.

[274] Andrew K. Kercher and Dennis C. Nagle. Microstructural evolution during charcoal carbonization by X-ray diffraction analysis. *Carbon*, 41(1):15–27, 2003.

[275] E (Erich) Clar. *The aromatic sextet*. Wiley-Interscience, Chichester, 1972.

[276] A. Ballard Andrews, John C. Edwards, Andrew E. Pomerantz, Oliver C. Mullins, Dennis Nordlund, and Koyo Norinaga. Comparison of coal-derived and petroleum asphaltenes by 13C nuclear magnetic resonance, DEPT, and XRS. *Energy and Fuels*, 25(7):3068–3076, 2011.

[277] Mahtab Ahmad, Anushka Upamali Rajapaksha, Jung Eun Lim, Ming Zhang, Nanthi Bolan, Dinesh Mohan, Meththika Vithanage, Sang Soo Lee, and Yong Sik Ok. Biochar as a sorbent for contaminant management in soil and water: A review. *Chemosphere*, 99:19–23, 2014.

[278] Imran Ali. The Quest for Active Carbon Adsorbent Substitutes: Inexpensive Adsorbents for Toxic Metal Ions Removal from Wastewater. *Separation & Purification Reviews*, 39(3-4):95–171, 11 2010.

[279] J. Rivera-Utrilla, M. Sánchez-Polo, V. Gómez-Serrano, P.M. M. Álvarez, M.C.M. C M Alvim-Ferraz, and J.M. M. Dias. Activated carbon modifications to enhance its water treatment applications. An overview. *Journal of Hazardous Materials*, 187(1-3):1–23, 3 2011.

[280] Jin Zhang, Mauricio Terrones, Chong Rae Park, Rahul Mukherjee, Marc Monthioux, Nikhil Koratkar, Yern Seung Kim, Robert Hurt, Elzbieta Frackowiak, Toshiaki Enoki, Yuan Chen, Yongsheng Chen, and Alberto Bianco. Carbon science in 2016: Status, challenges and perspectives. *Carbon*, 98:708–732, 3 2016.

[281] Anushka Upamali Rajapaksha, Season S. Chen, Daniel C.W. Tsang, Ming Zhang, Meththika Vithanage, Sanchita Mandal, Bin Gao, Nanthi S. Bolan, and Yong Sik Ok. Engineered/designer biochar for contaminant removal/immobilization from soil and water: Potential and implication of biochar modification. *Chemosphere*, 148:276–291, 4 2016.

[282] Junxian Shi, Xiaoliang Fan, Daniel C.W. Tsang, Fei Wang, Zhengtao Shen, Deyi Hou, and Daniel S. Alessi. Removal of lead by rice husk biochars produced at different temperatures and implications for their environmental utilizations. *Chemosphere*, 235:825–831, 11 2019.

[283] Ming Zhang, Bin Gao, Ying Yao, Yingwen Xue, and Mandu Inyang. Synthesis of porous MgO-biochar nanocomposites for removal of phosphate and nitrate from aqueous solutions. *Chemical Engineering Journal*, 210:26–32, 11 2012.

[284] Ming Zhang, Bin Gao, Sima Varnoosfaderani, Arthur Hebard, Ying Yao, and Mandu Inyang. Preparation and characterization of a novel magnetic biochar for arsenic removal. *Bioresource Technology*, 130:457–462, 2 2013.

[285] Peng Liu, Carol J. Ptacek, Krista M.A. Elena, David W. Blowes, W. Douglas Gould, Y. Zou Finfrock, Alana O. Wang, and Richard C. Landis. Evaluation of mercury stabilization mechanisms by sulfurized biochars determined using X-ray absorption spectroscopy. *Journal of Hazardous Materials*, 347:114–122, 4 2018.

[286] Xin Hu, Zhuhong Ding, Andrew R. Zimmerman, Shengsen Wang, and Bin Gao. Batch and column sorption of arsenic onto iron-impregnated biochar synthesized through hydrolysis. *Water Research*, 68:206–216, 1 2015.

[287] Anushka Upamali Rajapaksha, Md Samrat Alam, Ning Chen, Daniel S. Alessi, Avanthi Deshani Igalavithana, Daniel C.W. Tsang, and Yong Sik Ok. Removal of hexavalent chromium in aqueous solutions using biochar: Chemical and spectroscopic investigations. *Science of The Total Environment*, 625:1567–1573, 6 2018.

[288] Md Samrat Alam, Drew Gorman-Lewis, Ning Chen, Shannon L. Flynn, Yong Sik Ok, Kurt O. Konhauser, and Daniel S. Alessi. Thermodynamic Analysis of Nickel(II) and Zinc(II) Adsorption to Biochar. *Environmental Science & Technology*, 52(11):6246–6255, 6 2018.

[289] Md. Samrat Alam, Drew Gorman-Lewis, Ning Chen, Salman Safari, Kitae Baek, Kurt O Konhauser, and Daniel S Alessi. Mechanisms of the Removal of U(VI) from Aqueous Solution Using Biochar: A Combined Spectroscopic and Modeling Approach. *Environmental Science & Technology*, 52(22):13057–13067, 11 2018.

[290] Xiaoxiao Zhu, Chunyan Li, Jianfa Li, Bin Xie, Jinhong Lü, and Yimin Li. Thermal treatment of biochar in the air/nitrogen atmosphere for developed mesoporosity and enhanced adsorption to tetracycline. *Bioresource Technology*, 263:475–482, 9 2018.

[291] Anton R. Reed and Paul T. Williams. Thermal processing of biomass natural fibre wastes by pyrolysis. *International Journal of Energy Research*, 28(2):131–145, 2 2004.

[292] Fernanda R. Oliveira, Anil K. Patel, Deb P. Jaisi, Sushil Adhikari, Hui Lu, and Samir Kumar Khanal. Environmental application of biochar: Current status and perspectives. *Bioresource Technology*, 246:110–122, 12 2017.

[293] Ana S. Mestre and Ana P Carvalho. Nanoporous Carbon Synthesis: An Old Story with Exciting New Chapters. In Taher Ghrib, editor, *Porosity - Process, Technologies and Applications*, chapter 2. InTech, 4 2018.

[294] J. A. Ippolito, D. G. Strawn, K. G. Scheckel, J. M. Novak, M. Ahmedna, and M. A. S. Niandou. Macroscopic and Molecular Investigations of Copper Sorption by a Steam-Activated Biochar. *Journal of Environmental Quality*, 41(4):1150–1156, 7 2012.

[295] J. Lehman and S. Joseph. *Biochar for Environmental Management: Science and Technology*. Routledge, 2nd editio edition, 2009.

[296] Mohammad Boshir Ahmed, John L. Zhou, Huu H. Ngo, Wenshan Guo, and Mengfang Chen. Progress in the preparation and application of modified biochar for improved

contaminant removal from water and wastewater. *Bioresource Technology*, 214:836–851, 8 2016.

[297] R. Ryoo, S. H. Joo, M. Kruk, and M. Jaroniec. Ordered Mesoporous Carbons. *Advanced Materials*, 13(9):677–681, 5 2001.

[298] Laemthong Chuenchom, Ralph Kraehnert, and Bernd M. Smarsly. Recent progress in soft-templating of porous carbon materials. *Soft Matter*, 8(42):10801, 2012.

[299] Marit Jagtoyen and Frank Derbyshire. Some considerations of the origins of porosity in carbons from chemically activated wood. *Carbon*, 31(7):1185–1192, 1993.

[300] Bing Wang, Bin Gao, and June Fang. Recent advances in engineered biochar productions and applications. *Critical Reviews in Environmental Science and Technology*, 47(22):2158–2207, 11 2017.

[301] Anushka Upamali Rajapaksha, Mahtab Ahmad, Meththika Vithanage, Kwon-Rae Kim, Jun Young Chang, Sang Soo Lee, and Yong Sik Ok. The role of biochar, natural iron oxides, and nanomaterials as soil amendments for immobilizing metals in shooting range soil. *Environmental Geochemistry and Health*, 37(6):931–942, 12 2015.

[302] Wojciech Kiciński, Mateusz Szala, and Michał Bystrzejewski. Sulfur-doped porous carbons: Synthesis and applications. *Carbon*, 68:1–32, 3 2014.

[303] Mykola Seredych, Denisa Hulicova-Jurcakova, and Teresa J. Bandosz. Effect of the Incorporation of Nitrogen to a Carbon Matrix on the Selectivity and Capacity for Adsorption of Dibenzothiophenes from Model Diesel Fuel. *Langmuir*, 26(1):227–233, 1 2010.

[304] Mykola Seredych and Teresa J. Bandosz. Reactive adsorption of hydrogen sulfide on graphite oxide/Zr(OH)4composites. *Chemical Engineering Journal*, 166(3):1032–1038, 2011.

[305] Andrea Zitolo, Vincent Goellner, Vanessa Armel, Moulay Tahar Sougrati, Tzonka Mineva, Lorenzo Stievano, Emiliano Fonda, and Frédéric Jaouen. Identification of catalytic sites for oxygen reduction in iron- and nitrogen-doped graphene materials. *Nature Materials*, 14(9):937–942, 2015.

[306] Hsing-Cheng Hsi, Mark J. Rood, Massoud Rostam-Abadi, Shiaoguo Chen, and Ramsay Chang. Mercury Adsorption Properties of Sulfur-Impregnated Adsorbents. *Journal of Environmental Engineering*, 128(11):1080–1089, 11 2002.

[307] Shengsen Wang, Bin Gao, Yuncong Li, Ahmed Mosa, Andrew R. Zimmerman, Lena Q. Ma, Willie G. Harris, and Kati W. Migliaccio. Manganese oxide-modified biochars: Preparation, characterization, and sorption of arsenate and lead. *Bioresource Technology*, 181:13–17, 2015.

[308] Malgorzata M. Wiatros-Motyka, Cheng-gong Sun, Lee A. Stevens, and Colin E. Snape. High capacity co-precipitated manganese oxides sorbents for oxidative mercury capture. *Fuel*, 109:559–562, 7 2013.

[309] Evita Agrafioti, Dimitrios Kalderis, and Evan Diamadopoulos. Ca and Fe modified biochars as adsorbents of arsenic and chromium in aqueous solutions. *Journal of Environmental Management*, 146:444–450, 2014.

[310] Yunqiang Yi, Zhexi Huang, Baizhou Lu, Jingyi Xian, Eric Pokeung Tsang, Wen Cheng, Jianzhang Fang, and Zhanqiang Fang. Magnetic biochar for environmental remediation: A review. *Bioresource Technology*, 298:122468, 2 2020.

[311] Pengfei Sun, Cai Hui, Rashid Azim Khan, Jingting Du, Qichun Zhang, and Yu-Hua Zhao. Efficient removal of crystal violet using Fe3O4-coated biochar: the role of the Fe3O4 nanoparticles and modeling study their adsorption behavior. *Scientific Reports*, 5(1):12638, 2015.

[312] Hongbo Li, Xiaoling Dong, Evandro B. da Silva, Letuzia M. de Oliveira, Yanshan Chen, and Lena Q. Ma. Mechanisms of metal sorption by biochars: Biochar characteristics and modifications. *Chemosphere*, 178:466–478, 7 2017.

[313] Xiaofei Tan, Yunguo Liu, Guangming Zeng, Xin Wang, Xinjiang Hu, Yanling Gu, and Zhongzhu Yang. Application of biochar for the removal of pollutants from aqueous solutions. *Chemosphere*, 125:70–85, 4 2015.

[314] Mandu I. Inyang, Bin Gao, Ying Yao, Yingwen Xue, Andrew Zimmerman, Ahmed Mosa, Pratap Pullammanappallil, Yong Sik Ok, and Xinde Cao. A review of biochar as a low-cost adsorbent for aqueous heavy metal removal. *Critical Reviews in Environmental Science and Technology*, 46(4):406–433, 2 2016.

[315] Nan Zhao, Chuanfang Zhao, Yizhong Lv, Weifang Zhang, Yuguo Du, Zhengping Hao, and Jing Zhang. Adsorption and coadsorption mechanisms of Cr(VI) and organic contaminants on H3PO4 treated biochar. *Chemosphere*, 186:422–429, 11 2017.

[316] Xiaoling Dong, Lena Q. Ma, and Yuncong Li. Characteristics and mechanisms of hexavalent chromium removal by biochar from sugar beet tailing. *Journal of Hazardous Materials*, 190(1-3):909–915, 6 2011.

[317] Michael Komárek, Carla M. Koretsky, Krishna J. Stephen, Daniel S. Alessi, and Vladislav Chrastný. Competitive Adsorption of Cd(II), Cr(VI), and Pb(II) onto Nanomaghemite: A Spectroscopic and Modeling Approach. *Environmental Science & Technology*, 49(21):12851–12859, 11 2015.

[318] Minori Uchimiya, Lynda H. Wartelle, K. Thomas Klasson, Chanel A. Fortier, and Isabel M. Lima. Influence of pyrolysis temperature on biochar property and function as a heavy metal sorbent in soil. *Journal of Agricultural and Food Chemistry*, 59(6):2501–2510, 2011.

[319] Ahmad Alfarra, Elzbieta Frackowiak, and François Béguin. The HSAB concept as a means to interpret the adsorption of metal ions onto activated carbons. *Applied Surface Science*, 228(1-4):84–92, 4 2004.

[320] Omar R. Harvey, Bruce E. Herbert, Roy D. Rhue, and Li-Jung Kuo. Metal Interactions at the Biochar-Water Interface: Energetics and Structure-Sorption Relationships Elucidated by Flow Adsorption Microcalorimetry. *Environmental Science & Technology*, 45(13):5550–5556, 7 2011.

[321] Michael Lawrinenko and David A. Laird. Anion exchange capacity of biochar. *Green Chemistry*, 17(9):4628–4636, 2015.

[322] J. L. Munera-Echeverri, V. Martinsen, L. T. Strand, V. Zivanovic, G. Cornelissen, and J. Mulder. Cation exchange capacity of biochar: An urgent method modification. *Science of the Total Environment*, 642:190–197, 2018.

[323] Zohaib Abbas, Shafaqat Ali, Muhammad Rizwan, Ihsan Elahi Zaheer, Afifa Malik, Muhammad Ahsan Riaz, Muhammad Rizwan Shahid, Muhammad Zia ur Rehman, and Mohammad I. Al-Wabel. A critical review of mechanisms involved in the adsorption

of organic and inorganic contaminants through biochar. *Arabian Journal of Geosciences*, 11(16), 2018.

[324] E.I. El-Shafey. Removal of Zn(II) and Hg(II) from aqueous solution on a carbonaceous sorbent chemically prepared from rice husk. *Journal of Hazardous Materials*, 175(1-3):319–327, 3 2010.

[325] Xinde Cao, Lena Ma, Bin Gao, and Willie Harris. Dairy-Manure Derived Biochar Effectively Sorbs Lead and Atrazine. *Environmental Science & Technology*, 43(9):3285–3291, 5 2009.

[326] Peng Liu, Carol J. Ptacek, David W. Blowes, and Richard C. Landis. Mechanisms of mercury removal by biochars produced from different feedstocks determined using X-ray absorption spectroscopy. *Journal of Hazardous Materials*, 308:233–242, 5 2016.

[327] Jong-Hwan Park, Jim J. Wang, Baoyue Zhou, Joseph E.R. Mikhael, and Ronald D. DeLaune. Removing mercury from aqueous solution using sulfurized biochar and associated mechanisms. *Environmental Pollution*, 244:627–635, 1 2019.

[328] Simona Regenspurg and Stefan Peiffer. Arsenate and chromate incorporation in schwertmannite. *Applied Geochemistry*, 20(6):1226–1239, 6 2005.

[329] Laura Klüpfel, Marco Keiluweit, Markus Kleber, and Michael Sander. Redox Properties of Plant Biomass-Derived Black Carbon (Biochar). *Environmental Science & Technology*, 48(10):5601–5611, 5 2014.

[330] Antonin Prévoteau, Frederik Ronsse, Inés Cid, Pascal Boeckx, and Korneel Rabaey. The electron donating capacity of biochar is dramatically underestimated. *Scientific Reports*, 6:1–11, 2016.

[331] Zibo Xu, Xiaoyun Xu, Yue Zhang, Yulu Yu, and Xinde Cao. Pyrolysis-temperature dependent electron donating and mediating mechanisms of biochar for Cr(VI) reduction. *Journal of Hazardous Materials*, 388:121794, 4 2020.

[332] Jiwon Kim, Jinyoung Song, Seung-Mok Lee, and Jinho Jung. Application of iron-modified biochar for arsenite removal and toxicity reduction. *Journal of Industrial and Engineering Chemistry*, 80:17–22, 12 2019.

[333] Yang Yu, Qiang An, Lin Jin, Ning Luo, Zheng Li, and Junnan Jiang. Unraveling sorption of Cr (VI) from aqueous solution by FeCl3 and ZnCl2-modified corn stalks biochar: Implicit mechanism and application. *Bioresource Technology*, 297(174):122466, 2 2020.

[334] John Marsden and Ian House. *The chemistry of gold extraction*. Ellis Horwood series in metals and associated materials. Ellis Horwood, New York ;, 1992.

[335] H.C. C. Hughes and H.G. G. Linge. The kinetics of gold loading from gold(III) chloride solution onto fresh activated coconut carbon. *Hydrometallurgy*, 22(1-2):57–65, 6 1989.

[336] Serdar Aktas and M. Hakan Morcali. Gold uptake from dilute chloride solutions by a Lewatit TP 214 and activated rice husk. *International Journal of Mineral Processing*, 101(1-4):63–70, 11 2011.

[337] Jean-christophe Parisien-la Salle. *In-situ Adsorption of Gold ( III ) Chloride on Activated Carbon Under Pressure Oxidation-Leaching Conditions*. PhD thesis, McGill University, 2012.

[338] Marek Wojnicki, Magdalena Luty-Błocho, Robert P. Socha, Krzysztof Mech, Zbigniew Pedzich, Krzysztof Fitzner, and Ewa Rudnik. Kinetic studies of sorption and reduction

of gold(III) chloride complex ions on activated carbon Norit ROX 0.8. *Journal of Industrial and Engineering Chemistry*, 29:289–297, 2015.

[339] Y. F. Jia, C. J. Steele, I. P. Hayward, and K. M. Thomas. Mechanism of adsorption of gold and silver species on activated carbons. *Carbon*, 36(9):1299–1308, 1998.

[340] Gavin M. Mudd. Global trends in gold mining: Towards quantifying environmental and resource sustainability. *Resources Policy*, 32(1-2):42–56, 2007.

[341] Ronald Eisler and Stanley N Wiemeyer. Cyanide Hazards to Plants and Animals from Gold Mining and Related Water Issues. In *Reviews of Environmental Contamination and Toxicology*, pages 21–54. Springer New York, New York, NY, 2004.

[342] S Syed. Recovery of gold from secondary sources—A review. *Hydrometallurgy*, 115-116:30–51, 2012.

[343] Gavin Hilson and A. J. Monhemius. Alternatives to cyanide in the gold mining industry: what prospects for the future? *Journal of Cleaner Production*, 14(12-13 SPEC. ISS.):1158–1167, 2006.

[344] O.N. Kononova, A.G. Kholmogorov, N.V. Danilenko, S.V. Kachin, Y.S. Kononov, and Zh.V. Dmitrieva. Sorption of gold and silver on carbon adsorbents from thiocyanate solutions. *Carbon*, 43(1):17–22, 2005.

[345] W.P. Staunton. Carbon-in-pulp. In Mike D. Adams and B. A. Wills, editors, *Advances in Gold Ore Processing*, pages 562–587. Elsevier, 2005.

[346] François Farges, Julia A. Sharps, and Gordon E. Brown. Local environment around gold (III) in aqueous chloride solutions: An EXAFS spectroscopy study. *Geochimica et Cosmochimica Acta*, 57(6):1243–1252, 3 1993.

[347] Ingrid Berrodier, François Farges, Marc Benedetti, Markus Winterer, Gordon E. Brown, and Michel Deveughèle. Adsorption mechanisms of trivalent gold on iron- and aluminum-(oxy)hydroxides. Part 1: X-ray absorption and Raman scattering spectroscopic studies of Au(III) adsorbed on ferrihydrite, goethite, and boehmite. *Geochimica et Cosmochimica Acta*, 68(14):3019–3042, 7 2004.

[348] Kwang Soo Nam, Byoung Hi Jung, Jeon Woong An, Tae Jun Ha, Tam Tran, and Myong Jun Kim. Use of chloride–hypochlorite leachants to recover gold from tailing. *International Journal of Mineral Processing*, 86(1-4):131–140, 3 2008.

[349] J. Viñals, E. Juan, M. Ruiz, E. Ferrando, M. Cruells, A. Roca, and J. Casado. Leaching of gold and palladium with aqueous ozone in dilute chloride media. *Hydrometallurgy*, 81(2):142–151, 2 2006.

[350] A. M. Petrova, A. E. Nikolaev, and A. G. Kasikov. Extraction of gold(III) from hydrochloric acid solutions with high-molecular aliphatic alcohols. *Russian Journal of Applied Chemistry*, 87(2):234–240, 2014.

[351] Mohd Jumain Jalil, Haris Halimi Mohd Azam Zaki, Intan Suhada Azmi, Ariff Aminuddin Ahmad Zulkifli, Muhammad Hazim Abu Bakar, and Anas Bin Mohd Rashid. Recovery of Gold from Pregnant Thiourea Leaching Solution by Synergistic Extraction. *IOP Conference Series: Materials Science and Engineering*, 778(1):012046, 5 2020.

[352] L Gardea-Torresday, K. J. Tiemann, G. Gamez, K Dokken, I Canoaguilera, L.R. Furenlid, and M Renner. Reduction and Accumulation of Gold(III) by Medicago sativa Alfalfa

Biomass: X-ray Absorption Spectroscopy, pH, and Temperature Dependence. *Environmental Science and Technology*, 34:4392, 2000.

[353] Nilanjana Das. Recovery of precious metals through biosorption - A review. *Hydrometallurgy*, 103(1-4):180–189, 2010.

[354] Rumi Chand, Takanori Watari, Katsutoshi Inoue, Hidetaka Kawakita, Hom Nath Luitel, Durga Parajuli, Toshio Torikai, and Mitsunori Yada. Selective adsorption of precious metals from hydrochloric acid solutions using porous carbon prepared from barley straw and rice husk. *Minerals Engineering*, 22(15):1277–1282, 12 2009.

[355] Refiloe Tsolele, Fanyana Moses Mtunzi, Michael John Klink, and Vusumzi Emmanuel Pakade. An alternative low-cost adsorbent for gold recovery from cyanide-leached liquors: Adsorption isotherm and kinetic studies. *Adsorption Science & Technology*, 37(1-2):3–23, 3 2019.

[356] T.M. Sun and W.T. Yen. Kinetics of Gold Chloride Adsorption Onto Activated Carbon. *Minerals Engineering*, 6(I):17–29, 1993.

[357] Gloria J. McDougall and Robert D. Hancock. Gold complexes and activated carbon. *Gold Bulletin*, 14(4):138–153, 12 1981.

[358] Sabry M. Shaheen, Nabeel Khan Niazi, Noha E. E. Hassan, Irshad Bibi, Hailong Wang, Daniel C. W. Tsang, Yong Sik Ok, Nanthi Bolan, and Jörg Rinklebe. Wood-based biochar for the removal of potentially toxic elements in water and wastewater: a critical review. *International Materials Reviews*, 64(4):216–247, 5 2019.

[359] Francisco de la Pena, Eric Prestat, Vidar Tonaas Fauske, Pierre Burdet, Petras Jokubauskas, Magnus Nord, Tomas Ostasevicius, Katherine E MacArthur, Mike Sarahan, Duncan N Johnstone, Joshua Taillon, Jonas Lehnemann, Vadim Migunov, Alberto Eljarrat, Jan Caron, Thomas Aarholt, Stefano Mazzucco, Michael Walls, Tom Slater, Florian Winkler, pquinn-dls, Ben Martineau, Gael Donval, Robert McLeod, Eric R Hoglund, Ivo Alxneit, Daniel Lundeby, Trond Henninen, Luiz Fernando Zagonel, and Andreas Garmannslund. HyperSpy v1.5.2. *Zenodo*, 9 2019.

[360] A. J. Kropf, J. Katsoudas, S. Chattopadhyay, T. Shibata, E. A. Lang, V. N. Zyryanov, B. Ravel, K. McIvor, K. M. Kemner, K. G. Scheckel, S. R. Bare, J. Terry, S. D. Kelly, B. A. Bunker, and C. U. Segre. The new MRCAT (Sector 10) bending magnet beamline at the advanced photon source. *AIP Conference Proceedings*, 1234:299–302, 2010.

[361] Matthew Newville. Larch: An Analysis Package for XAFS and Related Spectroscopies. *Journal of Physics: Conference Series*, 430, 4 2013.

[362] Tsu-Chien Weng, Geoffrey S. Waldo, and James E. Penner-Hahn. A method for normalization of X-ray absorption spectra. *Journal of Synchrotron Radiation*, 12(4):506–510, 7 2005.

[363] Jari Hyväluoma, Sampo Kulju, Markus Hannula, Hanne Wikberg, Anssi Källi, and Kimmo Rasa. Quantitative characterization of pore structure of several biochars with 3D imaging, 2017.

[364] Keith Jones, Girish Ramakrishnan, Minori Uchimiya, and Alexander Orlov. New Applications of X-ray Tomography in Pyrolysis of Biomass: Biochar Imaging. *Energy & Fuels*, 29(3):1628–1634, 3 2015.

[365] Jean François Gaillard, Cheng Chen, Susa H. Stonedahl, Boris L.T. Lau, Denis T. Keane, and Aaron I. Packman. Imaging of colloidal deposits in granular porous media by X-ray difference micro-tomography. *Geophysical Research Letters*, 34(18):2–6, 2007.

[366] Myles Gray, Mark G. Johnson, Maria I. Dragila, and Markus Kleber. Water uptake in biochars: The roles of porosity and hydrophobicity. *Biomass and Bioenergy*, 61:196–205, 2 2014.

[367] Catherine E. Brewer, Victoria J. Chuang, Caroline A. Masiello, Helge Gonnermann, Xiaodong Gao, Brandon Dugan, Laura E. Driver, Pietro Panzacchi, Kyriacos Zygourakis, and Christian A. Davies. New approaches to measuring biochar density and porosity. *Biomass and Bioenergy*, 66:176–185, 7 2014.

[368] Xiangdong Zhu, Yuchen Liu, Feng Qian, Hua Shang, Xinchao Wei, Shicheng Zhang, Jianmin Chen, and Zhiyong Jason Ren. Carbon transmission of CO2 activated nano-MgO carbon composites enhances phosphate immobilization. *Journal of Materials Chemistry A*, 00:1–9, 2018.

[369] Dun Chen, Xiaobing Wang, Xiaoli Wang, Ke Feng, Jincheng Su, and Junneng Dong. The mechanism of cadmium sorption by sulphur-modified wheat straw biochar and its application cadmium-contaminated soil. *Science of The Total Environment*, 714:136550, 4 2020.

[370] Singfoong Cheah, Shealyn C. Malone, and Calvin J. Feik. Speciation of sulfur in biochar produced from pyrolysis and gasification of oak and corn stover. *Environmental Science and Technology*, 48(15):8474–8480, 2014.

[371] J. W. Watkins, R. C. Elder, Benjamin Greene, and Dennis W. Darnall. Determination of gold binding in an algal biomass using EXAFS and XANES spectroscopies. *Inorganic Chemistry*, 26(7):1147–1151, 4 1987.

[372] Christian Wurzer and Ondřej Mašek. Feedstock doping using iron rich waste increases the pyrolysis gas yield and adsorption performance of magnetic biochar for emerging contaminants. *Bioresource Technology*, 321(December 2020):124473, 2 2021.

[373] Timothy S. Pasakarnis, Maxim I. Boyanov, Kenneth M. Kemner, Bhoopesh Mishra, Edward J. O'Loughlin, Gene Parkin, and Michelle M. Scherer. Influence of Chloride and Fe(II) Content on the Reduction of Hg(II) by Magnetite. *Environmental Science & Technology*, 47(13):6987–6994, 7 2013.

[374] Christopher Hammond. Fourier analysis in diffraction and image formation. In *The Basics of Crystallography and Diffraction*, chapter Eleven, pages 329–361. Oxford University Press, 5 2015.

[375] Jean-Raymond Gavarri and Claude Carel. The complex nonstoichiometry of wüstite Fe1-O: Review and comments. *Progress in Solid State Chemistry*, 53(October 2018):27–49, 3 2019.

[376] G. Nihoul, J.-R. Gavarri, and C. Carel. The commensurate (10/4) cluster model in quenched wüstite P ". New simulation of HREM direct images. *Acta Crystallographica Section B Structural Science*, 47(3):333–337, 6 1991.

[377] Takashi Ishiguro and Shigemaro Nagakura. Structure of the Commensurate Phase P" of Wüstite Fe 0.902 O Studied by High Resolution Electron Microscopy. *Japanese Journal of Applied Physics*, 24(Part 2, No. 9):L723–L726, 9 1985.

[378] Md Samrat Alam, Brendan Bishop, Ning Chen, Salman Safari, Viola Warter, James M. Byrne, Tyler Warchola, Andreas Kappler, Kurt O. Konhauser, and Daniel S. Alessi. Reusable magnetite nanoparticles–biochar composites for the efficient removal of chromate from water. *Scientific Reports*, 10(1):19007, 12 2020.

[379] Alexander Gubbens, Melanie Barfels, Colin Trevor, Ray Twesten, Paul Mooney, Paul Thomas, Nanda Menon, Bernd Kraus, Chengye Mao, and Brian McGinn. The GIF Quantum, a next generation post-column imaging energy filter. *Ultramicroscopy*, 110(8):962–970, 7 2010.

[380] H.M. Freeman, J.P.H. Perez, N. Hondow, L.G. Benning, and A.P. Brown. Beam-induced oxidation of mixed-valent Fe (oxyhydr)oxides (green rust) monitored by STEM-EELS. *Micron*, 122(January):46–52, 7 2019.

[381] Anatoly I. Frenkel, Aaron Yevick, Chana Cooper, and Relja Vasic. Modeling the Structure and Composition of Nanoparticles by Extended X-Ray Absorption Fine-Structure Spectroscopy. *Annual Review of Analytical Chemistry*, 4(1):23–39, 7 2011.

[382] Anatoly I. Frenkel. Solving the structure of nanoparticles by multiple-scattering EXAFS analysis. *Journal of Synchrotron Radiation*, 6(3):293–295, 5 1999.

[383] A. Balerna, E. Bernieri, P. Picozzi, A. Reale, S. Santucci, E. Burattini, and S. Mobilio. A structural investigation on small gold clusters by EXAFS. *Surface Science*, 156:206–213, 6 1985.

[384] Huan Peng, Carolyn I. Pearce, Weifeng Huang, Zhenli Zhu, Alpha T. N'Diaye, Kevin M. Rosso, and Juan Liu. Reversible FeII uptake/release by magnetite nanoparticles. *Environmental Science: Nano*, 5(7):1545–1555, 2018.

[385] Ravinder K. Garlapalli, Benjamin Wirth, and M. Toufiq Reza. Pyrolysis of hydrochar from digestate: Effect of hydrothermal carbonization and pyrolysis temperatures on pyrochar formation. *Bioresource Technology*, 220:168–174, 11 2016.

[386] D. A. Outka and J. Stöhr. Curve fitting analysis of near-edge core excitation spectra of free, adsorbed, and polymeric molecules. *The Journal of Chemical Physics*, 88(6):3539–3554, 3 1988.

[387] Joachim Stöhr. *NEXAFS Spectroscopy*, volume 25 of *Springer Series in Surface Sciences*. Springer Berlin Heidelberg, Berlin, Heidelberg, 1 edition, 1992.

[388] Hai Nguyen Tran, Sheng Jie You, Ahmad Hosseini-Bandegharaei, and Huan Ping Chao. Mistakes and inconsistencies regarding adsorption of contaminants from aqueous solutions: A critical review. *Water Research*, 120:88–116, 2017.

[389] Ahsan Habib, Masaaki Tabata, and Ying Guang Wu. Formation of Gold Nanoparticles by Good's Buffers. *Bulletin of the Chemical Society of Japan*, 78(2):262–269, 2 2005.